WIMP Search and a Cherenkov Detector Prototype for ILC Polarimetry

Dissertation

zur Erlangung des Doktorgrades

des Department Physik

der Universität Hamburg

vorgelegt von

Christoph Bartels

aus Neustadt/Holstein

Hamburg

2011

Gutachterin/Gutachter der Dissertation	:	Dr. Jenny List Prof. Dr. Peter Schleper
Gutachterin/Gutachter der Disputation	:	Dr. Jenny List Dr. Erika Garutti
Datum der Disputation	:	7. September 2011
Vorsitzender des Prüfungsausschusses	:	Dr. Georg Steinbrück
Vorsitzender des Promotionsausschusses	:	Prof. Dr. Peter H. Hauschildt
Leiterin des Department Physik	:	Prof. Dr. Daniela Pfannkuche
Dekan der MIN Fakultät	:	Prof. Dr. Heinrich Graener

Abstract

The planned International Linear Collider (ILC) will be an essential experiment to precisely determine the properties and structure of physics at the TeV scale. An important feature of the ILC is the possibility to use polarized electrons and positrons.
In part 1 of this thesis, a model independent search for Weakly Interacting Massive Particles (WIMPs) at ILC is presented. The signal channel under study is direct WIMP pair production with associated Initial State Radiation (ISR), $e^+e^- \to \chi\chi\gamma$, where the WIMPs leave the detector without any further interaction, and only the emitted photon is detected. From the energy spectrum of the detected photons the coupling structure, cross sections, masses and the quantum number of the dominant partial wave in the production process can be inferred. The analysis includes the dominant SM, as well as machine-induced backgrounds, and is performed using a full simulation of the ILD detector concept. For an integrated luminosity of $\mathcal{L} = 500$ fb^{-1}, the signal cross sections can be measured to a precision of 3%, dominated by systematic uncertainties on the polarization measurement of the initial electrons and positrons. Masses can be measured to a precision of up to 2% by a comparison of the data photon spectrum to parametrized template spectra.
In part 2 of this thesis, a Cherenkov detector prototype for Compton polarimetry at ILC is presented. For the polarization measurement a systematic uncertainty of $\delta P/P = 0.25\%$ or better is envisioned. To achieve this goal, the Cherenkov detector has to be precisely aligned with the fan of Compton scattered electrons and its signal response needs to be highly linear. For the detector prototype data driven alignment strategies have been developed by comparing data recorded at the Elsa accelerator in Bonn, Germany, with detailed Geant4 simulations. With the use of multi-anode photomultipliers, data driven alignment strategies promise to provide the required precision. At ILC, these methods could reduce the luminosity spent on calibration scans considerably. The observed dynamic range and systematic uncertainties of the prototype detector are compatible with those expected for polarization measurements in an ILC-like environment.

Zusammenfassung

Der geplante International Linear Collider (ILC) wird die Eigenschaften neuer Physik an der TeV-Skala vermessen. Ein wichtiges Merkmal des ILC ist die Möglichkeit polarisierte Elektronen und Positronen zu nutzen.
In Teil 1 dieser Arbeit wird eine modellunabhängige Suche nach schwach wechselwirkenden schweren Elementarteilchen (WIMPs) vorgestellt. Der untersuchte Signalkanal ist WIMP Paarerzeugung mit assoziierter Initial State Radiation (ISR), $e^+e^- \rightarrow \chi\chi\gamma$. Die WIMP-Kandidaten verlassen den Detektor ohne weitere Wechselwirkung, und nur das emittierte Photon wird detektiert. Aus dem Energiespektrum der detektierten Photonen lässt sich auf die Kopplungsstruktur, die Wirkungsquerschnitte, die Massen und auf die Quantenzahl der dominierenen Partialwelle im Produktionsprozess schließen. Die Analyse beinhaltet den dominanten SM-Untergrund, sowie Beschleuniger-induzierte Untergründe und wurde in voller Simulation des ILD-Detektorkonzeptes durchgeführt. Mit einer integrierten Luminosität von $\mathcal{L} = 500$ fb^{-1} lassen sich die Wirkungsquerschnitte mit einer Präzision von 3% bestimmen. Die Unsicherheit wird dominiert von der Präzision der Polarisationsmessung für die Elektronen- und Positronenstrahlen. Durch einen Vergleich des gemessenen Photonspektrums mit parametrisierten Spektrumsvorhersagen sind die Massen der WIMP-Kandidaten mit einer Präzision von bis zu 2% messbar.
Teil 2 dieser Arbeit behandelt einen Prototypen eines Cherenkov-Detektors für Compton-Polarimetrie am ILC. Für Polarisationsmessungen am ILC ist eine systematische Unsicherheit von $\delta P/P = 0.25\%$ oder besser anvisiert. Zur Erreichung dieses Zieles muss der Cherenkov-Detektor präzise gegenüber dem Fächer gestreuter Comptonelektronen ausgerichtet werden und die Detektorantwort muss höchst linear sein. Für den Detektorprototypen wurden Ausrichtungsstrategien durch Abgleich von am ELSA-Beschleuniger in Bonn aufgezeichneten Daten mit einer detaillierten GEANT4-basierten Simulation entwickelt. Durch Benutzung segmentierter Photodetektoren verspricht eine daten-basierte Detektorausrichtung eine signifikante Reduktion der für Kalibrationsscans benötigten Luminosität. Der beobachtete dynamische Bereich des Detektors und die systematischen Unsicherheiten sind kompatibel mit den Anforderungen an Polarisationsmessungen in einer ILC-ähnlichen experimentellen Umgebung.

Contents

Chapter 1

Introduction

With the start-up of the Large Hadron Collider (LHC) at CERN in Geneva, Switzerland, a new region of particle physics is going to be explored at center-of-mass energies of up to 14 TeV. Although it is not clear yet, what will be found at the LHC, the discovery potential of the LHC is well studied. For example, if there is a Higgs boson, it is expected that its mass will be measured to the percent-level with the multi-purpose detectors ATLAS and CMS [1, 2]. If nature is supersymmetric, there is a good chance that the lightest Higgs and other particles of the supersymmetric sector will be observed.

Whatever the outcome of the LHC experiments will be, either the discovery of new physics, or maybe the lack thereof, the planned International Linear Collider (ILC) will be essential in precisely resolving the structure of the new physics, or in providing stringent boundaries to the possible parameter space. While the ILC center-of-mass energy of up to 1 TeV is lower than at LHC, its use of electrons and positrons as probes provides a well known, very clean initial state and benign environment, extending its reach to higher energies by its sensitivity to higher order loop corrections. An important feature of the ILC is the possibility to polarize the particle beams, which reduces backgrounds and enhances signals, and gives access to the structure of possible new physics.

In this thesis, two analyses are presented in the framework of the planned ILC. The first one focuses on the capability of the ILC in detecting and measuring the masses and coupling structure of weakly interacting Dark Matter (DM) particles χ, produced in radiative pair production $e^+e^- \to \chi\chi\gamma$. The DM candidates leave the interaction region of the ILC without any further interaction, and only the photons are detected. The analysis is performed in a model independent way, covering a broad range of possible extensions to the Standard Model of particle physics (SM). The properties of the DM candidates are inferred from the energy spectra of the emitted photons. The analysis is very sensitive to the precision of the polarization measurement of the initial beams. At ILC, the beam polarization P will be measured with a system of Compton polarimeters to an unprecedented systematic precision of $\delta P/P \leq 0.25\%$. An integral part of the polarization measurement is the detection of Compton scattered electrons with segmented Cherenkov detectors. The second analysis in this thesis presents the design and simulation of a first Cherenkov detector prototype and measurement results obtained in testbeam campaigns at the DESY II accelerator in Hamburg and the ELSA accelerator in Bonn, Germany.

In the following Chapter 2 the electroweak sector of the SM is reviewed and the observational evidence for cosmological DM presented. Chapter 3 introduces the ILC accelerator,

its baseline parameters and running scenarios. Closing this introduction, Chapter 4 outlines the ILD detector concept, on which the DM search is based.

Chapter 2

Theoretical context

2.1 The Standard Model of particle physics

The Standard Model of Particle Physics (SM) comprises our current knowledge of the fundamental particles and their interactions. Over the years since its formulation, it has proved to be remarkably successful in predicting and describing the known phenomena of the natural world on the smallest scales.

2.1.1 Historical development of the Standard Model

The success story of the SM began with the extension of the theory of quantum electrodynamics (QED) to the weak interaction by S. L. Glashow, S. Weinberg and A. Salam [1] [3, 4, 5] in the mid-sixties of the 20^{th} century. The authors proposed gauge invariance under $SU(2)\otimes U(1)$ as the fundamental symmetry for the unified theory of electromagnetic and weak interactions for the leptonic sector (GSW electroweak theory). In the GSW theory the weak interactions are mediated by heavy gauge bosons. Their large masses ensure the short range characteristics of the weak interaction, but the introduction of the boson masses spoils the gauge symmetry. To overcome this problem, the GSW theory is spontaneously broken by means of the Higgs mechanism [6, 7, 8, 9], proposed by P. Higgs, F. Englert and R. Brout. The GSW theory made the following important predictions:

- the existence of weak neutral currents.
- the weak interactions are mediated by three heavy gauge bosons.
- the existence of a neutral scalar particle responsible for the symmetry breaking and mass generation. This particle came to be known as the Higgs boson.

The first two of the above predictions were spectacularly confirmed in experiments at CERN. In 1973 the neutral weak interaction was observed in the Gargamelle bubble chamber in neutrino scattering processes [10]. Ten years later the existence of the predicted heavy gauge bosons Z, W^+ and W^- could be verified in $p\bar{p}$ collisions with the UA1 and UA2 experiments at

[1] Nobel Prize in 1979.

the CERN SPS [11]. Their masses and total widths have been measured at the LEP accelerator to be [12]:

$$M_Z = 91.186 \pm 0.0021 \text{ GeV} \quad (2.1)$$
$$\Gamma_Z = 2.4952 \pm 0.0023 \text{ GeV} \quad (2.2)$$
$$M_W = 80.398 \pm 0.0025 \text{ GeV} \quad (2.3)$$
$$\Gamma_W = 2.141 \pm 0.041 \text{ GeV} \quad (2.4)$$

The only prediction left to be verified is the Higgs mechanism. Although the Higgs boson has not yet been found, direct searches at LEP have provided an experimental lower bound on the Higgs mass of $m_H > 114.1$ GeV [13].

2.1.2 Gauge symmetries

In the standard model of particle physics, all fermions (spin-1/2 particles) are described by complex spinors $\Psi(x)$ with the space-time coordinates x. By demanding local gauge invariance of the equations of motion, the interactions between the fermions are naturally generated, and mediated through the exchange of gauge bosons (spin-1 particles).
Invariance under local gauge transformation means that a phase transformation

$$\Psi(x) \rightarrow \Psi'(x) = e^{i\chi(x)}\Psi(x) = U(x)\Psi(x) \quad (2.5)$$

leaves the Lagrangian $\mathcal{L}$ unchanged. The set of unitary transformations U ($U^\dagger U = 1$) forms a mathematical group. A general unitary transformation can be written as

$$U(x) = \exp\left[-i\sum_{j=1}^{n}\alpha_j(x)\mathcal{G}_j\right], \quad (2.6)$$

where the n generators $\mathcal{G}_j$ determine the algebra of the n-dimensional group of transformations, and the real-valued functions $\alpha_j(x)$ specify the local transformation. If the commutator of any two generators can be expressed as

$$[\mathcal{G}_i, \mathcal{G}_j] = i\sum_{k=1}^{n} f_{ijk}\mathcal{G}_k, \quad (2.7)$$

the group is called a Lie group. The parameters f_{ijk} are the totally antisymmetric structure constants. If the generators commute, i.e. $[\mathcal{G}_i, \mathcal{G}_j] = 0$, the group is called Abelian.
As an example, the principle of gauge invariance in quantum electrodynamics (QED) is shown here. The Lagrangian of a free fermion field with mass m is

$$\mathcal{L}_{free} = i\overline{\Psi}\gamma^\mu\partial_\mu\Psi - m\overline{\Psi}\Psi. \quad (2.8)$$

Because of the partial derivatives, a phase transformation under the abelian $U(1)$ symmetry group of the form of Equation 2.5 results in additional terms to the transformed Lagrangian. In order to fulfill the requirement of gauge invariance, the partial derivative ∂_μ is extended to the covariant derivative $\mathcal{D}_\mu$

$$\mathcal{D}_\mu = \partial_\mu - ieA_\mu, \quad (2.9)$$

introducing the vector gauge field A_μ, which transforms under the gauge transformation Equation 2.5 as

$$A_\mu \rightarrow A'_\mu = A_\mu + \frac{1}{e}\partial_\mu \chi. \tag{2.10}$$

With this gauge field, the Lagrangian

$$\mathcal{L}_{free} = i\overline{\Psi}\gamma^\mu \mathcal{D}_\mu \Psi - m\overline{\Psi}\Psi \tag{2.11}$$

is invariant under local gauge transformations. The vector field which was introduced according to the principle of local gauge invariance, is identified with the photon which couples to the fermion with the coupling strength e, the elementary electric charge. The Lagrangian of Equation 2.11 is however not a full description of a free fermion in QED, because it does not include a kinetic term associated with the just introduced gauge field A_μ. Adding such a term results in the final QED Lagrangian

$$\mathcal{L}_{QED} = \overline{\Psi}(i\gamma^\mu \partial_\mu - m)\Psi + e\overline{\Psi}\gamma^\mu A_\mu \Psi - \frac{1}{4}F_{\mu\nu}F^{\mu\nu} \tag{2.12}$$

with the gauge invariant electromagnetic field tensor $F_{\mu\nu} = \partial_\mu A_\nu - \partial_\nu A_\mu$. It is important to note that the QED Lagrangian does not include a mass term $m_\gamma^2 A_\mu A^\mu$ for the gauge boson. Such a term would inevitably spoil the gauge invariance, but since the photon is massless, such a term is not required. However, massive gauge fields as for the W and Z bosons can not be generated so easily. Their masses have to be introduced via the Higgs mechanism.

2.1.3 Electroweak theory

The fermionic particle content of the SM of particle physics is listed in Table 2.1. The leptons and quarks are grouped into three generations, which differ only in mass. The quarks and charged leptons of the second and third generations are unstable and decay into first generation fermions. While the quarks experience electroweak and strong interactions, the leptons only participate in the electroweak interactions.

	Generations			Quantum numbers		
	1.	2.	3.	Q	T_w^3	Y_w
leptons	$\begin{pmatrix}\nu_e \\ e\end{pmatrix}_L$	$\begin{pmatrix}\nu_\mu \\ \mu\end{pmatrix}_L$	$\begin{pmatrix}\nu_\tau \\ \tau\end{pmatrix}_L$	0 -1	$1/2$ $-1/2$	-1 -1
	e_R	μ_R	τ_R	-1	0	-2
quarks	$\begin{pmatrix}u \\ d'\end{pmatrix}_L$	$\begin{pmatrix}c \\ s'\end{pmatrix}_L$	$\begin{pmatrix}t \\ b'\end{pmatrix}_L$	$2/3$ $-1/3$	$1/2$ $-1/2$	$1/3$ $1/3$
	u_R	c_R	t_R	$2/3$	0	$4/3$
	d_R	s_R	b_R	$-1/3$	0	$-2/3$

Table 2.1: *The particles of the SM and their quantum numbers (electric charge Q, third component of the weak isospin T_w^3 and weak hypercharge Y_w). The primed quark states d', s', b' are eigenstates to the weak interaction and are mixtures of the mass eigenstates d, s, b.*

The interactions of the electroweak sector of the SM are introduced by demanding gauge invariance under $U(1)_Y \otimes SU(2)_L$ transformations, generated by the hypercharge Y and the weak isospin $\vec{T}$. The weak isospin is expressed by the Pauli matrices

$$\vec{T} = \frac{1}{2}\vec{\sigma}. \tag{2.13}$$

The third component of the weak isospin and the hypercharge Y are related to the electric charge by

$$Q = \frac{Y}{2} + T_3. \tag{2.14}$$

All fermions participate in the Neutral Current electroweak interaction, but only left-chiral fermion states experience Charged Current electroweak interactions. This behavior is represented by the grouping of the left-chiral fermions into isospin doublets in the first and second row of Table 2.1. The right-handed fermions e_R, u_R etc. are singlets under the non-abelian $SU(2)_L$ group. The weak eigenstates of the down-type quarks are not the same as the mass eigenstates, but are a linear combination of the down-type mass eigenstates, given by the coefficients of the Cabibbo-Kobayashi-Maskawa matrix (CKM)

$$d_L^{i\prime} = \sum_{j=1}^{3} V_{CKM}^{ij} d_L^j, \tag{2.15}$$

where the indices i, j indicate the fermion generation. This rotation in isospin space of the down-type quarks allows for flavor changing charged currents.
In a similar way as for QED, the requirement of gauge invariance under $U(1)_Y \otimes SU(2)_L$ introduces four gauge vector fields B_μ and W_μ^i, $i = 1, 2, 3$, which lead to the covariant derivative

$$\mathcal{D}_\mu = \partial_\mu - ig'YB_\mu - ig\vec{T}\cdot\vec{W}. \tag{2.16}$$

The gauge field B_μ is associated with the hypercharge Y, and the W_μ^i are related to the weak isospin $\vec{T}$. The parameters g and g' in Equation 2.16 are the coupling constants of $U(1)_Y$ and $SU(2)_L$, respectively. The electroweak Lagrangian for massless fermions f and their interactions with the gauge fields becomes:

$$\mathcal{L}_{EW}^{fermion} = i\sum_f \overline{\Psi}\gamma^\mu\mathcal{D}_\mu\Psi = i\sum_f \overline{\Psi}\gamma^\mu\partial_\mu\Psi + g'Y\sum_f \overline{\Psi}\gamma^\mu\Psi B_\mu + g\sum_f \overline{\Psi}_L\gamma^\mu\vec{T}\cdot\vec{W}_\mu\Psi_L. \tag{2.17}$$

The fields B_μ and W_μ^i are not identical with the photon field A_μ and the weak mediators $W^\pm$ and Z. However, the weak bosons B and W^i can be rotated to a physical basis which contains two charged bosons $W_\mu^\pm$ and two neutral bosons Z_μ and A_μ. The two bases are related via:

$$\begin{aligned} W^\pm &= \frac{1}{\sqrt{2}}(W^1 \pm iW^2) \\ \begin{pmatrix} Z \\ A \end{pmatrix} &= \begin{pmatrix} \cos\Theta_w & -\sin\Theta_w \\ \sin\Theta_w & \cos\Theta_w \end{pmatrix} \begin{pmatrix} W^3 \\ B \end{pmatrix}, \end{aligned} \tag{2.18}$$

with the weak mixing angle Θ_w. There exists a fundamental relationship between Θ_w and the coupling constants g and g':

$$\cos\Theta_w = \frac{g}{\sqrt{g'^2 + g^2}}. \tag{2.19}$$

Furthermore, requiring the coupling strength of the electromagnetic field to be the electric charge e, another important relation for the coupling constants can be deduced:

$$g' \cos\Theta_w = g \sin\Theta_w = e. \tag{2.20}$$

The full electroweak Lagrangian also has to include the kinetic terms of the gauge fields and their self-couplings:

$$\mathcal{L}_{EW}^{boson,kin} = -\frac{1}{4}\vec{W}_{\mu\nu}\vec{W}^{\mu\nu} - \frac{1}{4}B_{\mu\nu}B^{\mu\nu}, \tag{2.21}$$

where

$$\begin{aligned} \vec{W}_{\mu\nu} &= \partial_\mu \vec{W}_\nu - \partial_\nu \vec{W}_\mu + g\vec{W}_\mu \times \vec{W}_\nu \\ B_{\mu\nu} &= \partial_\mu B_\nu - \partial_\nu B_\mu. \end{aligned} \tag{2.22}$$

The self-coupling of the weak mediators originates from the non-abelian structure of the $SU(2)_L$ symmetry group. A local gauge transformation under $U(1)_Y \otimes SU(2)_L$ is given by

$$\Psi'(x) = U(x)\Psi(x) = \exp\left[\frac{i}{2}\left(\beta^j(x)\sigma_j + Y\alpha(x)\right)\right]\Psi(x) \tag{2.23}$$

with $j = 1, 2, 3$. In order to keep the Lagrangian invariant, the gauge fields have to transform according to:

$$\begin{aligned} W'_\mu &= U(x)W_\mu U^{-1}(x) + \frac{i}{g}\left[\partial_\mu U(x)\right]U^{-1}(x) \\ B'_\mu &= U(x)B_\mu U^{-1}(x) + \frac{i}{g'}\left[\partial_\mu U(x)\right]U^{-1}(x). \end{aligned} \tag{2.24}$$

With these transformations gauge invariance holds, but only as long as all particles and gauge fields are massless. From experiment however it is known that except for the photon (and the SM neutrinos) all particles carry mass. In particular, the vector bosons $W^\pm$ and Z are exceptionally heavy. The solution to this problem is provided by the Higgs mechanism.
To include the strong interaction into the SM, another gauge symmetry under transformations of the group $SU(3)$ is required, leading to the introduction of eight massless mediators, the gluons g_1 to g_8. The strong interaction is only transmitted between particles that carry color-charge, the quarks and gluons. The coupling constant of the strong interaction is called g_s. Like $SU(2)$, the color group $SU(3)$ is non-abelian, and so the gluons g_i experience self-interaction as well. In Table 2.2 the interactions of the SM and their gauge bosons are listed.

Interaction	Theory	Symmetry	Gauge bosons	Charge
Strong	QCD	$SU(3)$	gluons $g_1 \dots g_8$	color
Electroweak	GSW	$SU(2) \otimes U(1)$	$\gamma, \mathrm{W}^\pm, \mathrm{Z}$	weak isospin, weak hypercharge

Table 2.2: *The interactions within the SM.*

2.1.4 The Higgs mechanism

The simplest way to generate the masses of the vector bosons Z and $W^{\pm}$, while keeping the photon massless, is the Higgs mechanism. The Higgs mechanism proposes a scalar field Φ which has to carry isospin and hypercharge in order to couple to the gauge bosons. Therefore Φ has to be a doublet field. Furthermore, because there are three massive mediators of the weak interaction, three degrees of freedom are required. The Higgs field is written as a complex doublet field with four overall degrees of freedom,

$$\Phi(x) = \begin{pmatrix} \phi^+ \\ \phi^0 \end{pmatrix} = \begin{pmatrix} \phi_3 + i\phi_4 \\ \phi_1 + i\phi_2 \end{pmatrix}, \tag{2.25}$$

with the quantum numbers $Y = 1$ and $T = 1/2$. The potential of the Higgs field is given by

$$V = \frac{\mu^2}{2}\Phi^\dagger\Phi + \frac{\lambda}{2}(\Phi^\dagger\Phi)^2. \tag{2.26}$$

For stability reason the parameter λ needs to be positive ($\lambda > 0$) but a priori the sign of μ^2 is not constrained. To establish the symmetry breaking of the electroweak sector, one chooses $\mu^2 < 0$. The Higgs potential is shown in Figure 2.1 in terms of the fields ϕ_1 and ϕ_2. The

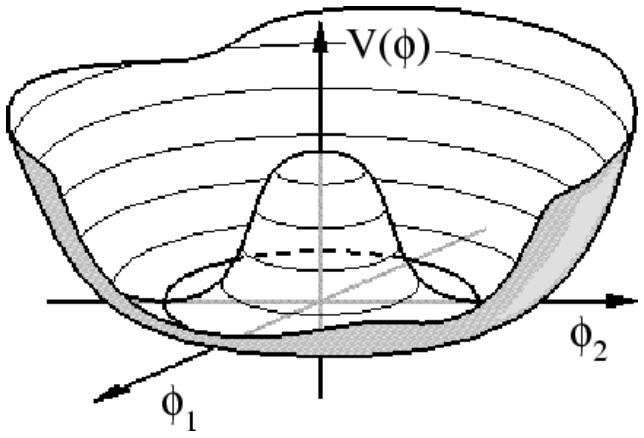

Figure 2.1: *The Higgs potential.*

potential minima lie along a circle with the radius $v = \sqrt{-\mu^2/\lambda}$, where v is called the non-vanishing vacuum expectation value (v.e.v). While the Higgs potential is fully symmetric, the symmetry is broken, or better said hidden, by expansion of the Higgs field about the potential minimum:

$$\Phi(x) = \begin{pmatrix} 0 \\ v + H(x) \end{pmatrix}. \tag{2.27}$$

This specific choice of the potential minimum is not completely arbitrary, because the conservation of the electromagnetic charge dictates that the ϕ^+ component has to vanish. The

real field $H(x)$ is identified with the physical Higgs boson. Inserting Expression 2.27 in the $SU(2)$ invariant Lagrangian of the Higgs boson

$$\mathcal{L}_{higgs} = \frac{1}{2}\mathcal{D}_\mu\Phi^\dagger\mathcal{D}^\mu\Phi - V \tag{2.28}$$

with the covariant derivative $\mathcal{D}_\mu$ of Equation 2.16 yields

$$\begin{aligned}\mathcal{L}_{higgs} &= \left(\frac{1}{2}g\right)^2 W^{-\mu}W^+_\mu(v+H)^2 + \frac{1}{8}(gW^\mu_3 - g'B^\mu)(gW^3_\mu - g'B_\mu)(v+H)^2 \\ &+ \frac{1}{2}(\partial_\mu H)(\partial^\mu H) - \frac{\mu^2}{2}(v+H)^2 - \frac{\lambda}{4}(v+H)^4.\end{aligned} \tag{2.29}$$

The first two terms contain the mass terms of the gauge bosons and terms for the trilinear and quadrilinear couplings to the new scalar Higgs boson. Using Equations 2.18 and 2.20, the Z and $W^\pm$ are identified, and one obtains for the masses of the gauge bosons:

$$M^2_W = \frac{1}{4}v^2g^2 \quad M^2_Z = \frac{1}{4}v^2(g^2+g'^2) \quad M_\gamma = 0. \tag{2.30}$$

The parameters v, g and g' are not determined by the theory, and have to be obtained by experiment, however, the masses of the heavy gauge bosons are related via

$$\frac{M_W}{M_Z} = \frac{g}{\sqrt{g^2+g'^2}} = \cos\Theta_w \tag{2.31}$$

which is confirmed by the electroweak data recorded in millions of physics events. In the last two terms of Equation 2.29, the expressions proportional to H^2 give rise to the mass of the Higgs boson $M_H = \sqrt{2\lambda}v$. The final term predicts Higgs tri- and quadrilinear self-interactions proportional to H^3 and H^4, respectively.
Finally, the so far massless fermions acquire their masses by the Higgs mechanism by adding the Yukawa Lagrangian

$$\mathcal{L}_{Yukawa} = -g_f[\overline{L}\Phi R + \overline{R}\Phi^\dagger L] = -\frac{1}{\sqrt{2}}g_f v\overline{f}f - \frac{1}{\sqrt{2}}g_f\overline{f}fH \tag{2.32}$$

to the electroweak Lagrangian. Here L and R represent the left-chiral doublets and right-chiral singlets under $U(1)_Y \otimes SU(2)_L$, and $f = e, \nu, u, d, ...$ are the individual fermion spinors. The first term describes the fermion masses $m_f = g_f v/\sqrt{2}$ while the second term describes the fermion couplings to the Higgs. The coupling constants g_f are not predicted by the theory, but have to be calculated from the measured fermion masses. One important result, however, is that the Higgs coupling to the fermion is proportional to the fermion masses. Experimental searches for the SM Higgs are therefore most promising for high center-of-mass energies, where the heavy particles of the SM can be produced.

2.1.5 Shortcomings of the Standard Model

While the SM of particle physics has enormous explanatory power and is supported by a wealth of data, it is widely accepted that it cannot be the final theory of the physical world, its

contents and interactions. Many questions arise from the theoretical point of view alone. For one, there is the rather arbitrary choice of gauge symmetry groups generating the interactions between the elementary particles. This choice has no deeper theoretical foundation. Also, there are at least nineteen constants to the theory that have to be determined experimentally, and they have no connection to each other in the SM. These constant are for example the fermion masses, the three gauge couplings of the electroweak and strong interactions, the two parameters μ and λ of the Higgs sector, as well as three charged weak mixing angles. In the SM the neutrinos are massless, but analysis of the solar neutrino flux and long baseline neutrino experiments have shown that neutrinos oscillate between the flavor eigenstates and therefore have to have a non-vanishing rest mass. For a full, self-contained "Theory of everything", gravitation has to be incorporated into the SM, which could not be done until now. Attempts to include gravitation into a quantum field theory lead to non-renormalizable descriptions of nature, with unphysical divergences at high energies of the Planck scale $M_p = \sqrt{\hbar c^5/G_N} \sim 10^{19}$ GeV. If one assumes that the SM is correct up to an energy scale Λ, which for a full theory

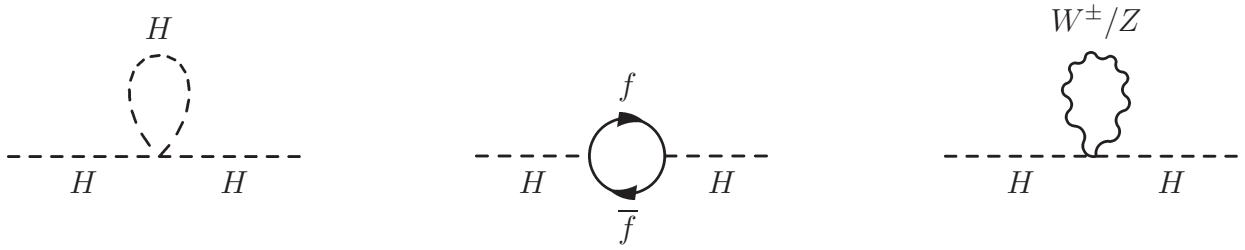

(a) (b) (c)

Figure 2.2: *Divergent loop diagrams contributing to the Higgs boson mass: (a) Higgs boson loop, (b) fermion loop and (c) gauge boson loop.*

could be associated with the Planck scale, radiative corrections to the Higgs self energy, and therefore its mass scale, blow up quadratically

$$\Delta M_H^2 \sim \Lambda^2. \tag{2.33}$$

These corrections to the Higgs mass are much larger than the physical value of $M_H \sim 10^2$ GeV. In Figure 2.2 the dominant contributions to the Higgs self energy are shown. Although fermion and gauge boson masses are protected from these kinds of divergences, their mass scale is sensitive to the Higgs v.e.v., and therefore to the energy scale Λ. This connection between the comparatively low energy scales of particle masses and the high cut-off Λ is known as the *hierarchy* or *naturalness* problem. Keeping the radiative corrections small requires an unphysical procedure of *fine-tuning* of the SM parameters.

A lower bound on the CP-violation required to explain the observed abundance of antimatter in the universe, can be inferred from the photon to baryon ratio $n_\gamma/n_{baryons} \approx 10^9$ and the amount of antimatter in the cosmos. However, the amount of CP-violation predicted from the SM via the CKM mechanism relating the mass eigenstates of the quarks to the weak eigenstates is by a factor of about 10^8 to small. This indicates that there has to be another source of CP-violation beyond the SM. Extending the SM to Supersymmetry (SUSY) could provide the missing CP-violation.

A range of cosmological observations indicate that only about 4% of the energy density in the

universe consists of ordinary baryonic matter (cf. Sec. 2.3). For the remaining 96%, the SM offers no explanation at all. In particular, for the estimated amount of Dark Matter in the cosmos, the SM has no candidate particle.
Finally, from an aesthetic point of view, it is compelling to think that at high energies, the electroweak and strong interactions unify to a single force. Radiative corrections result in running coupling constants described by the Renormalization group equations. In Figure 2.3(a) the energy dependence of the three couplings g, g' and g_s is shown for the SM. As can be seen, with rising energies the couplings seem to converge but do not meet in a single point. This behavior seems to support the idea of grand unification. Within SUSY however, the unification of the three forces is possible, since all three coupling constants meet in one point, as shown in Figure 2.3(b) within the minimal supersymmetric standard model (MSSM).

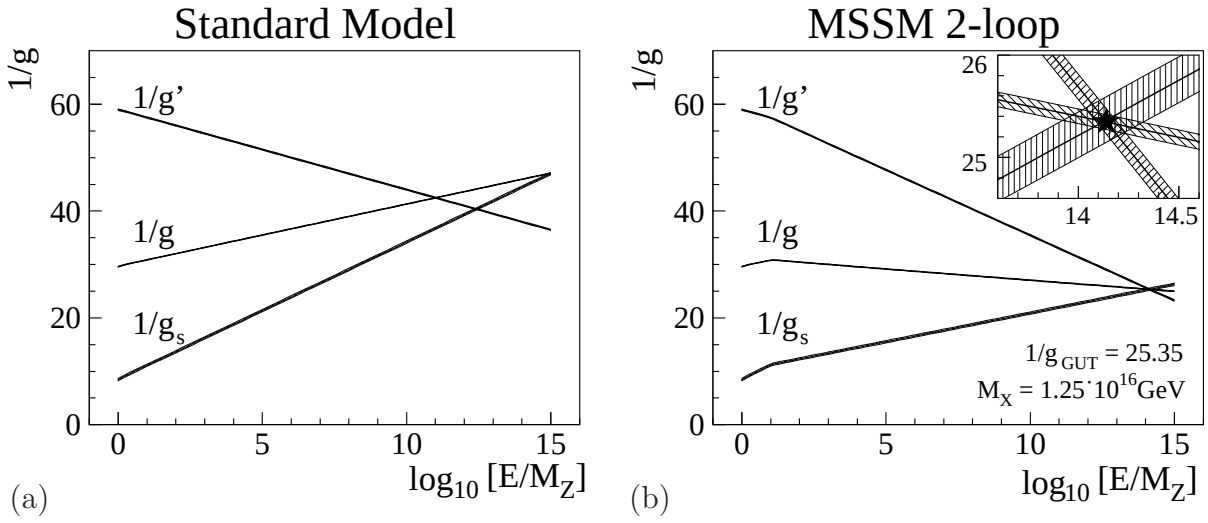

Figure 2.3: *Energy dependence of the electroweak coupling constants g and g' and of the strong interaction g_s in (a) the SM and (b) the MSSM. From [14].*

2.2 SUSY as an extension to the SM

Supersymmetry (SUSY) postulates an additional symmetry between fermions and bosons. This symmetry is introduced by a new Operator $\mathcal{Q}$ with the properties

$$\mathcal{Q}_\alpha \left| fermion_\alpha \right\rangle = \left| boson \right\rangle \qquad \mathcal{Q}_\alpha \left| boson \right\rangle = \left| fermion_\alpha \right\rangle , \tag{2.34}$$

where α is the spinor index. To every SM fermion there exists a bosonic superpartner, and every SM boson has a fermionic superpartner. Apart from their spin, the superpartners are identical to their SM counterparts. This identity includes also their mass. The experimental fact that, for example, no superpartner of the electron, the so-called selectron, has been observed, indicates that supersymmetry has to be broken in order to lift the mass degeneracy of particles and their superpartners. Since the number of degrees of freedom is conserved under $\mathcal{Q}$, for every spin-1/2 particle f two spin-0 superpartners exists: $\tilde{f}_L$, the partner of the left-handed fermion and $\tilde{f}_R$, the partner of the right-handed fermion. In SUSY, the problem

of the diverging corrections to the Higgs mass is overcome by additional contributions to the Higgs self-energy, that cancel the SM diagrams. Figure 2.4 shows some of these diagrams. Another theoretical advantage of SUSY is, that it can connect the gauge theories to gravity, as

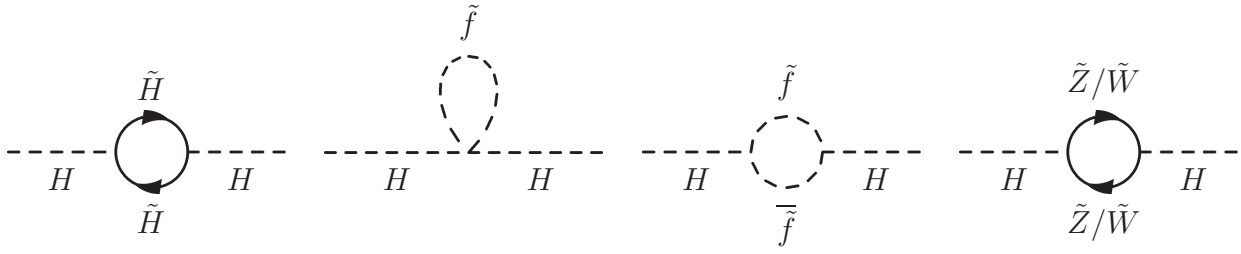

Figure 2.4: *Corrections to the Higgs mass self energy in supersymmetry.*

the supersymmetry operator $\mathcal{Q}$ (of the fermionic "dimension") is connected to the momentum operator P (the traditional "dimension") via the commutation relation

$$\{\mathcal{Q}_\alpha, \mathcal{Q}_\beta\} = 2\sigma^\mu_{\alpha\beta} P_\mu. \tag{2.35}$$

The mSugra model is realized by requiring the invariance of the complete SUSY Lagrangian under local SUSY transformations. While SUSY solves the hierarchy problem by stabilizing the Higgs mass, the fact that it has to be a broken symmetry requires a natural energy scale Λ_{SUSY} where the breaking takes place. This energy, however, cannot be too far away from the electroweak scale, since otherwise a new hierarchy problem emerges, now between the electroweak scale and the SUSY scale. Finally it has to be mentioned, that within SUSY, a grand unification of the three SM interactions is possible, as shown in Figure 2.3(b) in terms of the inverse coupling constants.

2.2.1 The MSSM and the neutralino sector

One possibility of breaking SUSY is a purely phenomenological one, where direct SUSY breaking terms are incorporated into the soft-breaking SUSY Lagrangian $\mathcal{L}_{soft}$. For a soft breaking, only logarithmically divergent terms are considered, leaving out any quadratically divergent terms, so as to not introduce any new quadratic divergences to the SM Higgs mass.
The minimal supersymmetric standard model (MSSM) requires the existence of two Higgs doublets with eight degrees of freedom in total. Like in the SM, three of these degrees are used for the mass generation of the gauge particles. The remaining five degrees of freedom correspond to a pair of charged Higgs H^+ and H^-, two scalar Higgs h^0 and H^0 and a pseudoscalar A^0. The most general Lagrangian $\mathcal{L}_{MSSM} = \mathcal{L}_{SUSY} + \mathcal{L}_{soft}$ that can be constructed in MSSM has 124 free parameters. This number can be reduced considerably by adding further assumptions. First one requires R-parity conservation, i.e. conservation of the quantum number

$$R = (-1)^{3(B-L)+S}, \tag{2.36}$$

where B and L are baryon number and lepton number, respectively, and S is the spin. With conserved R-parity, SUSY particles can only be produced in pairs and the lightest supersymmetric particle (LSP) is stable. The LSP, if uncharged, is a natural Dark Matter candidate.

Secondly, the mixing of flavor eigenstates (as for the SM quarks) is prohibited. Finally, mixing of the SUSY partners of the right-handed and left-handed fermion mass eigenstates is suppressed in the first two generations, while it is allowed in the third generation ($\sim m_{\tau,b,t}$). With no additional CP-violation in the MSSM Lagrangian, the number of free parameters is reduced to 24.
In SUSY, the superpartners of the B and W^3 gauge fields and the two scalar Higgs fields H_1^0 and H_2^0 (i.e. $\tilde{B}$, $\tilde{W}^3$,$\tilde{H}_1^0$ and $\tilde{H}_2^0$) mix to four neutral spin-1/2 neutralino mass eigenstates:

$$\begin{pmatrix} \tilde{\chi}_1^0 \\ \tilde{\chi}_2^0 \\ \tilde{\chi}_3^0 \\ \tilde{\chi}_4^0 \end{pmatrix} = \begin{pmatrix} M_1 & 0 & -m_Z c_\beta s & m_Z s_\beta s \\ 0 & M_2 & m_Z c_\beta c & -m_Z s_\beta c \\ -m_Z c_\beta s & m_Z c_\beta c & 0 & -\mu \\ m_Z s_\beta s & -m_Z s_\beta c & -\mu & 0 \end{pmatrix} \begin{pmatrix} \tilde{B} \\ \tilde{W}^3 \\ \tilde{H}_1^0 \\ \tilde{H}_2^0 \end{pmatrix}, \tag{2.37}$$

where M_1 and M_2 are the bino and wino mass terms in the soft MSSM Lagrangian $\mathcal{L}_{soft}^{MSSM}$, and μ is the mass mixing parameter of the two Higgs doublets. Furthermore, $s = \sin\Theta_w$, $c = \cos\Theta_w$, and $c_\beta = \cos\beta$ and $s_\beta = \sin\beta$ with $\tan\beta$ being the ratio of the v.e.v. of the two Higgs doublets. The mass of the Z boson enters via m_Z. The lightest neutralino $\tilde{\chi}_1^0$ is stable if R-Parity is conserved. With typical masses in the order of 100 GeV, it is a viable DM candidate.

2.3 Cosmological Dark Matter

2.3.1 Observational evidence

In the early 20^{th} century it became apparent that the observed cosmological mass density derived from the observation of luminous matter in the form of stars and interstellar/intergalactic gas could not account for the dynamical properties of large-scale objects like galaxies and galaxy clusters. In 1937, Fritz Zwicky applied the virial theorem to the Coma cluster of galaxies [15] and inferred the average mass of the galaxies in the cluster to be by a factor of ~ 160 greater as expected from the observed luminosity. He proposed the existence of an additional component to the cosmological matter density, named "Dark Matter" (DM) for its property of being non-luminous. Later in the 1960's to 1970's further research verified Dark Matter not only on the scale of galaxy clusters, but also as an important ingredient to the dynamics of individual galaxies [16, 17]. The observed rotational velocities of the stars in the outer regions of the galaxies deviate from the Keplerian motion expected for the mass concentration calculated from the luminosity of the galactic central bulge.
With the discovery of the Cosmological Microwave Background (CMB) [18] in 1965 by A. Penzias and R. Wilson [2], a new observational window for DM was opened. The CMB as a measure of the temperature of the universe had been predicted in a series of papers by Gamov, Apher and Herman in 1948 [19, 20, 21], in which they determined the relative abundance of chemical elements in the early universe. The CMB has been extensively studied in recent years with balloon-borne instruments (e.g. Boomerang), and also with instrumented satellites (COBE, WMAP). In 1992, the COBE[3] experiment confirmed a quadrupole fluctuation in the dipole

[2]Nobel Prize in 1978.
[3]Nobel Prize in 2006.

subtracted CMB [22]. With the follow-up experiment WMAP these measurements have been improved [23]. The observed angular spectral anisotropy in the CMB is in agreement with a flat universe and a contribution of Cold Dark Matter of $\approx 22\%$ to the cosmological energy density.

2.3.2 Dark Matter as a thermal relic of the Big Bang

One of the most compelling hypotheses is, that the DM content in the universe is made of Weakly Interacting Massive Particles (WIMPs). The strength of their interactions can be estimated when the WIMPs are considered to be a thermal relic of the Big Bang. In this case, the thermally averaged annihilation cross section $\langle \sigma v \rangle$ of cosmological DM particles can be estimated under the assumption, that the WIMPs were in thermal equilibrium with the SM particles after the time of baryogenesis. When the annihilation processes of WIMPs into SM particles and vice versa happend at equal rates, the number density n of the DM particles of mass m_χ follows the Boltzmann law

$$n \sim e^{-m_\chi / k_B T}, \tag{2.38}$$

with the Boltzmann constant k_B and temperature T. When the rate of expansion of the universe H_f exceeds the annihilation rate, the WIMPs effectively decouple from the remaining SM particles. This "freeze-out" happens at number densities n_f given by [24]

$$\langle \sigma v \rangle \, n_f t_f \sim 1 \tag{2.39}$$

at a time $t_f = 1/H_f$. After freeze-out, the co-moving WIMP number density n remains unchanged and their present relic density Ω_χ is given by

$$\Omega_\chi h^2 \simeq \text{const} \frac{T_0^3}{M_{\text{Pl}}^3 \langle \sigma v \rangle} \simeq \frac{0.1\text{pb} \cdot c}{\langle \sigma v \rangle}. \tag{2.40}$$

Here $h = H_0/100$ is the current Hubble rate of expansion, and the right-hand side of Equation 2.40 is evaluated for the CMB equivalent temperature T_0 and the Planck mass M_{Pl}. It follows from the observed cosmological DM density, that the average WIMP annihilation cross section is in the order of the SM weak interaction. Their weak interactions ensure the WIMP hypothesis to be compatible with the neutralino in MSSM and other extensions of the SM.
In Figure 2.5 the time evolution of the co-moving WIMP number density is depicted. In region (1), the WIMPs are in thermal equilibrium with the SM particles, and freeze out in region (2). Depending on the thermal average of the annihilation cross section, the number density n remains unchanged at different levels, see region (3).

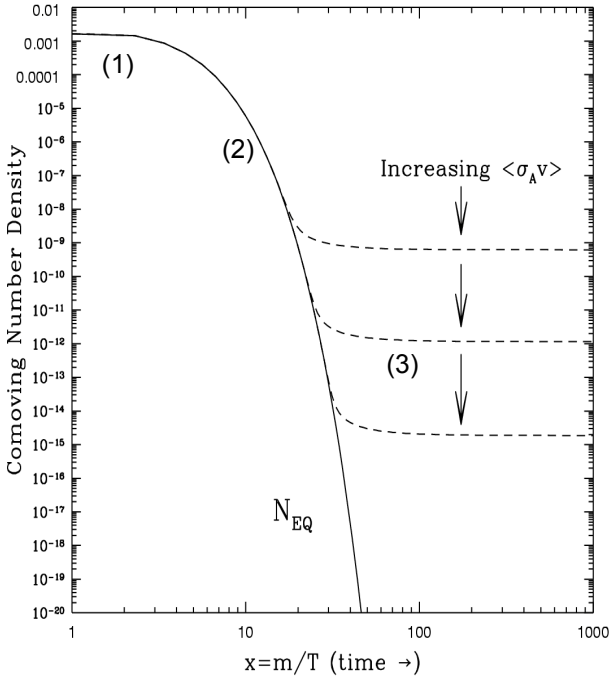

Figure 2.5: *The time evolution of the co-moving WIMP number density: In region (1), the WIMPs are in thermal equilibrium with SM particles, and freeze out in region (2). Depending on the thermal average of the annihilation cross section $\langle \sigma v \rangle$, the number density remains unchanged at different magnitudes, see region (3). From [25].*

Chapter 3

The International Linear Collider

In the last chapter it has been shown that new physics is expected at an energy scale of less than 1 TeV. Apart from the SM Higgs, a wealth of Dark Matter candidates are possible with masses in the 100 GeV to 1 TeV range. And, if the problems inherent in the SM of particle physics are overcome by Supersymmetry, the theory has to be broken at the TeV scale. The first steps into this energy realm have already been taken by the TEVATRON and with the start-up of the LHC. The TEVATRON is a proton-antiproton collider with a center-of-mass energy of 1.96 TeV [12]. As a collider of composite particles, the average available center of mass energy is, however, much lower. The TEVATRON will stop operation in 2011. During its running time, the discovery of the top-quark has been one of the most important discoveries [26, 27, 28]. In 2010 TEVATRON could set new 95% C.L. exclusion limits on the SM Higgs for masses between 158 GeV and 175 GeV [29].
The LHC accelerator started with first collisions in 2009 and took first physics data in 2010. LHC is a proton-proton collider with a maximum center-of-mass energy of 14 TeV. Like with the TEVATRON, the available center-of-mass energy for collisions is lower, but it is believed that the energy is high enough to discover the Higgs boson and to find first direct evidence of Beyond the SM (BSM) physics. Once new physics is discovered, precision measurements of the new phenomena have to be performed. Since the proton is a composite particle and the hadronic backgrounds are large, the LHC is not sensitive enough for this task. In general, lepton machines are better suited for high precision measurements, as has been demonstrated by e.g. the precise measurement of the Z resonance with the experiments at LEP [11].
The International Linear Collider (ILC) is a planned e^+e^- accelerator with an initial center-of-mass energy of 200 GeV to 500 GeV. In 2007, a "Reference Design Report" (RDR) [30, 31, 32, 33] was published by the international ILC community, proposing a conceptual design and machine parameters.

3.1 Physics program

The ILC is envisioned to extend the knowledge of SM physics, as well as to determine the underlying structure of new physics discovered at the LHC.
Although the SM has been tested extensively over the last two decades, improvements can still be made. Top-quark production at the ILC will play an important role in the physics program. Since it is the heaviest particle in the SM, it is also the one with the strongest

coupling to the Higgs sector [31]. Therefore, it is expected to play a fundamental role in revealing the dynamics behind the symmetry breaking mechanism. Top-quark measurements might help to solve the flavor problem and give indications for physics beyond the SM. If the existence of the Higgs were to be established, the measurement of the top Yukawa-coupling could discriminate between SM and non-SM Higgs scenarios.
Another one of the main goals of the ILC physics program will be the determination of the properties of the Higgs boson. Studies show that for a 120 GeV Higgs and a data sample of an integrated luminosity of $\mathcal{L} = 250$ fb^{-1} at a center-of-mass energy of 250 GeV the Higgs mass can be measured with a statistical precision of a few tens of MeV. This result is obtained by measuring the invariant mass of the system X recoiling against the Z in the processes $e^+e^- \to ZH \to e^+e^-X$ and $ZH \to \mu^+\mu^-X$ [34, 35]. The Higgs branching fractions to $b\bar{b}$, $c\bar{c}$ and gg can be measured with a precision of 2.7%, 12% and 29%, respectively by combining the channels $ZH \to l^+l^-q\bar{q}$, $ZH \to \nu\bar{\nu}H$ and $ZH \to c\bar{c}q\bar{q}$ [36, 37]. Other Higgs parameters that the ILC will be able to measure with an unprecedented precision will be the Higgs self-coupling and the Yukawa-coupling to the top quark which can be determined in $t\bar{t}H$ production, provided a center-of-mass energy of more than 500 GeV is available.
Finally, supersymmetry, if realized in nature, will be studied in detail. In case SUSY is broken at the TeV scale, many sparticles have masses directly accessible at the 500 GeV ILC. The reach will be even better after the 1 TeV upgrade. It is expected that the sparticle masses can be measured with a precision at the sub-percent level [38, 39].

3.2 Accelerator

The ILC is a high luminosity linear collider, bringing electrons and positrons to collisions at center-of-mass energies tunable from 200 GeV to 500 GeV and with a peak luminosity of $2 \times 10^{34}\text{cm}^{-2}\text{s}^{-1}$. The conceptual design allows for a future energy upgrade to 1 TeV. Super conducting 1.3 GHz RF cavities installed in two 11 km long linear accelerators (linacs) provide the acceleration. The overall length of the accelerator complex is approximately 31 km. A polarized electron source based on a photocathode DC gun delivers electrons which are pre-accelerated to 5 GeV and injected into a Damping ring (DR) of $\sim$ 6.7 km circumference. Afterwards the electrons are transported to the main linac, accelerated to up to 250 GeV and brought to collision with 250 GeV positrons in a single Interaction Region (IR). In the RDR layout, the positrons are created with an undulator-based source located in the electron main linac at a position where the electrons have an energy of about 150 GeV. The positrons are also injected in the DR and led to the main positron linac for acceleration. Figure 3.1 shows the basic layout of the ILC. For complementarity two detectors will share the single IR. This requires the development of a feasible scheme to move the detectors in and out of the beam. This "push-pull" scenario is a major topic in the R&D effort for the machine detector integration. It has to be ensured that the exchange of detectors can take place within a few days and that the movement does not induce too much mechanical stress on the detectors in order to reduce the calibration time to a minimum after each push-pull operation. Furthermore, sufficient shielding has to be provided so that maintenance tasks can be performed on the unused detector during data-taking with the other detector.

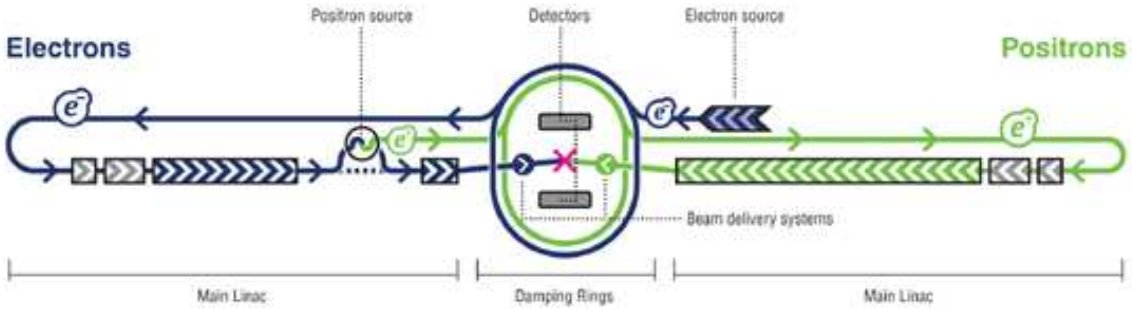

Figure 3.1: *Conceptual layout of the ILC in the RDR proposal. The positron source is located in the main electron linac. In the more recent SB-2009 design proposal, the positron source is moved to the end of the main electron linac.*

3.2.1 ILC baseline parameters

The ILC RDR baseline parameters are listed in Table 3.1. The center-of-mass energy of $\sqrt{s} = 500$ GeV is expected to be stable within 0.1% [32]. The possibility of an upgrade to $\sqrt{s} = 1$ TeV is recommended by several physics studies. The peak luminosity availability is 75%, consistent with producing $\mathcal{L} = 500$ fb^{-1} of data during the first four years of operation. Beam polarization is foreseen from the start with at least 80% for the electrons and $> 30\%$ for the positrons. A polarization upgrade for the positrons to 60% is recommended as an option. Furthermore, the machine design is flexible enough to provide options for e^-e^- and $\gamma\gamma$ collisions, and data-taking should also be possible at the Z-pole energy of $\sqrt{s} = 90$ GeV.

Parameter	Value	Units
Center of mass energy	500	GeV
Peak luminosity	$2 \cdot 10^{34}$	cm^{-1}s^{-1}
Repetition rate	5	Hz
Accelerating gradient in cavities	31.5	MV/m
Length of each Main Linac	11	km
Beam pulse length	1	ms
Average beam current in pulse	9.0	mA
Total site power consumption	230	MW

Table 3.1: *Global parameters for the ILC with $\sqrt{s} = 500$ GeV center-of-mass energy as proposed in the RDR [32].*

Table 3.2 lists the beam parameters of the ILC Reference Design Report [32] with the third column giving the nominal parameters. The stated parameter values are very correlated and cannot be varied independently. However, to achieve the desired luminosity several other parameter sets have been studied. In the *lowN* set, the bunch length and charge are reduced,

in order to deal with problems such as microwave instabilities in the damping rings, single bunch wakefield emittance dilusion and a large disruption parameter at the IP which can occur in the nominal set. The reduction in luminosity caused by the smaller bunch population is compensated by a tighter beam focussing at the IP. The *lowP* option deals with limitations of beam power and beam current. In this scenario the beam currents are reduced by 30% and the beam power is reduced by a factor of two. The reduction in luminosity is again balanced by a tighter beam focus at the IP. A downside of this parameter set is that the beamstrahlung can not be controlled by an increased bunch length. The strong focussing of the beams would double the amount of beamstrahlung.

Parameter	min.	nominal	max.	unit
Bunch population	1	2	2	$\times 10^{10}$
Number of bunches	1260	2625	5340	
Linac bunch interval	180	369	500	ns
RMS bunch length	200	300	500	μm
Normalized horizontal emittance at IP	10	10	12	mm·mrad
Normalized vertical emittance at IP	0.02	0.04	0.08	mm·mrad
Horizontal beta function at IP	10	20	20	mm
Vertical beta function at IP	0.2	0.4	0.6	mm
RMS horizontal beam size at IP	474	640	640	nm
RMS vertical beam size at IP	3.5	5.7	9.9	nm
Vertical disruption parameter	14	19.4	26.1	
Fractional RMS energy loss to beamstrahlung	1.7	2.4	5.5	%

Table 3.2: *Nominal beam parameters at the IP in the RDR proposal and the design ranges (min., max.). The parameters are highly correlated: a change in one parameter requires adjustments of several other parameters [32].*

Careful reviewing of the RDR baseline design in 2009 led to a new document (SB-2009) with a different set of parameters [40, 41]. The SB-2009 document aims for a significant cost reduction of the accelerator and is accompanied by several machine design changes.
The most important changes to the baseline design are a single tunnel solution for the main beamline and support systems and a relocation of the undulator positron source from a mid position to the end of the electron linac at 250 GeV. The beam current is halved by reducing the bunches per train by a factor of two. Stronger final focussing recovers the reduced luminosity, but also increases the beam induced backgrounds and $\gamma\gamma$ events (Sec. 5.2.1). The relocation of the positron source will give lower luminosity below a center-of-mass energy of $\sqrt{s} = 300$ GeV, and it will limit the ILC capability of energy scans since the electrons can not be decelerated after the undulator. In addition, a new focussing scheme, the travelling focus [42], has to be employed to uphold the total RDR luminosity. Otherwise the SB-2009 proposal yields a luminosity 25% lower than the RDR proposition for $\sqrt{s} = 500$ GeV. Another solution avoiding the reduction in luminosity is an increase in the repetition rate to 10 Hz which becomes feasible due to the spare RF-power when operating the machine at low energies. In that case, every second electron bunch train is accelerated to 150 GeV for the

production of positrons in the undulator, and every other bunch train is sent to the detector at lower energies to collide with the positrons.

3.3 Sources

The electron source consists of a laser illuminating the photocathode in a DC gun [32]. The system has to provide the nominal electron bunch trains with a repetition rate of 5 Hz and a polarization of more than 80%, with each bunch consisting of about 2.0×10^{10} electrons. The cathode material will most likely be a strained GaAs/GaAsP superlattice structure. GaAs/GaAsP cathodes have been shown to provide at least 85% polarization [43, 44, 45]. To match the bandgap energy of GaAs photocathodes, a 790 nm continuous-wave frequency-doubled Nd:YAG laser will be used. The emitted electrons are pre-accelerated to 76 MeV and afterwards accelerated to 5 GeV in a superconducting linac. To preserve the polarization, the spin vectors are rotated into the vertical by superconducting solenoids before the electrons (positrons) are injected into the damping rings.
The source of polarized positrons is a long helical undulator in the electron main linac. Electrons passing through the undulator generate a multi-MeV photon beam which strikes a thin Titanium-alloy target of 0.4 radiation lengths. The positrons from the resulting electromagnetic shower are separated from the electrons and injected into the damping rings after having been accelerated to 5 GeV in a superconducting linac. The circularly polarized photon beam from the undulator is responsible for the longitudinal polarization of the positrons. The degree of polarization is mainly determined by the length of the undulator. In the ILC baseline proposal an initial positron polarization of $P > 30\%$ is expected. In addition to the undulator positron source, a keep-alive source delivering $\sim 10\%$ of the design positron luminosity is planned, in case of a loss of the primary positron beam.

3.4 Polarimeters

The ILC electron source delivers in its baseline design already polarized electrons with a polarization degree of $P_{e^-} \geq 80\%$. Also, as stated in the RDR, the positrons are polarized to 30%, with the possibility of reaching a higher degree of polarization by extending the undulator source using the reserved space in the beamline. In order to fully exploit the physics potential of polarized beams, the polarization has to be determined with a relative precision of $\delta P/P = 0.25\%$ [46, 47], although a higher precision would be beneficial. A system of complementary and independent polarization measurements is planned to accomplish this ambitious goal. The instantaneous polarization is measured with Compton polarimeters both in front (upstream) and behind (downstream) the interaction region, while the absolute polarization scale is determined from the e^+e^- collision data [48, 49, 50].
In the RDR proposal, the upstream polarimeter is located approximately 1800 m before the electron-positron interaction point (IP), its downstream counterpart is located about 150 m behind the IP, as illustrated in Figure 3.2. Each polarimeter consists of a magnetic chicane of four to six dipole magnets [47]. At the Compton interaction point (Compton-IP), circularly polarized laser light ($E_\gamma \approx 2.3$ eV) is shot onto individual electron (positron) bunches. The Compton scattered electrons (positrons) are separated from the main beamline in the

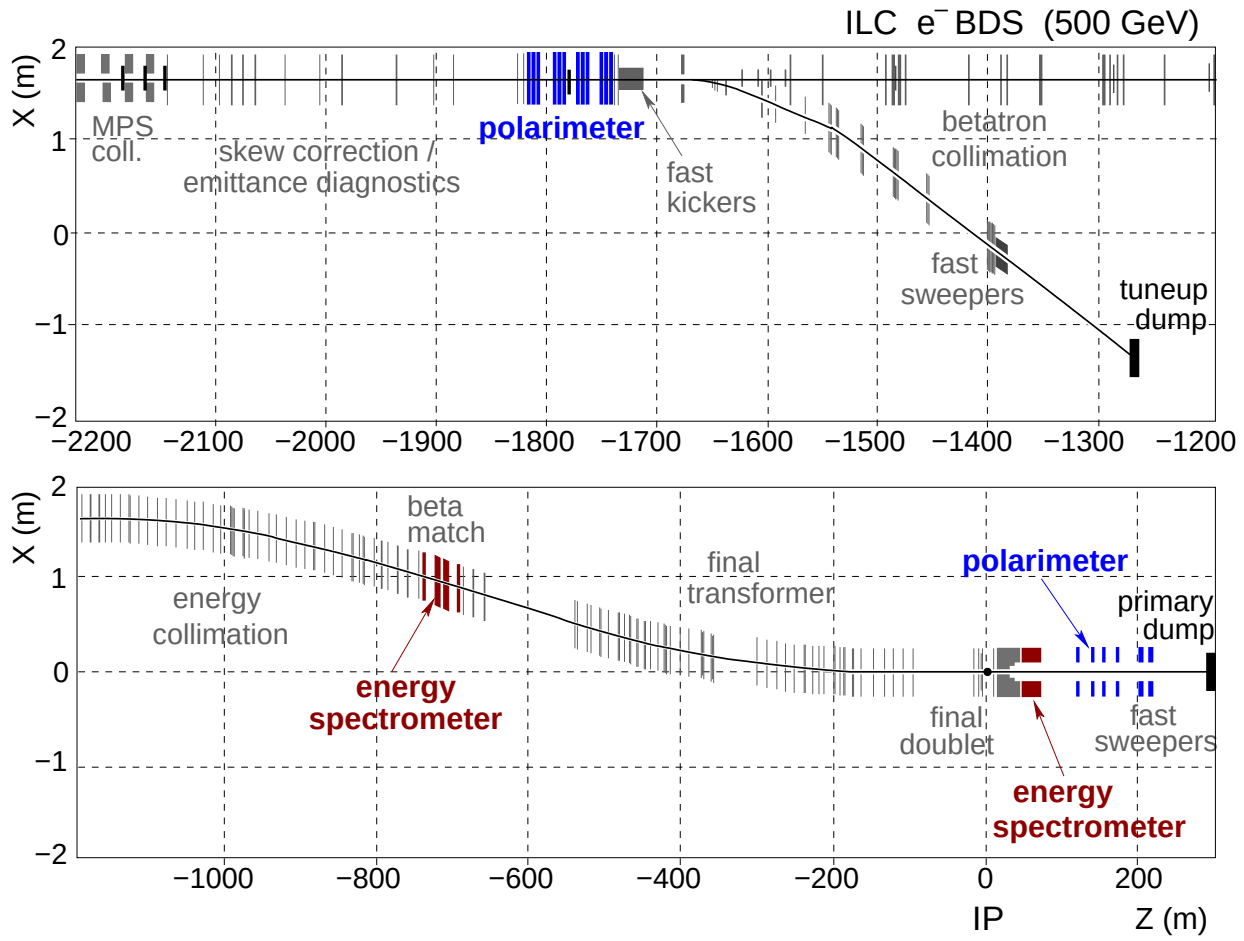

Figure 3.2: *The Beam Delivery System of the ILC in the RDR proposal. The polarimeters are indicated in blue at $z = -1800$ m and $z = +150$ m. In the more recent SB-2009 proposal, the upstream polarimeters have been relocated to a position behind the branch-off of the tuneup line [32].*

magnetic chicane and guided to segmented Cherenkov detectors which measure the spatial distribution of the scattered beam particles by means of Cherenkov radiation. The Compton polarimeters are explained in more detail in Section 9.1.

The upstream polarimeter benefits from the clean environment. It will be equipped with a laser with a repetition frequency matching the ILC bunch structure. This allows for a fast measurement of polarization variations within each train, as well as monitoring time dependent effects over a series of ILC bunch trains. The average statistical precision for each bunch position in the train will already be at the 1%-level after the passage of 20 trains, corresponding to four seconds. The statistical error for the average over two trains with opposite laser helicity will be 0.1% which is below the aim for the systematic uncertainty.

The polarization measurement downstream of the IP is somewhat more involved due to the higher expected backgrounds from disrupted beams and synchrotron radiation. Three lasers with higher power but lower repetition rate will be employed, each sampling a specific bunch position for a time interval of a few seconds to minutes. A statistical precision of less than

1% after one minute can be achieved for each beam position.
By combining the measurements of up- and downstream polarimeters for runs with and without collisions, depolarization effects from collisions can be measured.

Chapter 4

The International Large Detector

The International Large Detector (ILD) is one of two detector concepts for the ILC. Its design is driven by the requirements for high precision measurements permitted by the clean experimental environment due to the leptonic initial state. Since the ILC will operate in an energy regime, where the physics landscape is not yet known, and will be explored only partially by the LHC experiments at the time of the start of construction, the ILD is also designed to be a versatile and flexible detector.
Two complementary detectors share the single ILC Interaction Region (IR). Both detectors are mounted on a movable platform, allowing to move them in and out of the IR to make room for the second experiment. In order to realize this "push-pull" scenario (i.e. two large experiments being alternately operated in the IR), it has to be ensured that both detectors can be re-commissioned on reasonably short time scales, e.g. one to two days.
The ILD has been developed from a joint optimization effort of the GLD[1] [51] and LDC[2] [52] working groups. The conclusions of the optimization studies with respect to the detector design are documented in the Letter of Intent (LoI) [36] published in 2010. The requirements on precision measurements are met within the Particle Flow (PFlow) reconstruction concept. For the best overall event reconstruction, particles within jets should be reconstructed individually. This is achieved by excellent momentum and dE/dx measurements in the tracking system and highly granular calorimeters. The combination of both measurements (tracking and calorimetry) leads to a high jet-energy resolution which is essential for precise jet reconstruction needed in the analyses of many physics channels.

4.1 Particle Flow concept

The driving force of the detector design is the Particle Flow concept of reconstruction. The main idea of PFlow reconstruction is to measure each particle individually (also if it is part of a jet) and to do so with the detector component best suited for each measurement. This ability provides a powerful tool for event reconstruction and identification [53]. In contrast to LEP, where kinematic fitting enabled precise di-jet invariant mass resolution almost independent of the jet energy resolution, the invariant mass determination at the ILC relies heavily on the jet energy resolution. To efficiently separate W and Z decays for typical di-jet energies at ILC, a

[1] Gaseous Large Detector.
[2] Large Detector Concept.

jet energy resolution of $\sigma_E/E = 30\%/\sqrt{E}$ is necessary. At ILC this goal is achieved with the Particle Flow approach. PFlow calorimetry requires the reconstruction of the four-vectors of all visible particles in an event. In contrast to traditional calorimetry, only the energies of neutral hadrons are measured in the hadronic calorimeter, while kinematic information on the charged leptons and hadrons is obtained by measuring the particle momenta in the tracking system, see Figure 4.1. Photons are measured in the electromagnetic calorimeters. In this way, the hadronic calorimeter with its relatively poor energy resolution is used to only measure $\sim 10\%$ of the typical jet energies, and an efficient separation of W and Z decays is achievable.

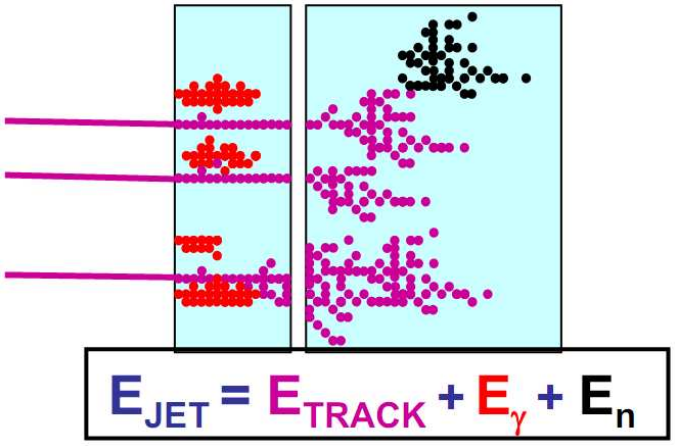

Figure 4.1: *Illustration of Particle Flow reconstruction concept. Each particle is measured with the detector component best suited: the energy of charged particles (violet) is measured with the tracking system, photon energies (red) are measured with the ECAL, and neutral hadrons (black) are measured with the HCAL [54].*

The separate measurement of neutral and charged energy, however, requires highly granular calorimeters and advanced pattern recognition algorithms to correctly assign the measured energy depositions to the detected individual particles. Otherwise, for example, when part of the energy of a charged hadron is identified as an individual particle, it is effectively counted twice, since it has already been accounted for by the track momentum measurement.
The currently most advanced reconstruction code to achieve this goal is the PandoraPFA algorithm. PandoraPFA performs calorimeter clustering and particle identification in a series of stages [53]. Tracks and track topologies are identified, and the clustering of charged energy contributions is seeded by the projection of the track endpoints on the calorimeters. The calorimeter hits are clustered with a cone-based projective method. Unseeded hits in the electromagnetic calorimeters are combined and identified as photons. Split clusters are merged on the basis of clear topological signatures. An iterative statistical re-clustering follows and tests the compatibility of the measured energies with the track momenta. The final stages include an improved photon tagging algorithm and the removal of the remaining fragments of charged energy depositions. Finally, particle candidates are identified from the measured momenta and the neutral hadronic energies.

4.2 General layout

The ILD is designed as a multi-purpose detector covering a large solid angle. Its central component is a gas-filled Time Projection Chamber (TPC) for the reconstruction of charged

particles. The TPC is surrounded by a highly granular electromagnetic calorimeter (ECAL) for photon detection and measurement of electromagnetic energy. Neutral hadrons are reconstructed in the hadronic calorimeter (HCAL) in conjunction with the ECAL. Figure 4.2

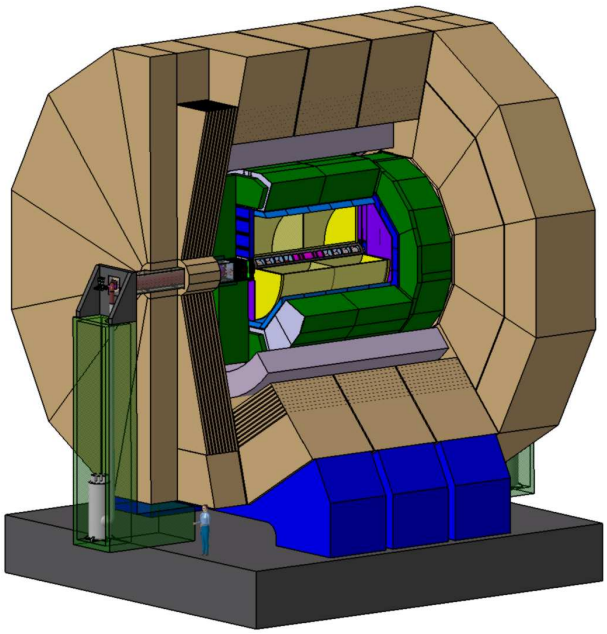

Figure 4.2: *View of the ILD detector concept [36].*

shows a cut-away schematic of the basic ILD layout. More detailed, the ILD consists of the following subsystems, listed from the IP outward in successive order [36]:

- A pixel-vertex detector (VTX) consisting of three super-layers, each comprising two layers. The VTX has a barrel geometry and is optimized for excellent point resolution and low material thickness. An alternative five layer geometry is under study.

- A system of silicon detectors (Si-strip and Si-pixel) surrounds the VTX. In the barrel region two layers of Si-strips bridge the gap between the VTX and the TPC. The forward region is instrumented with a system of Si-strip and Si-pixel detector discs (FTD) and extends the tracking to low polar angles.

- A large TPC with up to 224 points per track, optimized for a high 3-dimensional point resolution, provides particle identification capabilities via dE/dx measurements. Precise timing information is required to determine the longitudinal point coordinate.

- An intermediary system of Si-strip detectors behind the TPC endplate (ETD) and before the barrel ECAL (SET) extends the tracking to the ECAL with high precision space points.

- A highly segmented tungsten ECAL with 30 layers in radial direction and small transverse cell sizes precisely measures electromagnetic energies.

- A highly segmented HCAL of up to 48 layers measures hadronic energies. Steel is chosen as the absorber material. One option for the active material is an analogue system of 3×3 cm^2 scintillator tiles.
- Calorimetric coverage in the forward region is extended with a system of three calorimeters (LumiCal, BeamCal, LHCAL) which allow to monitor the beam quality and luminosity.
- A super conducting coil provides an axial B-field of 3.5 Tesla. The coil is located outside of the calorimeters to minimize the inactive material between the tracking and calorimetric systems.
- An iron yoke returns the magnetic flux and is instrumented for muon detection. It also serves as a tail catcher for punch-through hadronic showers.

Table 4.1 lists the angular coverage of the calorimetric and tracking systems.
The crossing angle of 14 mrad of the incoming beams leads to a deflection of the electrons and positrons in the detector solenoid and results in a small spin misalignment of polarized particles. Emission of synchrotron radiation from the deflection deteriorates the beam emittance. To avoid these effects, an additional dipole field is superimposed on the solenoid field. Two configurations have been considered. The DID (Detector Integrated Dipole) bends the solenoid field in the direction of the incoming beams, while the anti-DID field aligns the solenoid field to the outgoing particles [55, 56]. Although the anti-DID solution effectively doubles the spin misalignment, it is the preferred configuration due to its beneficial influence on the detector backgrounds.
The tracking system and the ECAL are explained in more detail in the following section.

Subsystem	Coverage in $\lvert\cos(\Theta)\rvert$	Coverage in Θ [deg]
ECAL Barrel	$\lvert\cos(\Theta)\rvert < 0.787$	$\Theta > 38.1$
ECAL EndCap	$0.761 < \lvert\cos(\Theta)\rvert < 0.987$	$9.25 < \Theta < 40.45$
ECAL Ring	$0.988 < \lvert\cos(\Theta)\rvert < 0.995$	$5.7 < \Theta < 9.0$
LumiCal		$1.8 < \Theta < 4.5$
BeamCal		$0.3 < \Theta < 2.4$
Active region	**Radial r [mm]**	**Longitudinal z [mm]**
Calorimeters	$r > 1843$	$z > 2450$
Tracking in TPC	$395.0 < r < 1739.0$	$z < 2247.5$

Table 4.1: *Angular coverage of selected ILD subsystems.*

4.3 The tracking system

Flavor tagging and the identification of displaced vertices close to the interaction point (IP) is done with the VTX. Optimal vertex identification requires the first layer of the VTX to be

as close as possible to the IP. With decreasing distance, however, the occupancy from beam related backgrounds increases rapidly.

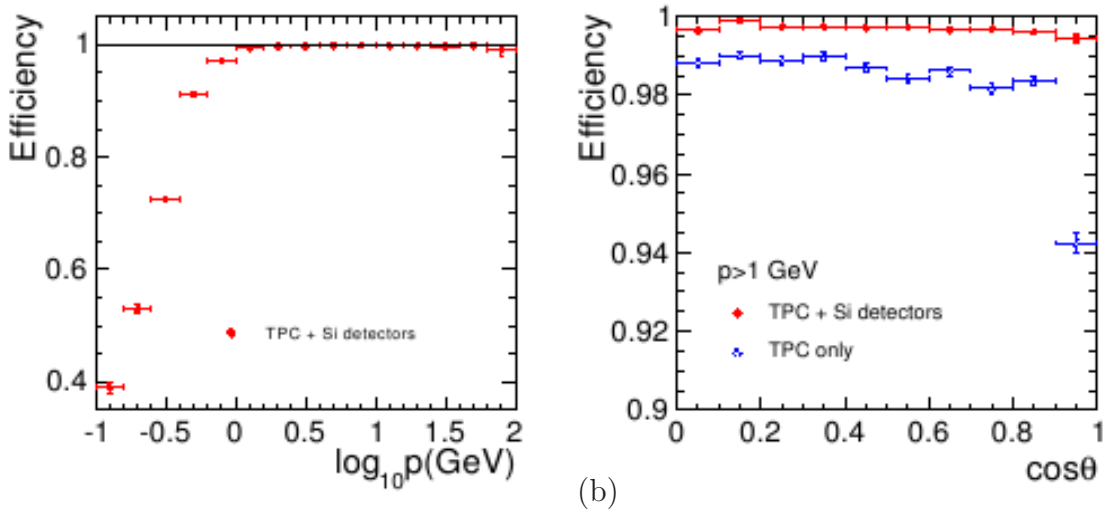

Figure 4.3: *ILD tracking efficiency for* $t\bar{t} \rightarrow 6$ *jets at* $\sqrt{s} = 500$ *GeV. The efficiency is plotted against (a) the decadal logarithm of particle momentum and (b) the polar angle* $\cos\Theta$ *[36].*

The main tracker of the ILD will be a gaseous Time Projection Chamber (TPC). In comparison with other options for tracking systems, e.g. silicon pixel detectors, a TPC has some advantages. For one, tracks can be measured with a large number of space points in r, ϕ, z. Secondly, the amount of material presented to particles traversing the tracking region is minimal, thus the impact of the tracking on the energy measurement in the calorimeters is low. This ensures optimal performance of the calorimeters. Additionally, the low material budget reduces the impact of beamstrahlung photons from e^+e^- conversions. With the full tracking system of VTX, FTD and TPC, a tracking efficiency of 99.5% is achieved for polar angles down to $\Theta = 7°$ as shown in Figure 4.3 [36].

4.4 Electromagnetic calorimeter

The design of the ECAL is strongly influenced by the requirements of optimal pattern recognition. This need has to be balanced with the achievable energy resolution. Effective pattern recognition requires a high spatial resolution, realized in the ILD electromagnetic calorimeter by a high granularity and the choice of tungsten as absorber material due to its small Molière radius $R_M = 9$ mm compared to $R_M = 17$ mm of iron. The tungsten radiation length of $X_0 = 3.5$ mm allows for a compact design and a good separation of electromagnetic showers generated by neighboring particles. The ECAL is segmented longitudinally in around 30 layers, each layer consisting of an active part of either silicon diodes or scintillators and an absorber part. In case of the silicon diodes, each layer is segmented vertically into cells with lateral sizes of 5 – 10 mm. This fine granulation is required for optimal pattern recognition. The overall calorimeter system exhibits an eight-fold cylindrical symmetry in the barrel region, see Figure 4.4(a). One octant of the ECAL barrel is called a stave. To ensure maximal hermeticity, the geometric arrangement of the staves is chosen such that the cracks in between

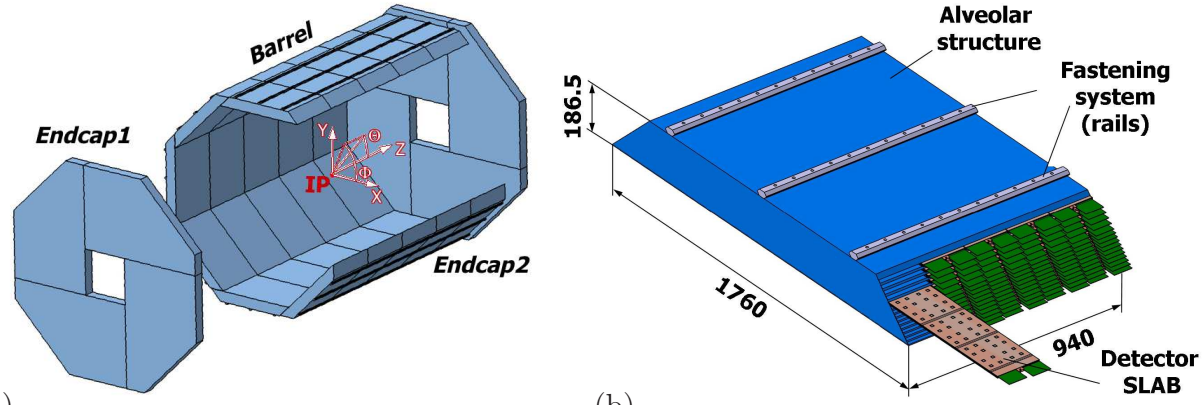

(a) (b)

Figure 4.4: *(a) Global layout of ECAL and (b) layout of one module [36].*

staves do predominantly not point to the e^+e^- IP, i.e. the cracks enclose a large angle with the radial direction. Along the beam axis the staves are segmented into five modules. Each module is build up of slabs holding the individual detector layers. The ECAL is closed by the ECAL endcaps. A detailed description of the ECAL can be found in [57].
For an adequate energy resolution of the silicon-tungsten ECAL, the first 12 radiation lengths are build up of 20 layers of 0.6 X_0 tungsten absorbers, followed by another nine layers of 1.2 X_0 tungsten absorbers. In the radial direction from the e^+e^- IP the calorimeter starts with an active layer. In total 10^8 readout channels will be installed in the final calorimeter. A prototype has been used for testbeam measurements by the CALICE collaboration. For this prototype an energy resolution of $\Delta E/E = (16.6 \pm 0.1)/\sqrt{E(GeV)} \oplus (1.1 \pm 0.1)\%$ has been determined [58, 59].

4.5 Hadronic calorimeter

The ILD Hadronic Calorimeter (HCAL) is conceived as a self-supporting sampling calorimeter with a very good energy resolution and a high granularity for PFLOW reconstruction which allows the separation of neutral and charged hadrons. The HCAL is located inside the field coil and, thus, needs to be constructed from non-magnetic materials. For the absorber, stainless steel has been chosen which also has the advantage of a moderate ratio of hadronic λ_I to electromagnetic interaction length X_0. Thus, a fine longitudinal segmentation in terms of X_0 can be realized within a few layers of a given hadronic interaction length.
For the active material two options are under investigation: either scintillator tiles read out in analog mode, or gaseous devices providing a digital signal. The HCAL design follows the eight-fold symmetry of the ECAL with a barrel region and two endcaps. A total hadronic interaction length of at least 5.5 λ_I is envisioned. For the analogue option, the scintillator cell size is 3×3 cm^2, and the radial segmentation is achieved by alternating absorber and active materials in 48 layers.

From simulations and testbeam data of the CALICE collaboration, a hadronic energy resolution of $49\%/\sqrt{E}$ seems achievable [60].

4.6 Forward calorimeters

The forward calorimeters are of special importance to the ILD detector. Three subsystems will be installed, the LHCAL, extending hadronic calorimetry to small polar angles, the LumiCal for a precise luminosity measurement and the BeamCal for a fast, bunch-by-bunch access to the luminosity. A schematic drawing of the forward calorimeters is shown in Figure 4.5. These detectors, the LumiCal and BeamCal in particular, have to be very radiation hard, as they are bombarded with e^+e^--pairs from Bhabha scattering and $\gamma\gamma$ processes. Since the

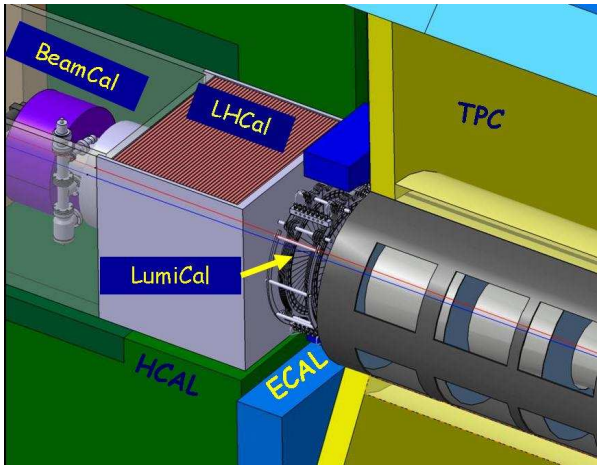

Figure 4.5: *Forward Instrumentation of* ILD *with LHCAL, LumiCal and BeamCal [61].*

BeamCal is used in the WIMP analysis in Part I of this thesis, the description of the forward calorimetry is constrained to this subsystem.
The BeamCal covers polar angles from 5 to 40 mrad and is constructed as a cylindrical solid-state-sensor tungsten sandwich calorimeter. It is longitudinally segmented into 30 discs of tungsten absorbers of 3.5 mm thickness corresponding to one radiation length, and each layer is equipped with sensors of approximately 1×1 cm^2 cross sectional area [61]. For each bunch crossing, the BeamCal will be hit with e^+e^--pairs, depositing several TeV of electromagnetic energy in the full system. The BeamCal has to be able to identify high-energy electrons on top of the steady beamstrahlung background, and dedicated shower-finding algorithms have to be developed for this purpose. The BeamCal's detection capability is required for background rejection in several physics analyses, e.g. searches for supersymmetric stau-leptons and also in the analysis presented in this thesis.

4.7 Muon system and tailcatcher

Beyond the magnetic coil of the ILD, an instrumented iron yoke returns the magnetic flux and also serves as a detector for muons with energies above a few GeV. The detection system will also be used to tag cosmics and beam halo muons. Important for the muon identification will be the linking between tracks identified in the central tracking system and hits recorded in the muon system. Additional instrumentation in the yoke provides limited hadronic calorimetry capabilities, and the yoke serves as a tailcatcher for punch-through hadronic showers as well. The return yoke will be equipped with 10 detector layers of 10 cm thick absorber plates close to the coil and a few detector layers further out for supporting measurements. Scintillator strip-detectors or gas detectors could provide a lateral segmentation in the range of centimeters. The total channel count of the muon system will be in the order of 10^5.

Part I

Model Independent WIMP Search

Chapter 5

WIMP detection via initial state radiation

One of the great advantages of the ILC is its clean environment of colliding leptons whose initial state is exactly known (cf. Chapter 3). This knowledge, in conjunction with the excellent momentum and energy resolution and the high hermeticity of the ILD detector, reduces the systematic uncertainties on the measurements. The high granularity of the calorimetric system optimized for Particle Flow event reconstruction allows for a precise reconstruction of the kinematic parameters of all particles pertaining to each recorded event. The ILD experiment therefore provides all the requisites for high precision measurements within the SM and physics beyond [36].
In this analysis the prospects of measuring the parameters of Weakly Interacting Massive Particles (WIMPs) at the ILC are studied. The analyzed production process is direct WIMP pair production with associated initial state radiation (ISR), $e^+e^- \to \chi\chi\gamma$, where the only detected particle is the emitted photon. This channel is studied in both a model independent ansatz and for the supersymmetry reference point SPS1a' of the cMSSM [39].
The precise measurement of the invariant mass of the unobserved WIMP system from the measured photon spectrum benefits strongly from the excellent ILD energy resolution and hermeticity. Furthermore, with the use of polarized beams at the ILC, the measured photon spectrum provides information on the coupling structure of the signal interaction.
In this chapter, the model independent approach to WIMP detection is introduced, and the relevant SM background processes are presented, as well as the accelerator induced background.

5.1 WIMP production at the ILC

In this section, both, the model independent cross section for generic WIMP pair production $e^+e^- \to \chi\chi\gamma$, and the neutralino pair production $e^+e^- \to \tilde{\chi}_1^0\tilde{\chi}_1^0\gamma$ in the supersymmetry parameter point SPS1a' of the cMSSM are introduced.

5.1.1 Model independent WIMP cross section

The first part of this analysis is based on a model independent cross section for ISR associated WIMP pair production $e^+e^- \to \chi\chi\gamma$ as described in [62], see Figure 5.1. The differential cross section is expressed in the dimensionless kinematic variables x and $\cos(\Theta_\gamma)$ of the emitted photon, where $x = \frac{2E_\gamma}{\sqrt{s}}$ with the photon energy E_γ and the center-of-mass energy $\sqrt{s}$, and Θ_γ is the polar angle of the photon with respect to the electron beam axis. The predictions of the resulting cross section are valid for a broad range of SM extensions containing WIMPs, such as supersymmetry (SUSY), universal extra dimensions, little Higgs theories, etc.
Model independence in this approach means that no assumptions on the production mechanism are made. The free parameters in this ansatz are the WIMP mass M_χ and spin S_χ. An additional free parameter is the angular momentum quantum number J_0 of the dominant

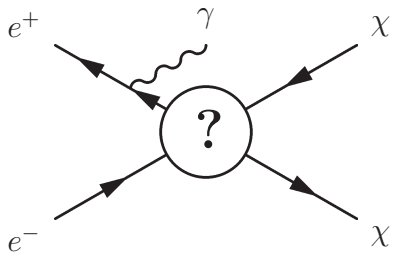

Figure 5.1: *Pseudo Feynman graph of radiative WIMP pair production. In the model independent approach no assumptions on the production mechanism are made, indicated by the question mark.*

partial wave in the production process. For the derivation of the production cross section the WIMP particle χ and its anti-particle $\bar{\chi}$ are considered identical.
The normalization of the total cross section is free but can be cosmologically constrained, if the WIMP is identified as the only component of the observed DM content in the cosmos, as shown in Figure 5.2(a). In the following, a short deduction of the WIMP production cross section is presented. For more details, the reader is referred to [62].

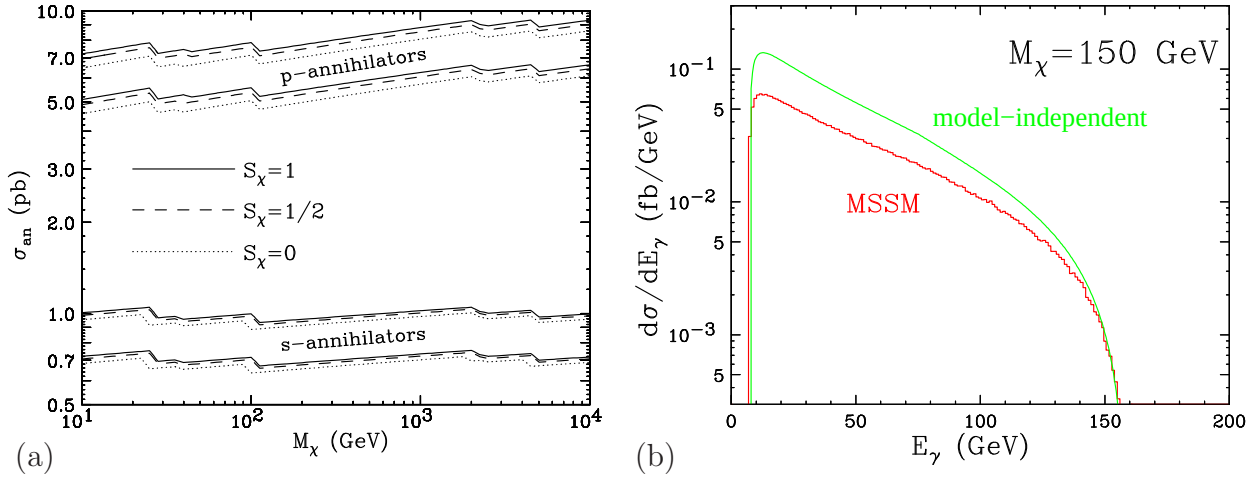

Figure 5.2: *(a) Cosmological constraints on the WIMP annihilation cross section σ_{an} as a function of the WIMP mass at the 2σ level for s- and p-wave annihilators. (b) Comparison between the photon spectra from the process $e^+e^- \to 2\tilde{\chi}_1^0\gamma$ in the MSSM and from the prediction of Eq. 5.8 for a 150 GeV WIMP. Both figures taken from [62].*

The proposed WIMPs can pair annihilate directly into SM particles $\chi\chi \to X_i\bar{X}_i$, where X_i can be any SM particle $(l, q, g, \nu...)$. The total annihilation cross section is given by the sum over the final states i,

$$\sigma = \sum_i \sigma_i. \tag{5.1}$$

Given interactions of weak strength and small relative velocities v[1] of the initial WIMPs, the cross section partial wave expansion

$$\sigma_i v = \sum_{J=0}^{\infty} \sigma_i^{(J)} v^{2J} \quad \text{or} \quad \sigma_i = \sum_{J=0}^{\infty} \sigma_i^{(J)} v^{2J-1} \tag{5.2}$$

can be truncated after the first two terms corresponding to $J_0 = 0$ (s-wave) and $J_0 = 1$ (p-wave) annihilation. For interactions invariant under time reversal, the spin averaged production and annihilation processes are related by the principle of detailed balancing:

$$\frac{\sigma(\chi\chi \to X_i\bar{X}_i)}{\sigma(X_i\bar{X}_i \to \chi\chi)} = 2\frac{v_X^2(2S_X+1)^2}{v_\chi^2(2S_\chi+1)^2}. \tag{5.3}$$

Using only the dominant term $\sigma_i^{(J_0)} v^{2J_0-1}$ of Equation 5.2 and the non-relativistic center-of-mass approximation $v = 2v_\chi$, Equation 5.3 becomes

$$\sigma(X_i\bar{X}_i \to \chi\chi) = 2^{2(J_0-1)}\kappa_i\sigma_{\text{an}}\frac{v_\chi^{2J_0+1}}{v_X^2}\frac{(2S_\chi+1)^2}{(2S_X+1)^2}, \tag{5.4}$$

with $\kappa_i = \frac{\sigma_i^{(J_0)}}{\sigma_{\text{an}}}$ being the spin averaged "annihilation fraction"[2] and $\sigma_{\text{an}} = \sum_i \sigma_i^{(J_0)}$ and with the WIMP velocity v_χ. For relativistic electrons ($X_i = e^-$) with the relative WIMP velocity $v_\chi^2 = 1 - \frac{4M_\chi^2}{s}$ and the center-of-mass energy squared s, the pair production cross section is:

$$\sigma(e^+e^- \to \chi\chi) = 2^{2(J_0-1)}\kappa_e\sigma_{\text{an}}\frac{(2S_\chi+1)^2}{2^2}\left(1 - \frac{4M_\chi^2}{s}\right)^{1/2+J_0}. \tag{5.5}$$

For soft/collinear ISR a relation between the processes $e^+e^- \to 2\chi$ and $e^+e^- \to 2\chi + \gamma$ is given by the factorization

$$\frac{d\sigma(e^+e^- \to 2\chi + \gamma)}{dx\ d\cos\Theta} \approx \mathcal{F}(x, \cos\Theta)\hat{\sigma}(e^+e^- \to 2\chi). \tag{5.6}$$

In Equation 5.6 $\hat{\sigma}$ is the WIMP pair production cross section of Equation 5.5 evaluated at the reduced center-of-mass energy $\hat{s} = (1-x)s$. The universal collinear factor $\mathcal{F}$ in Equation 5.6 is given by

$$\mathcal{F}(x, \cos\Theta) = \frac{\alpha}{\pi}\frac{1+(1-x)^2}{x}\frac{1}{\sin\Theta^2}. \tag{5.7}$$

With Equation 5.7, the model independent WIMP pair production cross section in e^+e^- collisions can be written as:

$$\frac{d\sigma}{dx\ d\cos\Theta} \approx \frac{\alpha\kappa_e\sigma_{\text{an}}}{16\pi}\frac{1+(1-x)^2}{x\sin\Theta^2}2^{2J_0}(2S_\chi+1)^2\left(1 - \frac{4M_\chi^2}{(1-x)s}\right)^{1/2+J_0}. \tag{5.8}$$

[1] $v = \beta$ for $c = 1$ (in natural units).

[2] Note that $\sum_i \kappa_i = 1$.

Despite the soft/collinear approximation, expression 5.8 also holds reasonably for a wide range of photon emission energies and polar angles [62]. If interpreted model-dependently, the main characteristics of the photon spectrum are conserved as shown in Figure 5.2(b), where the prediction of Equation 5.8 for $M_\chi = 150$ GeV is compared to the photon spectrum from the reaction $e^+e^- \to \tilde{\chi}_1^0\chi_1^0\gamma$ within the minimal supersymmetric standard model (MSSM). The MSSM parameters at the weak scale are $M_1 = 168$ GeV, $M_2 = 2M_1$, $\mu = 225$ GeV, $m_{\tilde{l}_R} = 177$ GeV and $\tan\beta = 10$. All other mass parameters are fixed to 1 TeV.
Figure 5.3 shows the differential cross section $d\sigma/dx$ (Eq. 5.8) in arbitrary units for (a) different WIMP masses of 120 GeV, 160 GeV and 200 GeV, and (b) for 160 GeV s- and p-wave WIMPs. As can be seen, the production cross section exhibits a mass dependent cut-off in the energy spectrum of the emitted photons. If a WIMP signal was observed at ILC, a determination of the cut-off position would be equivalent to a measurement of the WIMP candidate mass. Additionally, the behavior at the threshold E_γ provides a measurement of the dominant partial wave in the production process, see Figure 5.3(b).

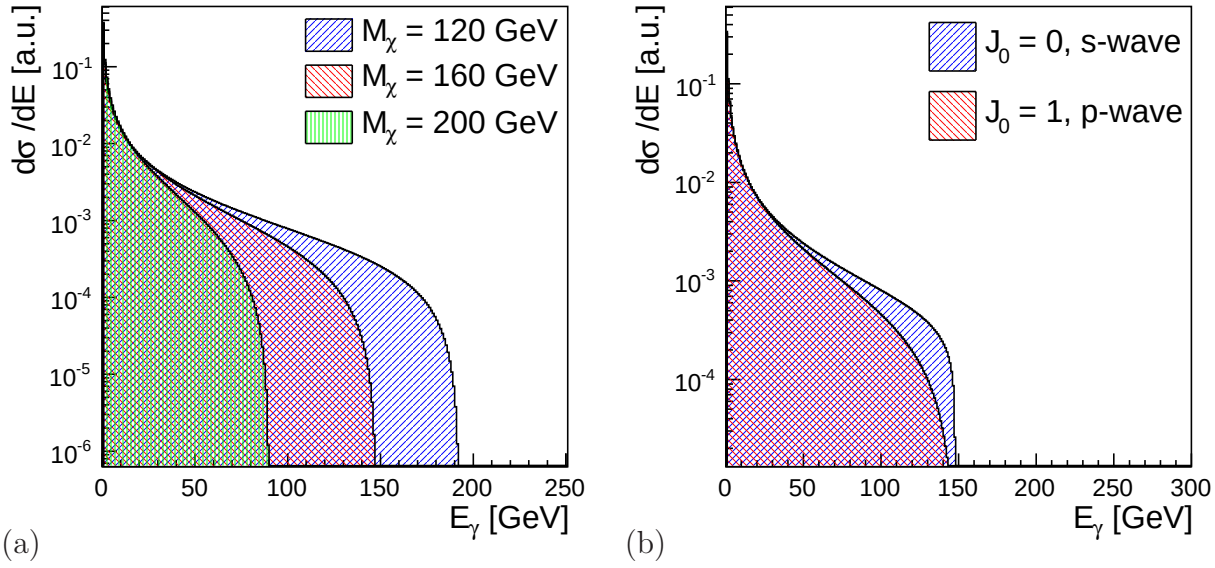

Figure 5.3: *Differential Wimp production cross section $d\sigma/dE$, (a) for different WIMP masses M_χ of 120 GeV, 160 GeV and 200 GeV, and (b) for 160 GeV s- and p-wave WIMPs. The cross sections are shown in arbitrary units.*

5.1.2 Points in parameter space

For polarized beams the spin averaged annihilation fraction κ_e in Equation 5.8 has to be replaced with

$$\begin{aligned}\kappa_e^{pol} &= \frac{1}{4}(1+P_{e^-})[(1-P_{e^+})\kappa(e_R^-e_L^+) + (1+P_{e^+})\kappa(e_R^-e_R^+)] \\ &+ \frac{1}{4}(1-P_{e^-})[(1+P_{e^+})\kappa(e_L^-e_R^+) + (1-P_{e^+})\kappa(e_L^-e_L^+)]. \end{aligned} \quad (5.9)$$

Here, the helicity dependent annihilation fraction $\kappa(e_R^-e_L^+)$ describes the strength of the WIMP couplings to right-handed electrons and left-handed positrons. The other couplings are to be

interpreted in the same manner[3]. To restrict the evaluated parameter space in this analysis, three special coupling scenarios are evaluated:

- **"Equal"**: In this scenario the WIMP couplings are independent of the helicity of the incoming electrons and positrons, i.e. $\kappa(e_R^-, e_L^+) = \kappa(e_R^-, e_R^+) = \kappa(e_L^-, e_L^+) = \kappa(e_L^-, e_R^+)$. The signal rate is unaffected by the beam polarizations.

- **"Helicity"**: The couplings conserve helicity and parity, $\kappa(e_R^-, e_L^+) = \kappa(e_L^-, e_R^+)$; $\kappa(e_R^-, e_R^+) = \kappa(e_L^-, e_L^+) = 0$. Due to the WIMP coupling to right-handed electrons and left-handed positrons, beam polarization can be used to increase the S/B ratio in regard to the dominant $e^+e^- \to \nu\nu\gamma$ SM background (cf. Sec. 5.2.1) since the neutrinos couple predominantly to left-handed electrons and right-handed positrons.

- **"Anti-SM"**: This scenario is a "best case" scenario, since the WIMPs couple only to right-handed electrons and left-handed positrons: $\kappa(e_R^-, e_L^+)$; with all other $\kappa(e^-, e^+) = 0$. With appropriately chosen beam polarizations the S/B ratio is maximally increased.

In the following each scenario is referred to by the labels **"Equal"**, **"Helicity"** and **"Anti-SM"**. Furthermore, only s-wave and p-wave processes are considered, since higher orders in the partial wave extension of Equation 5.2 are suppressed by the short range of weak interactions and the heavy, non-relativistic, final state WIMPs. As a pure multiplicative factor, the WIMP spin is not directly accessible and is subsumed under the normalization of the total cross section which is left as a free parameter alongside the WIMP mass (cf. Eq. 5.8).

5.1.3 WIMP production in supersymmetry: SPS1a'

The supersymmetry benchmark point SPS1a' has been defined in the Supersymmetry Parameter Analysis (SPS) convention project [39]. The aim of this project is to provide a well founded theoretical framework to calculate masses, mixings, decay widths and production cross sections for physics analyses at the LHC and ILC with theoretical accuracies matching the expected experimental precision. Although the colored content of the SPS1a' has been recently excluded by first results from LHC [63, 64], its general mass spectrum of the sleptons and neutralinos still provides a viable SUSY scenario, since the LHC results constrain only squark and gluino masses.
The CP- and R-Parity invariant SPS1a' benchmark point lies in the constrained MSSM (cMSSM or mSugra) parameter space. It is compatible with all high-energy mass bounds on the SUSY parameters as well as with the observed CDM data, calculated as $\mathcal{B}(b \to s\gamma) = 3.0 \times 10^{-4}$ [65], $\Delta[g-2]_\mu/2 = 34 \times 10^{-10}$ [66], $\Delta\rho_{\mathrm{SUSY}} = 2.1 \times 10^{-4}$ [66] and $\Omega_{\mathrm{CDM}}h^2 = 0.10$ [65].
The parameter point SPS1a' provides with the lightest stable neutralino $\tilde{\chi}_1^0$ a DM candidate. Because of R-Parity conservation the sparticles can only be produced in pairs. Table 5.1 gives the values of the universal gaugino mass $M_{1/2}$, the scalar mass M_0, the trilinear coupling A_0, as well as sign(μ) and tan (β). Table 5.2 and Figure 5.4 show the resulting mass spectrum

[3]Note that $1/4 \sum_{i,j=R,L} \kappa(e_i^- e_j^+) = \kappa_e$.

$M_{1/2}$	M_0	$\tan(\beta)$	$\mathrm{sign}(\mu)$	A_0
250.0 GeV	70.0 GeV	10	+1	−300.0 GeV

Table 5.1: *Values of the universal gaugino mass $M_{1/2}$, the scalar mass M_0, the ratio of the Higgs v.e.v's $\tan(\beta)$, the sign of the Higgs mass mixing parameter $\mathrm{sign}(\mu)$ and the trilinear coupling A_0 in the SPS1a' parameter point in the mSugra scenario.*

Particle	Mass [GeV]
h^0	116.0
H^0	425.0
A^0	424.9
H^+	432.7
$\tilde{\chi}_1^0$	97.7
$\tilde{\chi}_2^0$	183.9
$\tilde{\chi}_3^0$	400.5
$\tilde{\chi}_4^0$	413.9
$\tilde{\chi}_1^+$	183.7
$\tilde{\chi}_2^+$	415.4
$\tilde{e}_R$	125.3
$\tilde{e}_L$	189.9
$\tilde{\nu}_e$	172.5

Particle	Mass [GeV]
$\tilde{\tau}_1$	107.9
$\tilde{\tau}_2$	194.9
$\tilde{\nu}_\tau$	170.5
$\tilde{u}_R$	547.2
$\tilde{u}_L$	564.7
$\tilde{d}_R$	546.9
$\tilde{d}_L$	570.1
$\tilde{t}_1$	366.5
$\tilde{t}_2$	585.5
$\tilde{b}_1$	506.3
$\tilde{b}_2$	545.7
$\tilde{g}$	607.1

Table 5.2: *Masses of supersymmetric and Higgs particles in the mSugra SPS1a' reference point. The masses of the second generation sparticles coincide with those of the first generation sparticles [39].*

of the supersymmetric particles. All sleptons, the lightest higgs h^0, the lightest charginos $\chi_1^\pm$ and the two lightest neutralinos $\tilde{\chi}_1^0$ and $\tilde{\chi}_2^0$ can be produced at the ILC with a center-of-mass energy of $\sqrt{s} = 500$ GeV.
The production of the lightest neutralino $\tilde{\chi}_1^0$ has been studied in the di-muon channel $e^+e^- \to \tilde{\mu}_L\tilde{\mu}_L$ with the subsequent decay of the smuons $\tilde{\mu}$ to muons and neutralinos $\tilde{\mu}_L \to \mu\tilde{\chi}_1^0$ [67]. Identifying and measuring the lower and upper edges of the energy distribution of the detected muons allows to determine the $\tilde{\chi}_1^0$ mass with a relative statistical error of 1.09%.
In Figure 5.5, a selection of tree level diagrams for the signal process $e^+e^- \to \tilde{\chi}_1^0\tilde{\chi}_1^0\gamma$ is presented, the tree level amplitudes are given in [68]. In the bino, wino, higgsino base $(\tilde{B}, \tilde{W}, \tilde{H}_1^0, \tilde{H}_2^0)$, the composition of the lightest neutralino is

$$\tilde{\chi}_1^0 = -0.987\ \tilde{B} + 0.056\ \tilde{W} - 0.142\ \tilde{H}_1^0 + 0.051\ \tilde{H}_2^0. \tag{5.10}$$

From Equation 5.10 follows that the neutralino $\tilde{\chi}_1^0$ is predominantly bino in the SPS1a' parameter point. Due to the bino-like neutralino, and since the right-handed selectron $\tilde{e}_R$ is much lighter than the left-handed selectron $\tilde{e}_L$, the radiative neutralino production proceeds mainly via right-handed electrons and left-handed positrons, comparable to the **"Anti-SM"** WIMP scenario (cf. Sec. 5.1.2). Although the signal signature of a single high-energetic photon is

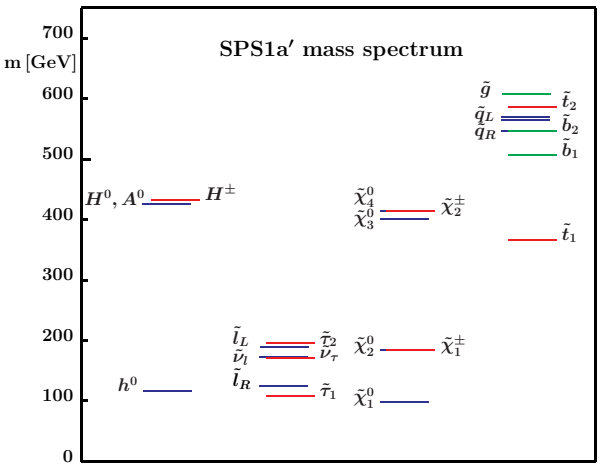

Figure 5.4: *Mass spectrum of supersymmetric particles in the SPS1a' reference point from Table 5.2 [39]. At ILC with $\sqrt{s} = 500$ GeV all sleptons, the lightest higgs and the neutralinos $\tilde{\chi}_1^0$ and $\tilde{\chi}_2^0$ are accessible.*

the same as for the model independent WIMP case, this process can not be studied in the same framework, because of the additional possibility of the photon being emitted from the selectron exchanged in the t-channel, Figure 5.5(b).
It has been pointed out that the spin of supersymmetric particles can be determined unambiguously at e^+e^- colliders [69] by examining the threshold behavior of the excitation curves for pair production and the angular distributions in the production and decay processes. Furthermore, the behavior of the cross section at the threshold energy for any non-diagonal neutralino pair production $e^+e^- \to \tilde{\chi}_i^0\tilde{\chi}_j^0$ $(i \neq j)$, in combination with the fermion invariant mass distribution of the decay $\tilde{\chi}_i^0 \to \tilde{\chi}_j^0 f\overline{f}$ near the endpoint, provides an unambiguous evidence for CP violation in the neutralino system [70]. In general, in CP-invariant supersymmetry the threshold excitation for diagonal neutralino pairs $e^+e^- \to \tilde{\chi}_i^0\tilde{\chi}_i^0$ proceeds via p-wave production, i.e. the production cross section is proportional to β^3 at threshold [69], with the neutralino velocity β. Thus, p-wave behavior is expected for the neutralino pair production in SPS1a'.
In this analysis the differential cross section $d\sigma/dx\ d\cos\Theta$ is calculated with a FORTRAN routine implemented by O. Kittel and U. Langenfeld [68, 71].

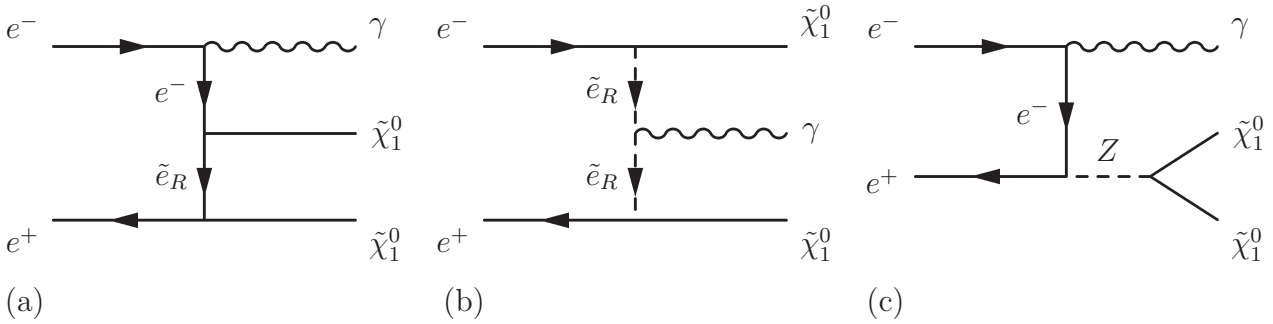

Figure 5.5: *Tree level diagrams of radiative neutralino production in e^+e^- collisions. In the SPS1a' parameter point the selectron exchange diagrams are dominated by right-handed selectrons.*

5.2 Background processes

Possible backgrounds to the single photon signal process comprise SM physics processes, as well as beam-induced backgrounds. Hadronic final states are not considered here, since they can be easily identified and rejected because of their high track multiplicity accompanied by a large number of clusters in the electromagnetic and especially in the hadronic calorimeters.

5.2.1 SM background

The SM backgrounds to the WIMP and neutralino single photon signal can be divided into reducible and irreducible backgrounds. Irreducible backgrounds are indistinguishable from the single photon signature of the WIMP pair production on an event-by-event basis. The dominant irreducible SM background is radiative neutrino pair production $e^+e^- \to \nu\overline{\nu}\gamma$, see Figure 5.6 [72, 73], where the neutrinos escape undetected like the WIMPs, carrying away large amounts of energy. At center-of-mass energies well above the Z mass, the process is

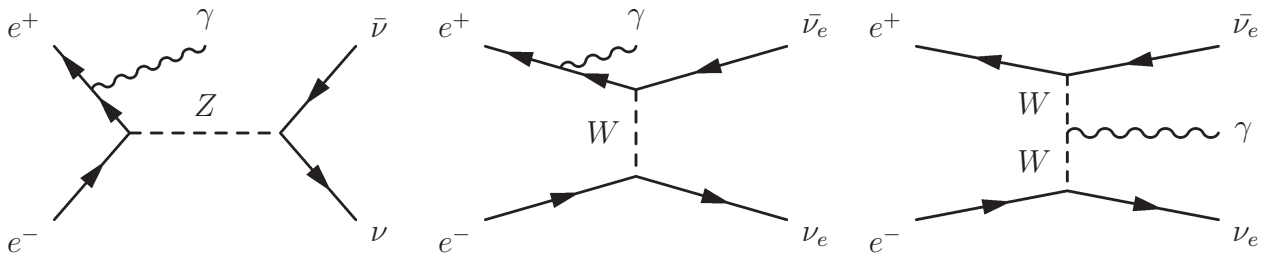

Figure 5.6: *Tree level diagrams for radiative neutrino production ($e^+e^- \to \nu\nu\gamma$) which constitutes the main SM background to the chosen signal process.*

dominated by W-exchange in the t-channel. The tree level amplitudes already including the emitted photon and the matrix elements squared for longitudinal beam polarizations can be found in [68].

The main reducible background is radiative Bhabha scattering $e^+e^- \to e^+e^-\gamma$. The final state electrons are usually very forward and escape through the beam pipe, leaving only the radiated photon to be detected. Also, very forward electrons do not enter the tracking region, and their energy depositions in the calorimeters at low polar angles can be mistaken for photons. The main means of rejecting Bhabha events is given by the forward calorimeters of BeamCal and LHCAL (see Sec. 4.6).

Electron-positron annihilation $e^+e^- \to \gamma\gamma$ contributes to a lesser amount to the reducible background. However, annihilation events can mimic the single photon signal signature if one of the photons is not correctly reconstructed.

An additional class of SM backgrounds, collectively called $\gamma\gamma$ background, originates from the interaction between virtual photons or between virtual and real photons (Fig. 5.7). Additional fermions arising from these interactions lead to huge backgrounds in the calorimeters and tracking system, because of their large cross sections in the order of 5×10^8 fb. Extensive studies have been performed to evaluate the impact of the $\gamma\gamma$ background on pattern recognition and event reconstruction [36].

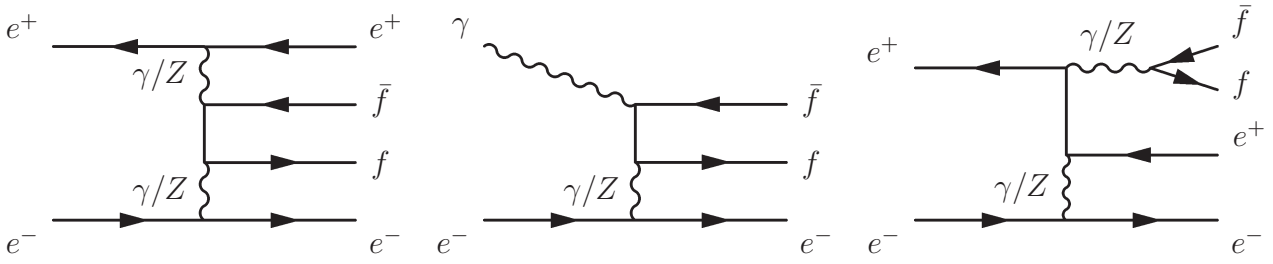

Figure 5.7: *Tree level Feynman diagrams of the SM $\gamma\gamma$ background. The angular distribution of the final state electrons is strongly peaked forward.*

If SUSY was realized in nature, another potential background would be radiative sneutrino production $e^+e^- \to \tilde{\nu}\tilde{\nu}^*\gamma$. When the sneutrino is lighter than the charginos and the next-to-lightest neutralino, as is the case for SPS1a', the sneutrinos can only decay invisibly to a neutrino and the neutralino LSP, $\tilde{\nu} \to \nu\tilde{\chi}_1^0$ [74, 75]. This process is not included in the studied backgrounds to maintain the model independence of the WIMP approach. Also, in case of the SPS1a' scenario, this background is excluded as well to still allow a comparison with the model independent ansatz. The inclusion of this background is subject to future studies.
As has been argued in [74, 75], the only possibility to access the sneutrino mass is by the precise determination of the kinematic distributions of cascade decays of e.g. $\tilde{\chi}_1^+ \to \tilde{\nu}_l l^+$ or in processes, where the sneutrino is exchanged in the t-channel. Such a measurement would entail experimental control of the radiative sneutrino production.

5.2.2 Beam-related backgrounds

The highly focused beams in conjunction with the strong electromagnetic fields in the interaction region lead to a number of different beam-related backgrounds that pose major challenges to the detector components [33, 36, 76, 77]. Especially the forward instrumentation has to withstand high levels of radiation. The main beam background sources are:

- Beamstrahlung: created by the mutual focussing of each beam in the strong electromagnetic field of the oncoming beam. Beamstrahlung disrupts the beams and generates very forward focused photons. Electron-positron pairs from the disrupted beam and from photon conversions are guided into the forward direction by the collective field from the oncoming beam and also by the detector solenoid magnetic field. Beamstrahlung pairs deposit energy of up to several TeV per bunch crossing in the BeamCal alone.

- Synchrotron radiation: created in the upstream final focussing elements of the beam delivery system near the interaction point. The largest fraction of synchrotron radiation is created by the non-gaussian tails of the electron (positron) bunches which deviate from the ideal orbit and experience stronger deflection.

- Muons: created in interactions between beam and collimators upstream of the Interaction Point (IP). They travel along the accelerator tunnel towards the detector.

- Neutrons created from electrons striking beamline components. Neutrons may also be backscattered from downstream interactions of the spent beams in the beam dumps.

Although most of these backgrounds leave the detector through the beampipe, a significant fraction has large enough polar angles to still get inside the sensitive volume of the tracking system (VTX and TPC) or the calorimeters (ECAL and HCAL). Secondary interactions of the beam-related backgrounds with the beam pipe and/or detector components are another major source of backgrounds. The effects of the beamstrahlungs background and the secondary interactions on the signal efficiency are included in this study (cf. Sec. 6.5.1). The muon background is not considered, since it can easily be suppressed by its unique signature in the muon system.

5.3 Analysis strategy

The present work is conceived as a model independent search. This requires a high level of flexibility with regard to the possible parameter space, both for an interpretation in the DM scenario, as well as for more model dependent interpretations, e.g. SUSY scenarios. The Monte-Carlo (MC) generation, followed by a full detector simulation and event reconstruction for a wide range of possible signal parameters was limited by the available CPU time. Therefore a different approach has been used.
Since the WIMP signature is indistinguishable from the dominant $e^+e^- \to \nu\nu\gamma$ background, the signal events are created by weighting the $e^+e^- \to \nu\nu\gamma$ background events with the ratio $w_{sig} = \sigma(\chi\chi\gamma)/\sigma(\nu\nu\gamma)$ of the WIMP pair and the neutrino pair production cross section. The weight is evaluated in terms of the photon energy E_γ of the selected high-energetic photon. A drawback of this method is that the statistical fluctuations in the signal spectra for different WIMP parameter sets are highly correlated since they arise from the MC statistics of the simulated SM background.

5.3.1 Division in independent samples

The simulated sample size of the irreducible background $e^+e^- \to \nu\nu\gamma$ corresponds roughly to an integrated luminosity of $\mathcal{L} = 125\ \text{fb}^{-1}$ (cf. Sec. 6.3). This sample statistic is not sufficient for a distribution estimate of the photon spectrum independent of the statistical uncertainty. To still acquire a smooth estimate of the $e^+e^- \to \nu\nu\gamma$ background in terms of the photon energy, the distribution is parametrized from a subset of the simulated and reconstructed event sample.
After the event selection (cf. Sec. 6.5) the simulated data is divided into three statistically independent samples. In the following these samples will be referred to as:

- The **Background** sample which is used to create the SM background data for the simulated detector output.
- The **Signal** sample which is used to create the signal contribution to the simulated detector output.
- The **Template** sample which is used for the parametrization of the SM background. The resulting parametrization is then, in turn, also used to generate the signal expectation.

Since only the $e^+e^- \to \nu\nu\gamma$ background is signal-like, all other backgrounds are only divided into the **Background** and **Template** samples. The $e^+e^- \to \nu\nu\gamma$ background, however, is divided into all three samples so that the statistics for the signal sample corresponds to roughly $\mathcal{L} = 50$ fb^{-1}. All data samples acquire additional weights of $\mathcal{O}(10)$ when extrapolated to higher luminosities.
The **Template** sample is parametrized by successively correcting the theoretical SM predictions for deviations from the simulation output. By means of this procedure, the parametrization accounts for machine and detector related effects on the photon energy spectra. These effects are caused by the luminosity spectrum, beamstrahlung, additional ISR, the detector energy resolution and effects from the event reconstruction.
The **Template** parametrization is two-fold: the background template is realized by parameterizing the full SM background, while only the signal-like $e^+e^- \to \nu\nu\gamma$ photon energy spectra are parameterized and then re-weighted with w_{sig} to provide the signal templates. The entire parametrization procedure of both the **Template** samples is subject of Section 6.6. The signal contribution to the data is only generated from the **Signal** sample which is solely a subsample of the $e^+e^- \to \nu\nu\gamma$ process. Each event acquires a signal weight, as described in the previous paragraph.

5.3.2 Luminosity and polarization weights

Apart from the signal weight, each simulated data sample (i.e. the **Background** and **Signal** samples) obtains additional weights for luminosity normalization and polarization mixing. The data samples have been simulated with four different polarization configurations $(P_{e^-}; P_{e^+}) = (-1.0; +1.0), (+1.0; -1.0), (+1.0; +1.0)$ and $(-1.0; -1.0)$, see Section 6.3. In order to obtain an arbitrary experimental polarization state $(P_{e^-}; P_{e^+})$, each sample is weighted with $w_{pol} = (1 \pm P_{e^-})(1 \pm P_{e^+})/4$ according to the cross section deconstruction for longitudinally polarized beams

$$\begin{aligned} \sigma_{P_{e^-}P_{e^+}} &= \frac{1}{4}\{(1+P_{e^-})(1+P_{e^+})\sigma_{RR} + (1-P_{e^-})(1-P_{e^+})\sigma_{LL} \\ &+ (1+P_{e^-})(1-P_{e^+})\sigma_{RL} + (1-P_{e^-})(1+P_{e^+})\sigma_{LR}\}. \end{aligned} \tag{5.11}$$

Here, σ_{LL} is the cross section for 100% left-handed electron and positron beams, i.e. for beams in the polarization state $(P_{e^-}; P_{e^+}) = (-1.0; -1.0)$. Table 5.3 lists the polarization weights for

Expected Pol.	Weights for the Polarized MC Samples $(P_{e^-}; P_{e^+})$			
$(P_{e^-}; P_{e^+})$	$(-1.0; +1.0)$	$(+1.0; -1.0)$	$(+1.0; +1.0)$	$(-1.0; -1.0)$
$(0.0;\ \ 0.0)$	0.25	0.25	0.25	0.25
$(0.8;\ \ 0.0)$	0.05	0.45	0.45	0.05
$(0.8; -0.3)$	0.035	0.585	0.315	0.065
$(0.8; -0.6)$	0.02	0.72	0.18	0.08

Table 5.3: *Typical polarization weights used in this analysis. Each event with a MC Sample Polarization* $(P_{e^-}; P_{e^+})$ *acquires a weight to mix with the other polarization to an experimental polarization listed in column 1.*

the polarization configurations studied in this analysis. The total event weight is the product of signal, luminosity and polarization weights:

$$w_{event} = \frac{\mathcal{L}_{exp}}{\mathcal{L}_{MC}} \times w_{pol} \times w_{sig}, \tag{5.12}$$

with the experimental and generated MC luminosities $\mathcal{L}_{exp}$ and $\mathcal{L}_{MC}$, respectively.

Chapter 6

Event simulation and selection

In the previous chapter a model independent cross section for radiative pair production of heavy neutral particles, e.g. WIMPs, has been introduced. The determination of the WIMP parameters from this process relies on the precise measurement of isolated single photons from associated initial state radiation (ISR). The goal of this study is to investigate which parameters can be measured to which accuracy and how this information can help to distinguish between different models. This chapter describes the generation and simulation of the Monte-Carlo data (MC) for this analysis.
Because of the large reducible and irreducible backgrounds to the WIMP signal, the treatment of ISR in the event generation and the impact of the detector energy resolution and the photon identification on the event reconstruction are of great importance to the results of this search. Uncertainties in the measured energy distribution of the detected photons directly influence the achievable mass resolution and limit the detectable cross sections. The statistical precision of the cross section measurements is dominated by the large amount of background versus signal events.

6.1 Signal definition

The signature of radiative WIMP pair production $e^+e^- \rightarrow \chi\chi\gamma$ consists of a single high-energetic isolated photon. This signal is easily distinguished from other possible physics events with hadrons and leptons in the final state, such as $e^+e^- \rightarrow \ hadrons$, $e^+e^- \rightarrow \tau\overline{\tau}$ and $e^+e^- \rightarrow \mu\overline{\mu}$. Hadronic and τ events are recognizable by a large amount of charged activity, i.e. tracks in the tracking system, grouped into distinct "jets". Muonic events on the other hand provide additional tracks in the muon system outside the central tracking and calorimetric volume. These final states are not considered in this analysis because the probability of misinterpreting a hadronic or muonic event as signal is negligible.
Apart from the SM backgrounds of radiative neutrino production, multi-photon final states and radiative Bhabha events (cf. Sec. 5.2.1), beam-related backgrounds and overlaid $\gamma\gamma$ events have to be considered for their effect on additional detector activity and the efficiency of the signal selection. The event rate of these processes is very high, and a substantial amount of signal events will have overlaid tracks from e^+e^- pairs, $\gamma\gamma$ events and secondary interactions. Therefore, veto conditions on tracks and any additional detector activity have to be carefully chosen to minimize the loss of signal statistics.

The single photon signature requires an excellent photon reconstruction. To provide optimal conditions for photon reconstruction, an event is considered signal-like when it contains at least one photon with

- $10\,\text{GeV} < E_\gamma < 220\,\text{GeV}$ and
- a polar angle of $|\cos(\Theta)| < 0.98$.

This signal definition ensures that the detected photons are within the tracking acceptance of the ILD detector to distinguish them from charged particles (see Table 4.1 on page 28). The requirement on the photon energy reduces the contributions from soft ISR and excludes the massless neutrino final state from the radiative Z-return at photon energies of 241 GeV. To reduce the required computation time, the event generation is restricted to this region of phase space including a safety margin.

6.2 Simulation chain

In this section the software chain from event generation to simulation and event reconstruction is described. A dedicated subsection covers the treatment of the BeamCal information due to its importance for the background rejection.

6.2.1 Event generation with WHIZARD

The SM background has been generated with the WHIZARD [78] event generator, version `1.96`. WHIZARD computes cross sections and distributions of observables and generates unweighted event samples for use in detector simulations. The program automatically computes polarized matrix elements on tree level for up to eight final state particles and integrates them over the phase space. The matrix elements are calculated with the help of the O'MEGA algorithm [79].
For the main $e^+e^- \to \nu\nu\gamma$ background, the "hard" photon is included in the matrix element and is treated exactly in QED. The beam energy spectrum and beamstrahlung particle distributions are calculated for nominal beam parameters (cf. Tab. 3.2, page 20) with GUINEA PIG [80] and are then passed to WHIZARD as input parameters. Additional initial state radiation distributed according to structure functions accounting for the leading-logarithm-approximation of multiple photon emission [81] is switched on in the event generation, resulting in up to two additional photons to the hard process.

6.2.2 Detector simulation with MOKKA

The detector simulation is performed with the GEANT4 based [82] simulation framework for the ILD detector MOKKA [83] (version `06-07-p01`). The simulated detector models are `ILD_00` and `LDC_PrimeSc_02`. Table 6.1 lists the most important geometry parameters of the `ILD_00` calorimeter system as implemented in MOKKA. For reference the corresponding values from the ILD Letter of Intent (LoI) document are also stated [36]. `LDC_PrimeSc_02` is a predecessor of `ILD_00` and has been used for the detector optimization studies that resulted in the `ILD_00` design. The two detector models differ only in the implementation of

Subsystem		Letter of Intent	Simulation MOKKA
Magnetic Field, B [T]		3.5	3.5
ECAL Barrel	R_{min}	1847.4	1843
	z_{max}	2350	2350
	Layers	$20 + 9$	$20 + 9$
	Total X_0	23.6	—
	Coverage	$\lvert\cos(\Theta)\rvert < 0.786$	$\lvert\cos(\Theta)\rvert < 0.787$
ECAL endcap	R_{min} (square)	—	400.0
	R_{max} (oct.)	2090	2088.8
	z_{min}	2450	2450
	Coverage	$0.761 < \cos(\Theta) < 0.987$	$0.761 < \cos(\Theta) < 0.987$
ECAL ring	R_{min}	280.0	250.0
	R_{max} (oct.)	390.0	390.0
	z_{min}	2450	2450
	Coverage	—	100 . . . 157.8 mrad
Lumical	R_{min}	80.0	80.0
	R_{max}	196	195.2
	z_{min}	2450	2506.9
	Coverage	32.6 . . . 79.8 mrad	31.9 . . . 77.7 mrad
BeamCal	R_{min}	(out beam) 20.0	(out beam) 20.0
	R_{max}	(supp.) 220.0	(sens.) 150.0
	z_{min}	3595	3595
	Coverage	5 . . . 40 mrad	5.6 . . . 41.7 mrad

Table 6.1: *ILD geometry of the calorimeters from the LoI document and as implemented in the simulation software* MOKKA. *All values are given in [mm] unless indicated otherwise. Support structures and sensitive areas are abbreviated (supp.) and (sens.), respectively.*

the forward region. In particular, the BeamCal, LumiCal and LHCAL are not represented in `LDC_PrimeSc_02`.
Because of the enormous pair background, the forward systems of both detector models are treated equivalently in a separate reconstruction step after the event simulation. Therefore, both models can be considered identical with respect to the simulation output. A homogeneous magnetic field of 3.5 T is used throughout the simulation. In contrast to the ILC baseline design the crossing angle of 14 mrad between the colliding beams is not simulated [36].

6.2.3 Event reconstruction with MARLIN

For Particle Flow event reconstruction (cf. Sec. 4.1) the PANDORAPFA algorithm [53], version `v03-01`, is used. The algorithm is part of the standard reconstruction chain for full simulation studies of the `ILD_00` detector model. All tracking information required by the

PFlow algorithm is provided by the MarlinReco [84] package of the Marlin reconstruction framework for linear collider studies [85] (version `00-10-04`). The reconstruction package MarlinReco not only performs full tracking but also digitizes the simulation output and provides common algorithms used in the event reconstruction. The simulation and reconstruction output is encoded in the LCIO event data model [86] (version `01-06`).

6.2.4 Treatment of the detector forward region

Due to the high event rates of machine induced and $\gamma\gamma$ backgrounds and because of the tremendous amount of energy deposited in the forward calorimeters per bunch crossing, the detector response of the BeamCal is not simulated. Therefore, after event reconstruction with PandoraPFA, an additional reconstruction algorithm provides the information of the forward calorimetry. The BeamCalTagEfficiency algorithm of the MarlinReco package takes the generator information of the outgoing particles, tracks them in the magnetic field to the forward calorimeters and calculates the BeamCal detection probability according to the expected occupancy from beamstrahlung and ISR. The detection probability is stored for each event. Figure 6.1(a) shows the energy deposited in the BeamCal for one bunch crossing and nominal beam parameters. To the left of the beam entrance/exit hole the energy deposited by a 250 GeV electron is overlaid [87]. Figure 6.1(b) shows the detection efficiency for electrons with energies from 50 GeV to 250 GeV as a function of the radial impact parameter. For radii of more than 8 cm, the detection efficiency for all energies is above 95%.
For further analysis the reconstructed event samples are transfered to a Root-based TTree data structure [88, 89].

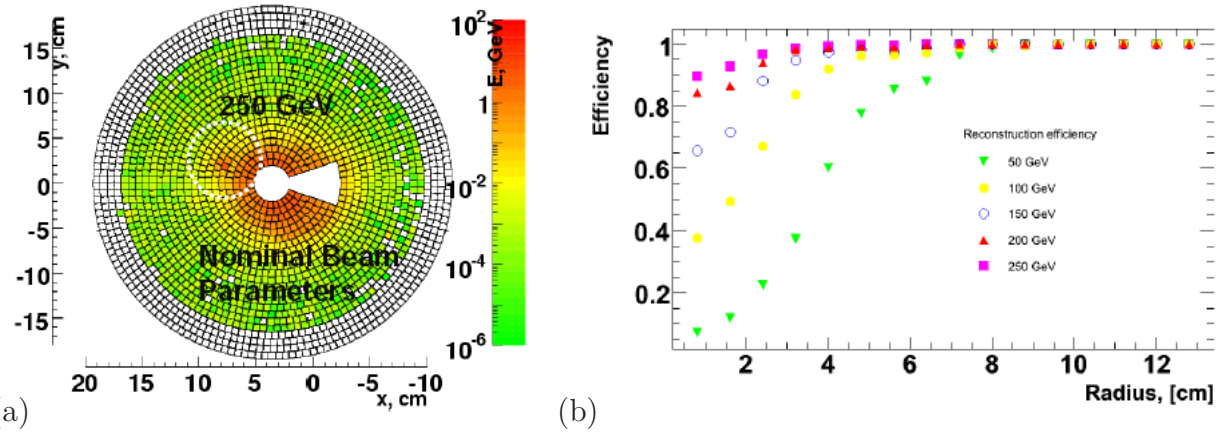

(a) (b)

Figure 6.1: *Pair background occupancy on BeamCal (a) with single overlaid 250 GeV electron to the left of entry/exit hole. (b) Reconstruction efficiency of high energetic electrons versus radial impact parameter in the BeamCal for electron energies from 50 to 250 GeV. Both figures taken from [87].*

6.3 Event samples and phase space definition

The set of SM background samples used in this analysis was generated in 2008 as part of the SLAC SM mass production [90] for the purpose of detailed physics studies and detector performance evaluation in the preparation of the ILD Letter of Intent [36]. The WHIZARD event generator has been initialized with the ILC RDR nominal beam parameter set (Table 3.2 on page 20, column 2) at a center of mass energy of $\sqrt{s} = 500$ GeV. The event samples generated and used in this analysis comprise the full neutrino pair production background with up to three photons in the final state calculated on tree level ($e^+e^- \to \nu\nu\gamma(N)\gamma$ ($N = 0, 1, 2$)) and multi-photon final states with up to four outgoing photons. These processes have been generated for two beam polarization configurations separately, namely for $(P_{e^-}; P_{e^+}) = (+1.0; -1.0)$ and for $(P_{e^-}; P_{e^+}) = (-1.0; +1.0)$. For the equal sign polarization configurations the cross sections of these processes vanish.
In addition, the Bhabha background has been generated for the four polarization configurations with $(P_{e^-}; P_{e^+}) = (\pm 1.0; \pm 1.0)$. All generated processes include additional ISR photons in the leading-logarithm-approximation from both the incoming electrons and positrons. The Bhabha background has been simulated prior to the 2008 SM mass production with the predecessing `LDC_PrimeSc_02` detector model.
The phase space of this analysis has been constrained on generator level with respect to the signal definition (see Sec. 6.1). Events from the irreducible $e^+e^- \to \nu\nu\gamma(N)\gamma$ SM background are required to have at least one photon with

- $E_\gamma > 8$ GeV and
- a polar angle $|\cos(\Theta)| < 0.995$

The requirement on the photon's polar angle relates to the ECAL coverage including the ECAL Ring, see Table 6.1. A secondary beneficial effect of these phase space criteria is that the required CPU time for detector simulation is reduced significantly since the generator samples are decreased in size by a factor of roughly 1/3. Table A.1 in the appendix lists the cross sections and beam polarization configurations of the generated and phase space constrained $e^+e^- \to \nu\nu\gamma(N)\gamma$ SM background. The phase space criteria were not imposed on the other SM background processes listed in Table A.2. Due to the amount of data that had to be simulated for the preparation of the ILD LoI, only limited computing time has been available for detector simulation and event reconstruction of the event samples. Therefore only half of the $e^+e^- \to \nu\nu\gamma$ SM events have been simulated, reducing the available statistics to $250\,\text{fb}^{-1}$, or, in case of the polarization state $(P_{e^-}; P_{e^+}) = (-1.0; +1.0)$, even to $125\,\text{fb}^{-1}$.

6.4 Photon reconstruction

After event reconstruction, two corrections are applied to the PFLOW photon candidates identified by the PANDORAPFA algorithm. First the fracturing of reconstructed electromagnetic clusters in the ECAL is addressed, since it leads to a large number of additional photon misdetections. The second correction concerns an energy re-calibration of the detected photon candidates.

6.4.1 Fractured electromagnetic clusters

For charged electromagnetic particles, the reconstruction algorithm makes use of the tracking information to match the track momenta with the energy deposited in associated electromagnetic clusters. In case of a mismatch between track momenta and cluster energies, the algorithm iteratively re-clusters the hits in the calorimeters until consistency is established. For photons, however, the reconstruction relies solely on the clustering of the calorimeter hits (cf. Sec. 4.1). PandoraPFA tends to split up true clusters in the initial clustering [53] which for charged particles is countered in the re-clustering stage. For improved photon tagging, a sophisticated shower-profile-based photon identification algorithm is used. Without the energy-momentum constraint, however, still some electromagnetic clusters from photons remain isolated. In effect, larger energy depositions from a single photon tend to be reconstructed as several distinct clusters, each identified as an individual electromagnetic particle candidate.

For the $e^+e^- \to \nu\nu\gamma$ background with $(P_{e^-}; P_{e^+}) = (-1.0; +1.0)$, Figure 6.2 depicts the average number $\overline{N_{rec}/N_{gen}}$ of reconstructed photon candidates per generated photon as function of (a) the generated photon's energy E_γ, (b) its polar angle $\cos(\Theta_\gamma)$ and (c) its transverse momentum $P_{T,\gamma}$. The photon candidate is considered reconstructed with respect to a specific MC photon when it originates from the latter on generator level and is within an angle of 0.1 rad (5.7 deg) of the generated photon. All photons are required to have reached the first sensitive layer of the ECAL to veto events, where the photons already converted in the tracking region or TPC endplate. Conversions close to the boundaries of the active tracking volume, in the TPC endplate or in between the tracking volume and the calorimeters provide no (or not enough) tracker hits for tracks to be reconstructed. The conversion products, electrons and positrons, are thus only detected in the ECAL as uncharged electromagnetic particle candidates mimicking the observed fracturing. As shown in Figure 6.2(a), for low photon energies on average one photon candidate is reconstructed per generated photon with the ratio $\overline{N_{rec}/N_{gen}}$ increasing steadily to about three photon candidates at $E_\gamma = 250$ GeV. The angular dependence of this ratio is approximately constant at about 1.4 in the barrel region, but rises steeply to 2.4 in the barrel/endcap overlap region at $\cos(\Theta_\gamma) = 0.8$, as can be seen in Figure 6.2(b). Photons showering in this region leave energy contributions in different ECAL subsystems, i.e. in the ECAL barrel and endcap, which are spatially separated by several centimeters due to the insensitive material of support structures and readout electronics. The complex geometry in this region makes the topological clustering non-trivial. The ratio in terms of the transverse momentum peaks at $P_{T,\gamma} = 150$ GeV, consistent with $E_\gamma = 250$ GeV photons in the overlap region, see Figure 6.2(c). Figure 6.2(d) shows the simultaneous dependence of the ratio on both the photon energy and the polar angle. The dominant contribution of the cluster fracturing for all photon energies is due to the barrel/endcap region, as seen from the ridge at $\cos(\Theta_\gamma) = 0.8$.

To counteract the effects of photon fragmentation, a procedure to combine photon candidates from split clusters has been established. Starting with the most energetic photon, all photon candidates within a cone from the IP are added to the first. The new photon momentum is calculated from the unweighted sum of the momenta of the contributing photon candidates, and normalized to the sum of energies. The procedure is repeated with the most energetic of the remaining photon candidates until no photon candidate remains. The cone opening angle has been optimized with respect to efficiency ε and purity p of the combination procedure.

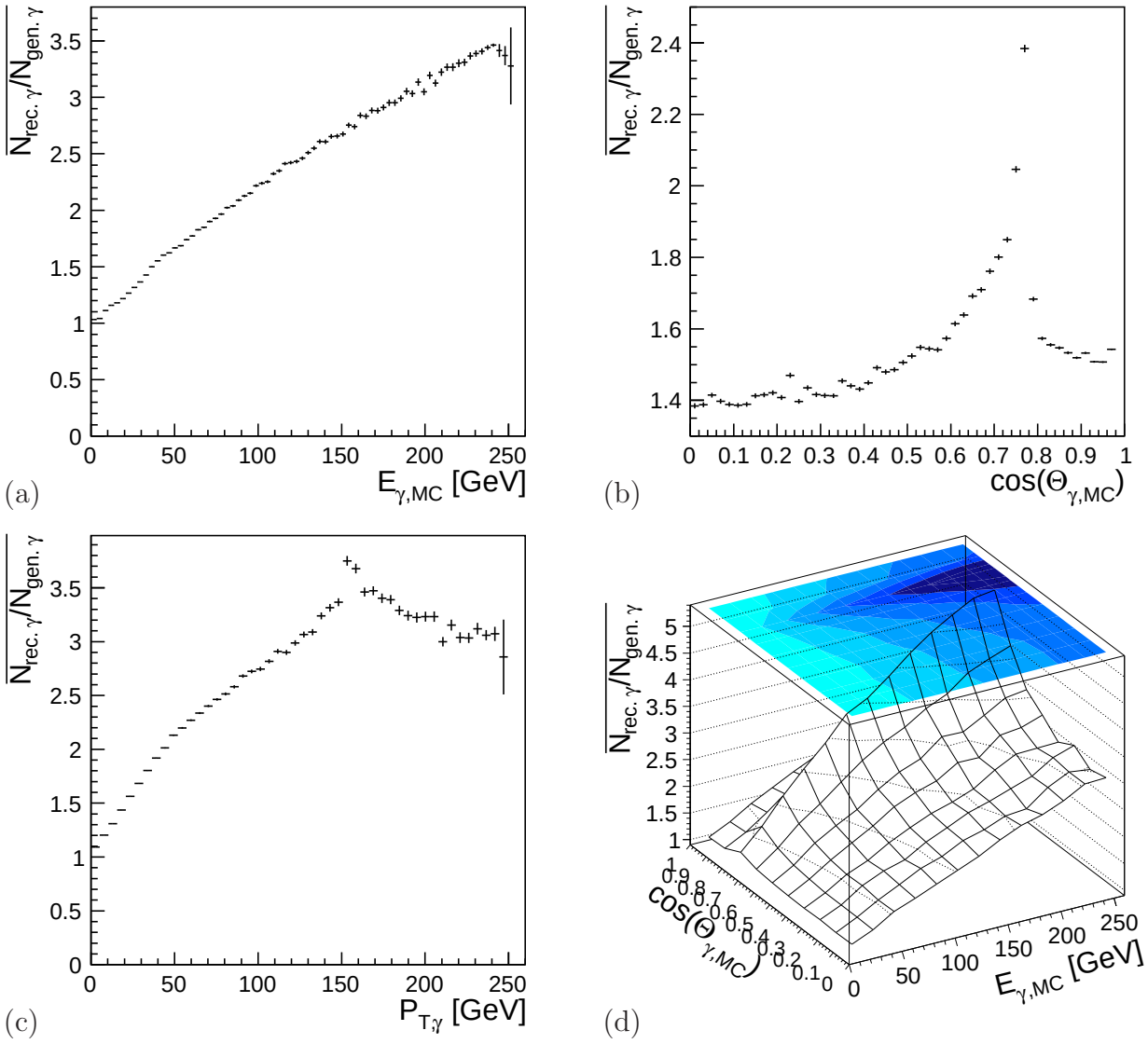

Figure 6.2: *Average ratio of reconstructed to generated photons for the* $e^+e^- \to \nu\nu\gamma$ *SM background as a function of (a) the MC photon energy* E_γ*, (b) the MC polar angle* $\cos(\Theta_\gamma)$ *and (c) the transverse momentum* $P_{T,\gamma}$*. (d) shows the ratio in two dimensions,* E_γ *and* $\cos(\Theta_\gamma)$*.*

The efficiency and purity are defined as:

$$\varepsilon = \frac{\#\ Found\ and\ correct\ matches}{\#\ Correct\ matches} \tag{6.1}$$

$$p = \frac{\#\ Found\ and\ correct\ matches}{\#\ Found\ matches}, \tag{6.2}$$

where *# Found and correct matches* is the number of photon candidates within the cone which are also related to the generated photon, *# Correct matches* is the number of all reconstructed photons related to the generated photon and *# Found matches* gives the number of photon objects within the cone. Efficiency and purity of the merging procedure for different cone

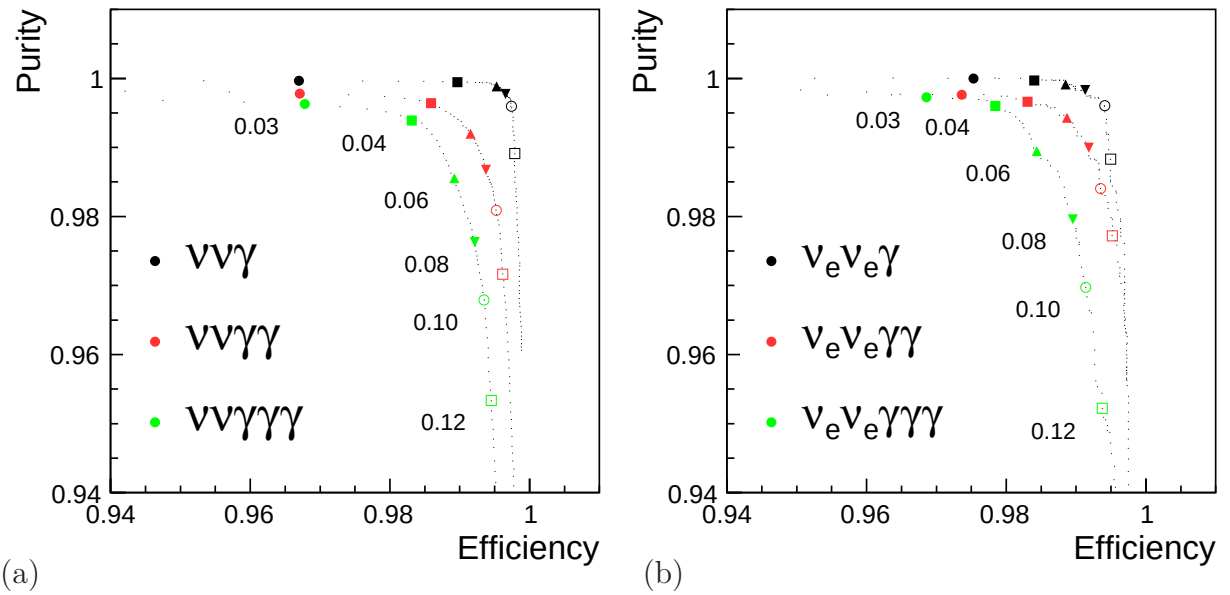

(a) (b)

Figure 6.3: *Efficiency and purity of the matching procedure for different cone opening angles from 0.03 to 0.12 radians: (a) for the processes* $e^+e^- \to \nu\nu\gamma(N)\gamma$ *with one to three radiated photons on tree-level summed over polarization states and neutrino generations and (b) for the specific process* $\nu_e\nu_e\gamma(N)\gamma$ *with* $(P_{e^-}; P_{e^+}) = (-1.0; +1.0)$.

sizes are shown in Figure 6.3(a) for the $e^+e^- \to \nu\nu\gamma(N)\gamma$ SM background with final states of one to three tree-level photons and combined for all simulated polarization states. Efficiency and purity are close to one for all examined opening angles. For final states with two or three photons the efficiency and purity are slightly lower since, with increasing probability, cluster fragments of different MC photons are close to each other and are thus more likely to get misassigned. Cone opening angles smaller than 0.04 rad rapidly decrease the efficiency without any increase in purity. For this reason and because of a preference of purity over efficiency, the opening angle has been set to 0.04 rad, corresponding to 2.3°.
Even though polarized beams change the photon energy spectrum for electron-neutrino final states by enhancing the t-channel W-exchange, the procedure is insensitive to beam polarization as shown exemplary for the first neutrino generation and polarization state $(P_{e^-}; P_{e^+}) = (-1.0; +1.0)$ in Figure 6.3(b). Efficiency and purity differ only slightly from the polarization and final state average in Figure 6.3(a).
The result of the merging procedure with respect to the ratio $\overline{N_{rec}/N_{gen}}$ is shown in Figure 6.4 in terms of the MC photon energy E_γ and the polar angle $\cos(\Theta_\gamma)$. Deviations from unity are below the percentage level within the acceptance of the ECAL barrel and endcap regions. In the overlap region of ECAL barrel and endcap at $\cos(\Theta_\gamma) \approx 0.8$ the ratio is at a level of 1.02 (see Fig. 6.4(b)), which is considered a negligible effect. Figure 6.4(a) in particular justifies the choice of a cone opening angle independent of the photon energy E_γ and polar angle Θ_γ.
The following analysis uses only these combined photon objects.

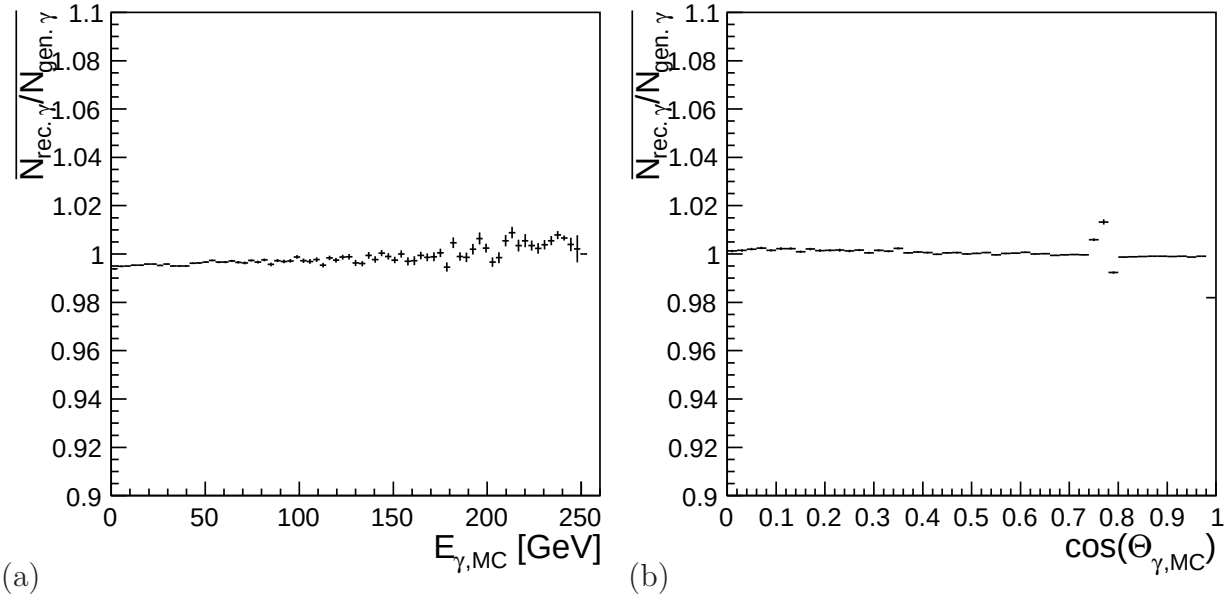

(a) (b)

Figure 6.4: *Average ratio of reconstructed per generated photons for the process* $e^+e^- \to \nu\nu\gamma$ *after merging procedure as function of (a) photon energy* E_γ *and (b) polar angle* $\cos(\Theta_\gamma)$.

6.4.2 Energy calibration

The energy calibration constants for the ECAL of the ILD experiment will be determined in dedicated runs at the Z-pole energy by measuring the invariant mass of the electron system in the decay $Z \to e^+e^-$. The calibration constants used for the event reconstruction in the ILD detector simulation are determined in a different manner. Samples of di-jet events are simulated and the calibration constants for the ECAL and the HCAL are calculated simultaneously by requiring the conservation of the total center-of-mass energy. Since these constants are derived for the specific ratio of hadronic to electromagnetic energy in typical jet events, they are not necessarily best suited for the reconstruction of pure leptonic and photonic events.

In this analysis, the energy calibration has therefore been re-evaluated for photons from the $e^+e^- \to \nu\nu\gamma$ background. Figure 6.5(a) shows the angular dependence of the average ratio of reconstructed and generated photon energies $\overline{E_{rec}/E_{gen}}$. The ratio is evaluated for photon candidates associated with MC photons hitting the first active layer of the ECAL. Only photons with energies above 2 GeV are considered. A fit to the most prominent features is overlaid in Figure 6.5(a). Several distinct dips correspond to the geometric boundaries of the different ECAL components. In the barrel/endcap overlap region around $\cos(\Theta) \approx 0.8$ on average less than 95% of the physical photon energy is reconstructed. The segmentation of the ECAL barrel into modules is visible from the two dips at $\cos(\Theta) \approx 0.2$ and $\cos(\Theta) \approx 0.6$. The difference in the segmentation-induced dips is due to the angle under which photons from the IP reach the insensitive ECAL boundary regions. The remaining small deviations at small $\cos(\Theta)$ can be identified with the internal structure of each ECAL module consisting of several staves (see Sec. 4.4). The photon energy is reconstructed to 99.4% of the MC energy within the angular acceptance of the ECAL modules, which is indicated by the constant term of the fit in Figure 6.5(a). Figure 6.5(b) shows the energy ratio in terms of the MC energy.

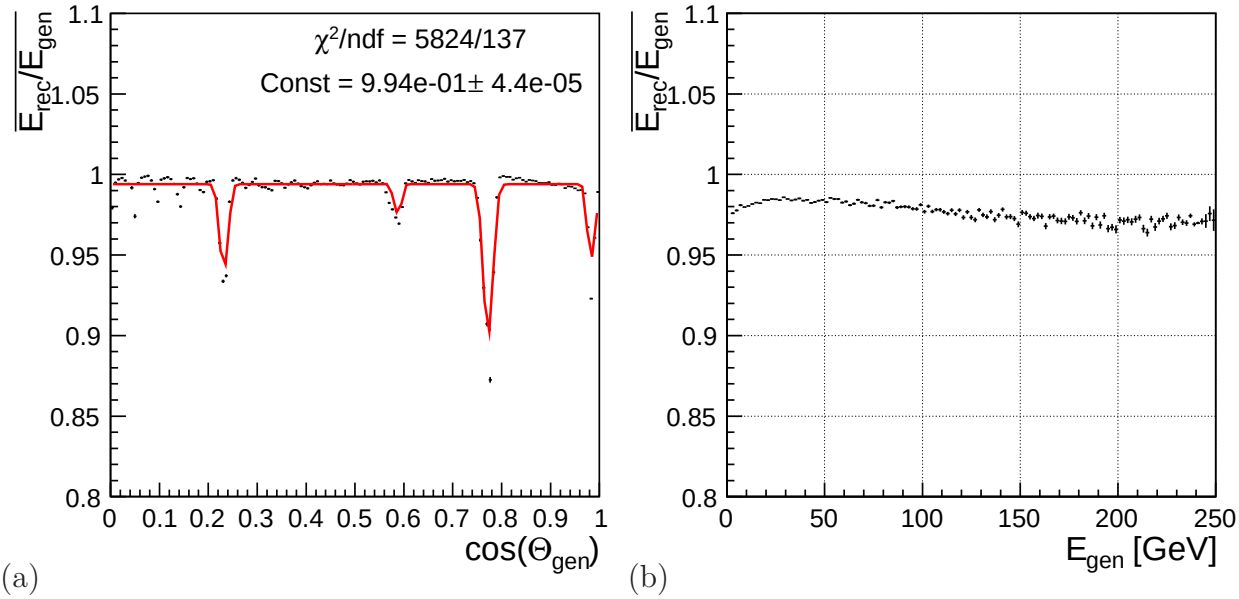

Figure 6.5: *Ratio of reconstructed to generated photon energy as a function of (a) the polar angle and (b) the generated energy. A fit to the most prominent features in the angular dependence is overlaid. The dips of the ratio in (a) correspond to the geometric boundaries of different ECAL components. Within the angular acceptance of the ECAL modules the photon energies are reconstructed to 99.4% of the MC energy, indicated by the constant term of the fit.*

Over the full energy range from 2 GeV to 250 GeV the ratio is relatively constant at a level of 97% of the generated photon energy.
For further analysis the reconstructed photon energy is calibrated versus the photon polar angle $\cos(\Theta)$ according to the fit displayed in Figure 6.5(a). The ratio $\overline{E_{rec}/E_{gen}}$ with the correction applied is shown in Figures 6.6(a) and (b). It is equal to unity for the constant fit over the full range of polar angles, as displayed in Figure 6.6(a). The very small remaining energy dependence below 100 GeV, where most of the signal events are expected, can safely be ignored (Fig. 6.6(b)). The effectiveness of the angular calibration method shows that the average reconstructed energy of 97% in Figure 6.5(b) is dominated by losses in the cracks between ECAL modules.

6.4.3 Reconstruction efficiencies

The photon reconstruction efficiency ε_{rec}, defined as the probability of detecting a photon from the relevant physics interaction, is influenced by several factors. One of the factors responsible for a reduced reconstruction efficiency is photon conversions into e^+e^- pairs in the detector material of the tracking system. The amount of material particles traverse on their way to the calorimeters depends on the polar angle with respect to the beam axis, thus the conversion probability is angle dependent as well. The distribution of insensitive material in the detector introduces an additional polar angle dependent reduction of the number of detected photon events. Furthermore, the effectiveness of the reconstruction algorithms has to be considered.

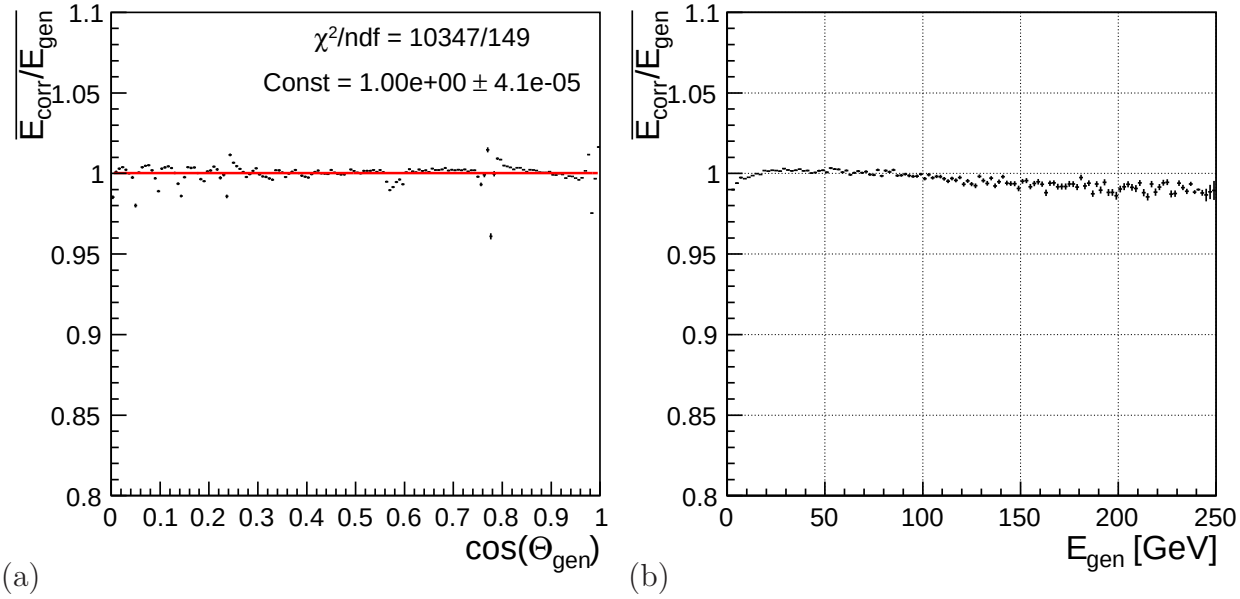

(a) (b)

Figure 6.6: *Ratio of calibrated to generated photon energy as a function of (a) the generated polar angle and (b) the generated energy.*

Figure 6.7(a) shows the photon reconstruction efficiency as a function of the generated polar angle $\cos(\Theta)$ for the simulated sample of the dominant $e^+e^- \to \nu\nu\gamma$ process. The efficiency is determined for all MC photons within the signal definition (cf. Sec. 6.1). For polar angles of $\cos(\Theta) > 0.8$, the increased material budget of the TPC anode-plates is visible in the reduced efficiency. The average reconstruction efficiency is at 96.8%. With respect to the MC photon

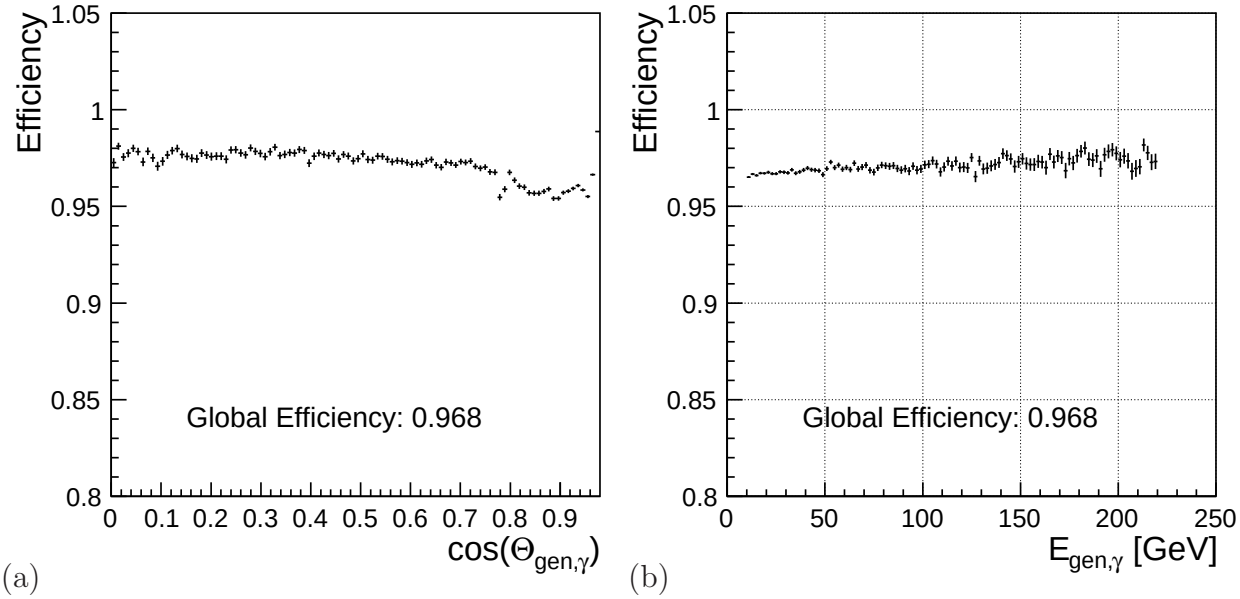

(a) (b)

Figure 6.7: *Photon reconstruction efficiency as a function of (a) the generated polar angle and (b) the generated energy. The efficiency is evaluated for the $e^+e^- \to \nu\nu\gamma$ SM background within the signal definition.*

energy, the reconstruction efficiency is approximately constant in the signal region between 10 GeV and 220 GeV as shown in Figure 6.7(b). To disentangle the effects from photon conversions and reconstruction algorithm artifacts, the material budget can be extrated from the observed reconstruction efficiency under the assumption that the losses are solely due to photon conversions. Deviations from the nominal material budget then point to contributions from the reconstruction algorithm and additional uncertainties in the detector geometry. The fraction of detected, i.e. unconverted photons, N_{uc} to all emitted photons N is related to the material budget in terms of the radiation length X_0 by the equations:

$$\begin{aligned} \frac{N_{uc}}{N} &= e^{-\frac{7}{9}\frac{x}{X_0}} \\ \frac{x}{X_0} &= -\frac{9}{7}\ln\left(\frac{N_{uc}}{N}\right). \end{aligned} \tag{6.3}$$

The observed material budget is compared to the expected budget defined in the ILD Letter of Intent in Figure 6.8. Except for the very forward and the very central region the computed values are in accordance with the expectation. In the forward region, which is excluded from the signal region, the differences between the two distributions can be related to the beam pipe material not considered in the expected distribution. The local deviation close to $\cos(\Theta) = 0$ is known to be caused by the simulation of the central TPC anode, whose thickness is severely overestimated in the GEANT4 representation of the ILD. Since the observed material budget is in agreement with the assumption of losses from photon conversions only, the effects from the reconstruction algorithms are considered negligible and do not contribute to the overall systematic uncertainties.

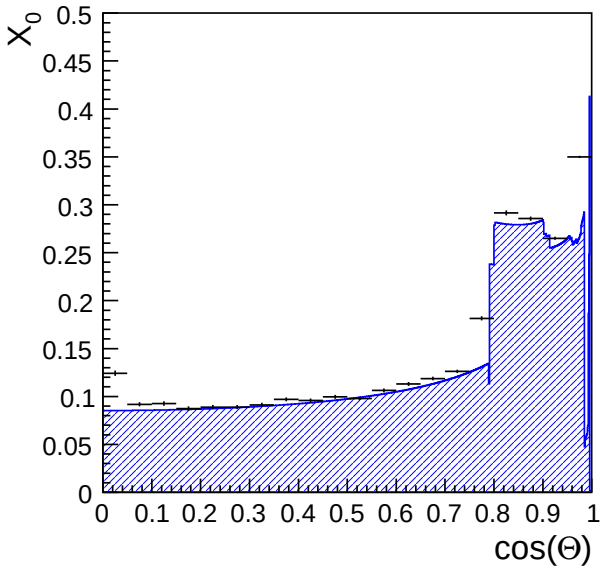

Figure 6.8: *Angular material budget of the ILD detector in terms of the radiation length X_0. The black dots represent the material budget extracted from the simulated photon events. For comparison the material budget quoted in the ILD Letter of Intent is displayed as the blue hatched histogram.*

6.5 Event selection

The event selection identifies signal events with high efficiency, while suppressing unwanted background events. The expected signal consists of a single high energetic photon without any further activity in the detector. This signal has to be distinguished from SM backgrounds like Bhabha scattering with associated ISR where the electrons are too forward to be identified in the tracking region, or multi-photon final states.
The WIMP signal is indistinguishable on an event-by-event basis from the dominant $e^+e^- \to \nu\nu\gamma$ SM background. This allows to select the simulated $\nu\nu\gamma$ background and to generate the WIMP signal events by reweighting the $\nu\nu\gamma$ samples after the selection. In addition to backgrounds from physics events, the $\gamma\gamma$ and beam related background processes have to be considered (cf. Sections 5.2.1 and 5.2.2). Unfortunately, tight selection criteria on tracks from these backgrounds increase the probability of rejecting signal events which reduces the usable statistics and lowers the significance $\sqrt{S}/B$.

6.5.1 Beam-induced background processes and $\gamma\gamma$ events

Because of the large cross section of $\sigma \approx 5 \times 10^8$ fb, hadronic overlays from $\gamma\gamma \to f\bar{f}$ interactions present considerably high background rates (cf. Sec. 5.2.1). On average 70% of signal events will be affected by these overlays. For an estimate of these processes, 3000 events corresponding to 4290 bunch crossings (BX) have been simulated using WHIZARD for event generation and MOKKA for the ILD detector simulation [91]. The transverse momentum distribution of the tracks from this background is shown in Figure 6.9 in black. After simulation about 0.7 tracks per BX are reconstructed. The momentum distribution peaks at low momenta, determined by the minimal transverse track momentum to reach the tracking region, and then falls of rapidly. A track veto in the selection must allow for these overlays in order to keep a high signal statistics. Of the simulated 4290 BX only 5 contain tracks with

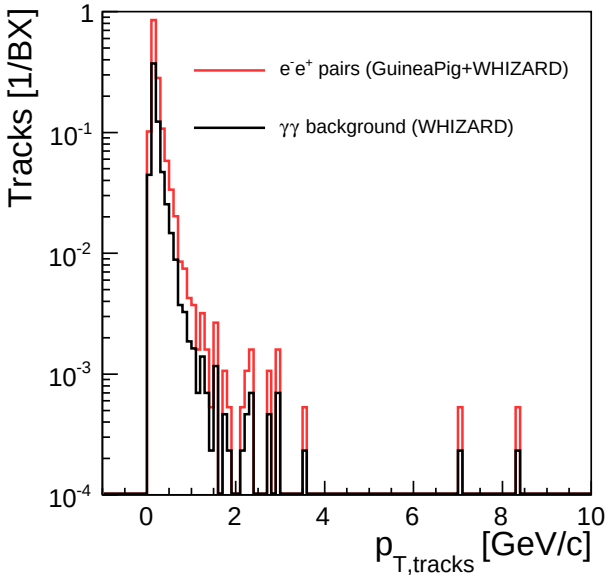

Figure 6.9: *Transverse momentum distribution of tracks from beam-related backgrounds and $\gamma\gamma$ events per bunch crossing. On average 1.5 tracks per bunch crossing (BX) are reconstructed from the beamstrahlung pair background (red/gray). For $\gamma\gamma$ processes 0.7 tracks per bunch crossing are expected (black). Only* 0.16% *of pair background tracks have a momentum above $p_T = 3.0$ GeV, and* 0.12% *of the $\gamma\gamma$ related tracks, respectively.*

a transverse momentum higher than 3 GeV. A constraint on the maximal transverse track momentum with $p_T < 3.0$ GeV therefore results in a loss of less than 0.12% of signal events from hadronic overlays.
Another source of event overlays stems from e^+e^- pairs from the beamstrahlung background (Sec. 5.2.2). Since the transfered momentum is typically small, these electrons spiral in the strong solenoid magnetic field towards the forward instrumentation. However, due to the large rates and secondary interactions, the expected number of detected events can not be neglected. For an estimate of the impact of beam-induced backgrounds, the beamstrahlung spectrum has been calculated with GuineaPig and fed into Whizard to generate beamstrahlung pairs for 1875 bunch crossings. The generated pairs have then been simulated with Mokka for the `ILD_00` detector. In order to correctly simulate the magnetic field in the forward region, a special field map incorporating inhomogeneities due to the Anti-DID dipole, has been used [76, 77]. On average about 1.5 tracks per BX are reconstructed. The distribution of transverse track momenta of beamstrahlung e^+e^--pairs is depicted in Figure 6.9 by the red (gray) histogram. Only 0.16% of pair background tracks have a momentum above $p_T = 3.0$ GeV.
In total, assuming that no event contains tracks with transverse momenta of $p_T > 3$ GeV from both the beamstrahlung pair background and $\gamma\gamma$ events, a selection criterion of $p_T < 3$ GeV results in a loss of less than 0.27% of signal events. This loss can safely be ignored.

6.5.2 Event selection

The photon energy distribution per fb^{-1} and GeV is shown in Figure 6.10 for signal-like SM background processes and for unpolarized beams (cf. Sec. 6.1 for the signal definition). The

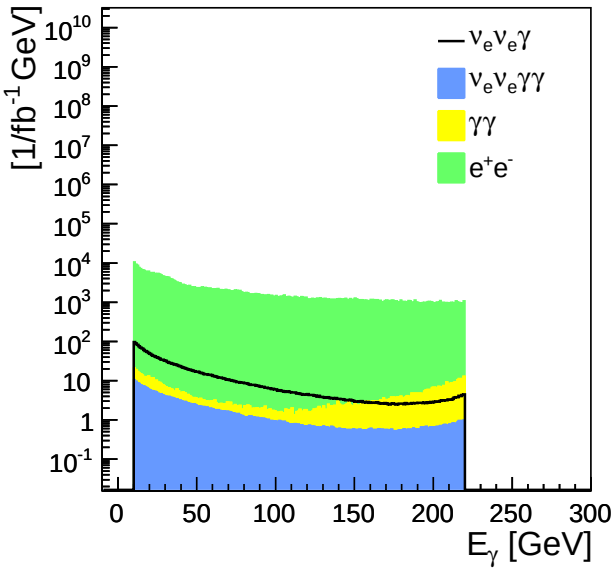

Figure 6.10: *Photon energy distribution for signal-like SM background processes. An event is categorized signal-like if the most energetic photon detected is consistent with the signal definition. The open black histogram shows the irreducible SM $e^+e^- \to \nu\nu\gamma$ background. The underlying stacked histogram contains the contributions from other SM background processes, i.e. $e^+e^- \to \nu\nu\gamma\gamma$ (blue/ dark gray), $e^+e^- \to \gamma\gamma$ (yellow/light gray) and radiative Bhabha scattering (green/gray). All distributions are for unpolarized beams.*

$e^+e^- \to \nu\nu\gamma$ background to be selected is shown as the open black histogram. The distribution of signal-like photons from the $e^+e^- \to \nu\nu\gamma\gamma$ (blue/dark gray), $e^+e^- \to \gamma\gamma$ (yellow/light gray) and radiative Bhabha backgrounds (green/gray) are depicted in the underlying stacked histogram. The Bhabha events clearly dominate over the full signal range from 10 GeV to

220 GeV.
The discriminating variables for the event selection are the track momenta p_T, the visible energy excluding the selected photon $E_{vis} - E_\gamma$, and the tagging efficiency of the BeamCal for high energetic particles in the forward region. The following selection criteria are applied:

- a maximal transverse track momentum $p_T < 3.0$ GeV.
- a visible energy $E_{vis} - E_\gamma < 20.0$ GeV.
- the rejection of events with particles detected in the BeamCal.

p_T of tracks

Figure 6.11 illustrates the distribution of track momenta (a) up to 300 GeV and (b) up to 14 GeV, respectively. All distributions are dominated by low-p_T tracks with less than 10 GeV/c. A veto on events with at least one track of $p_T > 3.0$ GeV needed to reject

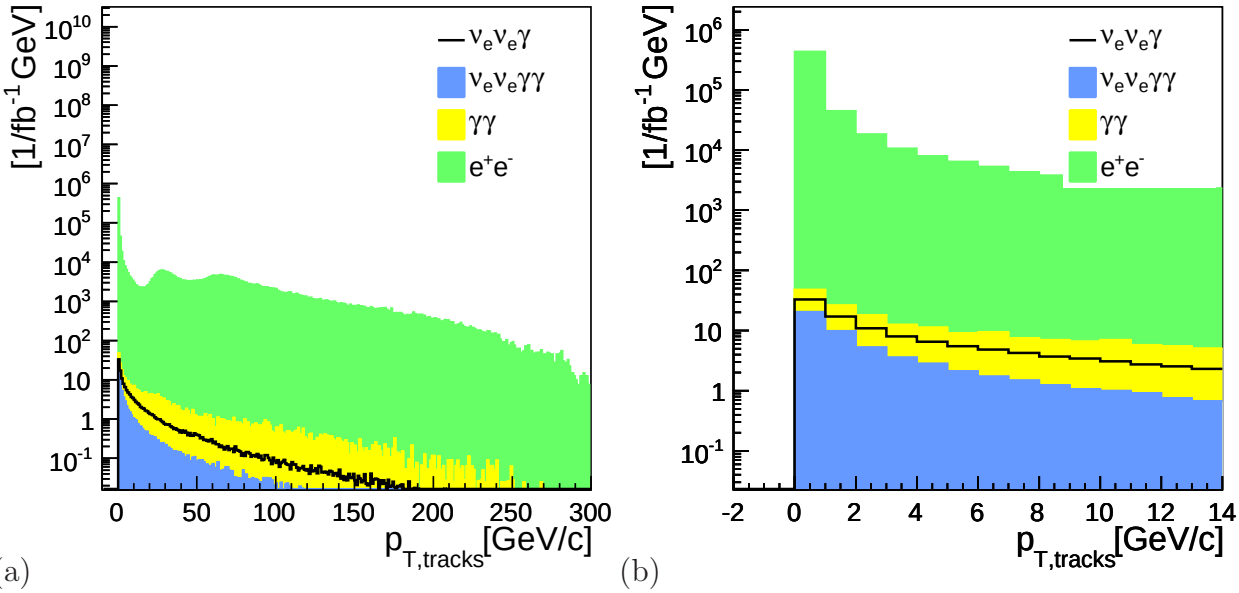

Figure 6.11: *Distribution of transverse track momenta p_T. In (a) the full p_T range up to 300 GeV is shown, in (b) only tracks with momenta below 14 GeV are displayed. Track momentum distributions from $e^+e^- \to \nu\nu\gamma\gamma$, $e^+e^- \to \gamma\gamma$ and radiative Bhabha backgrounds are shown in (blue/dark gray), (yellow/light gray) and (green/gray), respectively.*

hadronic and muon events also rejects a considerable amount of Bhabha and $e^+e^- \to \gamma\gamma$ events. With respect to the machine-related backgrounds and hadronic $\gamma\gamma$ events, a veto on tracks with more than 3 GeV rejects about 2.7 ‰ of signal events (see Sec. 6.5.1).
In Figure 6.12(a) the photon spectrum is shown after the condition on the transverse track momenta has been applied. The reduction of the Bhabha background (green/gray) is clearly visible. For photon energies above 100 GeV only few Bhabha events survive. However, these obtain weights of ~ 100 due to the normalization to $1\,\mathrm{fb}^{-1}$ because of the limited simulated statistics of $0.1\,\mathrm{fb}^{-1}$ of which roughly 10% are used for the evaluation of the selection criteria.

Visible energy $E_{vis} - E_\gamma$

In addition to the veto on high-p_T tracks, a selection criterion on the full visible event energy excluding the most-energetic photon is applied to further reduce hadronic and muonic backgrounds. The same criterion is also helpful in rejecting events from processes with a multi-photon final state.

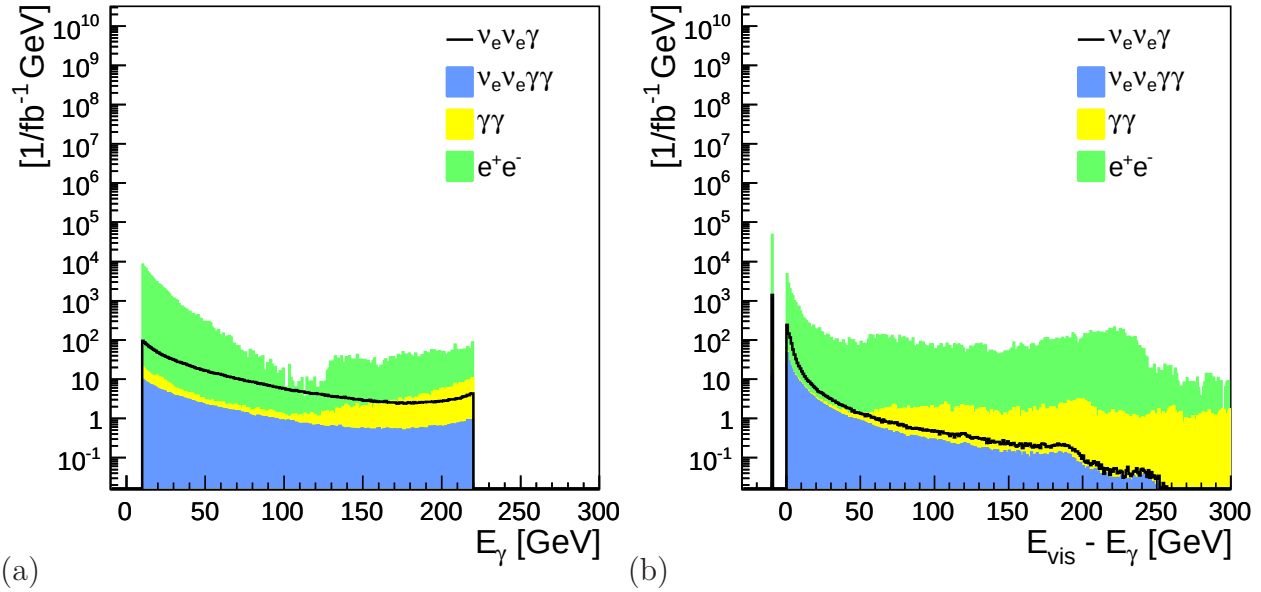

(a) (b)

Figure 6.12: *(a) Photon energy distribution of signal-like events after vetoing events with high-p_T tracks. The low simulated statistics are apparent in the Bhabha spectrum. (b) Visible event energy excluding the selected photon energy. The $e^+e^- \to \gamma\gamma$ background only contributes for energies above 20 GeV.*

Figure 6.12(b) shows the distribution of $E_{vis} - E_\gamma$ after the veto on high-p_T tracks. The entries in the bin with $E_{vis} - E_\gamma = -10$ GeV correspond to the events where $E_{vis} = E_\gamma$, i.e. events where only one particle, the hard photon, is detected. The $e^+e^- \to \gamma\gamma$ contribution in the photon spectrum of Figure 6.12(a) is mirrored in Figure 6.12(b), where the variable $E_{vis} - E_\gamma$ for this process is dominated by the spectrum of the second detected photon. At about 20 GeV, the amount of these events, as well as those of the Bhabha background, increase relatively to the $e^+e^- \to \nu\nu\gamma$ irreducible background which is selected as the WIMP signal. A Veto on events with $E_{vis} - E_\gamma > 20$ GeV reduces the $\gamma\gamma$ background almost completely and lowers the Bhabha background by another 10%. Figure 6.13(a) shows the remaining events after the application of the visible energy criterion. For photon energies below 100 GeV the radiative Bhabha events still dominate the distribution. The seemingly hard cut-off in the Bhabha spectrum at $E_\gamma = 110$ GeV is caused by the large event weights for this background.

BeamCal tagging efficiency

In Figure 6.13(b) the tagging efficiency of the BeamCal for the Bhabha background is displayed for the polarization configuration $(P_{e^-}; P_{e^+}) = (-1.0; +1.0)$. On average, 87% of this background is tagged. In untagged events the particles either leave the detector through the

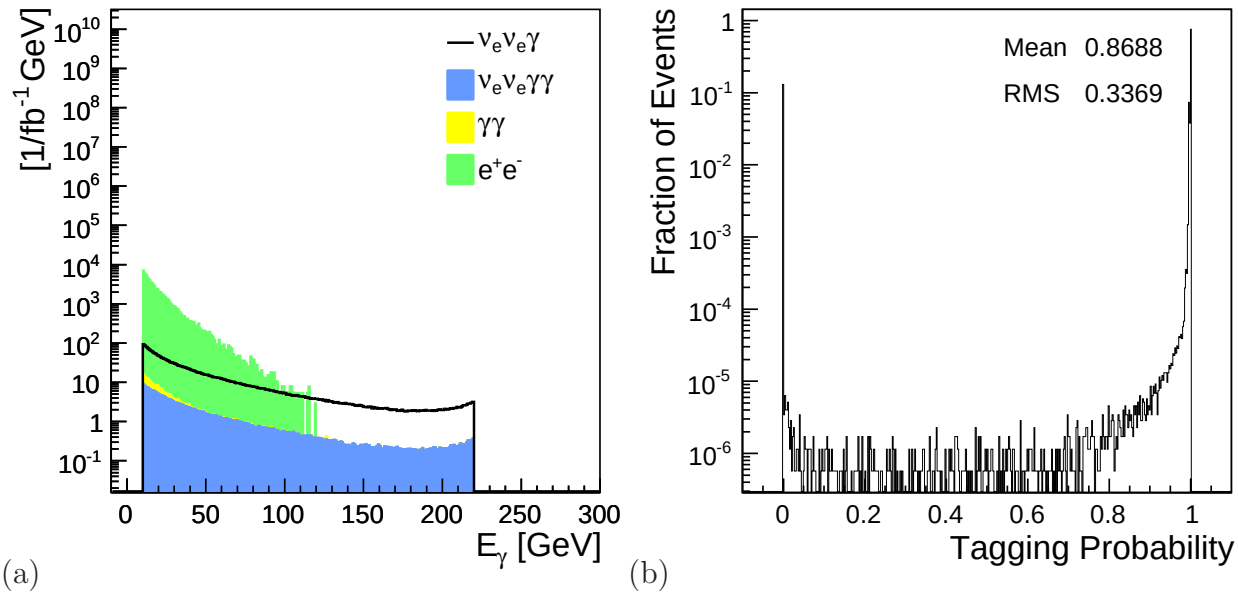

(a) (b)

Figure 6.13: *(a) Photon energy distribution for signal-like processes after the application of the visible energy criterion. The Bhabha background dominates below 100 GeV. (b) BeamCal tagging efficiency for the Bhabha background and a polarization configuration of* $(P_{e^-}; P_{e^+}) = (-1.0; 1.0)$*. On average 87% of the Bhabha background is tagged in the BeamCal.*

exit hole in the BeamCal, or the particles can not be distinguished from the massive energy deposition of the beamstrahlung background (cf. Sec. 6.2.4). From events tagged with a probability w_{tag} a fraction of $1 - w_{tag}$ will not be rejected by the BeamCal selection criterion. Therefore, each event obtains an additional weight $(1 - w_{tag})$ reflecting the probability that the event under question would not have been detected in the BeamCal.
The final photon spectrum is shown in Figure 6.14.

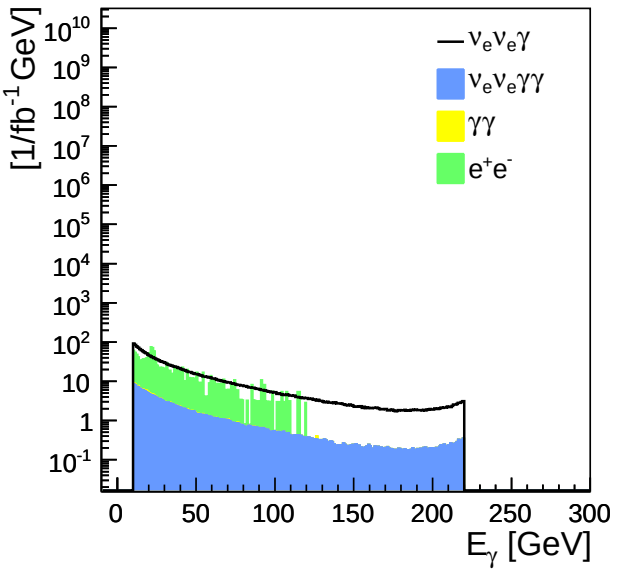

Figure 6.14: *Photon energy distribution of the selected signal-like events of the SM background. The open black histogram represents the irreducible SM* $e^+e^- \to \nu\nu\gamma$ *background selected as WIMP signal. The background distributions of photons from signal-like processes* $e^+e^- \to \nu\nu\gamma\gamma$*,* $e^+e^- \to \gamma\gamma$ *and radiative Bhabha scattering are depicted in the underlying stacked histograms. All distributions are for unpolarized beams.*

Table 6.2 summarizes the selection efficiencies for all polarization states studied in this analysis. The two selection criteria, the track veto and the rejection of BeamCal-tagged events, have the strongest influence on the Bhabha background, while the condition on the visible energy mainly reduces the multi-photon backgrounds.

Process	simulated	signal def.	$p_{T,track}$	$E_{vis} - E_\gamma$	BeamCal tag	Eff. [%]
Polarization Configuration	$(P_{e^-}; P_{e^+}) = (+0.0; +0.0)$					
$\nu\nu\gamma$	4354	2493.3	2435.4	2283.88	2239.63	89.8
$\nu\nu\gamma\gamma$	613	344.3	325.4	238.52	228.51	66.4
$\nu\nu\gamma\gamma\gamma$	45	25.4	23.2	11.82	11.05	43.5
$\gamma\gamma$	6497	578.1	457.3	60.74	5.80	1.0
$\gamma\gamma\gamma$	1079	145.0	112.7	4.65	0.10	0.1
$\gamma\gamma\gamma\gamma$	97	19.5	14.7	0.15	0.03	0.2
Bhabha	17377544	421533.1	88935.9	67389.80	1228.70	0.3
Polarization Configuration	$(P_{e^-}; P_{e^+}) = (+0.8; -0.3)$					
$\nu\nu\gamma$	1263	548.1	526.7	460.99	438.01	79.9
$\nu\nu\gamma\gamma$	214	97.4	89.4	49.51	43.45	44.6
$\nu\nu\gamma\gamma\gamma$	19	9.2	8.1	2.53	2.05	22.3
$\gamma\gamma$	8055	715.4	571.3	75.71	7.13	1.0
$\gamma\gamma\gamma$	1339	187.1	138.5	5.60	0.13	0.1
$\gamma\gamma\gamma\gamma$	120	25.2	19.5	0.13	0.06	0.2
Bhabha	17382269	423848.9	89074.7	67016.50	1204.30	0.3
Polarization Configuration	$(P_{e^-}; P_{e^+}) = (-0.8; +0.3)$					
$\nu\nu\gamma$	9536	5635.3	5513.1	5203.03	5116.28	90.7
$\nu\nu\gamma\gamma$	1307	757.2	717.7	542.03	523.26	69.1
$\nu\nu\gamma\gamma\gamma$	95	53.7	49.4	26.79	25.35	47.2
$\gamma\gamma$	8059	718.4	562.7	74.91	7.26	1.0
$\gamma\gamma\gamma$	1338	184.8	141.1	5.93	0.13	0.1
$\gamma\gamma\gamma\gamma$	120	23.1	16.9	0.24	0.00	< 0.1
Bhabha	17424441	425324.9	88734.4	67761.60	1226.50	0.3

Table 6.2: *Selected events for the main background processes for an integrated luminosity of* $\mathcal{L} = 1\,\mathrm{fb}^{-1}$*. The selection criteria are specified in detail in Section 6.5.2. The second column contains the event numbers in the simulation, where the neutrino pair production background is already reduced by the preselection criteria. The third column lists the event numbers for the case where the emitted photon lies in the signal phase space. The last column lists the selection efficiencies.*

6.5.3 WIMP selection efficiencies

The selection efficiency for the $e^+e^- \rightarrow \nu\nu\gamma$ background depends on the detected photon energy E_γ, as shown in Figure 6.15(a). Starting at 96% for photon energies of 10 GeV, the efficiency decreases to about 70% for photon energies above 200 GeV. For high photon energies, a slightly increased photon fragmentation remains even after the merging procedure, discussed in Section 6.4.1. The energy deposited by these photon fragments adds to the visible energy E_{vis}, and the corresponding event has a higher probability of being rejected by the selection criterion on $E_{vis} - E_\gamma$. The energy dependent selection efficiency is approximated with a linear function. Higher order deviations are visible, but they are covered by the linear approximation which converges with a $\chi^2/ndf = 0.3$.

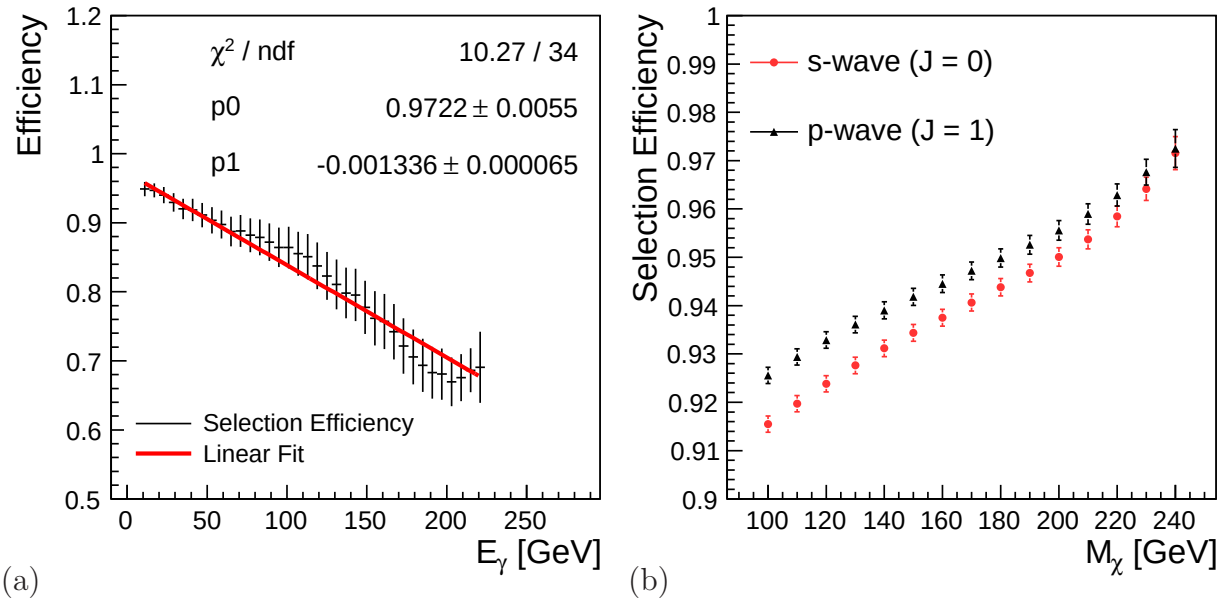

Figure 6.15: *(a) Differential selection efficiency in terms of the detected photon energy E_γ for the SM $e^+e^- \rightarrow \nu\nu\gamma$ background. A linear fit to the selection efficiency is shown in red. (b) Selection efficiencies for WIMP masses M_χ between 100 GeV and 240 GeV for s-wave (red/gray) and p-wave (black) WIMPs.*

Since the range of the photon energy spectrum for the WIMP signal process depends on the WIMP mass (cf. Fig 5.3(a), page 38), the selection efficiency for WIMPs of different masses varies as well. For each mass hypothesis, however, the major part of the signal events is located in the lower end of the photon energy spectrum. Figure 6.15(b) shows the resulting selection efficiencies for WIMP candidates ranging in mass from 100 GeV to 240 GeV. The efficiencies are well above 90% for all WIMP masses and partial wave quantum numbers ($J = 0$, s-wave annihilator (red/gray circles); $J = 1$, p-wave annihilator (black triangles)). For a fixed total cross section the spectrum of p-wave WIMPs is peaked sharper at low photon energies (cf. Fig 7.7(a) on page 85), resulting in slightly higher selection efficiencies for p-wave WIMPs of all masses.
In the running ILD experiment, the experimental signal efficiency ε (i.e. the product of reconstruction and selection efficiency) will be calibrated with theoretically well known SM processes. The radiative Z-return could be used for this purpose because it is a pure elec-

troweak process which can be calculated with negligible systematic uncertainty compared to the data statistics. A calibration on the peak of the radiative Z-return provides an absolute efficiency estimate that has to be extrapolated to the WIMP signal region at the low end of the photon spectrum. The experimental signal efficiency ε can be determined within the statistical uncertainty of the recorded data by evaluating the relation

$$\sigma = \frac{N}{\mathcal{L} \times \varepsilon} \quad \Leftrightarrow \quad \varepsilon = \frac{N}{\mathcal{L} \times \sigma}, \tag{6.4}$$

between the signal cross section σ, the number of signal events N and the integrated luminosity $\mathcal{L}$. Kinematically the photon spectrum from the radiative Z-return peaks at 241.68 GeV for a center-of-mass energy of $\sqrt{s} = 500$ GeV. Figure 6.16 shows the photon spectrum of

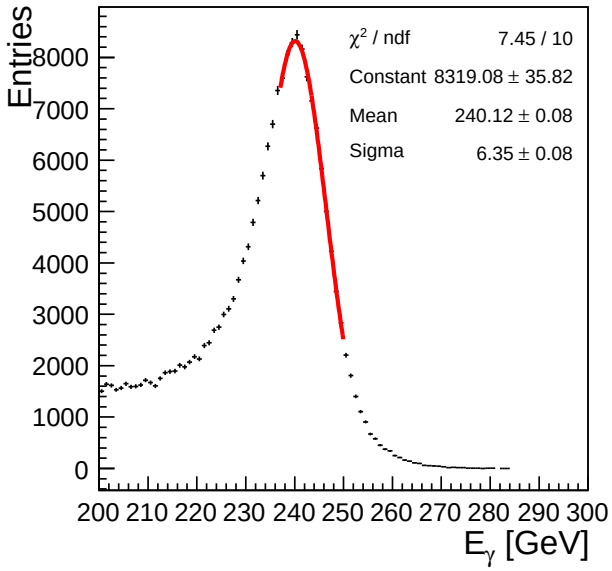

Figure 6.16: *Radiative Z-return for an integrated luminosity of $\mathcal{L} = 500$ fb^{-1} after the event selection without the veto on photons with $E_\gamma > 220$ GeV. The errors on the parameters of the gaussian fit provide an estimate on the systematic uncertainties on the signal efficiency and luminosity weighted beam energy.*

the radiative Z-return for an integrated luminosity of $\mathcal{L} = 500$ fb^{-1} after the event selection (cf. Sec. 6.5). For the radiative Z-return events, however, the photon energy is not bounded from above in contrast to the selection criteria on the WIMP signal events. The peak is approximated with a gaussian fit to a small region around the maximum. The gaussian signal shape is the result of the energy resolution of the electromagnetic calorimeters folded with the intrinsically narrow line shape of the radiative Z-return (cf. Sec 6.6). The uncertainty on the normalization of the gaussian fit is determined by the data statistics, and hence provides an upper bound on the error of the efficiency in Equation 6.4, provided the uncertainties on the signal cross section σ and luminosity measurement $\mathcal{L}$ are negligible. From the constant term of the fit, an estimate of $\delta\varepsilon/\varepsilon = 0.43\%$ for the systematic uncertainty on the selection efficiency at energies of 240 GeV is determined. Extrapolating this uncertainty to the lower part of the photon spectrum, accounting for the errors on the linear fit of the selection efficiency in Figure 6.15(a), yields an additional relative systematic uncertainty of $\leq 1.5\%$ to the selection efficiency ε at $E_\gamma = 10$ GeV. In total, the systematic uncertainty on the selection efficiency adds up to $\delta\varepsilon/\varepsilon = 1.56\%$. Within this uncertainty the p-wave and s-wave WIMP selection efficiencies are compatible.

In principle, the measurement of the radiative Z-return provides an additional cross check on the calibration of the polarization measurement. However, the deviation of the measured from the intrinsic shape of the radiative Z-return is dominated by the beam energy spectrum and effects from the detector energy resolution which are themselves afflicted by systematic uncertainties. Beam polarization has the strongest influence on the photon spectrum at lower photon energies, where the neutrino pair production is dominated by the t-channel W-exchange. The extrapolation of the uncertainty on the line shape from the radiative Z-return to lower photon energies is therefore dominated by the beam energy spectrum and detector effects and cannot be used to infer additional information on the polarization measurement.

6.6 Background and signal parametrization

After the signal selection, the simulated samples are divided into three statistically independent subsamples, the **Background**, the **Signal** and the **Template** sample (cf. Sec. 5.3.1, page 44). In order to overcome the limited generated statistics, the theoretical background and signal distributions are generated via a parametrization of the **Template** sample. The **Background** and **Signal** samples are used as data distributions.

Background expectation

The **Template** sample is parametrized twice. The first parametrization uses the full **Template** sample for a description of the expected SM background. The second parametrization is performed only on the $e^+e^- \to \nu\nu\gamma$ subset of the **Template** sample and used for the generation of the expected signal distributions.
In both cases the starting point is the differential cross section $d\sigma/dE_\gamma$ of the dominant $e^+e^- \to \nu\nu\gamma$ SM background. The cross section of this process[1] [68, 71] is successively corrected for deviations from the photon energy distribution in the **Template** sample. The first correction takes into account the expected intrinsic detector energy resolution for electromagnetic clusters, as given in the Letter of Intent [36] to

$$\frac{\Delta E}{E} = 16\% \times \frac{1}{\sqrt{E}} \oplus 0.9\%. \tag{6.5}$$

Figure 6.17(a) shows the differential cross section on tree level (black) in units of [fb/GeV]. Overlaid in red/gray is the result after folding the cross section with the detector energy resolution. The influence of the detector resolution on the spectrum is clearly visible at high photon energies of 240 GeV, i.e. close to the peak of the radiative Z-return. The intrinsic lineshape is clearly broadened and the event rate on the pole reduced. In a second step the folded cross section is corrected for the phase space criteria of the signal definition and the angular reconstruction efficiencies, as well as the selection efficiency for the SM background (Fig. 6.17(b)). Even with these corrections, the expected distribution still differs significantly from the reconstructed photon energy distribution of the $e^+e^- \to \nu\nu\gamma$ background.
In Figure 6.18(a) the corrected tree-level cross section (red/gray) is compared to the **Template** distribution (black) of the $e^+e^- \to \nu\nu\gamma$ background process, normalized to the generated statistics of $\mathcal{L} = 50$ fb^{-1} in the **Template** sample and for unpolarized beams.

[1] The FORTRAN implementation of the cross section was kindly provided by O. Kittel and U. Langenfeld.

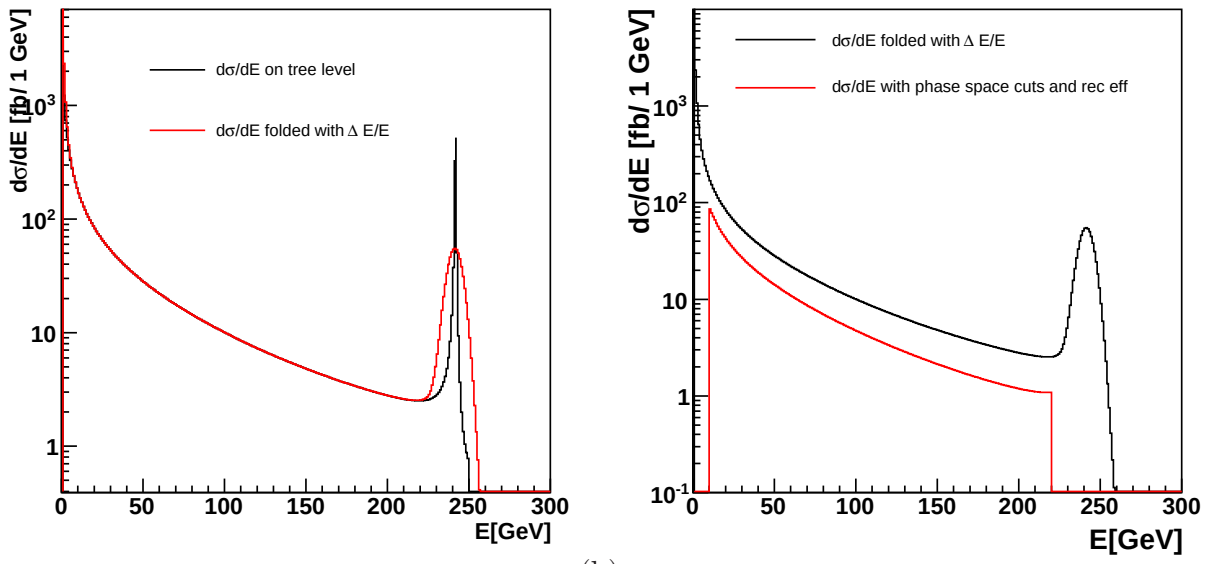

(a) (b)

Figure 6.17: *(a) $e^+e^- \to \nu\nu\gamma$ cross section on tree level (black) and folded with detector resolution (red/gray). (b) Folded $e^+e^- \to \nu\nu\gamma$ cross section (black) corrected for the signal definition phase space criteria, the reconstruction and selection efficiencies (red/gray).*

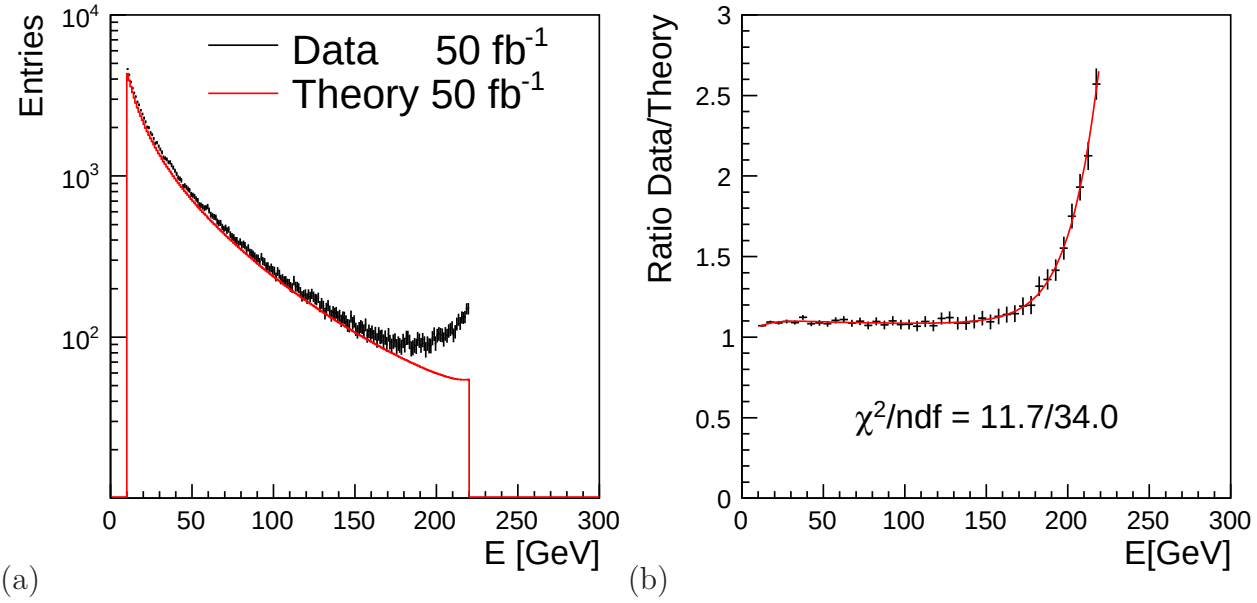

(a) (b)

Figure 6.18: *(a) Comparison of the SM $e^+e^- \to \nu\nu\gamma$ data in the* **Template** *sample with the corrected theoretical $e^+e^- \to \nu\nu\gamma$ cross section for $\mathcal{L} = 50$ fb^{-1}. (b) Ratio of the two distributions together with a 7^{th} order polynomial fit in red.*

The major sources of the difference are the beam energy spectrum and the additional leading-logarithm ISR generated in the WHIZARD sample. Emission of additional ISR and signal events in the low energy tail of the beam energy spectrum reduce the available center-of-mass energy, and photons from the radiative Z-return migrate to lower energies. The main distri-

bution characteristics are, however, similar.
The remaining differences to the simulation output are parametrized with a seventh order polynomial fit to the ratio of the **Template** data and the folded and corrected theoretical cross section. The distribution ratio is displayed in Figure 6.18(b) in black, and the polynomial of seventh order is overlaid in red.
With the polynomial correction applied to the folded cross section, the simulated background in the **Template** sample is described very well within the statistical fluctuations of the 50 fb^{-1} sample, as shown in Figure 6.19. Again, the photon spectrum of the **Template** sample (black) is compared to the parametrized distribution (red). The parametrization procedure is performed for all studied beam polarization configurations, where the simulated samples are mixed according the polarization weights introduced in Section 5.3.2.

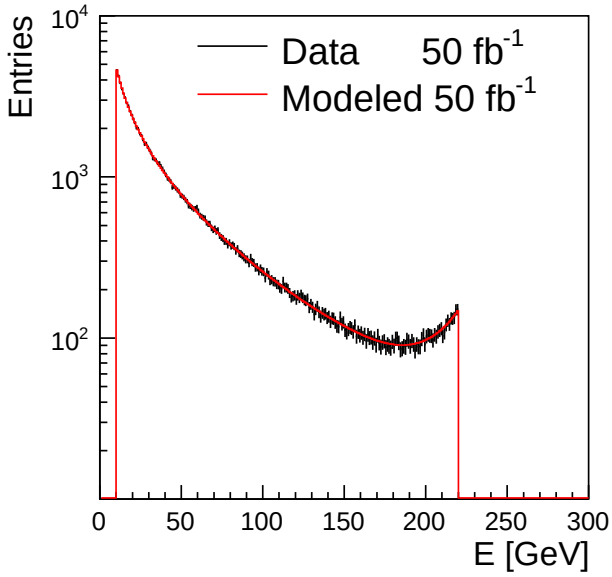

Figure 6.19: *SM background of the* **Template** *sample for* $\mathcal{L} = 50$ fb^{-1} *and unpolarized beams in black. The parametrized distribution is overlaid in red.*

While the parametrization of the pure $e^+e^- \to \nu\nu\gamma$ background is straightforward, a similar parametrization of the full SM background is complicated by the small statistics of the simulated Bhabha background, corresponding to an integrated luminosity of only $\mathcal{L} = 0.1$ fb^{-1}. Thus, an intermediate step is needed in the background parametrization to take care of the Bhabha background.

Treatment of Bhabha background

Because of the low statistics of the Bhabha background each event is given a large weight to compensate the small simulated luminosity. This poses a problem, since only few events survive the signal selection. As a result the photon energy spectrum of the Bhabha background exhibits large fluctuations, as visible in Figure 6.14. The final Bhabha spectrum after selection is therefore approximated by the spectrum before the event tagging with the BeamCal information (see Fig. 6.13(a)) and then scaled with the correct selection efficiency and lumi-

nosity. In the parametrization of the full SM background this scaled spectrum is used instead of the spectrum of selected Bhabha events.

Signal expectation

In order to obtain signal predictions for different polarization configurations, the parametrized $e^+e^- \rightarrow \nu\nu\gamma$ subset of the **Template** sample with the beam polarization configuration $(P_{e^-}; P_{e^+}) = (0.0; 0.0)$ is re-weighted with the ratio of the WIMP pair production cross section (cf. Eq. 5.8) for a given polarization configuration and the neutrino pair production cross section [68] for $(P_{e^-}; P_{e^+}) = (0.0; 0.0)$:

$$w_{sig} = \frac{d\sigma_{\chi\chi\gamma}(P_{e^-}, P_{e^+})}{d\sigma_{\nu\nu\gamma}(0.0, 0.0)}. \tag{6.6}$$

The cross section ratio is evaluated in terms of the photon energy. In this way, templates of the photon energy spectra for all polarization configurations and different WIMP parameters are created. The template spectra are produced for all three WIMP scenarios **"Equal"**, **"Helicity"** and **"Anti-SM"** and in each scenario a specific template is generated for the following WIMP parameters:

- WIMP mass: 100 GeV $< M_\chi <$ 250 GeV in 1 GeV steps,
- WIMP spin: $S_\chi = 1/2$,
- WIMP partial wave: $J_0 = 0$ (s-wave) and $J_0 = 1$ (p-wave) WIMPs,

resulting in a total of 900 templates per polarization configuration.
The signal contribution in the pseudo data is generated in the same manner from the spectrum of the **Signal** data sample.
A single-photon signature can also be interpreted in a model-dependent way, for example within the supersymmetry mSugra scenario. Therefore, signal expectations and data distributions are created for neutralino masses ranging from 82 GeV to 112 GeV in a region about the SPS1a' parameter point.

Chapter 7

Results

If an excess of high energy photons from the process $e^+e^- \to \chi\chi\gamma$ is observed at ILD, the total number of detected events and the shape information of the photon energy distribution can be used to determine the production cross section, the particle mass and the coupling structure of the interaction involved. Furthermore, the quantum number of the dominant partial wave of the production process is accessible via the shape information, allowing for a discrimination between the produced s- and p-wave particles. The particle in question can be either a generic WIMP or a specific DM candidate, e.g. the lightest neutralino $\tilde{\chi}_1^0$ in SUSY. While the total production cross section is related to the observed number of signal events, the coupling structure is inferred from the combination of four independent cross section measurements with different beam polarization configurations and the cross section deconstruction for polarized beams (compare to Sec. 5.3.2):

$$\begin{aligned}\sigma_{P_{e^-}P_{e^+}} &= \frac{1}{4}\{(1+P_{e^-})(1+P_{e^+})\sigma_{RR} + (1-P_{e^-})(1-P_{e^+})\sigma_{LL} \\ &+ (1+P_{e^-})(1-P_{e^+})\sigma_{RL} + (1-P_{e^-})(1+P_{e^+})\sigma_{LR}\}. \end{aligned} \tag{7.1}$$

Here, σ_{LL} is the cross section for 100% left-handed electron and positron beams. The other cross sections are to be interpreted in the same way.
The WIMP candidate mass is measured by a χ^2 comparison between the photon spectrum of signal plus background and template spectra of WIMP candidates with different masses (cf. Sec. 6.6). The template method is also used for the partial wave determination.
The analysis results for the cross section and mass measurement in the model independent WIMP scenario are presented in the following Section 7.1. The corresponding determination of the neutralino parameters for the mSugra SPS1a' parameter point (see Sec. 5.1.3) is described in Section 7.2.

7.1 Model independent WIMP scenario

In Section 5.1.1 the model independent WIMP scenario has been introduced. In this section the results of the parameter measurements are presented. The model is investigated in the three coupling scenarios **"Equal"**, **"Helicity"** and **"Anti-SM"** (cf. Sec 5.1.2). The cross section of the signal for unpolarized beams and in the chosen phase space is set to 100 fb throughout. This cross section value is in the same order of magnitude as the signal cross

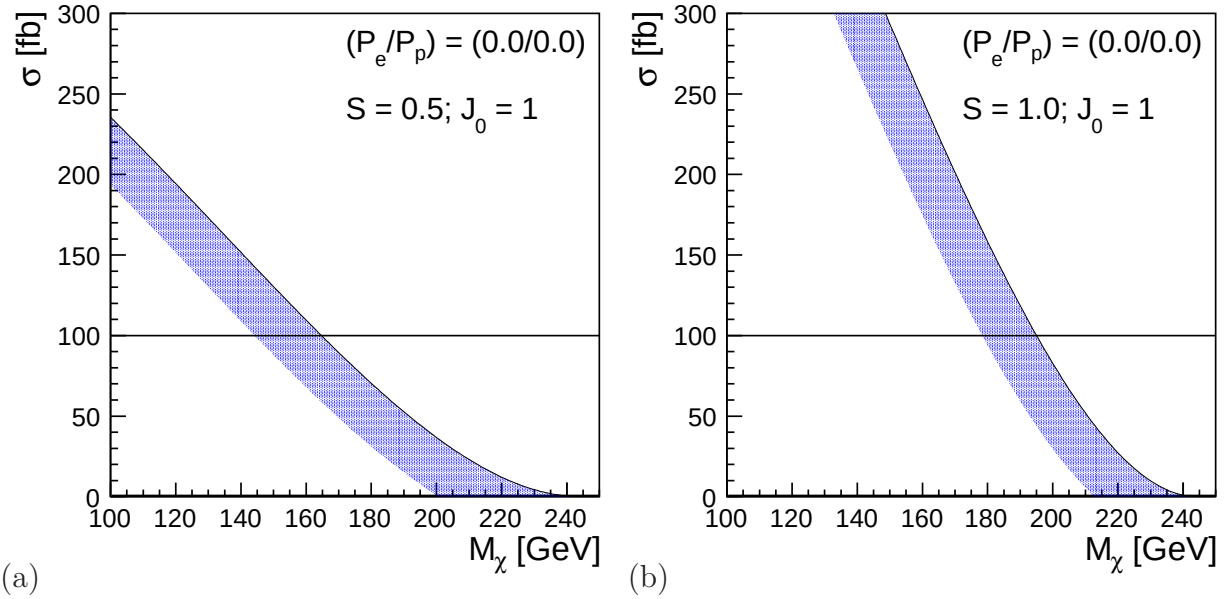

Figure 7.1: *Maximal allowed signal cross sections as a function of the WIMP mass. The limits are computed for p-wave WIMPs of (a) spin-1/2 and (b) spin-1. Other parameters are set to $\kappa_e = 1.0$ and $\sigma_{an} = 6.0$ pb, see Equation 5.8 and Figure 5.2(a).*

section of 134.3 fb for the SPS1a' neutralino. In Figure 7.1, the maximal unpolarized cross sections within the signal region are shown as a function of the WIMP mass. The limits are computed for p-wave WIMPs with $\kappa_e = 1.0$[1] and $\sigma_{an} = 6.0$ pb, for (a) spin-1/2 and (b) spin-1 particles, see Equation 5.8 and Figure 5.2 (a). The chosen cross section of 100 fb is compatible with the constraints on spin-1/2 WIMPs with masses of up to 165 GeV, see Figure 7.1(a). For spin-1 WIMPs, the assumption holds for almost the full analyzed mass range of 100 GeV to 200 GeV, compare Figure 7.1(b). In principle, for WIMP masses below $M = 160$ GeV, an additional constraint on the energy of the detected photon of

$$E_\gamma > \frac{\sqrt{s}}{2}\left(1 - \frac{8M^2}{s}\right) \tag{7.2}$$

has to be set, since otherwise the produced WIMPs become relativistic, and the measured cross sections can not be directly compared to the cosmological DM constraints which are calculated for non-relativistic DM. In the present analysis this kinematic criterion is not used in order to allow for a comparison of the results with the SPS1a' neutralino with a mass of 97.7 GeV. Nevertheless, the assumed cross section of 100 fb is still roughly compatible to the DM constraint for the analyzed mass range.

For the determination of the cross section and helicity structure it is assumed that an integrated luminosity of $\mathcal{L} = 500$ fb^{-1} is distributed to the different beam polarization configurations $(+|P_{e^-}|; -|P_{e^+}|)$, $(-|P_{e^-}|; +|P_{e^+}|)$, $(+|P_{e^-}|; +|P_{e^+}|)$ and $(-|P_{e^-}|; -|P_{e^+}|)$. The equal sign configurations share 20% of the luminosity, while the opposite sign configurations obtain 40% of running time each. In total numbers the luminosity is distributed as:

[1] A value of $\kappa_e = 1.0$ means, that the WIMPs couple to electrons and positrons only.

- 200 fb^{-1} with $(+|P_{e^-}|; -|P_{e^+}|)$,
- 200 fb^{-1} with $(-|P_{e^-}|; +|P_{e^+}|)$,
- 50 fb^{-1} with $(+|P_{e^-}|; +|P_{e^+}|)$,
- 50 fb^{-1} with $(-|P_{e^-}|; -|P_{e^+}|)$.

The absolute polarization values are assumed to be $|P_{e^-}| = 0.8$ and $|P_{e^+}| = 0.3$ or $|P_{e^+}| = 0.6$ respectively. The WIMP mass is fixed to 150 GeV.
For the mass measurement the total luminosity of $\mathcal{L} = 500$ fb^{-1} is spent on the particular polarization configuration under investigation. The range of WIMP masses analyzed is constrained to 100 GeV $< M_\chi <$ 250 GeV. Both s- and p-wave WIMPs are assumed. For statistical compatibility, results for the simulated statistics of $\mathcal{L} = 50$ fb^{-1} are also presented.

7.1.1 Cross sections and coupling structure

The signal cross sections $\sigma_{P_{e^-}P_{e^+}}$ and statistical uncertainty $\Delta\sigma_{P_{e^-}P_{e^+}}$ for the polarization configuration $(P_{e^-}; P_{e^+})$ are calculated from the observed data events N_D by

$$\sigma_{P_{e^-}P_{e^+}} = \frac{N_D - < N_B >}{\mathcal{L} \times \varepsilon} \qquad \Delta\sigma_{P_{e^-}P_{e^+}} = \frac{\sqrt{N_D}}{\mathcal{L} \times \varepsilon}, \tag{7.3}$$

where $< N_B >$ is the expected number of background events for the luminosity $\mathcal{L}$. The efficiency ε is the product of the energy independent photon reconstruction efficiency ε_{rec} (cf. Sec. 6.4.3) and the mass dependent signal efficiency ε_{sel} of Section 6.5.3. From the independent cross section measurements with the four polarization configurations, the coupling structure is obtained by using Eq. 7.1, resulting in the equation system:

$$\begin{aligned}
\sigma_{+-} &= \frac{1}{4}\{(1+|P_-|)(1-|P_+|)\sigma_{RR} + (1-|P_-|)(1+|P_+|)\sigma_{LL} \\
&\quad + (1+|P_-|)(1+|P_+|)\sigma_{RL} + (1-|P_-|)(1-|P_+|)\sigma_{LR}\} \\
\sigma_{-+} &= \frac{1}{4}\{(1-|P_-|)(1+|P_+|)\sigma_{RR} + (1+|P_-|)(1-|P_+|)\sigma_{LL} \\
&\quad + (1-|P_-|)(1-|P_+|)\sigma_{RL} + (1+|P_-|)(1+|P_+|)\sigma_{LR}\} \\
\sigma_{++} &= \frac{1}{4}\{(1+|P_-|)(1+|P_+|)\sigma_{RR} + (1-|P_-|)(1-|P_+|)\sigma_{LL} \\
&\quad + (1+|P_-|)(1-|P_+|)\sigma_{RL} + (1-|P_-|)(1+|P_+|)\sigma_{LR}\} \\
\sigma_{--} &= \frac{1}{4}\{(1-|P_-|)(1-|P_+|)\sigma_{RR} + (1+|P_-|)(1+|P_+|)\sigma_{LL} \\
&\quad + (1-|P_-|)(1+|P_+|)\sigma_{RL} + (1+|P_-|)(1-|P_+|)\sigma_{LR}\},
\end{aligned} \tag{7.4}$$

or in matrix notation:

$$\begin{pmatrix} \sigma_{+-} \\ \sigma_{-+} \\ \sigma_{++} \\ \sigma_{--} \end{pmatrix} = A_{P_-,P_+} \begin{pmatrix} \sigma_{RR} \\ \sigma_{LL} \\ \sigma_{RL} \\ \sigma_{LR} \end{pmatrix}, \tag{7.5}$$

where the matrix A_{P_-,P_+} explicitly depends on the experimental polarization configuration. For a clearer notation the electron and positron polarization are denoted P_- and P_+, and

the subscripts of $\sigma_{\{+,-\}}$ indicate the sign of the electron and positron polarization, respectively. Multiplication of Equation 7.5 with the inverted matrix A^{-1} yields the cross sections $\sigma_{\{L,R\}}$. Errors, statistical and systematic, are propagated quadratically from the individually measured cross sections $\sigma_{\{+,-\}}$.

Systematic uncertainties

The total systematic uncertainty $\delta\sigma_{P_{e^-}P_{e^+}}$ on a measurement $\sigma_{P_{e^-}P_{e^+}}$ is given from Equation 7.3 by the systematics on the background process cross section $\delta\sigma_{bg}$ and the uncertainty on the efficiency $\delta\varepsilon$ and luminosity $\delta\mathcal{L}$:

$$\delta\sigma^2_{P_{e^-}P_{e^+}} = \delta\sigma^2_{bg} + \frac{\sigma^2_{P_{e^-}P_{e^+}}}{\varepsilon^2}\delta\varepsilon^2 + \frac{\sigma^2_{P_{e^-}P_{e^+}}}{\mathcal{L}^2}\delta\mathcal{L}^2. \tag{7.6}$$

For an estimation of the systematic uncertainties from the dominant SM background process $e^+e^- \to \nu\nu\gamma$ Equation 7.1 can be simplified, because σ_{LL} and σ_{RR} vanish. Equation 7.1 becomes:

$$\sigma_{bg} = \sigma_{0,bg}[1 + (P_{e^+} - P_{e^-})A_{LR} - P_{e^-}P_{e^+}] \tag{7.7}$$

with the unpolarized cross section $\sigma_{0,bg}$ and the Left-Right-Asymmetry A_{LR},

$$\begin{aligned} \sigma_{0,bg} &= \frac{\sigma_{LR} + \sigma_{RL}}{4} \\ A_{LR} &= \frac{\sigma_{LR} - \sigma_{RL}}{\sigma_{LR} + \sigma_{RL}}. \end{aligned} \tag{7.8}$$

At center-of-mass energies well above the Z mass the process $e^+e^- \to \nu\nu\gamma$ is dominated by the t-channel W-exchange, for which $A_{LR} \approx 1$, resulting in a systematic uncertainty on the SM background of:

$$\delta\sigma^2_{bg} = \sigma^2_{0,bg}[(1 + P_{e^+})^2\delta P^2_{e^-} + (1 - P_{e^-})^2\delta P^2_{e^+}]. \tag{7.9}$$

Here, the theoretical uncertainty on the background cross section $\sigma_{0,bg}$ is considered negligible since the emitted photon is included in the matrix element in the generation of the background spectrum, and its influence is calculated exactly, see Section 6.2.1. The uncertainty of the polarization measurement enters the signal cross section determination via this term[2]. For the ILC polarization measurement the systematic uncertainty is expected to be $\delta P/P \leq 0.25\%$ per beam with negligible statistical errors.
The uncertainty on the selection efficiency has been determined to $\delta\varepsilon/\varepsilon = 1.56\%$ from the efficieny calibration with mass dependent selection efficiencies of about 95%, see Section 6.5.3. As will be shown in Section 7.1.2, uncertainties on the beam energy spectrum result in a distortion of the WIMP signal spectra similar to the change in the signal spectrum when comparing s- and p-wave WIMP production. The beam energy spread mimics effectively 1/16 of the relative difference of the s- and p-wave spectra. With reference to Figure 6.15(b), systematics on the beam energy spectrum translate to a change in the WIMP selection efficiency. Because the cross section measurement is not sensitive to the partial wave of the production process,

[2]Radiative Bhabha scattering constitutes another prominant background, but because this process is largely polarization independent, it does not introduce further polarization dependent uncertainties, see Table 6.2.

another contribution to the selection efficiency uncertainty is estimated from the maximal difference of selection efficiencies for WIMP masses of 100 GeV to $\delta\varepsilon/\varepsilon = 0.9\%$. The total uncertainty on the selection efficiency is the combination of the uncertainty on the efficiency calibration and the uncertainty on the beam energy spread, $\delta\varepsilon/\varepsilon = 1.75\%$.
At ILC the luminosity $\mathcal{L}$ will be measured to a precision of $\delta\mathcal{L}/\mathcal{L} = 10^{-4}$. Column 1 of Table 7.1 lists the individual contributions to the cross section measurement.
In solving the equation system 7.5 for the cross sections $\sigma_{\{L,R\}}$, the explicit polarization dependence of the matrix A introduces an additional systematic uncertainty. The order of this contribution is accounted for by variation of the experimental polarization at the level of $\delta P/P = 0.25\%$ and hence a variation of the coefficients of A^{-1}.

Parameter	value	$\delta\sigma$ [fb]
$\delta P/P$	0.25%	5.7
$\delta\varepsilon/\varepsilon$	1.75%	1.7
$\delta\mathcal{L}/\mathcal{L}$	0.01%	0.01
Total		5.9

Table 7.1: *Contributions to the systematic uncertainty on the cross section measurement in the* **"Equal"** *scenario for an unpolarized cross section of 100 fb,* $P_{e^-} = 0.8$ *and* $P_{e^+} = -0.3$ *and* $\mathcal{L} = 200$ fb^{-1}. *The dominant contribution is attributed to the polarization measurement. See also Table 7.2.*

Results of cross section measurement and coupling structure determination

In Figure 7.2(a) the data spectrum for a 150 GeV p-wave WIMP in the **"Equal"** scenario is shown in black with the parametrized SM background in red (dark gray) and the expected signal photon spectrum in green (light gray). The signal cross section for unpolarized beams is set to 100 fb. The statistics correspond to the simulated luminosity of $\mathcal{L} = 50$ fb^{-1}. The beam polarization is set to $(P_{e^-}; P_{e^+}) = (0.8; -0.3)$. The background corrected data spectrum is shown in Figure 7.2(b). The statistical errors are given by the data statistics. Within the errors the background corrected data is compatible with the expected signal.
In Table 7.2 the results of the cross section measurement in the **"Equal"** scenario for a 150 GeV p-wave WIMP are listed. The electron and positron polarizations are $|P_{e^-}| = 0.8$ and $|P_{e^+}| = 0.3$. To check for statistical consistency the integrated luminosity is $\mathcal{L} = 50$ fb^{-1} comparable to the generated statistics. The luminosity is distributed to the polarization configurations according to Section 7.1. The unpolarized signal cross section is set to 100 fb. In the **"Equal"** scenario the polarization has no influence on the WIMP signal rates. All measured cross sections are compatible with the input cross section of 100 fb. The best individual measurement with $(P_{e^-}; P_{e^+}) = (+0.8; -0.3)$ and the highest luminosity yields a statistical uncertainty of 10 fb, because of the maximal background suppression. The systematic uncertainties are dominated in all measurements by the polarization measurement, transmitted via the uncertainty on the SM background prediction. Also shown in Table 7.2 are the corresponding results for an integrated luminosity of $\mathcal{L} = 500$ fb^{-1}. In that case, the statistical errors are reduced by a factor of $1/\sqrt{10}$ according to the increased luminosity, and the individual measurements are systematically limited by the polarization uncertainty.

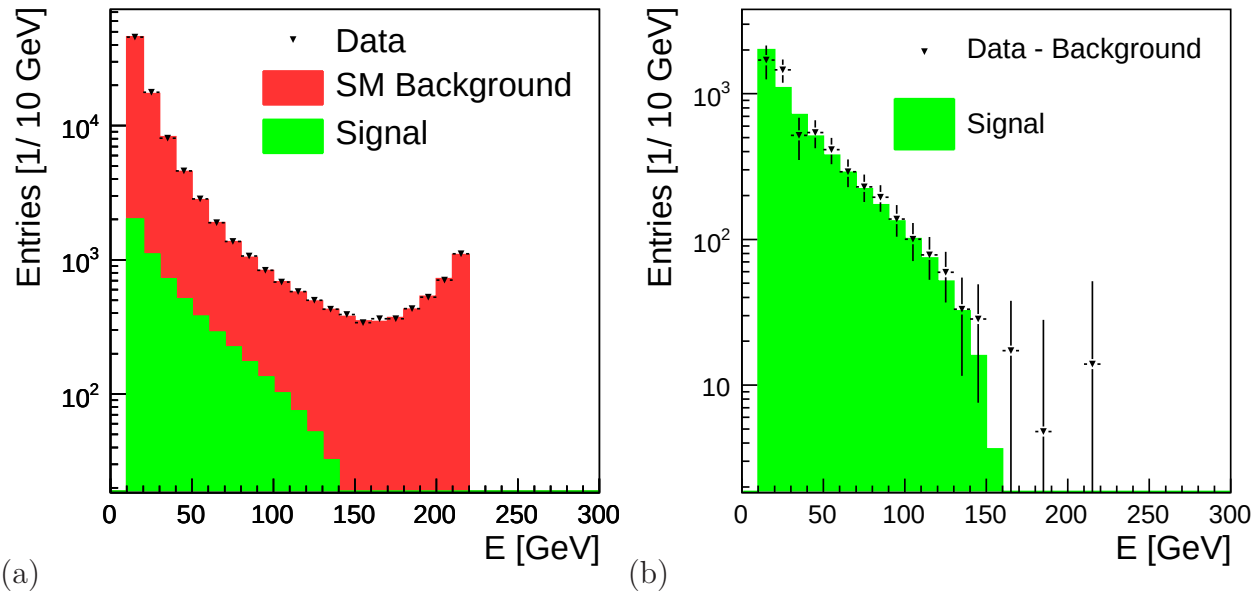

(a) (b)

Figure 7.2: *(a) Photon spectrum for a 150 GeV p-wave WIMP in the* **"Equal"** *scenario (black) with the expected SM background (red/dark gray) and signal (green/light gray) spectra as stacked histograms. (b) Background subtracted data (black) and expected signal spectrum (green/light gray). All spectra correspond to an integrated luminosity of* 50 fb^{-1} *and* $(P_{e^-}; P_{e^+}) = (0.8; -0.3)$.

Furthermore the measured cross sections in the **"Helicity"** and **"Anti-SM"** scenario for $\mathcal{L} = 500\ \text{fb}^{-1}$ are presented in Table 7.2. All following results are for an integrated luminosity of $\mathcal{L} = 500\ \text{fb}^{-1}$, again distributed to the beam polarization states as explained in Sec. 7.1. From the individual cross section measurements the coupling structure is extracted by solving Equations 7.4. The results of the coupling structure determination, i.e. the measurement of the fully polarized cross sections $\sigma_{\{L,R\}}$, are listed in Table 7.3 and depicted in Figures 7.3 and 7.4. In all cases the candidate is assumed to be a 150 GeV p-wave WIMP. In Figures 7.3(a) and (b) the couplings are expressed in terms of the ratio $\sigma_{\{L,R\}}/\sigma_0$ for the **"Equal"** scenario for a beam polarization configuration of (a) $|P_{e^-}| = 0.8$, $|P_{e^+}| = 0.3$ and (b) $|P_{e^-}| = 0.8$, $|P_{e^+}| = 0.6$. From Equation 7.1 for $P_{e^-} = P_{e^+} = 0$ follows $\sum_{(i,j)\in\{R,L\}} \sigma_{(i,j)} = 4 \times \sigma_0$, with the cross section σ_0 for unpolarized beams. The systematic polarization error is $\delta P/P = 0.25\%$. The systematic errors are given by the red error bars, the black error bars represent the total of statistical and systematic errors. The corresponding results for the **"Helicity"** and **"Anti-SM"** scenario are shown in Figures 7.3(c)+(d) and 7.3(e)+(f), respectively. In all cases the measurement is limited by the systematic polarization uncertainty transmitted via the SM background.

The cross sections $\sigma_{\{R,L\}}$ are determined to a precision of 20 fb to 40 fb for an positron polarization of $|P_{e^+}| = 0.3$, see column 2 of Table 7.3 with $\sigma_0 = 100$ fb. For an increased electron polarization of 60% the uncertainties on the individual cross sections are significantly lowered to 10 fb to 30 fb. This is in particular the case for σ_{RL} which is predominantly determined by the measurement of σ_{+-}, where the SM background is maximally reduced.

Pol. config. $(P_{e^-}; P_{e^+})$	$\mathcal{L}$ [fb^{-1}]	σ [fb]	stat. $\pm\delta\sigma$[fb]	syst. contributions $\pm\delta P$	$\pm\delta\varepsilon$	$\pm\delta\mathcal{L}$ [fb]	total $\pm\delta\sigma$ [fb]
"Equal" scenario and $\mathcal{L} = 50.0$ fb^{-1}							
$(+0.8; -0.3)$	20	99.4	10.4	5.7	1.7	0.01	12.0
$(-0.8; +0.3)$	20	97.3	20.5	11.9	1.7	0.01	23.8
$(+0.8; +0.3)$	5	99.5	22.1	10.6	1.7	0.01	24.6
$(-0.8; -0.3)$	5	98.5	32.5	7.9	1.7	0.01	33.5
"Equal" scenario and $\mathcal{L} = 500.0$ fb^{-1}							
$(+0.8; -0.3)$	200	99.4	3.3	5.7	1.7	0.01	6.8
$(-0.8; +0.3)$	200	97.3	6.5	11.9	1.7	0.01	13.7
$(+0.8; +0.3)$	50	99.5	7.0	10.6	1.7	0.01	12.8
$(-0.8; -0.3)$	50	98.5	10.3	7.9	1.7	0.01	13.1
"Helicity" scenario and $\mathcal{L} = 500.0$ fb^{-1}							
$(+0.8; -0.3)$	200	123.4	3.3	5.7	2.1	0.01	7.0
$(-0.8; +0.3)$	200	121.3	6.5	11.9	2.1	0.01	13.7
$(+0.8; +0.3)$	50	75.5	7.0	10.6	1.3	0.01	12.8
$(-0.8; -0.3)$	50	74.5	10.2	7.9	1.3	0.01	13.0
"Anti-SM" scenario and $\mathcal{L} = 500.0$ fb^{-1}							
$(+0.8; -0.3)$	200	233.4	3.4	5.7	4.0	0.02	7.8
$(-0.8; +0.3)$	200	11.3	6.4	11.9	0.2	0.00	13.6
$(+0.8; +0.3)$	50	125.5	7.0	10.6	2.2	0.01	12.9
$(-0.8; -0.3)$	50	24.5	10.2	7.9	0.4	0.00	12.9

Table 7.2: *Measured polarized cross sections for p-wave WIMP with a mass of 150 GeV and an unpolarized cross section of $\sigma_0 = 100$ fb: in the* **"Equal"** *scenario for an integrated luminosity of $\mathcal{L} = 50$ fb^{-1} (first part) and for $\mathcal{L} = 500$ fb^{-1} (second part); in the* **"Helicity"** *scenario (third part) and the* **"Anti-SM"** *scenario (fourth part) also for an integrated luminosity of $\mathcal{L} = 500$ fb^{-1}. In each scenario, the integrated luminosity is distributed to the four polarization configurations as described on page 73.*

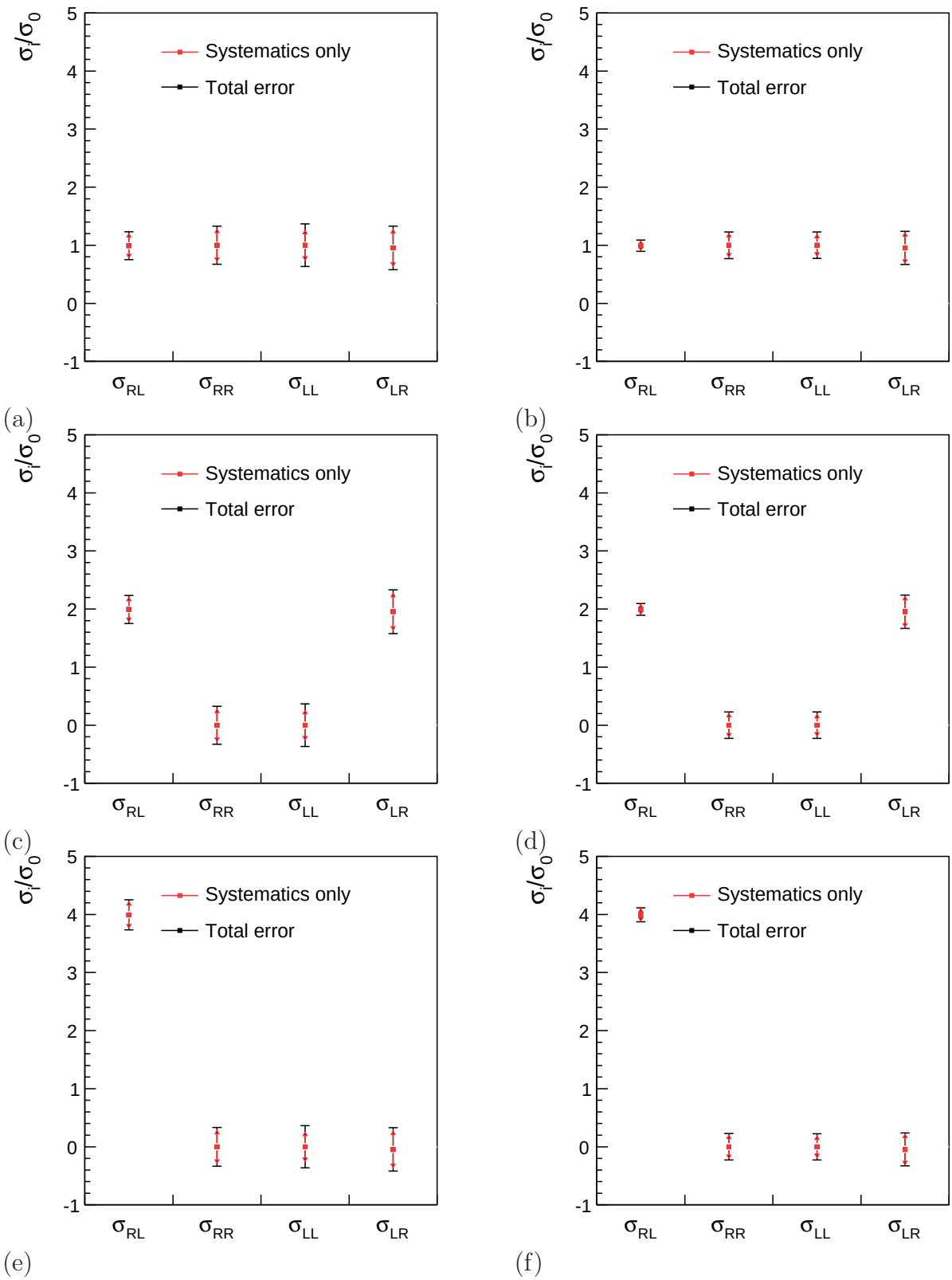

Figure 7.3: *Polarized cross sections σ_{ij}/σ_0 for (a)+(b) the* **"Equal"**, *(c)+(d) the* **"Helicity"** *and (e)+(f) the* **"Anti-SM"** *scenario with 150 GeV WIMPs. In the left column the results for a beam polarization of $|P_{e^-}| = 0.8; |P_{e^+}| = 0.3$ are shown. The right column depicts the measurement for $|P_{e^-}| = 0.8; |P_{e^+}| = 0.6$. The polarization uncertainty is assumed to be $\delta P/P = 0.25\%$.*

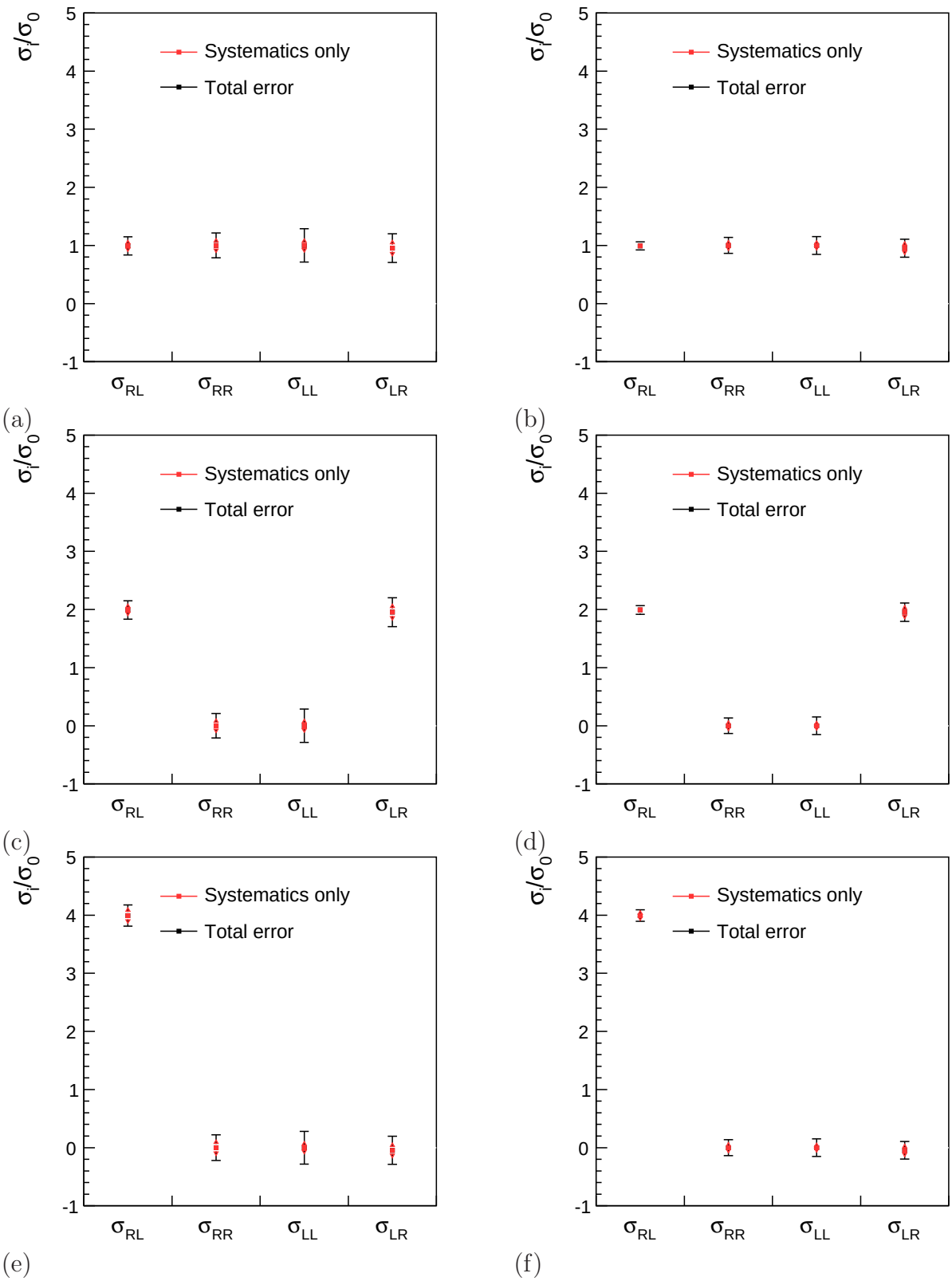

Figure 7.4: *Polarized cross sections σ_{ij}/σ_0 for (a)+(b) the* **"Equal"**, *(c)+(d) the* **"Helicity"** *and (e)+(f) the* **"Anti-SM"** *scenario with 150 GeV WIMPs. In the left column the results for a beam polarization of $|P_{e^-}| = 0.8; |P_{e^+}| = 0.3$ are shown. The right column depicts the measurement for $|P_{e^-}| = 0.8; |P_{e^+}| = 0.6$. The polarization uncertainty is assumed to be $\delta P/P = 0.1\%$. Compare to Figure 7.3.*

	$(\lvert P_{e^-}\rvert;\lvert P_{e^+}\rvert) = (0.8;0.3)$		$(\lvert P_{e^-}\rvert;\lvert P_{e^+}\rvert) = (0.8;0.6)$	
"Equal" scenario				
σ_{RL}/σ_0	0.99 ± 0.24	(0.16)	0.99 ± 0.10	(0.07)
σ_{RR}/σ_0	1.00 ± 0.33	(0.21)	1.00 ± 0.23	(0.14)
σ_{LL}/σ_0	1.00 ± 0.37	(0.29)	1.00 ± 0.23	(0.15)
σ_{LR}/σ_0	0.95 ± 0.38	(0.25)	0.95 ± 0.28	(0.15)
"Helicity" scenario				
σ_{RL}/σ_0	1.99 ± 0.24	(0.16)	1.99 ± 0.10	(0.08)
σ_{RR}/σ_0	0.00 ± 0.33	(0.21)	0.00 ± 0.23	(0.14)
σ_{LL}/σ_0	0.00 ± 0.37	(0.29)	0.00 ± 0.23	(0.15)
σ_{LR}/σ_0	1.95 ± 0.38	(0.25)	1.95 ± 0.29	(0.16)
"Anti-SM" scenario				
σ_{RL}/σ_0	3.99 ± 0.26	(0.18)	3.99 ± 0.12	(0.10)
σ_{RR}/σ_0	0.00 ± 0.33	(0.22)	0.00 ± 0.23	(0.14)
σ_{LL}/σ_0	0.00 ± 0.36	(0.28)	0.00 ± 0.23	(0.15)
σ_{LR}/σ_0	-0.05 ± 0.37	(0.24)	-0.05 ± 0.28	(0.15)

Table 7.3: *Fully polarized cross sections $\sigma_{\{R,L\}}$ measured within three WIMP scenarios and for two different absolute polarizations of electrons and positrons. The values are normalized to the input unpolarized cross section of $\sigma_0 = 100$ fb. The quoted uncertainties are the squared sum of statistical errors and systematic uncertainties, with the bracketed values corresponding to an increased precision on the polarization measurement of $\delta P/P = 0.1\%$.*

When the polarization measurement precision is increased to $\delta P/P = 0.1\%$, the uncertainties on the cross sections are reduced by a factor of roughly 2/3, as can be seen from the bracketed values in Table 7.3. The measurement uncertainty is dominated by the statistics for $|P_{e^-}| = 0.8$, $|P_{e^+}| = 0.3$, as shown in the corresponding Figures 7.4(a), (c) and (e). With an increased positron polarization of $|P_{e^+}| = 0.6$, the total errors equal the systematic uncertainties, see Figures 7.4(b), (d) and (f).
The scenarios are clearly distinguishable. Table 7.4 lists the χ^2/ndf and p-values of the scenario comparison for $|P_{e^+}| = 0.3$. For each coupling scenario realized in the data, the other two scenarios can be excluded with a value of $p < 10^{-8}$.
Once the coupling structure has been inferred from the measurement, the unpolarized cross section σ_0 is related to the measured cross section with polarized beams $\sigma_{P_{e^-}P_{e^+}}$ by Equation 7.1. In the same way as for the SM background in Equation 7.7, the cross sections for the three WIMP coupling scenarios **"Equal"**, **"Helicity"** and **"Anti-SM"** are reduced to:

$$\begin{aligned} \text{"}\mathbf{Equal}:\text{"} \quad & \sigma_{P_{e^-}P_{e^+}} = \sigma_0 \\ \text{"}\mathbf{Helicity}:\text{"} \quad & \sigma_{P_{e^-}P_{e^+}} = \sigma_0[1 - P_{e^-}P_{e^+}] \\ \text{"}\mathbf{Anti-SM}:\text{"} \quad & \sigma_{P_{e^-}P_{e^+}} = \sigma_0[1 - P_{e^-}P_{e^+} + P_{e^-} - P_{e^+}]. \end{aligned} \tag{7.10}$$

Data Scenario	p-values (χ^2/ndf) for different Theory Scenarios					
	"Equal"		**"Helicity"**		**"Anti-SM"**	
"Equal"	≈ 1.0	(0.0)	$< 10^{-8}$	(14.0)	$< 10^{-8}$	(60.0)
"Helicity"	$< 10^{-8}$	(13.4)	≈ 1.0	(0.0)	$< 10^{-8}$	(31.9)
"Anti-SM"	$< 10^{-8}$	(53.0)	$< 10^{-8}$	(29.9)	≈ 1.0	(0.0)

Table 7.4: *Comparison between measured coupling structure and the three assumed theoretical scenarios in terms of the p-value and χ^2/ndf. The p-value is evaluated for the χ^2 probability density function for three degrees of freedom.*

Equations 7.7 and 7.10 provide a relation between the total unpolarized cross section and the measured cross sections $\sigma_{P_{e^-}P_{e^+}}$ for polarized beams.
Systematic errors are propagated for example in the **"Helicity"** scenario as:

$$\delta\sigma_0^2 = \frac{1}{(1-P_{e^-}P_{e^+})^2}\delta\sigma^2_{P_{e^-}P_{e^+}} + \frac{\sigma_0^2 P_{e^+}^2}{(1-P_{e^-}P_{e^+})^2}\delta P^2_{e^-} + \frac{\sigma_0^2 P_{e^-}^2}{(1-P_{e^-}P_{e^+})^2}\delta P^2_{e^+}, \tag{7.11}$$

and analogously for the other coupling scenarios. From each of the four individual measurement of $\sigma_{P_{e^-}P_{e^+}}$ per coupling scenario, the unpolarized cross section $\sigma_{0,i}$ ($i = 1...4$) is obtained from the corresponding Equation 7.10. The measurements are combined via

$$\sigma_0 = \frac{1}{w}\sum_{i=1}^{4}\frac{\sigma_{0,i}}{\delta\sigma^2_{0,i,total}} \qquad \text{with} \qquad w = \sum_{i=1}^{4}\frac{1}{\delta\sigma^2_{0,i,total}}, \tag{7.12}$$

where $\delta\sigma_{0,i,total}$ are the total uncertainties on the four measurements $\sigma_{0,i}$. The measured cross sections σ_0 in the three coupling scenarios for an integrated luminosity of $\mathcal{L} = 500$ fb^{-1} are given in Table 7.5.
The cross section σ_0 is determined to a precision of 3 to 5 percent given an uncertainty of 0.25% on the polarization measurement. With $\delta P/P = 0.1\%$ the total error on the cross section measurement is reduced to $\approx 2.5\%$.

Data scenario (simulated)	Unpolarized cross section: $\sigma_0 \pm$ stat $\pm$ sys ($\pm$ total) [fb] $(\lvert P_{e^-}\rvert; \lvert P_{e^+}\rvert) = (0.8; 0.3)$		$(\lvert P_{e^-}\rvert; \lvert P_{e^+}\rvert) = (0.8; 0.6)$	
Assumed polarization uncertainty $\delta P/P = 0.25\%$				
"Equal"	99.0 $\pm$ 2.8 $\pm$ 4.3	($\pm$ 5.1)	99.2 $\pm$ 2.7 $\pm$ 3.5	($\pm$ 4.4)
"Helicity"	99.1 $\pm$ 2.3 $\pm$ 4.0	($\pm$ 4.6)	99.4 $\pm$ 2.0 $\pm$ 2.8	($\pm$ 3.4)
"Anti-SM"	99.8 $\pm$ 1.4 $\pm$ 2.8	($\pm$ 3.2)	99.7 $\pm$ 1.1 $\pm$ 2.1	($\pm$ 2.4)
Assumed polarization uncertainty $\delta P/P = 0.10\%$				
"Equal"	99.0 $\pm$ 2.6 $\pm$ 2.0	($\pm$ 3.3)	99.1 $\pm$ 2.6 $\pm$ 1.9	($\pm$ 3.2)
"Helicity"	99.1 $\pm$ 2.3 $\pm$ 2.0	($\pm$ 3.0)	99.3 $\pm$ 2.0 $\pm$ 1.8	($\pm$ 2.6)
"Anti-SM"	99.6 $\pm$ 1.4 $\pm$ 1.8	($\pm$ 2.3)	99.7 $\pm$ 1.2 $\pm$ 1.7	($\pm$ 2.1)

Table 7.5: *Measured unpolarized cross section σ_0 by a combination of cross section measurements with polarized beams for an integrated luminosity of $\mathcal{L} = 500$ fb^{-1}.*

7.1.2 Mass determination

The ISR photon energy spectrum of the process $e^+e^- \rightarrow \chi\chi\gamma$ exhibits an upper threshold energy E_{thr} given by the beam energy E_b and the WIMP mass M_χ by

$$E_{thr} = \frac{E_b^2 - M_\chi^2}{E_b}. \tag{7.13}$$

In principle, the WIMP candidate mass can be determined from this threshold. Since the number of signal events in this region is very small compared to the large number of background events and because of the small simulated luminosity, the current analysis is not sensitive to the threshold. However, for a given total cross section and partial wave, the shape of the photon spectrum at lower energies is determined by the WIMP mass via the last term in the production cross section in Equation 5.8, page 37. Hence, the mass can be extracted from the data spectrum by a χ^2 comparison between the data and template spectra of the same total production cross section but different masses.
Throughout this section the total WIMP production cross section is fixed to 100 fb which can be measured with an accuracy of a few percent, see the previous Section. The mass measurement is performed for the polarization configurations $(P_{e^-}; P_{e^+}) = (0.8; 0.0)$, $(P_{e^-}; P_{e^+}) = (0.8; -0.3)$ and $(P_{e^-}; P_{e^+}) = (0.8; -0.6)$. The WIMP candidates in the data are assumed to be p-wave annihilators. By testing template spectra for s- and p-wave WIMPs against the data spectrum, the mass can be determined, and an indication of the partial wave is obtained.

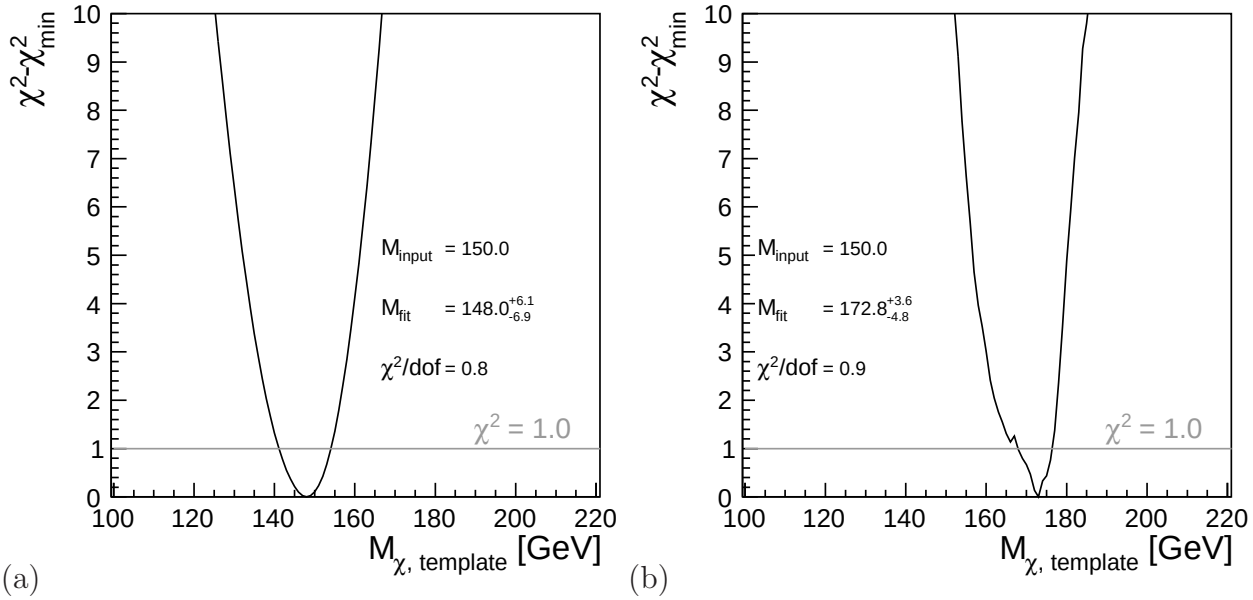

Figure 7.5: χ^2 *comparison of a p-wave 150 GeV data mass in the* **"Equal"** *scenario with (a) the correct p-wave expectation and (b) the wrong s-wave expectation for a simulated luminosity of* $\mathcal{L} = 50$ fb^{-1} *and a beam polarization of* $(P_{e^-}; P_{e^+}) = (0.8; -0.3)$.

Figure 7.5 shows the χ^2 comparison of the data for a p-wave annihilator, 150 GeV WIMP with different partial wave templates in the **"Equal"** scenario for a simulated luminosity of

$\mathcal{L} = 50$ fb^{-1}. The beam polarization is set to $(P_{e^-}; P_{e^+}) = (0.8/-0.3)$. In Fig 7.5(a) the data mass is compared to the correct p-wave templates, while in (b) the wrong s-wave spectrum is assumed for the templates. In both cases the χ^2/ndf is close to one, indicating statistical compatibility. With the correct p-wave assumption the fit returns a mass of $148.0^{+6.1}_{-6.9}$ GeV, while the s-wave assumption gives $172.8^{+3.6}_{-4.8}$ GeV. This difference in measured masses between the s- and p-wave assumptions is observed over the full analyzed mass range from 120 GeV to 240 GeV. Figure 7.6 shows the fit mass versus the true mass for an integrated luminosity of

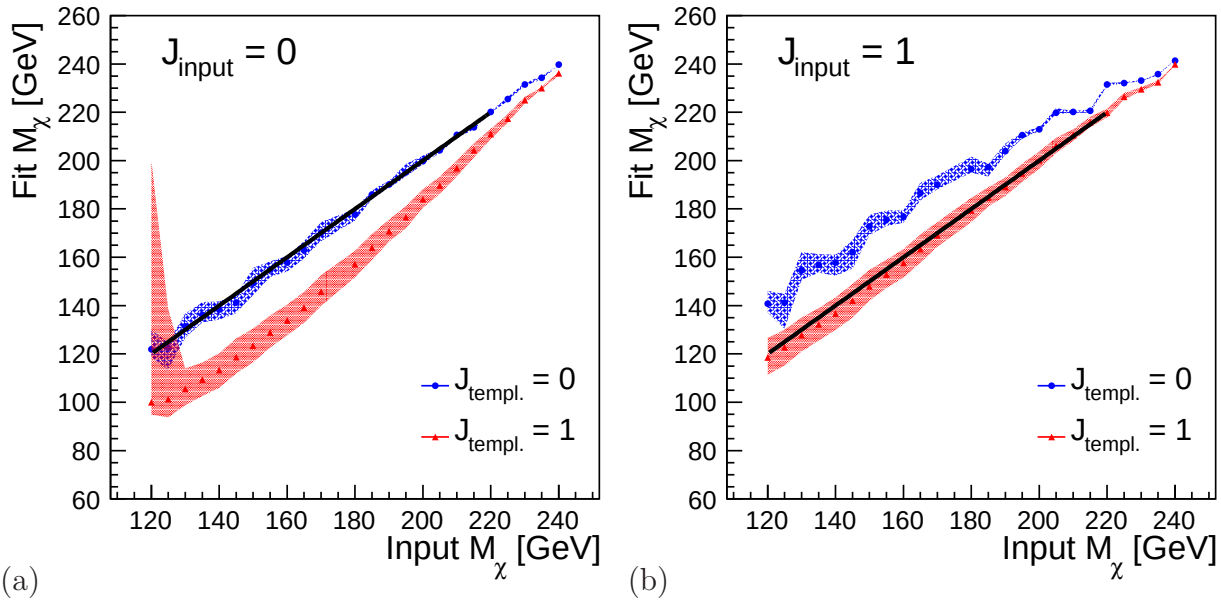

(a) (b)

Figure 7.6: *Fit mass versus true mass in the* **"Equal"** *scenario for an integrated luminosity of* $\mathcal{L} = 50$ fb^{-1} *and* $(P_{e^-}; P_{e^+}) = (0.8/-0.3)$. *The data candidate is assumed to be (a) an s-wave WIMP, and (b) a p-wave WIMP. In both cases the data spectra are tested against s- and p-wave templates. For the wrong assumption a systematic shift of the fit mass is observed.*

$\mathcal{L} = 50$ fb^{-1} in the same coupling and beam polarization scenario. In Figure 7.6(a) the data WIMP is an s-wave annihilator ($J_0 = 0$) and is tested against s-wave and p-wave template spectra. Within the statistical uncertainty the mass is recovered for the correct annihilator type WIMP. For the wrong p-wave annihilator assumption, the fit mass is systematically lower than the true mass. The reverse case of a p-wave data WIMP is displayed in Figure 7.6(b), where the true mass is recovered for the correct assumption, but the wrong assumption of an s-wave WIMP leads to systematically higher measured masses.

The reason for this behavior can be traced back to the low simulated statistics. The kinematic threshold energy lies in a regime with low background statistics and therefore relatively high fluctuations in which the small signal offset vanishes. The template comparison is effectively sensitive to the crossing point of the signal spectra of s-wave and p-wave WIMPs. Figure 7.7(a) shows the pure signal spectra for s- and p-wave WIMPs, normalized to a total cross section of 100 fb. The spectra exhibit a crossing point at approximately 50 GeV. While the signal statistics at energies higher than 50 GeV differ in only a few counts, the difference below the crossing is considerably higher. Since the difference at high energies is not resolvable in the background fluctuations, the fit converges for the best concordance of the template

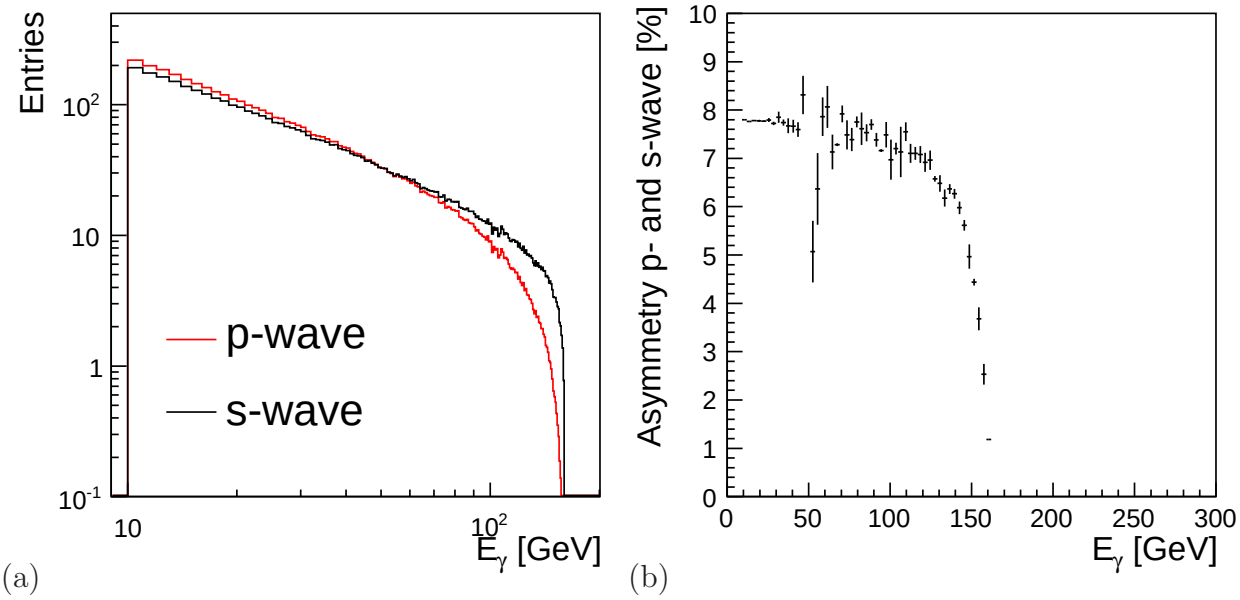

(a) (b)

Figure 7.7: *(a) s- and p-wave spectra for a 100 GeV WIMP candidate, normalized to 100 fb. The spectra exhibit a crossing point at approximately 50 GeV. (b) Asymmetry of the spectra relative to the crossing point, i.e. the asymmetry above and below 50 GeV is roughly* 8%.

and data spectrum at low energies. For a fixed total cross section this means for the wrong s-wave assumption that higher masses are favored, since these require higher statistics at low energies. With higher data statistics, the signal threshold should become more prominent, and the measured WIMP masses for the s- and p-wave assumptions should converge.
The masses obtained by the fit with the s-wave templates are comparably more unstable than the fit values of the p-wave templates, regardless whether the data WIMP exhibits s-wave or p-wave behavior. Like the shift in the measured masses, the characteristic photon energy distribution of signal events for s-wave WIMPs is responsible for this, where a considerable amount of signal events is found at higher photon energies. These signal events are spread over a large energy interval, where they are obscured by the strong statistical fluctuations of the low simulated background statistics.
Apart from the shift in fitted masses between both assumptions the value of χ^2/ndf of the corresponding fits indicates the correct partial wave quantum number of the production process. In Figure 7.8, the χ^2/ndf of the best fit are displayed in the **"Helicity"** scenario. In the first column, the data candidate is an s-wave WIMP, in the second column, the data exhibits a p-wave behavior. The results in the first row are for unpolarized beams, the second and third row are for $(P_{e^-}; P_{e^+}) = (0.8; -0.3)$ and $(P_{e^-}; P_{e^+}) = (0.8; -0.6)$, respectively. In all cases, the correct partial wave assumption $\mathrm{J}_{templ.}$ has a lower χ^2/ndf over large ranges in WIMP masses. For high WIMP masses, the signal spectrum is compressed in only a few bins at low photon energies and becomes indistinguishable in the χ^2 comparison for a fixed cross section. For unpolarized beams (Figures 7.8(a) and (b)), the χ^2/ndf are fluctuating strongly within 2% or less, making the discrimination difficult. For polarized beams however, the relative difference in terms of the χ^2/ndf values is stable at about 2% or better, and the partial waves for masses up to 210 GeV are distinguishable.

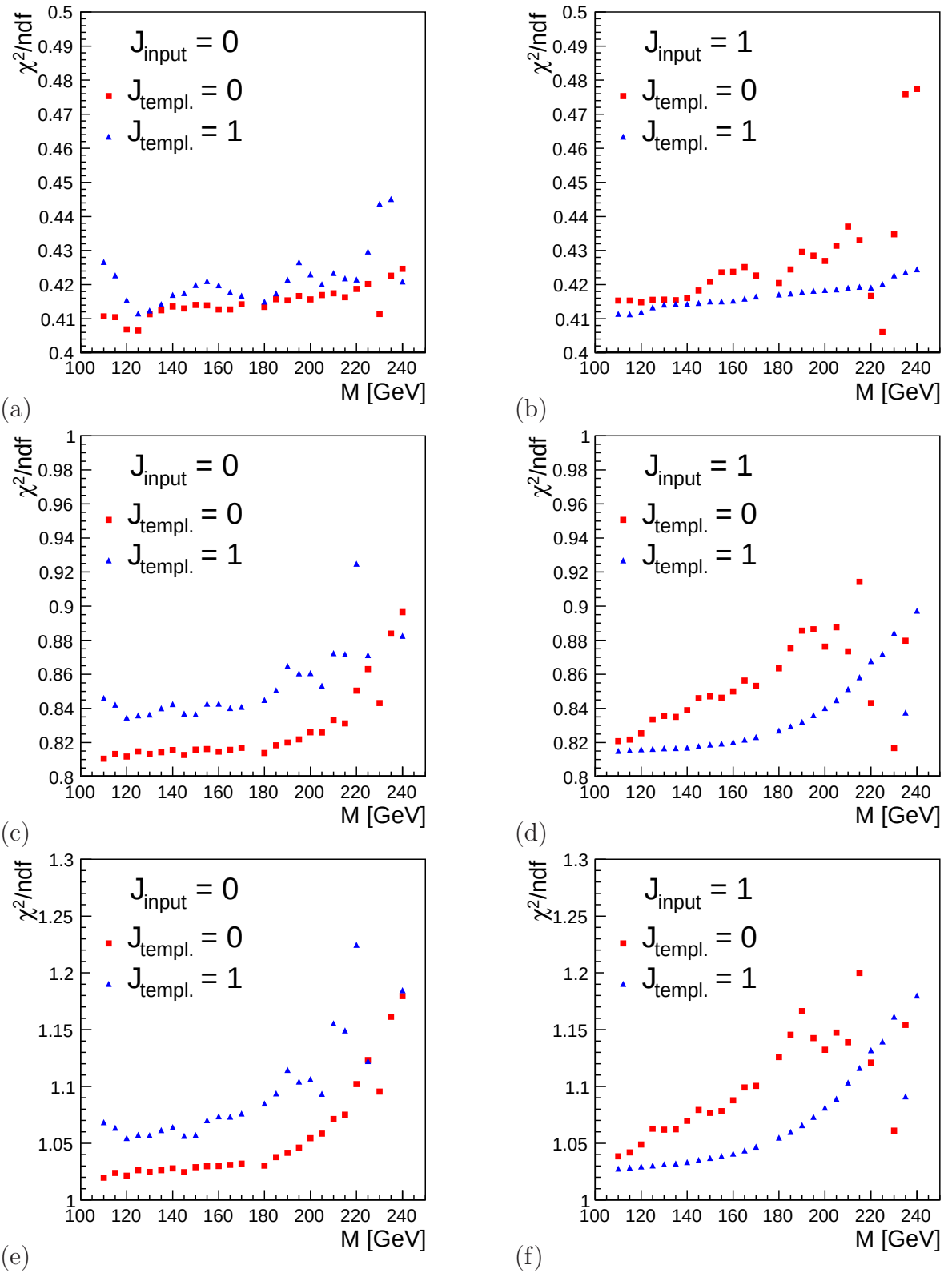

Figure 7.8: *Values of χ^2/ndf for s- and p-wave fits as a function of the WIMP mass. In the first column, the data candidate is an s-wave WIMP, in the second column, the data exhibits a p-wave behavior. The results in the first row are for unpolarized beams, the second and third row are for $(P_{e^-}; P_{e^+}) = (0.8; -0.3)$ and $(P_{e^-}; P_{e^+}) = (0.8; -0.6)$, respectively.*

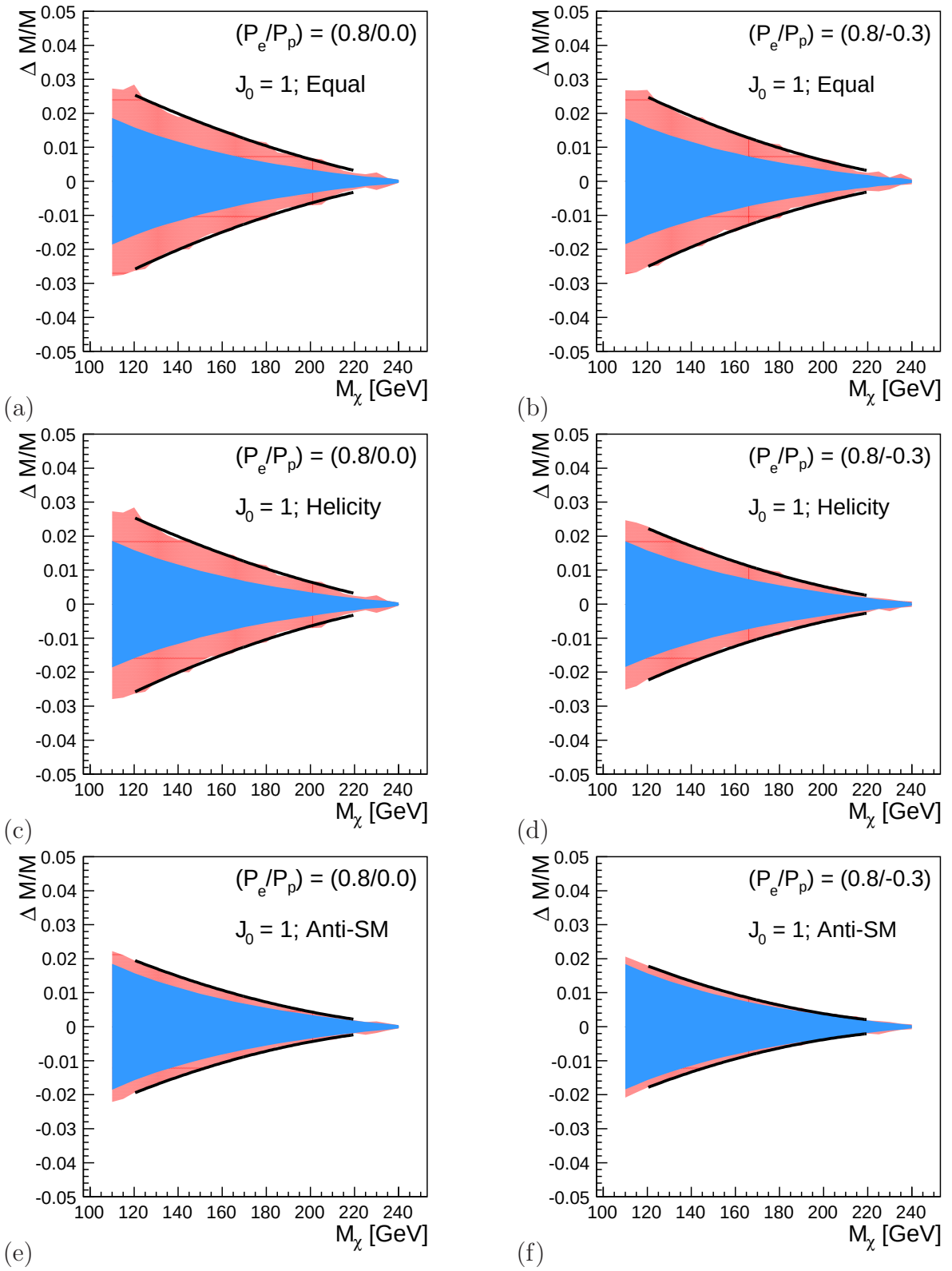

Figure 7.9: *Relative error $\Delta M/M$ as function of the WIMP mass for $(P_{e^-}; P_{e^+}) = (0.8/0.0)$ (left column) and $(P_{e^-}; P_{e^+}) = (0.8/-0.3)$ (right column) and coupling scenarios* **"Equal"** *((a) and (b)),* **"Helicity"** *((c) and (d)) and* **"Anti-SM"** *((e) and (f)).*

Mass [GeV]	WIMP mass: $\pm$stat. $\pm\delta E$ (sys.) $\pm\delta\mathcal{L}$ (sys.) (total) [GeV] $(P_{e^-};\, P_{e^+}) = (0.8;\, 0.0)$	$(P_{e^-};\, P_{e^+}) = (0.8;\, -0.3)$	$(P_{e^-};\, P_{e^+}) = (0.8;\, -0.6)$
"Equal" scenario			
120	$2.67 \pm 0.07 \pm 1.91$ (3.29)	$2.48 \pm 0.07 \pm 1.90$ (3.12)	$2.24 \pm 0.07 \pm 1.90$ (2.93)
150	$2.11 \pm 0.05 \pm 1.47$ (2.57)	$1.98 \pm 0.05 \pm 1.46$ (2.46)	$1.83 \pm 0.05 \pm 1.45$ (2.33)
180	$1.78 \pm 0.03 \pm 1.00$ (2.04)	$1.69 \pm 0.03 \pm 1.00$ (1.96)	$1.57 \pm 0.03 \pm 1.00$ (1.86)
210	$0.78 \pm 0.02 \pm 0.54$ (0.95)	$0.79 \pm 0.02 \pm 0.54$ (0.96)	$0.74 \pm 0.02 \pm 0.54$ (0.91)
"Helicity" scenario			
120	$2.67 \pm 0.07 \pm 1.91$ (3.29)	$1.92 \pm 0.07 \pm 1.89$ (2.70)	$1.53 \pm 0.07 \pm 1.89$ (2.43)
150	$2.11 \pm 0.05 \pm 1.47$ (2.57)	$1.62 \pm 0.05 \pm 1.46$ (2.18)	$1.23 \pm 0.05 \pm 1.45$ (1.90)
180	$1.78 \pm 0.03 \pm 1.00$ (2.04)	$1.36 \pm 0.03 \pm 1.00$ (1.69)	$0.94 \pm 0.03 \pm 1.00$ (1.37)
210	$0.78 \pm 0.02 \pm 0.54$ (0.95)	$0.67 \pm 0.02 \pm 0.54$ (0.87)	$0.59 \pm 0.02 \pm 0.54$ (0.80)
"Anti-SM" scenario			
120	$1.37 \pm 0.07 \pm 1.89$ (2.34)	$1.04 \pm 0.07 \pm 1.88$ (2.15)	$0.82 \pm 0.07 \pm 1.88$ (2.05)
150	$1.16 \pm 0.05 \pm 1.45$ (1.86)	$0.81 \pm 0.05 \pm 1.45$ (1.66)	$0.72 \pm 0.05 \pm 1.44$ (1.61)
180	$0.89 \pm 0.03 \pm 1.00$ (1.34)	$0.66 \pm 0.03 \pm 1.00$ (1.19)	$0.37 \pm 0.03 \pm 1.00$ (1.06)
210	$0.57 \pm 0.02 \pm 0.54$ (0.79)	$0.16 \pm 0.02 \pm 0.55$ (0.59)	$0.09 \pm 0.02 \pm 0.55$ (0.59)

Table 7.6: *Statistical and systematic uncertainties on the measured WIMP masses for an integrated luminosity of* $\mathcal{L} = 500$ fb^{-1} *in the three coupling scenarios* **"Equal"**, **"Helicity"** *and* **"Anti-SM"** *for three different polarization configurations.*

Therefore, for the determination of the WIMP mass, the correct partial wave can be assumed. For a quantitative measurement the relative errors on the mass determination are shown in Figure 7.9 and summarized in Table 7.7 for an integrated luminosity of $\mathcal{L} = 500$ fb^{-1}. For each WIMP coupling structure and for two different beam polarizations the relative error is plotted versus the WIMP candidate mass. The inner error bands (blue) show the systematic limit of the measurement, the outer contours give the total uncertainty of systematic and statistical errors. To ensure stability of the results and errors, the error band is approximated with a second order polynomial to the upper and lower bounds. The errors listed in Tables 7.6 and 7.7 are estimated from the fitted polynomial. In general, all WIMP masses are recovered to the percent level. For high masses, a measurement precision at the sub-percent level is achieved. For fully polarized beams, the mass measurement becomes systematically limited by the uncertainty on the luminosity spectrum, especially in the **"Anti-SM"** coupling scenario.

Systematic uncertainties

The dominant sources of the systematic errors contributing to the mass measurement uncertainty are the measurement of the beam energy scale and the uncertainty of the luminosity spectrum. The beam energy scale uncertainty is estimated from the photon spectrum of the radiative return in Figure 6.16. The peak position of the Z-return is determined by

Mass [GeV]	WIMP mass relative error: $\Delta M/M$ [%] (0.8; 0.0)	(0.8; −0.3)	(0.8; −0.6)
"Equal" scenario			
120	2.5	2.5	2.4
150	1.7	1.7	1.6
180	1.0	1.0	0.9
210	0.5	0.5	0.4
"Helicity" scenario			
120	2.5	2.2	2.0
150	1.7	1.5	1.3
180	1.0	0.9	0.7
210	0.5	0.4	0.3
"Anti-SM" scenario			
120	2.0	1.8	1.7
150	1.3	1.1	1.1
180	0.7	0.6	0.6
210	0.3	0.3	0.3

Table 7.7: *WIMP mass relative errors $\Delta M/M$ for three coupling scenarios and three different beam polarizations, listed for four selected WIMP masses from 120 GeV to 210 GeV.*

the luminosity weighted beam energy and the calibration of the calorimetric system of the ILD detector. Since the detector calibration scale can be independently determined with Z-decays into electrons, $Z \to e^+e^-$, the radiative Z-return can be used to directly calibrate the luminosity weighted beam energy. The systematic uncertainty on the beam energy scale is taken from the fitted mean of the Z-return peak to $\delta E_s = 0.08$ GeV. The same relative uncertainty is assumed for the full energy range.
The WIMP mass can be determined from the spectrum endpoint by:

$$M_\chi^2 = E_{beam}^2 - E_{beam}E_{thr}, \tag{7.14}$$

compare Fig. 5.3(a) on page 38. The energy scale uncertainty translates into a systematic uncertainty on the mass measurement as:

$$\delta M_{\chi,sys} = \frac{E_{beam}}{2M} \times \delta E_s. \tag{7.15}$$

The width of the Z-return is the result of the intrinsic Z-lineshape, folded with the detector energy resolution and the beam energy spectrum. While the Z-lineshape is theoretically extremely well known, the detector energy resolution will be measured in the experiment with $Z \to e^+e^-$ decays. Given real data, this knowledge allows for a cross check of how well the beam energy spread is known and simulated in the Monte Carlo data. The statistical uncertainty on the width of the Z-return is the figure of merit for this comparison.

For a quantitative statement on the influence of the luminosity spectrum on the mass measurement, the WIMP signal spectra for two different sets of beam parameters, the RDR and SB-2009 (cf. Sec. 3.2.1 on page 19), are compared. The effect of the SB-2009 parameter set on

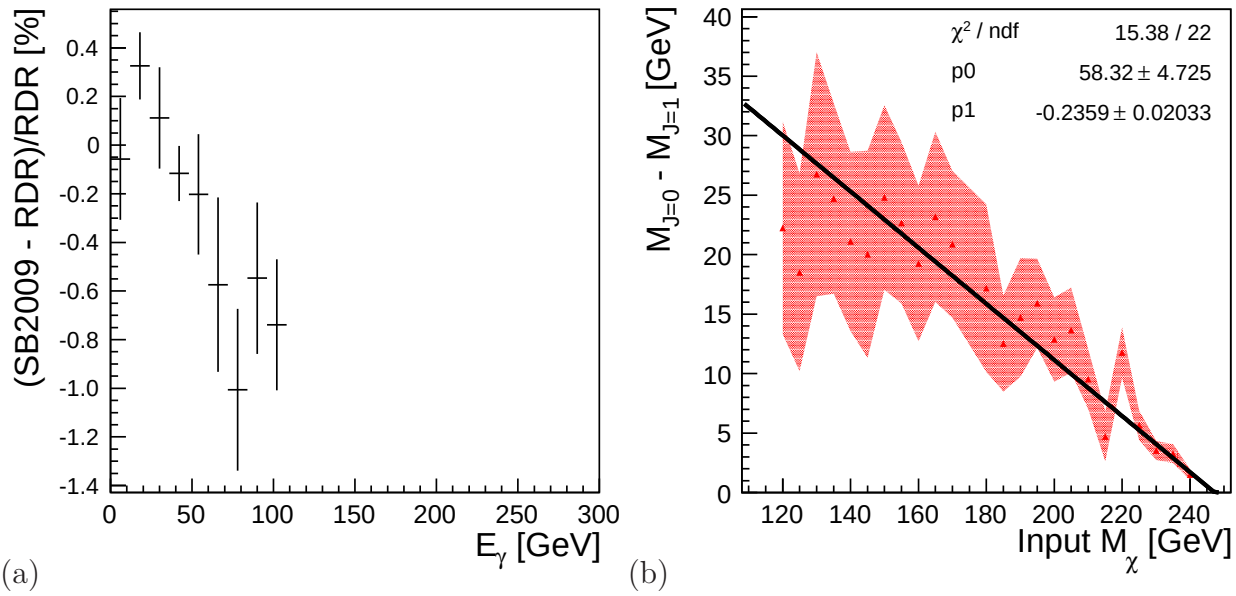

(a) (b)

Figure 7.10: *(a) Relative differences between the WIMP spectra for the SB-2009 and RDR beam parameters. (b) Absolute difference between the mass measurements with the correct and the wrong partial wave assumption as function of WIMP mass.*

the signal spectrum is comparable to the shape difference of s- and p-wave spectra, induced by migration of high energetic photon events to lower energies. Figure 7.10(a) shows the relative deviation of the signal spectra for a 150 GeV WIMP between the SB-2009 and RDR beam parameter sets in the relevant photon energy region from 10 to 100 GeV. The relative difference is positive with a conservative value of $\sim 0.5\%$ at low energies and negative with one percent at ≈ 100 GeV. Comparing the maximal deviation of $\sim 0.5\%$ percent in the low energy region to the signal asymmetry between the s- and p-wave spectra in Figure 7.7(b) on page 85, the uncertainty in the beam energy spectrum accounts for roughly $\frac{1}{16}$ of the difference between s- and p-wave WIMP spectra. In Figure 7.10(b), the difference in the measured masses for the s- and p-wave assumption is shown as function of the true mass, compare to Figures 7.6. Assuming that this difference is determined by the spectrum asymmetry between s- and p-wave production, the luminosity spectrum contributes $\frac{1}{16}$ of the mass difference to the systematic errors in the mass measurement.

Because of the limited simulated statistics available, the measurement of the candidate mass relies on the determination of the shape of the photon spectrum at lower energies, where uncertainties on the background prediction are polarization dependent. With a data set equivalent to $\mathcal{L} = 500$ fb^{-1}, the mass measurement would become increasingly sensitive to the photon spectrum endpoint. The endpoint position is independent of the beam polarization, and only systematic uncertainties of the beam energy scale and the detector energy resolution for electromagnetic particles are relevant. Therefore, the systematic uncertainties

on the WIMP mass measurement quoted in Table 7.6 do not include the uncertainty on the polarization measurement.

7.2 SPS1a' scenario

The methods for the determination of the cross section, coupling structure and particle mass used in the model independent analysis of Section 7.1 can also be used to extract the parameters of the lightest neutralino of the SPS1a' parameter point. The neutralino in the SPS1a' cMSSM point is predominantly bino and thus couples mainly to right-handed electrons and left-handed positrons. It has a mass of 97.7 GeV. The production cross section in the signal phase space for the process $e^+e^- \to \tilde{\chi}_1^0\tilde{\chi}_1^0\gamma$ is $\sigma = 134.261$ fb for unpolarized beams. The results are presented in the next Section.

7.2.1 Coupling structure and mass determination

The neutralino production cross section is by 33% larger than the assumed cross section for the model independent WIMP production. Almost all measurements in the model independent WIMP analysis were already dominated by systematics. Hence, the parameter determination for the neutralino LSP of SPS1a' will be systematically dominated throughout, due to the larger production cross section. The results of the coupling structure determination are shown in Figure 7.11, and listed in Table 7.8 for polarization configurations of $(|P_{e^-}|; |P_{e^+}|) = (0.8; 0.3)$ and $(|P_{e^-}|; |P_{e^+}|) = (0.8; 0.6)$. All errors are calculated analogously

SPS1a′ parameter point: Polarized cross sections $\sigma_{R,L}/\sigma_0 \pm$ total [fb]	$(\lvert P_{e^-}\rvert; \lvert P_{e^+}\rvert) = (0.8; 0.3)$	$(\lvert P_{e^-}\rvert; \lvert P_{e^+}\rvert) = (0.8; 0.6)$
σ_{RL}/σ_0	3.89 ± 0.21 (0.15)	3.89 ± 0.10 (0.09)
σ_{RR}/σ_0	0.00 ± 0.26 (0.18)	0.00 ± 0.18 (0.11)
σ_{LL}/σ_0	0.00 ± 0.28 (0.22)	0.00 ± 0.17 (0.12)
σ_{LR}/σ_0	0.11 ± 0.29 (0.19)	0.11 ± 0.22 (0.12)

Table 7.8: *Fully polarized cross sections $\sigma_{\{R,L\}}$ in the SPS1a′ scenario for two different absolute positron polarizations. The squared sum of statistical and systematic errors is given as error; bracketed values correspond to an improved polarization measurement ($\delta P/P = 0.1\%$).*

to those in the WIMP analyses. The numbers in brackets give the error on the fully polarized cross sections for an increased polarization measurement precision of $\delta P/P = 0.1\%$. For a polarization configuration of $(|P_{e^-}|; |P_{e^+}|) = (0.8; 0.3)$, an integrated luminosity of $\mathcal{L} = 500$ fb^{-1} and a polarization measurement precision of $\delta P/P = 0.25\%$, the cross section ratio σ_{RL}/σ_0 can be measured to a relative precision of about 5%, or, correspondingly, σ_{RL} is determined to ≈ 29 fb. For a more precise polarization measurement of $\delta P/P = 0.1\%$, the precision on the measurement of σ_{RL} is increased by 30%. A positron polarization of $|P_{e^+}| = 0.6$ yields a measurement precision on σ_{RL} of 13 fb and 12 fb for $\delta P/P = 0.25\%$ and for $\delta P/P = 0.1\%$, respectively.
The individual measurements with polarized beams are combined to calculate the unpolarized cross section σ_0 to $\sigma_0 = 132.1 \pm 6.0$ fb for a positron polarization of $|P_{e^+}| = 0.3$ and to $\sigma_0 = 131.2 \pm 5.0$ fb for $|P_{e^+}| = 0.6$, respectively. An additional increase in the precision of the cross section measurement is obtained by increasing the precision of the polarization measurement to $\delta P/P = 0.1\%$, see Table 7.9.

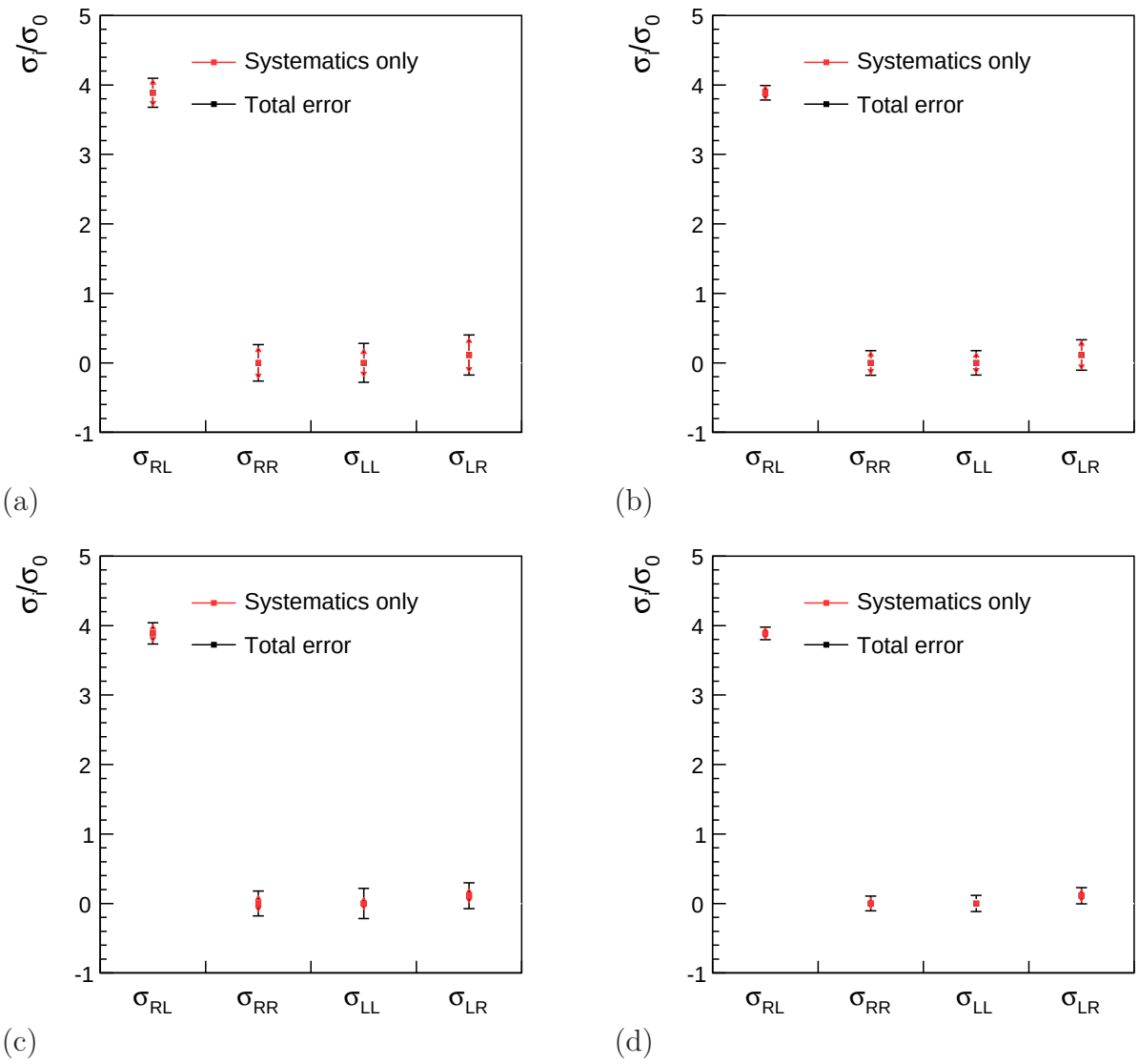

Figure 7.11: *Polarized cross sections σ_{ij}/σ_0 for the SPS1a' Neutralino. In the upper row the polarization precision is assumed to be $\delta P/P = 0.25\%$, while for the lower row a precision of $\delta P/P = 0.1\%$ is assumed. In the first column (a,c), the polarization configuration is $|P_{e^-}| = 0.8; |P_{e^+}| = 0.3$, in the second column (b,d), it is $|P_{e^-}| = 0.8; |P_{e^+}| = 0.6$.*

The results of the mass measurement are listed in Table 7.10 for a luminosity of $\mathcal{L} = 500$ fb^{-1} and beam polarization configurations of $(P_{e^-}; P_{e^+}) = (0.8; 0.0)$, $(0.8; -0.3)$ and $(0.8; -0.6)$. The statistical errors are below the stepwidth of the signal spectrum templates used in the χ^2 comparison, as shown in Figure 7.12. The total error is completely dominated by the uncertainty on the luminosity spectrum, resulting in an minimal error on the mass of 2.3 GeV. As pointed out in Section 5.1.3 (cf. page 39) in CP-invariant supersymmetry the process $e^+e^- \to \tilde{\chi}_i^0\tilde{\chi}_i^0$ proceeds via p-wave production. Thus, determining the threshold behavior, provides an indication of possible CP-violation.
With reference to the second column of Figure 7.8 on page 86, an extrapolation to 97 GeV yields almost identical values of χ^2/ndf for the s- and p-wave hypothesis in comparison to the p-wave data spectrum. If, however, the neutralino production exhibited s-wave behavior,

SPS1a′ param. point: $\delta P/P$	Unpolarized cross sections $\sigma_0 \pm$ stat $\pm$ sys $(\pm$total$)$ [fb] $(\lvert P_{e^-}\rvert; \lvert P_{e^+}\rvert) = (0.8; 0.3)$	$(\lvert P_{e^-}\rvert; \lvert P_{e^+}\rvert) = (0.8; 0.6)$
0.25 %	132.1 ± 1.8 ± 5.7 (±6.0)	131.2 ± 1.3 ± 4.8 (±5.0)
0.10 %	131.5 ± 1.8 ± 3.9 (±4.3)	131.2 ± 1.5 ± 4.1 (±4.4)

Table 7.9: *Measured unpolarized cross section σ_0 by a combination of cross section measurements with polarized beams for an integrated luminosity of $\mathcal{L} = 500$ fb^{-1}.*

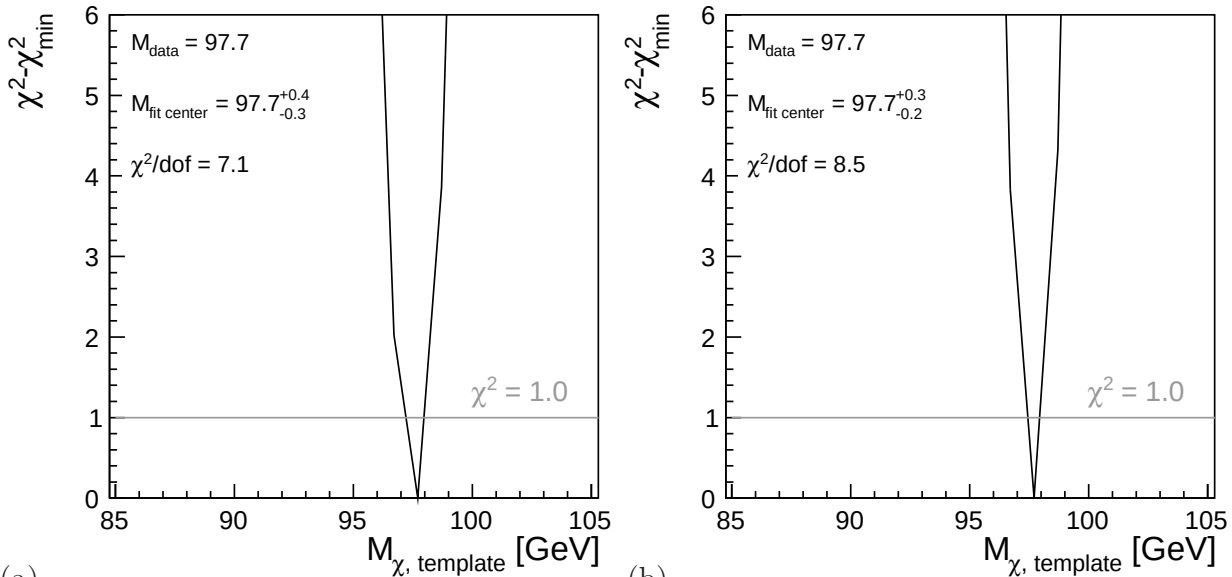

Figure 7.12: *χ^2 comparison of the mass measurement for the SPS1a' neutralino for an integrated luminosity of $\mathcal{L} = 500$ fb^{-1} and a polarization configuration of (a) $P_{e^-} = 0.8; P_{e^+} = -0.3$ and (b) $P_{e^-} = 0.8; P_{e^+} = -0.6$.*

$M_{\tilde{\chi}_1^0}$ [GeV]	$\pm$stat. $\pm$sys. $(\delta E \pm \delta\mathcal{L})$ (total) [GeV]	$(P_{e^-}; P_{e^+})$
97.7 (input)	0.68 ± 0.09 ± 2.20 (2.31)	(0.8; 0.0)
97.7 (input)	0.38 ± 0.09 ± 2.20 (2.24)	(0.8; −0.3)
97.7 (input)	0.25 ± 0.09 ± 2.20 (2.22)	(0.8; −0.6)

Table 7.10: *Neutralino mass determined from a template comparison for an integrated luminosity of $\mathcal{L} = 500$ fb^{-1} and three different beam polarizations. The neutralino data mass is assumed as $M_{\tilde{\chi}_1^0} = 97.7$ GeV.*

a clear separation between the two hypothesis in terms of χ^2/ndf is expected, as seen in the first column of Figure 7.8. Therefore, the spread in χ^2/ndf values could be used to determine the dominant partial wave in the production process.
The simulated data luminosity for this analysis is only about $\mathcal{L} = 50$ fb^{-1}. Increasing the event statistics is expected to provide a higher discrimination power also for p-wave production.

Part II

Cherenkov Detector Prototype

Chapter 8

Polarimetry

An integral aspect of the ILC is the possibility of using polarized beams in collisions. The longitudinal beam polarization can be exploited in several physics channels to increase the signal to background ratio [46] and is beneficial to uncover the spin structure of possible new physics. For ILC, the envisioned systematic precision of $\delta P/P \leq 0.25\%$ on the polarisation measurement is at least by a factor of two better than the previous best polarization measurement of the SLC polarimeter [11, 92]. This goal demands improvements in various areas of the overall polarization measurement and detectors.
The longitudinal polarization P of an electron beam is defined as

$$P = \frac{w_\uparrow - w_\downarrow}{w_\uparrow + w_\downarrow}, \tag{8.1}$$

where $w_\uparrow$ and $w_\downarrow$ are the probabilities of an electron having its spin oriented parallel or anti-parallel to the direction of motion. A measurement of $P = 1$ means that all particle spins are parallel to the beam axis.
For the final polarization measurement at ILC, several techniques will be employed to measure the beam polarization to an unprecedented precision. While the absolute degree of the polarization on long time scales will be determined by analyses of the collision data themselves [49], short time corrections are required for the envisioned precision. These corrections are measured with a system of dedicated polarimeters up- and downstream of the interaction region (IR). For these high precision measurements, Compton polarimeters will be used. In addition to the main polarimeters, supporting polarization measurements will be made close to the electron source with a Mott polarimeter in a separate diagnostics line. No low energy polarimetry for the positrons is forseen, but the possibility of a Bhabha polarimeter after the positron pre-accelerator is being studied [48].
In the Compton polarimeters, the individual electron bunches are shot at with a laser under a small crossing angle. The back-scattered electrons are separated from the main beamline and detected with a segmented Cherenkov detector.
The physics behind Compton polarimetry is explained in the following section, while the polarimeter system is described in more detail in Section 9.1.
In 2008 a Cherenkov detector prototype for ILC polarimetry was designed and built at DESY and tested with electron beams at DESY II in Hamburg and at the ELSA accelerator in Bonn. Construction and simulation of this prototype and a discussion of the results from the testbeam campaigns are the subject of Chapters 10 and 11.

8.1 Compton polarimetry basics

Compton polarimetry for determination of the longitudinal and transverse polarization of electron beams has been suggested more than 30 years ago [93] and has been employed in the HERA storage ring at DESY [94] and at the SLC linear collider [92]. At HERA a fractional systematic uncertainty on the longitudinal polarization of $\delta P/P = 1.6\%$ has been achieved [94], while the systematic uncertainty at SLC was determined to 0.67% [92].
For the polarization measurement both the backscattered photons and electrons can be used, since the kinematics of the scattering process $e^-\gamma \to e^-\gamma$ is completely determined if the four-vector of only one of the final state particles is known. However, to achieve a similar statistical performance at ILC as at HERA and SLC, the polarimeters have to operate in a regime of multiple Compton interactions per electron bunch [95]. This makes photon detection as means of a polarization measurement unsuitable, because the individual events cannot be disentangled. To maximize the number of Compton interactions, a high power laser is required.

8.1.1 Compton scattering

The cross section for unpolarized compton scattering was derived in 1929 by O. Klein and Y. Nishina [96] as one of the first results of the newly developed QED. The cross section can be expressed in the dimensionless variable

$$y = 1 - \frac{E}{E_0}, \tag{8.2}$$

with E_0 and E being the respective energies of the electron before and after the scattering. The cross section reads:

$$\left(\frac{d\sigma}{dy}\right)_{unpol} = \frac{2\pi r_0}{x}\left[\frac{1}{1-y} + 1 - y - 4r(1-r)\right], \tag{8.3}$$

where r_0 is the classical electron radius and $r = \frac{y}{x(1-y)}$ with

$$x = \frac{4E_0\omega_0}{m^2}\cos\left(\theta_0/2\right)^2 \simeq \frac{4E_0\omega_0}{m^2}. \tag{8.4}$$

The parameters in the dimensionless variable x are:

- ω_0, the initial photon energy,
- m, the electron rest mass,
- θ_0, the crossing angle between electron and photon.

Note that $\cos\left(\theta_0/2\right)^2 \simeq 1$ for the ILC polarimeter with a laser crossing angle of $\theta_0 \approx 10$ mrad. For the spin-dependent cross section, Equation 8.3 has to be modified [95] to yield

$$\frac{d\sigma}{dy} = \frac{2\pi r_0}{x}\left[\frac{1}{1-y} + 1 - y - 4r(1-r) + P\lambda(1-2r)(2-y)\right]. \tag{8.5}$$

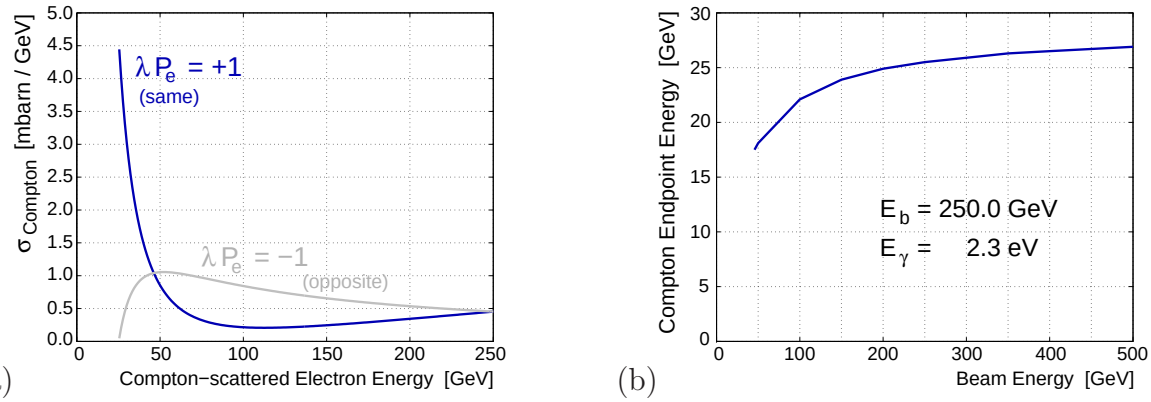

Figure 8.1: *(a): Differential Compton cross section versus scattered electron energy for same (blue / dark gray) and opposite (light gray) helicity configuration of photon and electron. The beam energy is 250 GeV and the photon energy is 2.3 eV. (b) Compton edge energy as function of the beam energy [47].*

The beam polarization enters this equation as the parameter P. The laser helicity is given by the variable λ.
In Figure 8.1(a) the differential Compton cross section as a function of the scattered electron energy is plotted for same (blue / dark gray) and opposite (light gray) helicity configuration of photon and electron, for a beam energy of 250 GeV, and a photon energy is 2.3 eV [47]. The cross sections show a clear asymmetry which is strongest near the Compton edge with an energy of the backscattered electrons of approximately 25 GeV. The large asymmetry can be used to extract the beam polarization, when the laser helicity is known. Figure 8.1(b) illustrates the slight dependence of the Compton edge energy on the initial beam energy. The dependence is rather small over the ILC beam energy range of 45–250 GeV with a stronger dependence at low electron energies. By factoring out the unpolarized cross section Equation 8.3, Equation 8.5 can be rewritten as

$$\frac{d\sigma}{dy} = \left(\frac{d\sigma}{dy}\right)_{unpol} \left[1 + P\lambda \cdot \mathcal{AP}\right], \tag{8.6}$$

introducing the Analyzing Power $\mathcal{AP}$ defined as

$$\mathcal{AP} = \left.\frac{d\sigma^+ - d\sigma^-}{d\sigma^+ + d\sigma^-}\right|_{P=1}. \tag{8.7}$$

Here the (+) and (-) denote opposite and like sign helicity configurations of beam particle and laser photon, i.e. $P\lambda = \pm 1$.
The experimental quantity is the rate asymmetry

$$A = \frac{N^+ - N^-}{N^+ + N^-}. \tag{8.8}$$

Here $N^{\pm}$ is the number of detected electrons for opposite and like sign helicity configurations of beam and laser. The Analyzing Power is the special case of the Asymmetry for 100% positive electron polarization. Using Equation 8.6 the rate asymmetry A is related to the Analyzing Power via

$$A = P\lambda \cdot \mathcal{AP}. \tag{8.9}$$

or, given an ideal laser polarization of $|\lambda| = 1$,

$$P = \frac{A}{\mathcal{AP}}. \tag{8.10}$$

The asymmetry and analyzing power change sign at the crossover point with

$$E_c = E_0 \frac{1}{1 + x/2}. \tag{8.11}$$

The location of the crossing point is independent from both the electron and laser helicity.

8.1.2 Principle of polarization measurement

To extract the beam polarization, the numbers $N^{\pm}$ of scattered electrons in certain energy intervals i are sampled and the rate asymmetries A_i calculated. The asymmetries A_i are then divided by the analyzing power integrated over the corresponding energy interval. Because the measured polarization is inversely proportional to the analyzing power $\mathcal{AP}$, systematic uncertainties on P are minimal for energy intervals with maximal values of $\mathcal{AP}$. When averaging over several energy intervals, those with large $\mathcal{AP}$ values obtain the largest statistical weights. As shown in Figure 8.1(a), the maximal analyzing power is expected near the Compton edge of the scattered electron energies. The statistical uncertainty on the Polarization P is determined from error propagation with respect to $\Delta N^{\pm} = \sqrt{N^{\pm}}$. The relative error is:

$$\frac{\Delta P}{P} = \frac{1}{\sqrt{\sum_i w_i (N_i^+ - N_i^-)}}. \tag{8.12}$$

The sum extends over all energy intervals of interest. The statistical weights are defined in reference [95]:

$$w_i = \frac{1}{1 + P^{-2} \mathcal{AP}_i^{-2}}. \tag{8.13}$$

Chapter 9

ILC polarimetry

In this chapter, the system of Compton polarimeters for the ILC is described. Compton scattering and the detection of Cherenkov light for polarization measurement at ILC has been chosen for the following reasons [47]:

- The Compton scattering process can be calculated to a high precision in QED. Radiative corrections amount to less than 0.1%.
- Compton polarimetry leaves the main beam undisturbed. The beam polarization can be measured parasitic during physics data taking in collision mode.
- Background rates can be easily measured with laser-off pulses.
- The laser helicity can be selected pulse-by-pulse which allows for sampling of individual bunches in a train and fast measurement of polarization fluctuations inside single trains.
- With a magnetic chicane acting as an energy spectrometer, the spatial distribution of many simultaneously arriving electrons can be measured to a high precision. Because of the high rate of Compton interactions per electron bunch in the order of $\mathcal{O}(10^3)$ at the upstream position, the statistical precision for each of the 3000 bunch positions in a train is expected to be at 1% after only 4 seconds. The statistical error for the average train polarization is below 0.1% after one second [47].
- At ILC beam energies the Compton edge in the electron spectrum is at about 25 GeV. For these relativistic electrons, the Cherenkov radiation is independent of the electron energy. Therefore the measured Cherenkov signal is directly proportional to the number of detected electrons.
- The high flux of 10^7 electrons passing through the detector per second requires radiation hard materials. Typical Cherenkov media like gases or quartz satisfy this requirement.

9.1 Polarimeter location and layout

In the SB-2009 proposal [40] for the ILC layout, the upstream polarimeter is located about 1600 m before the e^+e^- IP in the Beam Delivery System (BDS), see Figure 9.1. It is positioned directly behind the branch-off of the DC-tuning line which allows to abort the beam during

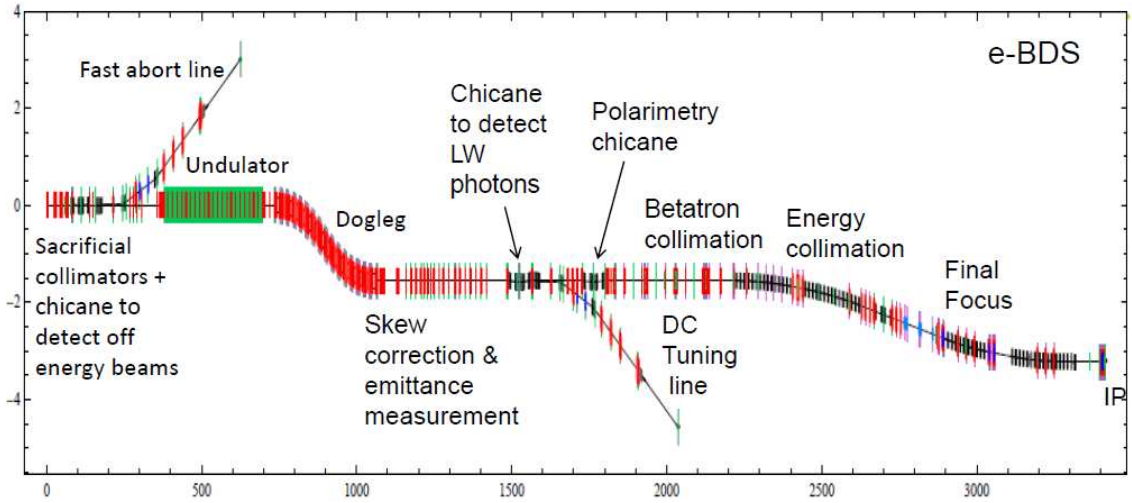

Figure 9.1: *Location of the upstream polarimeter chicane in the BDS of the SB-2009 design proposal [97].*

tune-up to protect the detectors at the e^+e^- IP as well as the focusing and diagnostics components of the BDS. The downstream polarimeters are set roughly 150 m behind the e^+e^- IP, analyzing the polarization of the spent beam. Both polarimeters consist of a magnetic chicane, a laser system and a Cherenkov detector. While the upstream polarimeter chicane has a four dipole layout, the downstream polarimeter has six magnets. Figure 9.2 shows

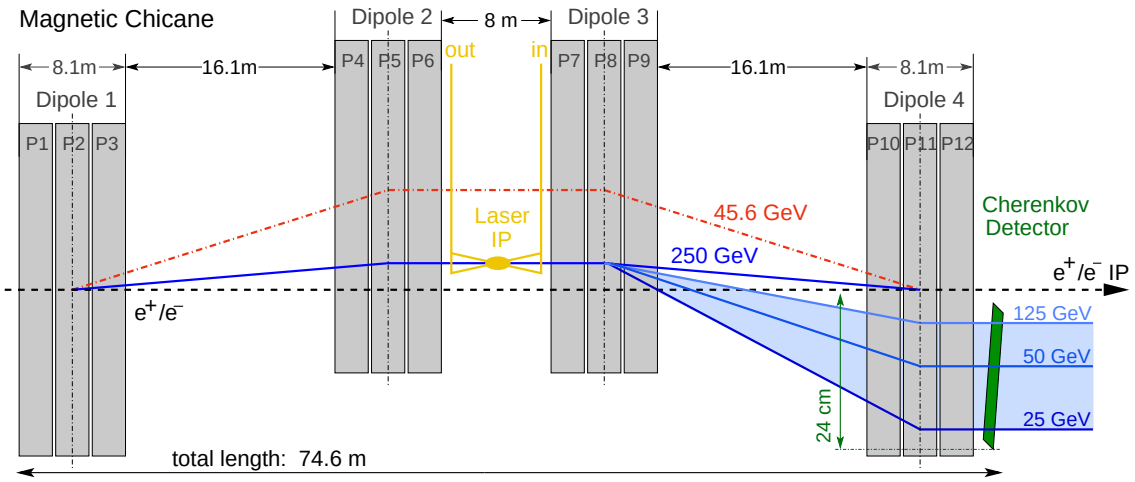

Figure 9.2: *Layout of the magnetic chicane for the* ILC *upstream polarimeter [47].*

the layout of the upstream chicane. The electrons enter the chicane from the left and are horizontally deflected via the first two dipoles by about 10 cm. In between the second and third dipole, circularly polarized laser light is shot under a small angle of less than 10 mrad onto the individual electron and positron bunches. For a precise measurement, the beam direction at the Compton IP has to be within 50 μrad of the beam at the IP in the e^+e^- interaction region. Per bunch about 10^3 electrons are scattered and separated from the main beam line with dipoles three and four. The Compton electrons are detected with a segmented Cherenkov

detector. The magnetic chicane converts the energy spectrum of the Compton electrons into a spatial distribution on the front face of the Cherenkov detector. The Compton edge at about 25 GeV is located on the far side from the main beam line. For constant magnetic fields of the chicane dipoles, the lateral displacement of the beam electrons depends on the beam energy, as indicated in Fig. 9.2 for energies of 45 GeV and 250 GeV. Therefore, the laser system has to be moveable horizontally over a range of approximately 10 cm. A design study for the final optics of the laser system is shown in Figure 9.3.

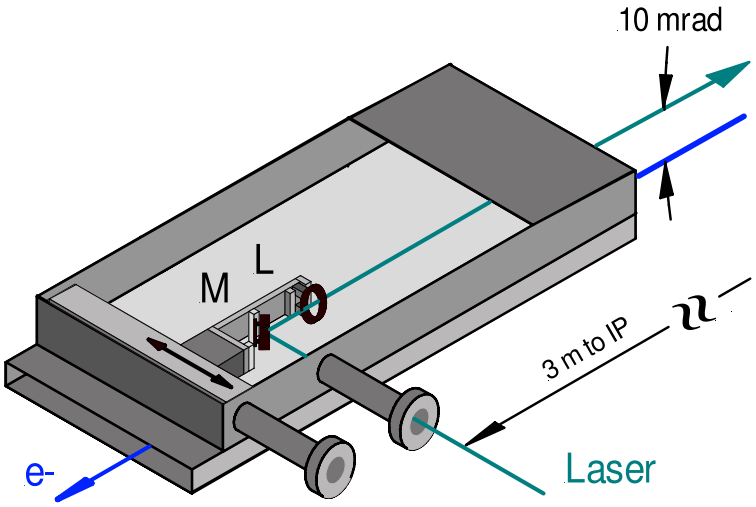

Figure 9.3: *Movable final optics of the polarimeter laser [47].*

Up- and downstream polarimeters are complementary since they provide two independent measurements of the beam polarization. Without collisions, both polarimeters can cross calibrate each other and measure the spin transport from the upstream position to the downstream position. This gives feedback to beamline simulations and provides an estimate of the systematic uncertainties on the beam quality. During collisions the system of up- and downstream polarimeters provides a handle on the depolarization from the beam-beam interaction in the mutually seen high fields of the oncoming bunch at the IP.

9.2 Cherenkov detector

For a precise detection of the scattered Compton electrons by Cherenkov radiation, the foreseen Cherenkov detector has to fulfill the following requirements:

- A high and homogeneous light yield leads to a high statistical precision and limits systematic uncertainties on the detector channel acceptance. Since Cherenkov radiation is characterized by a $1/\lambda^2$ distribution, the reflectivities of the channel walls have to be excellent at ultraviolet wavelengths in the range of 200–300 nm. A homogeneous transmission of the Cherenkov photons to the photodetectors requires smooth and planar channel surfaces. Homogeneity of the light transmission furthermore requires excellent light-tightness of the detector channels.

- Low background rates from the accelerator and the Cherenkov detector itself. Thin walls between the detector channels reduce the showering of electrons. Since knowledge of the detector channel acceptance, or response function, is essential for the analyzing power calibration, a contamination from electron showers needs to be suppressed to limit systematic uncertainties. The Cherenkov detector has to be shielded against the close-by main beamline for reduction of accelerator backgrounds. A medium with a high Cherenkov threshold in the MeV regime for relativistic electrons reduces backgrounds from low energetic electrons and muons. The photomultipliers (PMTs) have to be located sufficiently far away from the Compton fan.

- Self calibration capabilities and slow control of gas pressure and temperature. For self calibration, light from LEDs or from a laser can be coupled into the individual channels. With fast LEDs a continuous calibration is possible with laser off pulses or even between beam trains. Measurements of the temperature, especially at the PMT location, and for the PMTs themselves help to keep PMT dark currents under control. For stable operation, the Cherenkov detector has to be gas-tight.

The ILC Cherenkov detector will consist of 18 to 20 staggered u-shaped aluminum tubes filled with a Cherenkov gas. Figure 9.4(a) shows a conceptual drawing with a reduced number of channels. The tubes are aligned along the exit window of the tapered beampipe. The tapered beampipe suppresses wakefields that might decrease the energy and therefore spatial resolution of the polarimeter. On top of the hind u-leg photomultipliers are located, detecting the Cherenkov radiation emitted by the scattered electrons traversing the u-base. The front u-leg houses a calibration system. Such a calibration system could consist of high quality LEDs operating in the ultra-violet region or of laser light coupled into the channels through a thin window atop the front leg. The u-shaped design is chosen to locate the PMTs and the calibration system well outside the Compton fan for background suppression and protection. In Figure 9.4(b) a single Cherenkov tube is shown. A scattered Compton electrons travels through the base of the channel and produces Cherenkov radiation in the gas. A mirror at the end of the u-base reflects the light upwards towards the PMT atop the hind u-leg. In contrast to the SLD polarimeter the u-legs are orthogonal to the Compton fan, avoiding cross talk between the channels. At SLD this design could not be realized because of spatial restrictions. A description of the SLD polarimeter can be found in [98].
Also shown in Figure 9.4 is the global right-handed coordinate system that is used throughout this document. The z-axis points in the direction of the electron beam and the Compton electrons. The x-axis points to the left when looking into beam direction and the y-axis points upwards.

9.3 Critical parameters

Because of the high statistics of Compton scattered electrons, polarimetry at ILC is already limited by systematic uncertainties after measurement times of only a few seconds. Apart from detector related parameters that have to be known precisely, the spin transport to the e^+e^- IP and the luminosity measurement lead to further systematic uncertainties on the final polarization measurement.

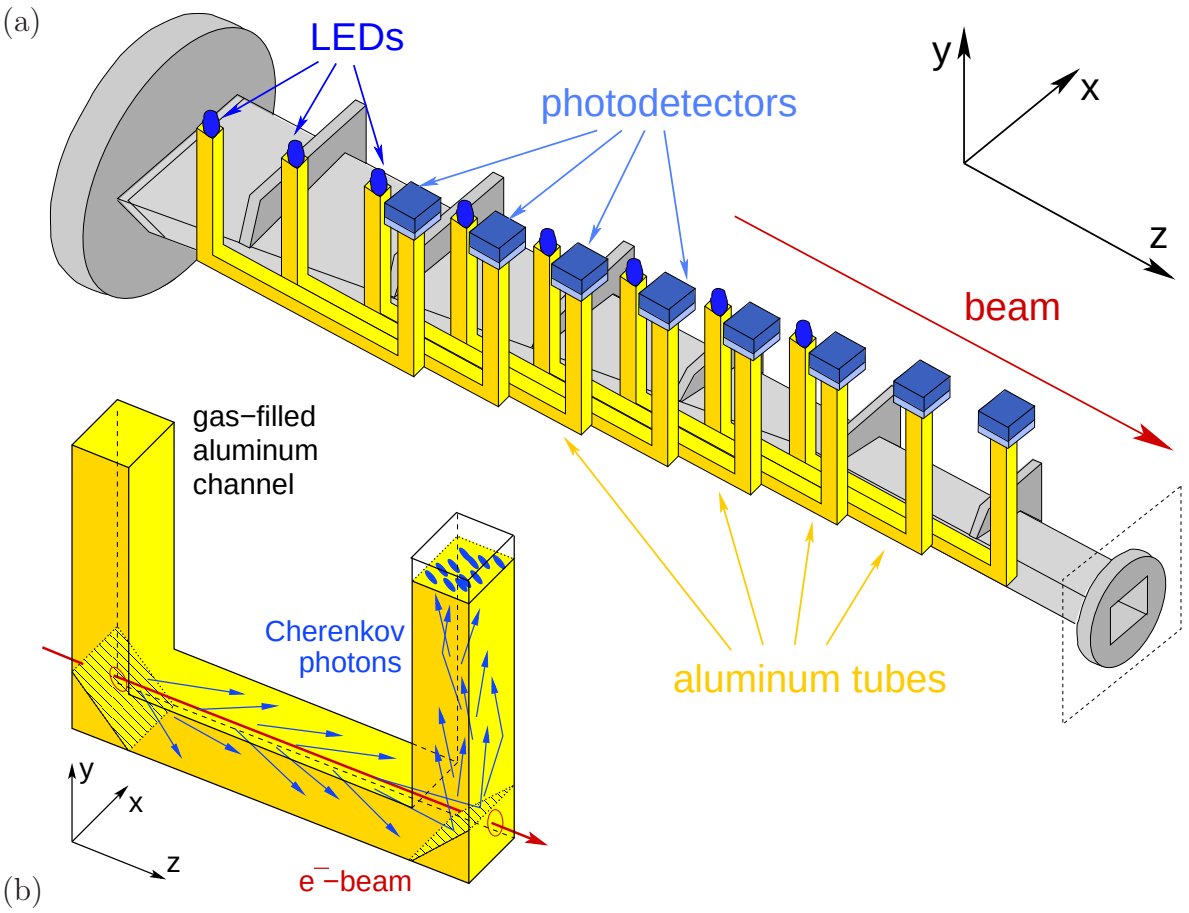

Figure 9.4: *(a) Design study for the segmented Cherenkov detector. Only eight channels are drawn, each channel equipped with photodetectors and an LED calibration system.*
(b) Schematic Drawing of one of the Cherenkov channels with the electrons entering the channel base from the left and the produced light reflected upward to the photodetector.

9.3.1 Luminosity weighted polarization

The important quantity for physics with polarized beams is the luminosity weighted polarization defined as

$$P_{lum} = \frac{\int n(E)P(E)\mathcal{L}(E)dE}{\int n(E)\mathcal{L}(E)dE}, \tag{9.1}$$

where $n(E)$ is the beam energy spectrum, $P(E)$ the measured polarization and $\mathcal{L}(E)$ the luminosity spectrum. The luminosity weighted polarization differs from the measured polarization, because off-energy electrons in the electron bunches produce little-to-no luminosity but still contribute to the measured polarization. As the luminosity spectrum will be measured to a precision of 10^{-3} to 10^{-4}, luminosity related uncertainties on P_{lum} will be small compared to the other contributions. Furthermore, with the polarization measurement from collision data, the luminosity weighted polarization is directly accessible. An accuracy of 10^{-3} on P_{lum} seems achievable. A possible method for the determination of the luminosity weighted longitudinal polarization is the study of W-pair production. By fitting the polarization dependent angular distributions of the W^- to the data, the beam polarization can be extracted. With

this method, the desired precision of 10^{-3} on P_{lum} is reached for $P_{e^-} = 0.8$ and $P_{e^+} = 0.6$ with a data set of $\mathcal{L} = 300\,\mathrm{fb}^{-1}$ for both the electron and positron polarization [99].

9.3.2 Laser helicity

Lasers which can be pulsed with the same time structure as the ILC electron beam do exist and are for example in operation at the TTF/Flash experiment at DESY. From Equation 8.9 it follows directly that

$$\frac{\Delta P}{P} = \frac{\Delta \lambda}{\lambda}. \tag{9.2}$$

Laser polarizations are readily determined to a precision of 0.1% [92, 94].

9.3.3 Analyzing power calibration and response function

Measuring the polarization from the rate asymmetry A_i in detector channel i requires the knowledge of the analyzing power $\mathcal{AP}_i$ in this channel (cf. Sec. 8.1.2 and Eq. 8.10). The analyzing power $\mathcal{AP}$ describes the rate asymmetry for an electron polarization $P = 1$ and maximal laser helicities of $\lambda = \pm 1$, measured with an ideal channel acceptance ρ, also called response function. The ideal rectangular response function of the ILC Cherenkov detector channels is, however, smeared by backrounds from electrons showering in the channel walls and the PMT acceptance (cf. Sec. 11.4.6). The analyzing power $\mathcal{AP}_i$ of channel i corrected for the response function is defined as

$$\mathcal{AP}_i = \frac{\int \left(\frac{d\sigma}{ds}\right)_{unpol} \mathcal{AP}(s)\rho(s)ds}{\int \left(\frac{d\sigma}{ds}\right)_{unpol} \rho(s)}, \tag{9.3}$$

where s is the transverse spatial coordinate at the detector. $\mathcal{AP}_i$ is the average Compton asymmetry, weighted by the unpolarized cross section and the detector response function $\rho(s)$ for channel i. As for the laser helicity, uncertainties on the analyzing power propagate directly to the Polarization measurement:

$$\frac{\Delta P}{P} = \frac{\Delta \mathcal{AP}}{\mathcal{AP}}. \tag{9.4}$$

Since the cross section can be calculated in pure QED, the response function ρ dominates the analyzing power calibration. At SLD the analyzing power calibration contributed to the systematic uncertainty by 0.3% [92]. For ILC the goal is to limit this contribution to 0.2%. For a precise calibration of $\mathcal{AP}$, not only the exact form of the response function is required, but also the relative location of the Compton spectrum w.r.t. to the detector channels. The response function will be obtained from detailed simulations and has to be validated with data. Calibration scans serve to locate the Compton edge and thus help to gain information on the detector position relative to the Compton spectrum (endpoint calibration).

9.3.4 Detector alignment

Rotational misalignment of the Cherenkov detector w.r.t the Compton fan introduces a new potential source of errors. At the SLD polarimeter, a detector rotation about the vertical y-axis resulted in a change of the analyzing power of 0.08% per milliradian of misalignment

for channel 6 and 0.03% for channel 7 [100]. While a rotation could not be detected by a change of the endpoint calibration, it introduced a measurable shift of the observed channel centers. The quoted results were obtained by correcting for these shifts. In contrast to the SLD polarimeter, no pre-radiator will be required at the ILC polarimeter. The pre-radiator was installed to increase the signal rate, but it also had the additional effect of smearing the response function considerably from the pure geometric channel acceptance. Without the pre-radiator, a rotation induced change in the endpoint calibration might be easier to detect. However, it should nevertheless be possible to achieve angular alignment to a precision of 1 mrad (0.06 deg).

9.3.5 Detector linearity

The rate asymmetries A_i are determined from the PMT response $D(N^{\pm})$ to the Compton electrons $N^{\pm}$ traversing the detector channel i for helicity configuration $P\lambda = \pm 1$. The PMT response is, in general, a function of the PMT quantum efficiency (QE) and the PMT gain g. Since rate asymmetries are used in the polarization measurement, the effects of QE and gain cancel for a linear response and a homogeneous spectral PMT acceptance. In case of non-linearities in the detector response, the exact relationship of $D(N^{\pm})$ has to be known. Possible further non-linearities in the signal digitization also have to be considered. For ILC these effects have to be under control at a level of 0.1%. The precise determination of these effects has been studied in [101].

9.3.6 Spin transport and depolarization

The polarization measured at the polarimeter locations can be different from the polarization at the e^+e^- interaction point. Three factors contribute to this possible difference. One is the chromaticity effect which is the difference between measured and luminosity weighted polarization (cf. Sec 9.3.1). Other effects are due to the beam transport from the polarimeter locations to the e^+e^- IP, as well as depolarization by collisions in the interaction region.
The precession of spins in magnetic fields is fully described by the T-BMT equations [102]. For a particle motion in a plane transverse to a magnetic field, the angle of the spin precession θ_s is related to the orbital angle θ_b via

$$\theta_s = \gamma \frac{g-2}{2} \theta_b, \tag{9.5}$$

where γ is the Lorentz factor and $(g-2)/2 = 1.159652 \times 10^{-3}$ is the anomalous magnetic moment of the electron. For ILC energies a misalignment of 50 μrad of the Compton-IPs with the e^+e^- IP translates to a spin precession of 0.028 rad in the ILD IR. For an electron beam polarization of 80%, this translates to a systematic uncertainty of $\delta P/P \approx 0.05\%$.
During collisions, the mutually experienced strong electromagnetic fields from the oncoming bunch lead to further depolarization. Therefore these effects have to be precisely studied in simulations and confronted with data. The physical processes for depolarization in beam-beam interactions are spin-precession and spin-flip, as well as coherent and incoherent pair production. These effects have been studied and found to lead to a depolarization of $0.2\% \pm 0.03\%$, dominated by spin-precession effects [103]. This depolarization will be monitored by comparing the upstream and downstream polarization measurements.

9.3.7 Machine induced backgrounds

There are several background processes that can interfere with the Compton scattering process $\gamma e \to \gamma e$. The three most important ones are discussed below [95]. While the first two are only relevant above a certain energy threshold, the bremsstrahlung background from residual beam pipe gas is present at all machine parameters [104, 105].

- $\gamma\gamma \to e^+e^-$ **(two-step conversion)**
  In this process one of the photons originates from a prior Compton event and interacts with a photon from the laser beam. Although in principle, this process is possible at ILC, ($x_{thresh} = 4.83$ or $E_0 \approx 137$ GeV, cf. Sec 8.1.1) it requires extremely high photon energy densities in the laser focus to be significant and can safely be ignored.

- $\gamma e \to e e^+e^-$ **(direct pair production)**
  This higher order QED process has a threshold of $x_{thresh} = 8$ ($E_0 \approx 230$ GeV). For the TESLA polarimeter, corrections to the analyzing power due to this background process have been calculated and estimated to be $\leq 0.05\%$.

- $eX \to eX\gamma \to eXe^+e^-$ **(beam gas background)**
  With a residual gas pressure in the beam pipe of $(O) = 10^{-9}$ mbar, the bremsstrahlung background for bunches with 2×10^{10} electrons has been estimated to about 0.05 electrons per bunch in the Cherenkov detector of the TESLA polarimeter [95]. In comparison with the expected 10^3 Compton events this background is negligible as well.

Chapter 10

Cherenkov detector prototype

In 2008 a prototype Cherenkov detector has been designed and constructed at DESY [106][1]. Its design reflects the key requirements for a Cherenkov detector for polarization measurements at the ILC, described in Chapter 9.2. The construction has been accompanied by a GEANT4 based optical simulation. In 2009 and 2010 the detector prototype has been operated at testbeams at DESY II and at the ELSA accelerator in Bonn. The evaluation of the recorded data is subject of Chapter 11.
In this Chapter, the prototype design, its setup options and the Data Acquisition system (DAQ) are presented. Furthermore, results from the optical simulation are given.

10.1 Prototype design and construction

The basic design of the prototype consists of two non-staggered, u-shaped Cherenkov channels. The channel structure is build from aluminum plates and slabs of 1 cm thickness. Figure 10.1(a) shows a technical drawing of the assembled channel structure. The cross sectional area of each channel is 8.5×8.5 mm^2. The electrons travel along the base of the u-shaped channels which has a length of 15 cm for central electrons. The length of the u-legs is 10 cm. The dividing inter-channel wall is made of two back-to-back aluminum foils of 0.15 mm thickness, clamped between the aluminum slabs comprising the outer walls of the channels. At the front and the end of the u-base, polished aluminum plates are attached at 45° w.r.t. to the u-base. The mirror plate at the front serves to reflect light from a calibration light source atop the front u-leg into the u-base, while the hind mirror reflects Cherenkov photons (or calibration light) upwards into the hind u-leg towards the photomultiplier. The assembled channel structure is located in a surrounding outer aluminum box with dimensions $230 \times 90 \times 150$ mm^3 (L × W × H). Figure 10.1(b) shows the channel structure inside the open outer box. On top of the u-legs, outside the detector box, mountings for photodetectors (PD) and an LED calibration system are provided. The mountings allow for an easy exchange of the PMTs and calibration system without changing the overall prototype setup. The electrons enter and exit the box through two 0.15 mm aluminum sheets, fixed to the box with aluminum rings.
During operation, the box is flooded with Cherenkov gas which can be filled into the box

[1]The author would like to thank B. Frentsche and J. Pelz for the CAD studies and S. Fleig and his entire team at Hamburg University workshop for their support.

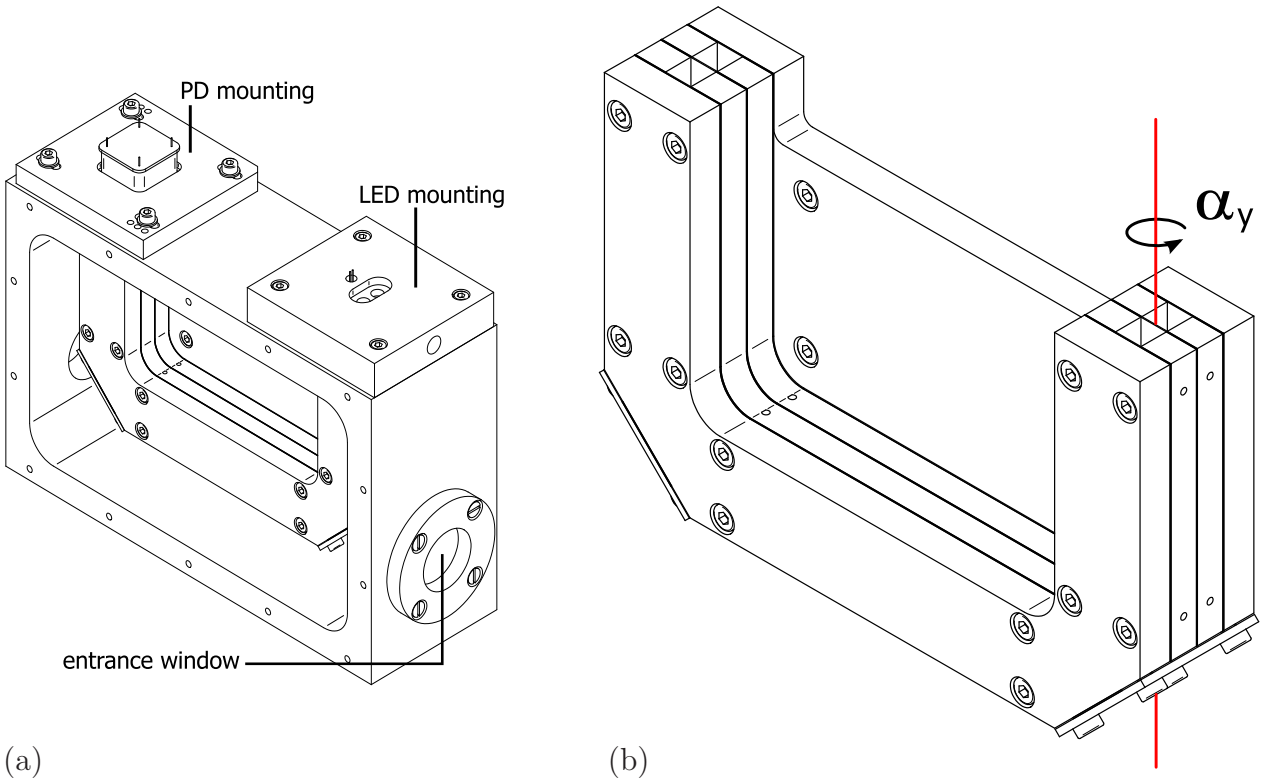

(a) (b)

Figure 10.1: *Technical drawing of the prototype Cherenkov detector. The inner channel structure is depicted in (a) with the two side-by-side detector channels build from aluminum slabs and plates of 1 cm thickness. Figure (b) shows the channel structure located inside the aluminum detector box. Also shown are the mountings for the LED calibration system and the photodetectors, on top of the front and hind u-leg, respectively.*

through an opening in the LED mounting. Perfluorbutane (C_4F_{10}) has been chosen as Cherenkov gas for its high threshold of 10 MeV, suppressing low energy backgrounds. In addition, C_4F_{10} is non-flammable allowing for safe operation. To ensure gas- and light tightness, the box is closed with a 1 cm thick aluminum lid. The lid, the entrance/exit windows and the mountings are sealed with rubber seal rings.
For a high and homogeneous light yield the aluminum of the channel structure has been diamond cut and polished. Its reflectivity at short wavelengths has been measured beforehand (cf. Sec. 10.5). The inter-channel wall, which is required to be thin to reduce showering of the electrons could not be manufactured from diamond cut aluminum for mechanical reasons. It has therefore been decided to construct it from high reflectivity rolled aluminum foil, purchased from GoodFellow[2]. Because of the rolling process, one side of the foil exhibits a better reflectivity behavior than the other. Different reflectivities in the two detector channels are unwanted, so the inter-channel wall consists of two sheets of the 0.15 mm thin aluminum

[2]GoodFellow GmbH, Germany; Aluminum foil: AL000601 (thickness: 0.15 mm, purity: 99.0%, hardness: hard).

foil attached back-to-back with the higher reflectivity side facing the active volume in each channel. The reflectivity of the aluminum foil has also been measured before construction. Figure 10.2(a) shows a photograph of the assembled inner channel structure located in the open outer aluminum box of the detector prototype. In Figure 10.2(b) a photograph of the closed outer detector box is shown. The aluminum lid holds a pressure gauge for future pressure monitoring.

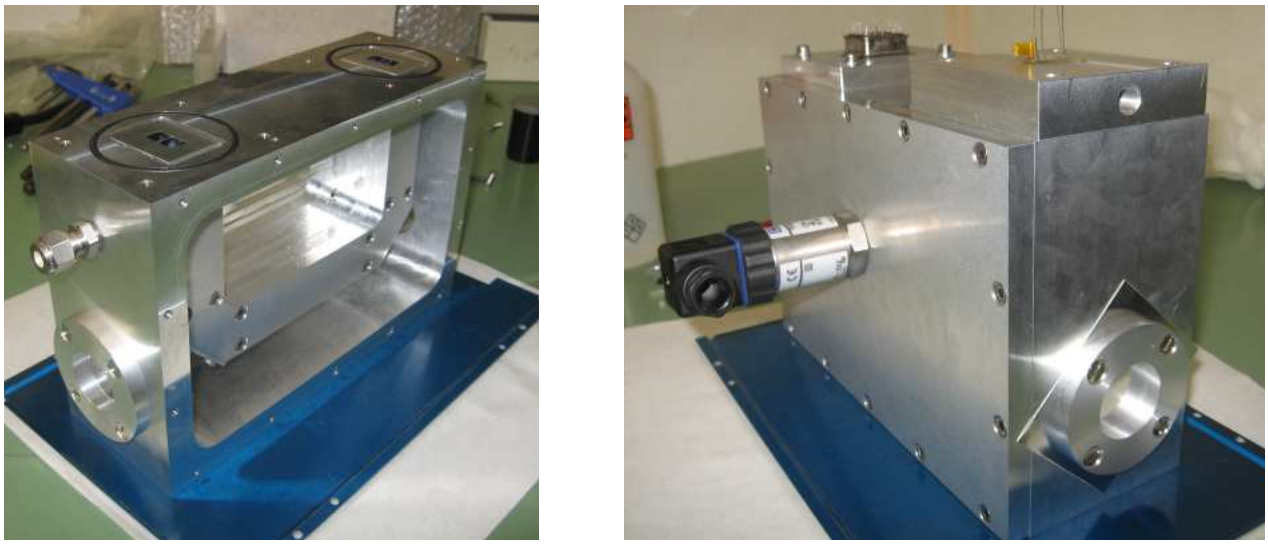

(a) (b)

Figure 10.2: *Photographs of (a) inner channel structure of the Cherenkov detector prototype located in the outer box, and (b) outer prototype box closed with aluminum lid holding pressure gauge.*

10.2 Photodetectors and mountings

The choice of the cross sectional area of the Cherenkov channels has been influenced by the conceptual design for the ILC polarimeter. The exact values, however, were chosen to match the sensitive area of the used photodetectors. For the testbeam campaigns in 2009 and 2010 six different photomultiplier models (PMT) have been ordered and operated. The PMTs were chosen by criteria important for the detection of Cherenkov radiation in experimental environments comparable to the ILC experiment. For Cherenkov light detection the photomultipliers are required to have a high quantum efficiency at short wavelengths in the ultraviolet region. Secondly, the dynamic range of the photomultipliers should cover the detection of single-electron events up to multi-electron events with several hundred electrons simultaneously.
Table 10.1 lists the PMTs employed in the testbeam campaigns. Five of the six PMTs are from the company Hamamatsu, the last one is manufactured by Photonis. The photodetectors fall into two categories, Single Anode Photomultipliers (SAPMs) and Multi Anode Photomultipliers (MAPMs). The SAPMs have a circular cross section that is covered entirely by the Cherenkov channel in case of the R7400U-06(03), or, in case of the R4125 and

photodetector	sensitive area	wavelength range [nm]	typical gain	response time	number of anode pads
R7600U-03-M4 [(a)]	18.0×18.0 mm^2	185 - 600	1.8×10^6	11.0 ns	4
R7600-00-M64 [(a)]	18.1×18.1 mm^2	300 - 600	0.3×10^6	13.4 ns	64
R7400U-06(03) [(a)]	= 8 mm	160(185) - 600	0.7×10^6	6.5 ns	1
R4125 [(a)],2010	= 15 mm	300 - 650	0.9×10^6	18.5 ns	1
XP1911/UV [(b)],2009	= 15 mm	200 - 600	0.9×10^6	28.0 ns	1

Photodetector from: (a) HAMAMATSU, (b) PHOTONIS.

Table 10.1: *Key characteristics of the four different photomultipliers from* HAMAMATSU *and* PHOTONIS *[107, 108, 109, 110]. The two MAPMs (R7600U-03-M4 and R7600-00-M64) have a quadratic cross-section of similar size, but differ in the number of anodes and in their wavelength range. The three SAPMs (R7400U-03, R7400U-06 and R4125) differ in the size of their sensitive areas and slightly in wavelength range.*

XP1911/UV, is larger than the channel diameter. Thus, the latter two SAPMs are in part sensitive to Cherenkov light emitted in the neighboring channel. The XP1911/UV has been included for comparison with the SLD polarimeter [111] but proved not to be suited for the detector prototype and will not be investigated further. Two MAPM models have been used: the R7600U-03-M4 (M4) has four anodes, each with a quadratic cross section of 8.9×8.9 mm^2, allowing for a simultaneous readout of the two detector channels and cross talk readings with the remaining two anodes. The anode spacing is 0.2 mm. The R7600-00-M64 (M64) has 64 anodes of 2×2 mm^2 each with a spacing of 0.3 mm in between the anodes. When mounted on the detector box, 4×4 anodes monitor the left and right channel each with the remaining anodes available for cross talk readings.
Apart from the anode configuration and sensitive cross sectional area, the PMTs differ in their wavelength range and rise times. Because of the $1/\lambda^2$ dependency of the Cherenkov spectrum, only PMTs with peak sensitivities in the violet part of the spectrum at ≈ 400 nm were chosen. The sensitivity range of the PMTs extends to below 200 nm with the exception of the M64 and R4125 which are only sensitive down to 300 nm. The Cherenkov medium in the detector prototype is C_4F_{10} which is fully transparent in the UV-range. If C_4F_{10} is contaminated with water vapor, its transparency can drop significantly below 200 nm [112, 113]. This decrease in transparency provides a natural limit on the required sensitivity at lower wavelengths. The response times range from 6.5 to 28.0 ns. Compared to the bunch spacing of ≈ 400 ns for the nominal beam parameter set of the ILC, these response times are sufficiently short to allow measuring each bunch in a train. The signal rise times are in the order of 1 ns which is equivalent to the bunch length in the ILC Linac. Only the rise times of the R4125 and the XP1911/UV exceed the bunch length by a factor of 2.5 which makes them less suited for operation in an ILC polarimeter detector. Corrections due to the signal rise time introduce systematic uncertainties on the signal measurement. Typical gain values are about 1×10^6. Figure 10.3 shows the anode configurations of the employed PMTs in correct relative scaling. The relative location of the detector channels is indicated by the red frames.
For each PMT a special mounting has been manufactured. For electrical insulation these

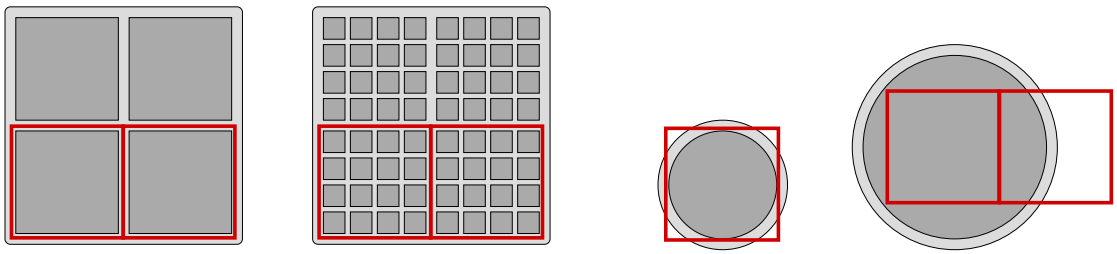

Figure 10.3: *Anode schemes of the different photomultipliers in correct relative scaling. From left to right: R7600U-03-M4 (M4), R7600-00-M64 (M64), R7400U-06(03) and R4125. The relative location of the detector channels is indicated by the red frames.*

mountings were cut out of solid blocks of poly-oxy-methylene (POM). The two MAPMs were ordered from HAMAMATSU without their plastic casings, since they had to be glued into their mountings to ensure a gas- and light-tight connection between the Cherenkov channels and the respective PMTs. As glue, epoxy resin mixed with black paint has been used. The R7400U-06(03) SAPMs have been ordered without the lens windows to ensure a planar contact surface with the top of the detector channel u-legs. The round SAPMs were fixed in their respective mountings with O-ring seals.
The mountings are affixed to the hind u-leg of the detector box. They are turnable by 180° allowing to swap the anodes from the left to the right detector channel. Additional pin holes were drilled into the MAPM mountings for three positions of the PMT anodes relative to the detector channels. In Figure 10.4 these positioning options are illustrated for the M4 MAPM.

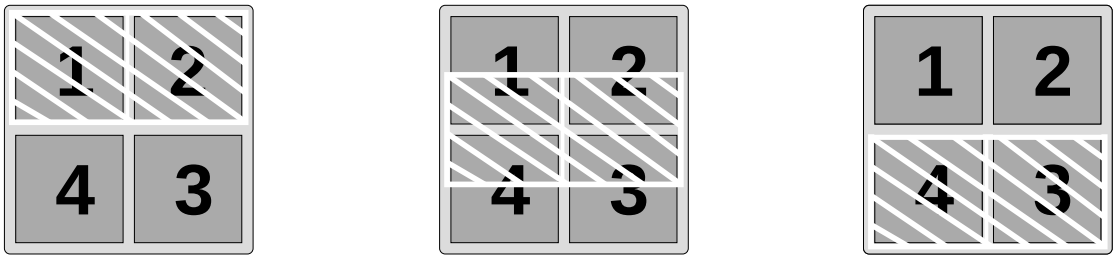

(a) (b) (c)

Figure 10.4: *Mounting positions of the M4 and M64 MAPMs relative to the detector channels. The detector channels are shown as the white hatched areas.*

The anodes are depicted in gray, and the relative detector channel positions are shown as the white hatched areas.
During the two data-taking periods in 2009 and 2010, the anode signals were digitized with an 8 channel and a 16 channel QDC, respectively (see Sec. 10.4). Therefore the 64 anodes of the M64 were grouped in four different configurations as shown in Figure 10.5. The grouped anodes are numbered clockwise for each detector channel and are referred to by their respective number in the following. In Anode configuration 3, sixteen anodes are read out

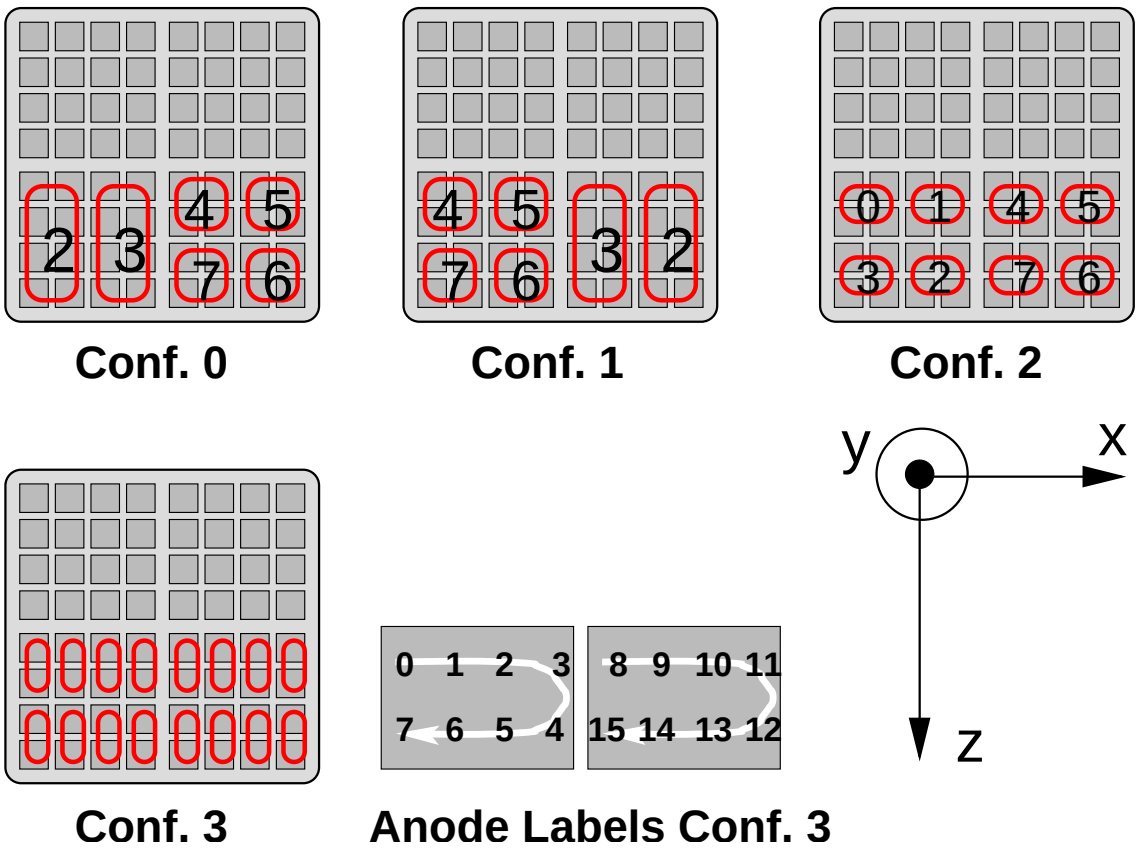

Figure 10.5: *Anode configurations for the M64 MAPM used in 2009 and 2010. Configurations 0 and 1 were used in 2009 when only six of the eight QDC channels were functional. In configuration 3 eight QDC channels per detector channel were read out simultaneously.*

simultaneously, labeled 0 to 7 in the right channel (as seen in the beam direction along the z-axis) and from 8 to 15 in the left channel. Anode configurations 0 and 2 were used in the 2009 ELSA testbeam campaign when only six of the eight QDC channels were available.
The four anodes of the M4 are labeled from 4 to 7 clockwise, see Figure 10.6. The different anode configurations 0 to 2 are adjusted by the positioning of the PMT mounting on the hind u-leg. In Conf. 0 anodes 7 and 6 are on top of the detector channels, in Conf. 2 anodes 4 and 5 are on the channels. Conf. 1 is an intermediary position, where all four anodes are partially atop the detector channels (compare Fig. 10.4(b)).
On top of the front u-leg an additional aluminum mounting with two LEDs (HLMP-CB30-NRG, Agilent Technologies [114]) is located. The LEDs have a peak wavelength of 470 nm. They are glued into the mounting with blackend epoxy resin. The LEDs are used for functional tests of the PMTs and for calibration purposes. Figure 10.7 shows a detail of the inner side of the LED mounting facing the u-leg. Two slender POM tubes ensure that the light from each LED is guided into one detector channel only. In the upper half of the circular clearance the inflow opening for the Cherenkov gas is visible. The clearance allows the Cherenkov gas to flow freely between the two detector channels and the surrounding outer box volume. In between the POM tubes a temperature sensor is visible that can be used in future for temperature readings of the Cherenkov gas.

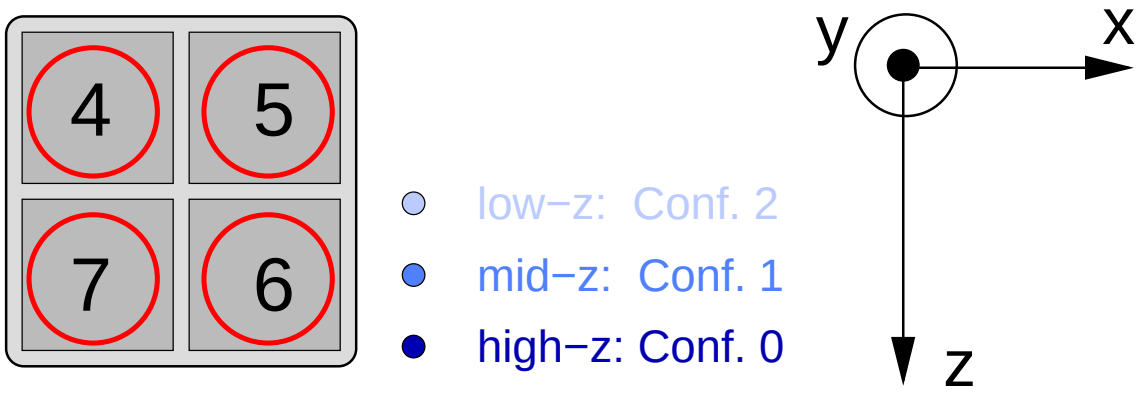

Figure 10.6: *Anode configurations for the M4 MAPM used in 2009 and 2010. The colored dots indicate the positioning of the PMT mounting on the hind u-leg. In Conf. 0 anodes 7 and 6 are atop the detector channels, in Conf. 2 anodes 4 and 5 are atop the channels. Conf. 1 is the midway position, compare Fig. 10.4(b).*

Figure 10.7: *Detail of the LED mounting on the front u-leg. Visible are the two slender POM tubes, guiding the light from the LEDs in the two detector channels. The circular clearance allows the Cherenkov gas to flow freely between the two detector channels and the surrounding outer box volume. In between the POM tubes the temperature sensor is visible.*

10.3 Additional components

During the functional tests at DESY, it became clear that light could enter the MAPM dynode system via the glass coating of the anode output pins. Therefore, light-tight boxes have been constructed, each one encasing the MAPM in its mounting and the MAPM base. Each box is made from aluminum and POM as front face, into which a HV connector and LEMO

connectors for signal readout are embedded. The lid of the detector box holds an electronic pressure gauge for future remote read-out.
In order to rotate the entire detector box about the y-axis, a POM baseplate has been manufactured. The detector box is fixed to the baseplate with an aluminum pin located below the center of the inter-channel wall of the front u-leg, see Figure 10.1(a) on page 110, where the axis of rotation is indicated in red. The detector box can be rotated in reproducible steps of 0.125°. The full system of baseplate, detector box and mountings is affixed to a movable stage for horizontal/vertical adjustments of the detector in the plane orthogonal to the electron beam at the testbeam location.

10.4 Data acquisition system

The data acquisition system (DAQ) consists of a VME crate with a controller and readout modules, and an optical connection to a PC. For signal digitization a CAEN V965A 8 Channel (and also a V965 16 Channel) Dual Range [115] charge-to-digital converter (QDC) is used [101]. A QDC is a special type of analog-to-digital converter (ADC). While an ADC converts analog pulses (usually voltages) to a digital binary range, a QDC integrates analog pulses and digitizes them, providing for example a charge measurement for input current pulses. ADCs are typically used for slower signals that have already been integrated. PMT output signals are fast changing electric currents which makes a QDC more suitable for this type of measurement.
Both CAEN QDC models (i.e. the 8 channel and 16 channel QDCs) have a 12-bit resolution resulting in $2^{12} = 4096$ QDC channels[3]. Ideally, the QDC channels are equidistant with one QDC channel corresponding to a constant charge range. Both QDC models are also dual range QDC with 200 fC per QDC channel in the high range and 25 fC in the low range. The resolution per range is called the Least Significant Bit (LSB), i.e. in the low range LSB = 25 fC. The full dynamic range in the latter option is therefore 4096×25 fC $= 102.4$ pC.
For the CAEN QDCs, the charge from each of the 8 (or 16) input channels is converted to a voltage amplitude with a charge-to-amplitude converter (QAC). The QAC output is then routed through a multiplexer and fed to a 12-bit ADC. The digitized signal is stored in a FIFO[4] event buffer and read out via the VME bus. The digitization cycle and length is provided by an external gate signal. The QDC integrates the incoming signal pulses as long as the gate signal is applied. The digitization is started once the gate is removed. The full digitization including settle time and QAC reset time takes 7.2 μs during which no further gates are accepted.
For measuring the rate asymmetries in the polarization determination, a highly linear QDC response w.r.t. the input PMT signal is required. Two different types of non-linearities have to be considered. The differential non-linearity (DNL) is defined as the deviation of the QDC response to a small change in the signal input ΔS at different working points S_i. For a linear response, this deviation is independent of the working point S_i. It is calculated from the ratio of the measured to the ideal bin width. The integrated non-linearity (INL) is the maximum deviation from the linear expectation over the full signal range and represents cumulative

[3]The dynamic range of a QDC is conveniently given in channels, not to be confused with the readout channels of the PMT anodes.

[4]First in, First out.

effects of the DNL. For the QDC models used here, the DNL and INL have been measured in a dedicated experiment [101]. The maximal DNL has been found to be 0.01 LSB, or ≤ 1 fC for the high range. For the INL, a maximal non-linearity of 3 LSB or 1% of the full dynamic range has been observed. Correcting the recorded signals for the measured QDC differential non-linearities, introduces negligible errors on the linearity of the whole system of PMT and QDC.
Another component of the DAQ system is a TEKTRONIX function generator (model AFG 3011) [116], which provides sufficiently short pulses for the gating of the QDC, and a Linux PC for data storage and analysis.

10.5 Reflectivity measurements

The wavelength dependent reflectivity of both, the diamond-cut aluminum and the rolled aluminum foil, used for the detector channel walls have been measured with a modified transmission spectrometer. The PERKINELMER Lambda 800/900 spectrometer [117] uses two radiation sources to cover the electromagnetic spectrum from the near infrared to the ultraviolet. The infrared and visible part of the spectrum is provided by a halogen lamp, the ultraviolet is covered by a deuterium lamp. Optical filters pre-filter the light from the light sources. Two monochromators isolate a specific wavelength with an accuracy of ± 0.8 nm in the UV and visible spectrum and ± 0.3 nm in the near infrared. A mirror plated chopper wheel splits the light beam into a reference and a sample beam. In transmission mode, the sample beam passes through a probe, and the remaining intensity at a given wavelength is compared to the reference beam by integration of the response of a PMT. The integration times required are in the order of 0.1 to 10 seconds. The photometric accuracy on the transmission T is below 0.1%. In Figure 10.8(a) the sample compartment of the spectrometer is shown. The setup has been modified to measure the reflectivity R instead of the transmission T by reflecting the sample beam off four aluminum blocks of the diamond-cut quality. The sample reflectivity for an incidence angle of 45° is then given by:

$$T = R^4. \tag{10.1}$$

For the rolled aluminum foil measurement, the reference beam has been calibrated to the diamond-cut reflectivity, and the foil has been put in front of the last aluminum block, thus the reflectivity is measured directly. The measured wavelength dependent reflectivities are shown in Figure 10.8(b) for the diamond-cut aluminum (black) and the rolled aluminum foil (gray). The setup showed a high sensitivity to the adjustment of the aluminum blocks, and therefore the measured values only provide a lower limit on the true reflectivity. A lower average reflectivity for the aluminum foil was expected because of the visibly worse surface quality. For unpolarized light the reflectivity of aluminum for a wavelength of 200 nm under 45° is expected to be $R = 0.92457$ [118, 119], with only a small dependence on the incident angle. The measurement with the spectrometer is 15% off, probably caused by the surface quality. The values obtained for the aluminum foil are strongly underestimated (cf. Section 11.3). This underestimation has its likely cause in the strong sensitivity of the measurement to the alignment of the aluminum blocks. Also, at the position of the last aluminum block on which the aluminum foil has been attached, the sample beam has already undergone three

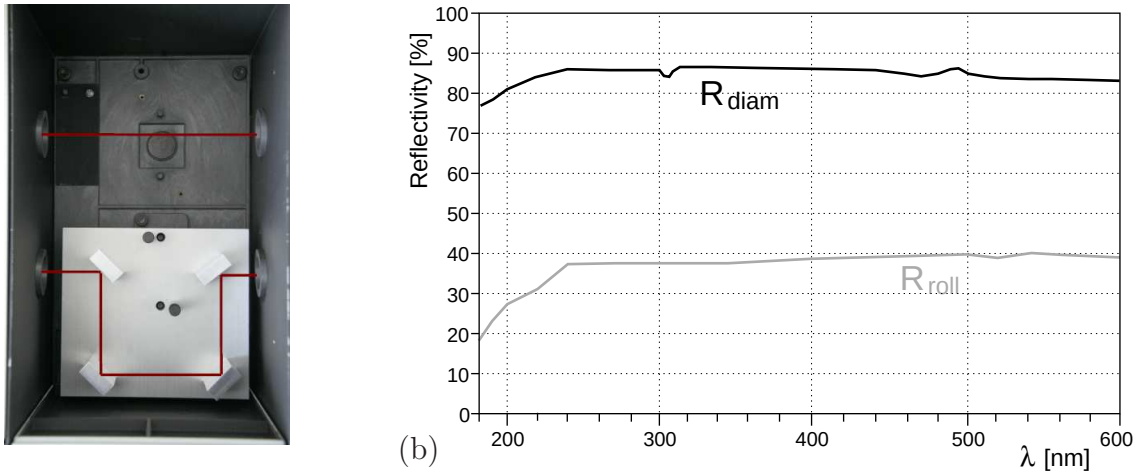

Figure 10.8: *(a) Photo of the modified sample compartment of the* PerkinElmer *spectrometer. The reference beam passes the compartment in the upper part of the picture, indicated by the red line. The sample beam is reflected off aluminum blocks four times under an incident angle of 45° degrees. (b) Measured lower limits on the wavelength dependent reflectivities for the diamond-cut aluminum (black) and the rolled aluminum foil (gray).*

reflections off the prior aluminum blocks. The sample beam might have been widened from these reflections and imperfect surface properties.

10.6 Geant4 simulation

Accompanying the design and construction process of the detector prototype, a detailed Geant4 based simulation of the internal channel structure has been set up. The geometry has been carefully implemented. Figure 10.9 shows an event display of the simulated two channel detector, with an electron (red/black) travelling on-axis of the global coordinate system through the base of the right detector channel, and producing Cherenkov light (green). The Cherenkov light is diverted upwards to the PMT on top of the hind u-leg. The different PMT types are not included in the Geant4 simulation. At the location of the PMT entrance windows, the photon energies and positions are stored in Root TTree structures [88, 89]. The inter-channel wall is indicated by the light gray area. In the event display, the electron produces additional Cherenkov radiation before and after it enters the channel structure. This light, however, can not reach the PMT positioned on the hind u-leg.
The wavelength of the Cherenkov photons is larger than the typical atomic spacing. Therefore they are treated as "optical" photons in the simulation [120]. For optical photons the relevant processes are turned on. These are in particular: absorption in the PMT entrance window, boundary effects (like reflection and absorption) at the channel walls, as well as Rayleigh elastic scattering. For electrons and positrons, emission of Cherenkov radiation, multiple scattering, ionization, bremsstrahlung and annihilation are simulated. For muons, which are a part of the possible accelerator background, the same processes are taken into account, except for annihilation . The inter-channel wall and the outer channel walls are distinguished

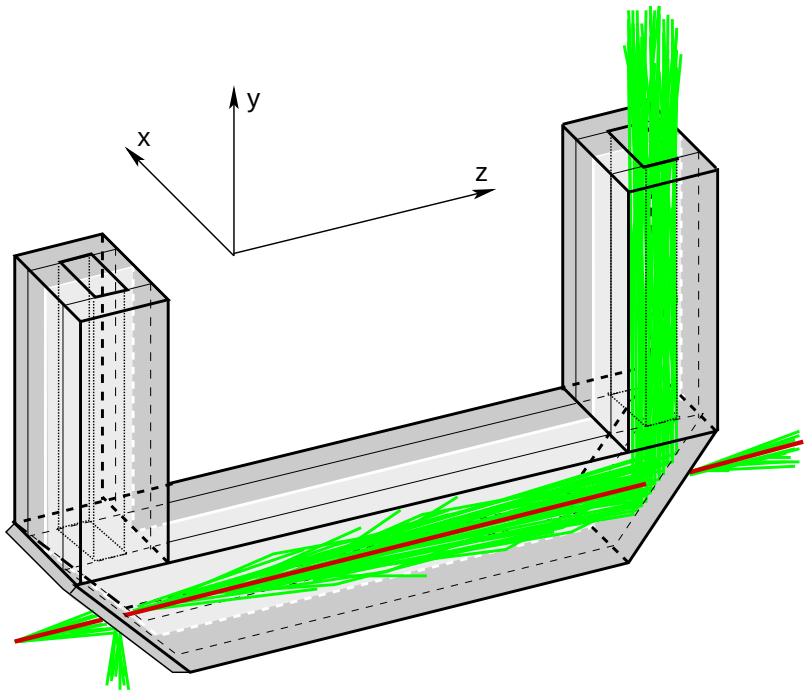

Figure 10.9: *Event display of the prototype simulation. The electron beam (red/black) passes from left to right through the U-basis of the aluminum tubes filled with perfluorobutane, C_4F_{10}, and emits Cherenkov photons (green/dark gray). These are reflected upwards to a photodetector mounted on the hind U-leg. The channels are separated by a thin foil (light gray). Due to a surrounding gas-filled box (not shown), Cherenkov radiation is also emitted before/after the electron beam enters/exits the aluminum tubes, but cannot reach the photodetector.*

in the simulation by a different wavelength dependent reflectivity. For the outer channel walls, the reflectivity values obtained from the reflectivity measurement for the diamond cut aluminum have been implemented for wavelengths from 160 nm to 900 nm. This wavelength range covers all employed PMTs. The reflectivities are linearly interpolated in between the values given in Table 10.2. The reflectivities of the inter-channel wall can be implemented in two ways: one option is to directly implement the measured lower limits given in Table 10.2, the other option is the implementation of the scaled reflectivity values of the outer channel walls. The latter option has been implemented as it became clear that the reflectivity measurements drastically underestimated the true reflectivities of the inter-channel wall. In this option, the inter-channel wall reflectivity can be adjusted via the ratio of the two materials' reflectivities $r_{ref} = R_{\text{roll}}/R_{\text{diam}}$.
The same Cherenkov gas, C_4F_{10}, as used in the detector box during testbeams is implemented in the simulation. The refractive index n of C_4F_{10} is wavelength dependent with $(n-1) = A/[\lambda_0^{-2} - \lambda^{-2}]$. This has been measured at the Ring Imaging Cherenkov Detector of the DELPHI experiment at LEP [112, 113]. For refractive indices close to one, $(n-1)$ is inversely proportional to the gas temperature and pressure [121]. The values given in Table 10.3 are calculated with the Sellmeier coefficients $A = 2.375 \times 10^{-7}$ and $\lambda_0 = 73.63$ nm from [121].

wavelength	R_{diam}	R_{roll}
160 nm	74 %	11 %
200 nm	81 %	27 %
220 nm	84 %	30 %
240 nm	86 %	37 %
500 nm	85 %	40 %
520 nm	84 %	40 %
650 nm	83 %	40 %
900 nm	82 %	39 %

Table 10.2: *The reflectivities of diamond-milled quality aluminum R_{diam} and of rolled quality aluminum R_{roll} as determined with the* PerkinElmer *spectrometer and implemented in the* Geant4 *simulation.*

wavelength	n
160 nm	1.00174
200 nm	1.00160
220 nm	1.00155
240 nm	1.00152
300 nm	1.00146
420 nm	1.00142
580 nm	1.00140
900 nm	1.00138

Table 10.3: *Wavelength dependent refractive indices C_4F_{10} for a few wavelengths.*

The beam profile can be chosen as a 2-dimensional Gaussian in the x-y-plane with the parameters σ_x and σ_y, or as an elongated beam profile consisting of the superposition of two different Gaussian beam profiles.
The detector box can be rotated about the three axes of the global coordinate system. In the simulation the pressure and temperature are kept constant at $p = 1\text{atm} = 1.01325$ bar and $T = 20°\text{C}$. Simulation runs with a pressure of $p = 2$ atm showed no significant difference in the number and distribution of Cherenkov photons.

10.6.1 Cherenkov spectrum and refractive index

The wavelength spectrum of Cherenkov radiation is given by [106]:

$$\frac{dN^\gamma}{d\lambda} = 2\pi\alpha \left(1 - \frac{1}{n^2\beta^2}\right) \frac{1}{\lambda^2}\,\ell\,, \qquad \text{with:} \quad \begin{array}{lcl} N^\gamma & : & \text{number of photons,} \\ \lambda & : & \text{wavelength,} \\ \alpha & : & \text{fine structure constant,} \\ n & : & \text{radiator's refractive index,} \\ \beta & : & \text{velocity } (\beta = \frac{v}{c}), \\ \ell & : & \text{radiator length} \end{array} \tag{10.2}$$

where the refractive index n is wavelength dependent. Since the emission of Cherenkov radiation is statistical in nature, the average number of Cherenkov photons per incident electron is expected to be poisson distributed. Figure 10.10(a) shows the average number of photons

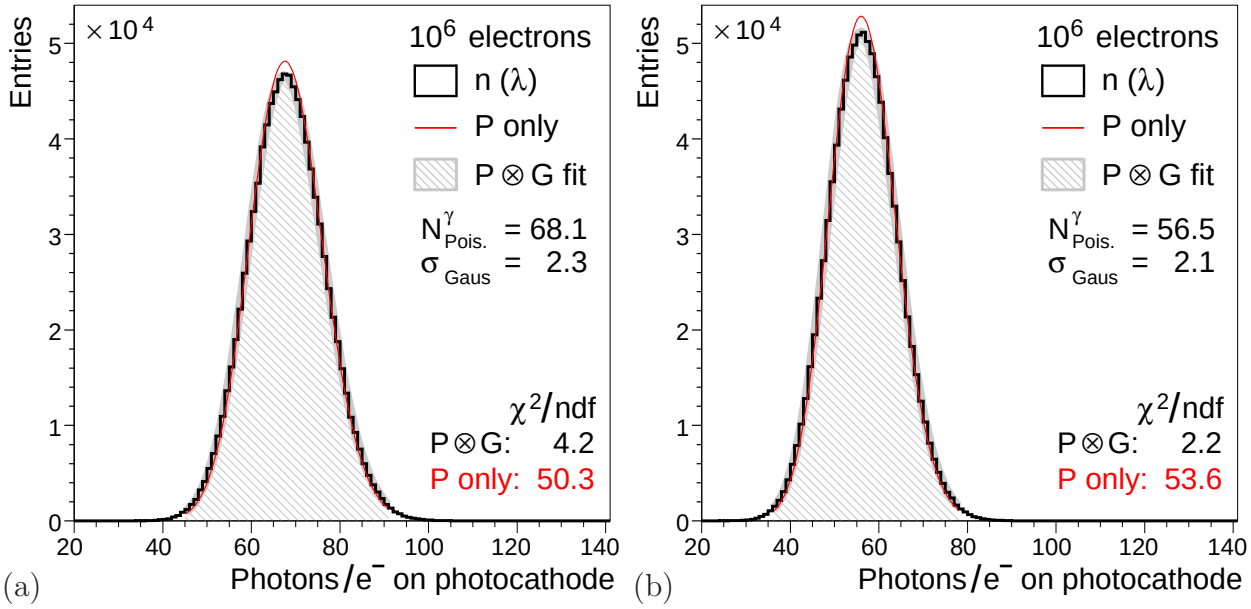

Figure 10.10: *Average number of photons reaching the photocathode per primary electron: (a) with equal reflectivities for all inner channel surfaces and (b) with a reduced reflectivity for the inter-channel wall. A poissonian fit to the spectrum is shown in both figures by the red/dark gray line. The fit of a convolution of a poissonian with a gaussian is shown by the light gray hatched area.*

per incident electron reaching the PMT, simulated for an inter-channel wall reflectivity of 100% of the outer wall reflectivity ($r_{ref} = 1.0$) and 1 million electrons. The beam spread is $\sigma_x = \sigma_y = 0.5$ mm, and the C_4F_{10} refractive index is wavelength dependent. On average 68.1 photons reach the PMT cathode. A poissonian fit (red/dark gray) to the distribution yields a χ^2/ndf of 50.3. The result can be improved when an additional gaussian contribution to the number spectrum is allowed for. The convoluted gauss/poisson fit (P⊗G, light gray hatched) converges with a χ^2/ndf of 4.2. The width of the gaussian is $\sigma = 2.3$. Figure 10.10(b) shows the same number distribution for $r_{ref} = 0.5$. Again, the number spectrum is best described with a gaussian contribution to the poissonian fit. Possible explanations considered for the deviation from the pure poissonian distribution are influences from the non-point like beam profile and the wavelength dependent refractive index n.

Figure 10.11 shows the number distribution of photons at the photocathode per incident electron, simulated for 10^6 e^- and a point-like beam. The black histogram shows this distribution for a wavelength dependent refractive index, while the green (dark gray) histogram is for a refractive index set to a constant value of $n = 1.0014$. In case of the wavelength dependent refractive index, the average number of photons is unchanged with 68.1. The poisson-only fit yields a very large χ^2/ndf of 48.5, and the gaussian-convoluted fit (P⊗G) has a χ^2/ndf of 3.8 with a gaussian width of 2.3.

The distribution for a constant refractive index n yields on average 64.3 detected photons per

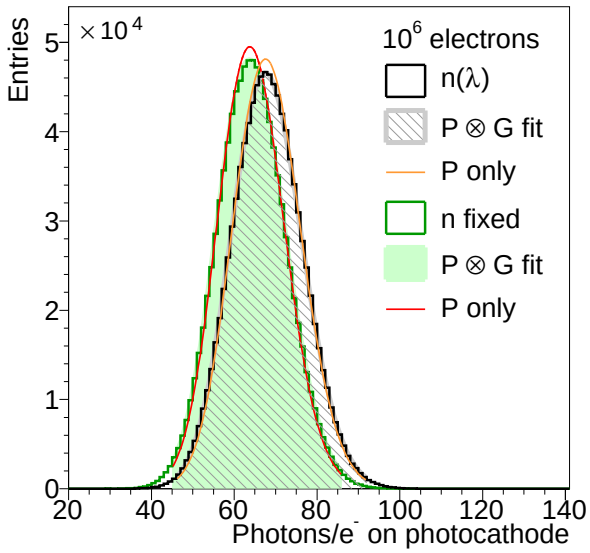

Figure 10.11: *(a) Number distribution of photons at the photocathode per incident electron, simulated for* 10^6 *electrons and a point-like beam profile. The black histogram shows the distribution for a wavelength dependent refractive index. The orange line shows the poissonian fit to the distribution and the gray hatched area is the result of a fit with a convolution of poissonian and gaussian yielding a mean of 68.1 photons. Analogously, the green histogram is the distribution for a fixed refractive index* $n = 1.0014$*. The convoluted poissonian and gaussian (green area) with a mean of 64.3 reproduces the distribution better than the pure poissonian (red line). The* χ^2/ndf *values are mentioned in the text.*

incident electron. The average number of photons is reduced, since the bulk of the Cherenkov photons is produced at small wavelengths, where the wavelength dependent refractive index exceeds the constant value. Still, the poissonian only fit is with $\chi^2/ndf = 42.1$ very large, and an additional gaussian width of 2.2 is required ($\chi^2/ndf = 2.8$). In conclusion, both considered effects (the beam profile and the wavelength dependent refractive index) are not responsible for the gaussian contribution to the number distribution of detected photons.
In Figure 10.12(a) the wavelength distribution of Cherenkov photons per incident electron on the PMT cathode is shown in the dotted histogram. The spectrum is cut-off according to the range of implemented refractive indices of the Cherenkov gas C_4F_{10}. The distribution has the expected $1/\lambda^2$ dependency. In order to obtain the number of detected photons, this spectrum has to be folded with the quantum efficiency (QE) of the employed PMT. The QE is the wavelength dependent probability of detecting a photon in the wavelength interval $(\lambda; \lambda + d\lambda)$. In the inlay of Figure 10.12(a) the QE of the M4 MAPM is depicted, with a peak efficiency of $\approx 25\%$ at 400 nm. The photon spectrum after folding is shown in black in Figure 10.12(a), and with a different scale in Figure 10.12(b). Integration over the spectrum yields an average of 6.5 detected Cherenkov photons per incident electron. In comparison, simulations of the SLD Cherenkov detector yield between 5.5 to 6.6 photoelectrons per incident electron [111]. The SLD detector had a 33% longer Cherenkov length, but also a more complicated channel

geometry with more reflections on average which, in turn, partially canceled the higher photon yield from the longer Cherenkov section.

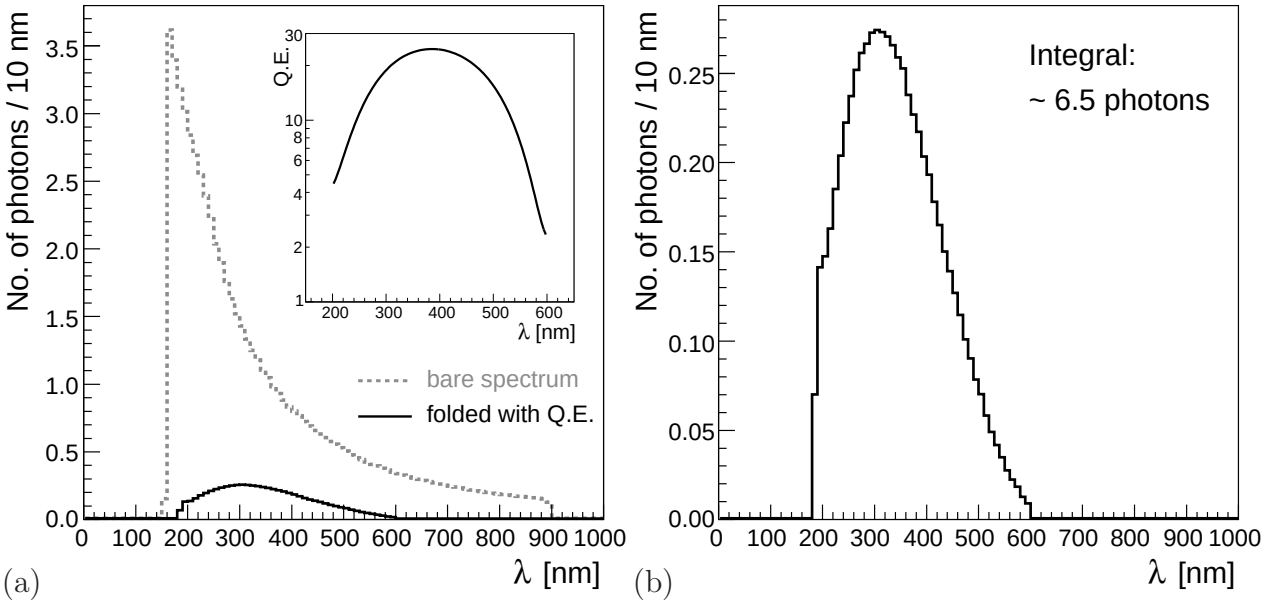

Figure 10.12: *Cherenkov spectra: (a) after the* GEANT4 *simulation (dotted line) at the surface of the photodetector, (b) convoluted with the quantum efficiency of the 2×2 MAPM (R7600U-03-M4), see the insert in (a). The convoluted spectrum is also superimposed in (a) as the solid black line.*

10.6.2 Light yield and distribution on photo cathode

The light distribution on the photocathode for an optimally aligned detector is influenced by the channel geometry and the reflectivity ratio r_{ref} between the inter-channel wall and the outer walls. Figure 10.13(a) and (b) show the light yield on the photocathode for a relative reflectivity $r_{ref} = 1.0$ and $r_{ref} = 0.5$, respectively. The light distributions are simulated for the left detector channel. The inter-channel wall is also located on the left, since the x-axis of the global coordinate system points to the left. As a general feature, in both cases an x-shaped structure is visible in the light distribution.

This structure is the result of folding the Cherenkov cone with the quadratic channel cross section as illustrated in Figure 10.14(a). The Cherenkov cone on the PMT surface for all photons with at least one reflection is drawn as the dashed red circle. Folded with the quadratic cross section of the Cherenkov channel the arcs outside the channel cross section are reflected inwards, resulting in the x-shaped light distribution. Further visible features are the depleted zones at $z \approx \pm 1$ mm. Backtracing of the photon paths as depicted in Figure 10.14(b) revealed a correspondence between these depleted zones and two distinct regions of the channel walls from which no light is reflected towards the PMT. Finally, in Figure 10.13(b), for a reduced inter-channel wall reflectivity a left-right light asymmetry is observed, with a reduced light yield on the side of the inter-channel wall.

The effect of the inter-channel wall on the light distribution is schematized in Figure 10.15. Depicted are the light paths of Cherenkov photons emitted from electrons travelling along the

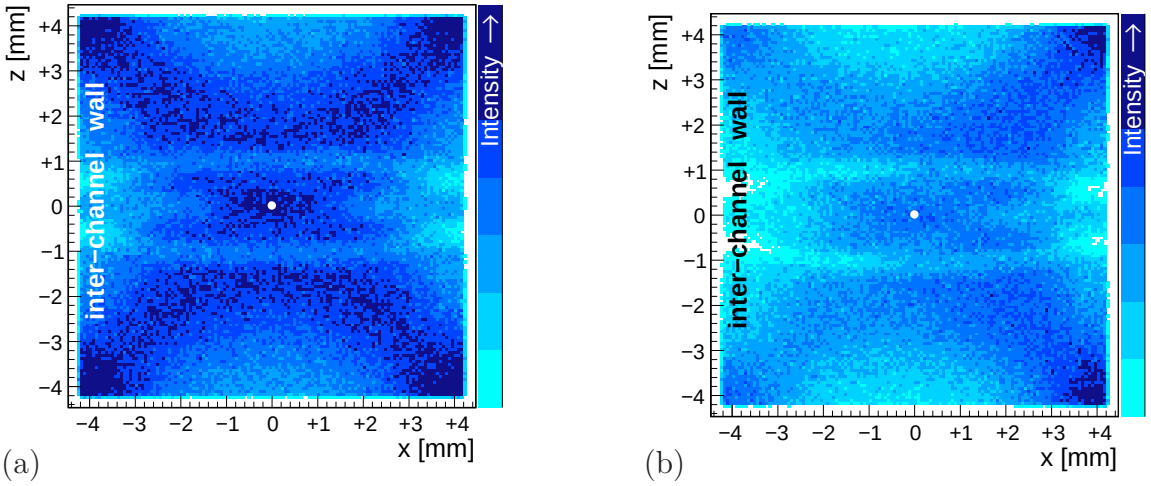

Figure 10.13: *Light yield distribution on the photocathode. (a) For equal reflectivies of inter and outer channel walls, the distribution is symmetric about $x = 0$ mm. (b) With a reduced inter-channel wall reflectivity, the light yield is asymmetric about $x = 0$ mm. The white dot indicates the central position of the incident electrons, translated to the cathode position.*

central axis of the detector channel. On average, only one reflection for Cherenkov photons from on-axis electrons is observed. Photons emitted horizontally or vertically in the x-z-plane or the y-z-plane, respectively are evenly distributed on the PMT cathode (Fig. 10.15(a)). For all other directions the effective channel width increases, and the light ends up primarily on the same side it has been emitted into (Fig. 10.15(b)). The reduced reflectivity of the inter-channel wall therefore leads to a reduced light yield on the same channel side. In the Figures, the 90° reflection at the end of the Cherenkov length is indicated by the dotted vertical line. This additional reflection has no influence on the symmetry of the light distribution in x.

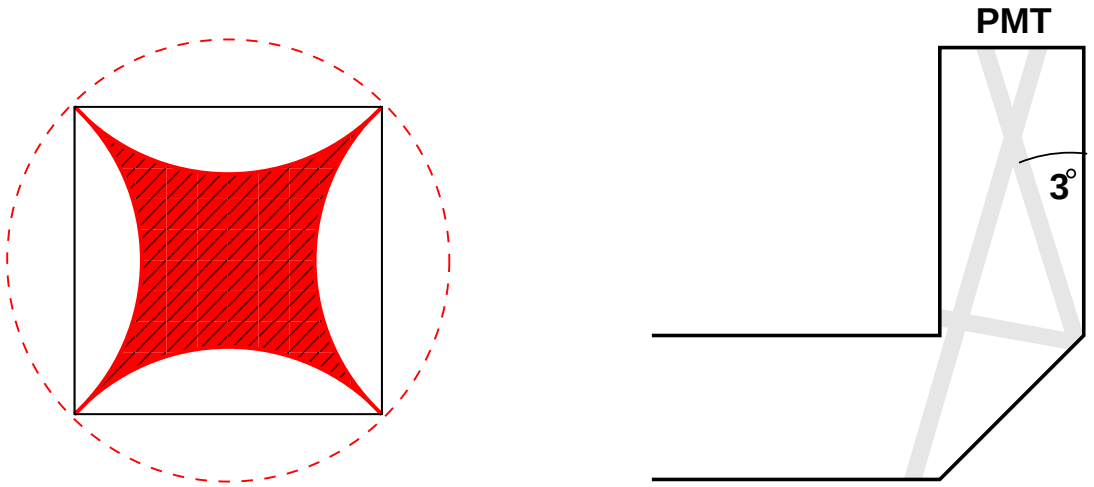

Figure 10.14: *(a) Quadratic channel cross section with Cherenkov cone cross section for photons with at least one reflection. The Cherenkov cone is folded to the inside of the channel, resulting in the x-shaped structure of the light distribution. (b) Origin of the depleted zones visible in the light distribution at $z = \pm 1$ mm. The depleted zones are traced back assuming the typical Cherenkov cone angle of $\approx 3°$ for relativistic electrons in C_4F_{10} (Picture not to scale).*

(a) horizontal/vertical emittance of photons

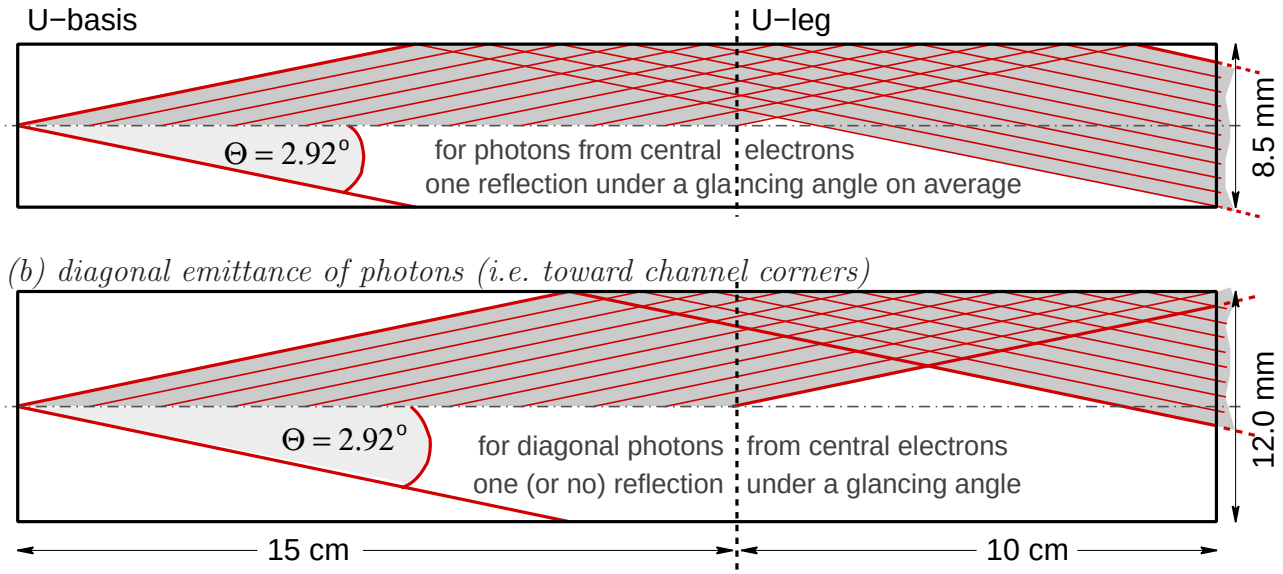

Figure 10.15: *Light paths for Cherenkov photons emitted from electrons travelling along the central axis of a detector channel. (a) Light paths for photons emitted in the horizontal (x-z) and vertical (y-z) plane. (b) Light paths for photons emitted towards the channel corners, for which the effective channel width increases. The 90° reflection at the end of the Cherenkov length is indicated by the dotted vertical line. It has no influence on the symmetry of the light distribution in x.*

Chapter 11

Testbeam campaigns

In 2009 the assembled Cherenkov detector prototype has been operated in the testbeam area 22 of the DESY II accelerator for the purpose of functional tests. Results from this testbeam period were used for improvements of the experimental setup, implemented in two testbeam periods at the ELSA accelerator in 2009 and 2010.

11.1 Experimental setup

In both testbeam campaigns at DESY II and ELSA, the experimental setup was intended to allow for a range of measurements, including functional tests, HV-scans and relative movements of the prototype with respect to the electron beam.

11.1.1 DESY testbeam

The detector prototype was tested in testbeam area 22 with a "tertiary" beam of the 7 GeV synchrotron DESY II. First, a bremsstrahlung beam is generated by a carbon fiber inserted into the primary electron beam circling in the synchrotron. Secondly, the photons are converted to electron/positron pairs via a metal plate converter target. With a following dipole magnet, the electrons are separated from the positrons, then collimated and finally guided to the different experimental areas. Figure 11.1 shows a schematic of the creation of the DESY II tertiary beam [122]. The maximal extraction rate is 5 kHz. During the testbeam campaign, the energy collimator was used to select 3 GeV electrons. Because of the flat electron energy distribution and the collimation, only single electrons reached the experimental area and thus the prototype.
The detector prototype was located on a heavy, remote-operable movable stage. The baseplate with the rotational mechanism was not installed. For read-out, the PMT signal was transferred to the control hut of area 22 by LEMO cables of $l \approx 15$ m length. The setup could only be used for functional tests since a precise movement and orientation of the detector box w.r.t. the beam was not possible. The movable stage could be steered in 1 mm steps which, however, proved to be unreproducible. The testbeam campaign was therefore primarily used to perform functional tests, and record single-electron data at high PMT voltages, to be compared to the results of the multi-electron events recorded during the ELSA testbeam

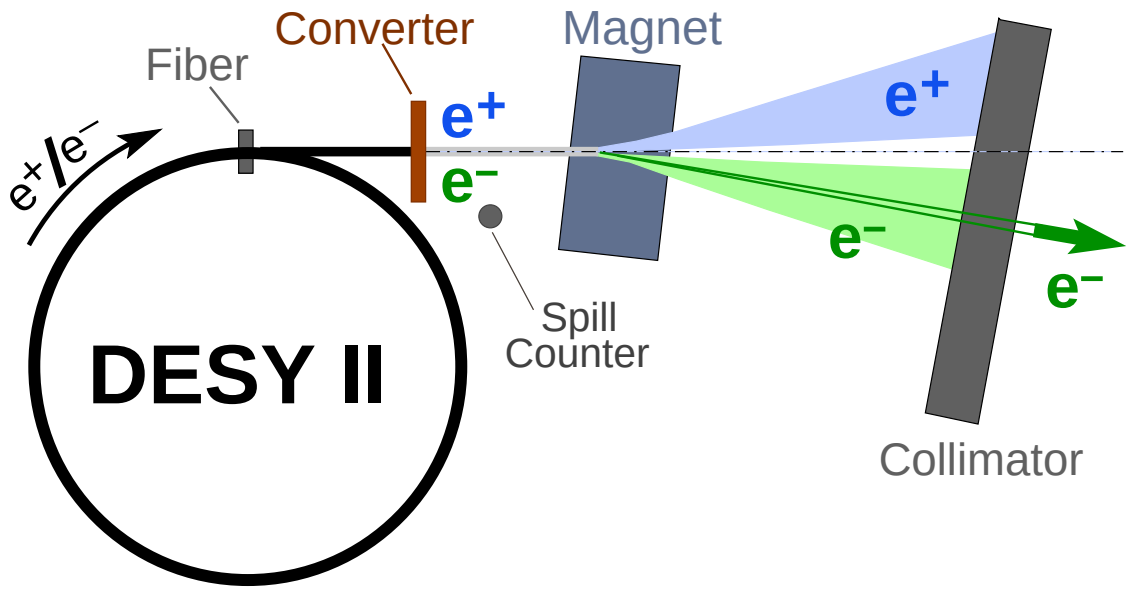

Figure 11.1: *Schematic drawing of the* DESY II *accelerator and the creation of the tertiary beam [122].*

campaigns. In addition, the data driven alignment method for the angle α_y was developed and tested (cf. Sec. 11.2).

11.1.2 ELSA testbeam

During the testbeam campaigns at the ELSA accelerator in Bonn, the Cherenkov detector prototype was set up in the extraction line of the former SAPHIR experiment. The SAPHIR area is located in the upper left of the ELSA site plan in Figure 11.2 [123]. The Electron-Stretcher-Anlage (ELSA) in Bonn is a three stage electron accelerator [124]. Two linacs inject either 26 MeV polarized or 20 MeV unpolarized electrons into a booster synchrotron of 0.5–1.6 GeV. The synchrotron acts as pre-accelerator to the ELSA stretcher ring. The electrons are transferred to the stretcher ring which can be operated in three different modes:

- **Stretcher mode:** Single pulses from the synchrotron are injected into ELSA. With a slow extraction at a third integer tune, an electron beam of constant intensity is obtained.
- **Booster mode:** ELSA is used as an additional acceleration stage. Several synchrotron pulses are injected, and accelerated to the maximum energy of 3.5 GeV.
- **Storage mode:** When ELSA is used as a synchrotron radiation source, a large number of pulses is stored in ELSA for several hours.

During the testbeam campaigns the accelerator was operated in booster mode, with the electrons injected into the stretcher ring at 1.2 GeV and then accelerated to 2.0 GeV. The momentum uncertainty on the extracted electrons is $\Delta p/p = 0.05\%$.

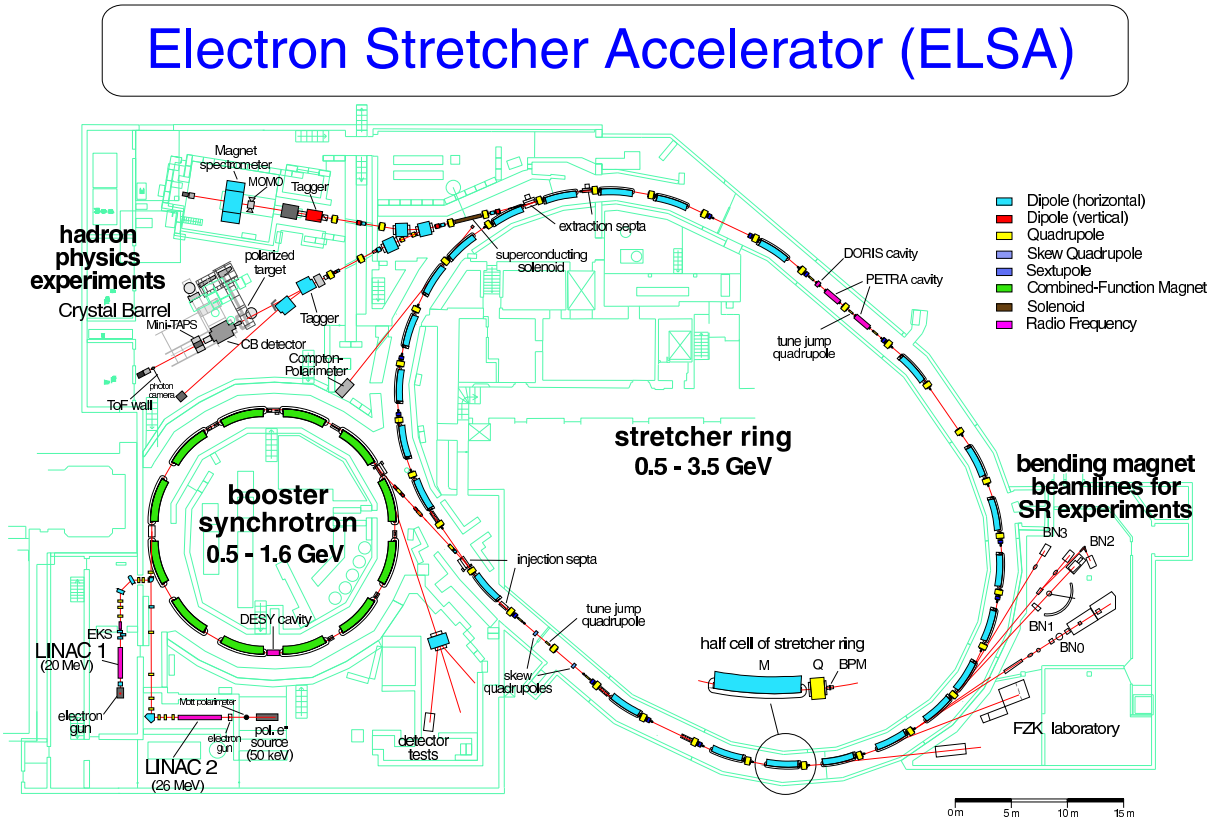

Figure 11.2: *Site plan of* ELSA *in Bonn. The beam tests with the prototype detector were done in the former* SAPHIR *experimental area, at the uppermost left extraction line of the stretcher ring [123].*

In the testbeam area a dipole magnet bent the extracted electrons downward to a beam dump in the floor resulting in a slope of the beamline of roughly 7.5 degrees. The prototype itself was mounted on a movable stage[1] and located directly in the downward sloping beamline after the dipole magnet. With the momentum uncertainty of 0.05% a dispersion of ≤ 0.1 mrad is expected, negligible w.r.t. the size of the beam profile in the order of millimeters.
Figure 11.3 shows the setup of the Cherenkov detector. The bending dipole is located to the left of the picture, the beam dump is in the lower right. The movable stage enabled detector movements along the x- and y-axis in steps of 0.2 mm, effectively scanning the electron beam over the front face of the detector. The detector box is mounted on the black base plate with the rotating mechanism. On top of the detector to the right a round single-anode photodetector (SAPM) in its mounting is visible. The employed photomultipliers were connected to a HV source and the signal was read out with one of the CAEN QDCs (V965A,

[1]The movable stage and steering software were kindly provided by the TPC group of Bonn university.

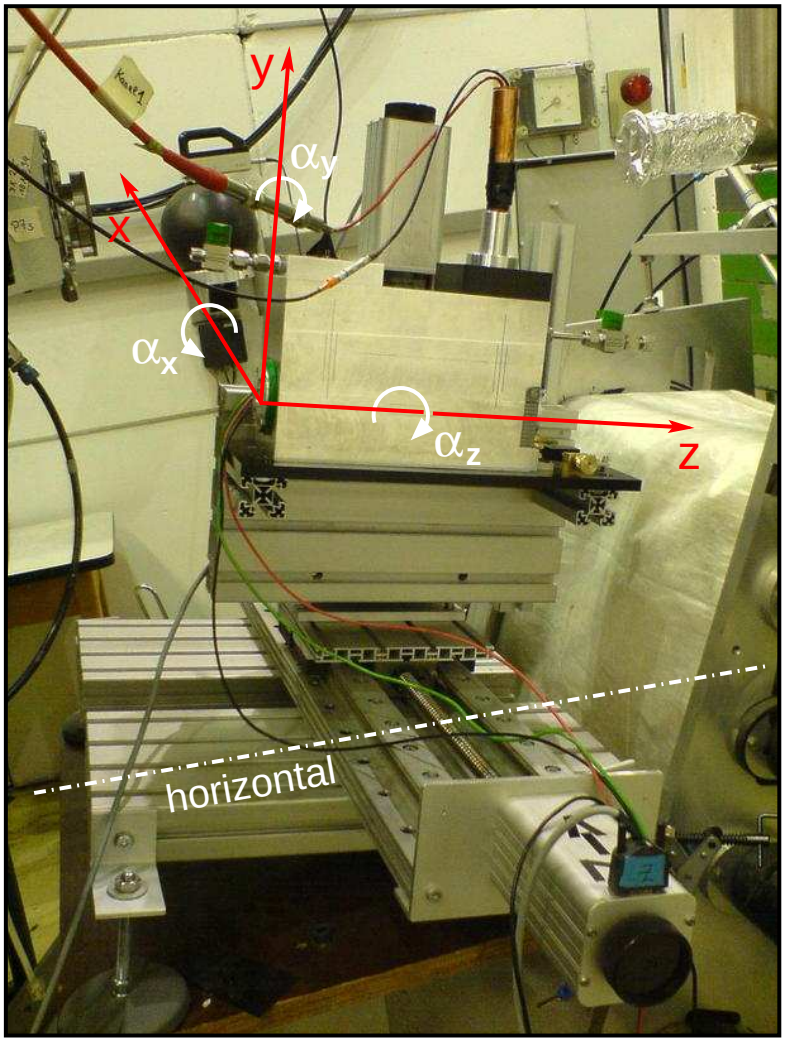

Figure 11.3: *The prototype Cherenkov detector on its base plate (black, with the rotational mechanism visible on the right) is mounted on a stage moveable along the x- and y-axis.*

V965). The digitized QDC responses were transmitted via VME bus to a PC. The data was stored in the ROOT TTREE data format. For reference, a textfile with all run parameters was automatically written.
The gate signal was provided by the ELSA beam clock with the revolution time of 548 ns and a function generator was used to set gate lengths in between 100 ns and 480 ns, depending on the measurement objectives. Figure 11.4 shows a simplified block diagram of the readout chain. Depicted is the 8 channel QDC (model V965A) used in 2009. In 2010 the QDC was exchanged for a 16 channel QDC (model V965).
The extraction cycle had a period of 5.1 s. During the first 4.0 seconds the beam is extracted, the remaining 1.1 seconds are used to refill the stretcher ring and accelerate the electrons again. During these "refill and acceleration phases", no electrons are extracted, and the data recorded in this time shows only the pedestal current of the employed QDC.
Figure 11.5 shows the fill structure of the stretcher ring for four revolution cycles of 548 ns each. Of the 274 available buckets a variable fraction can be filled. For the measurement about half of the buckets were used. The extracted current could be adjusted from approximately

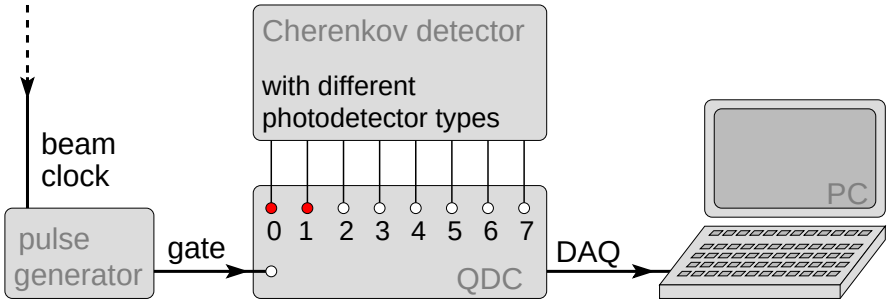

Figure 11.4: *Block diagram of the readout chain during the* Elsa *testbeam campaigns. During the 2009 campaign an 8-channel QDC was used, in 2010 a different QDC was employed that could digitize 16 channels simultaneously.*

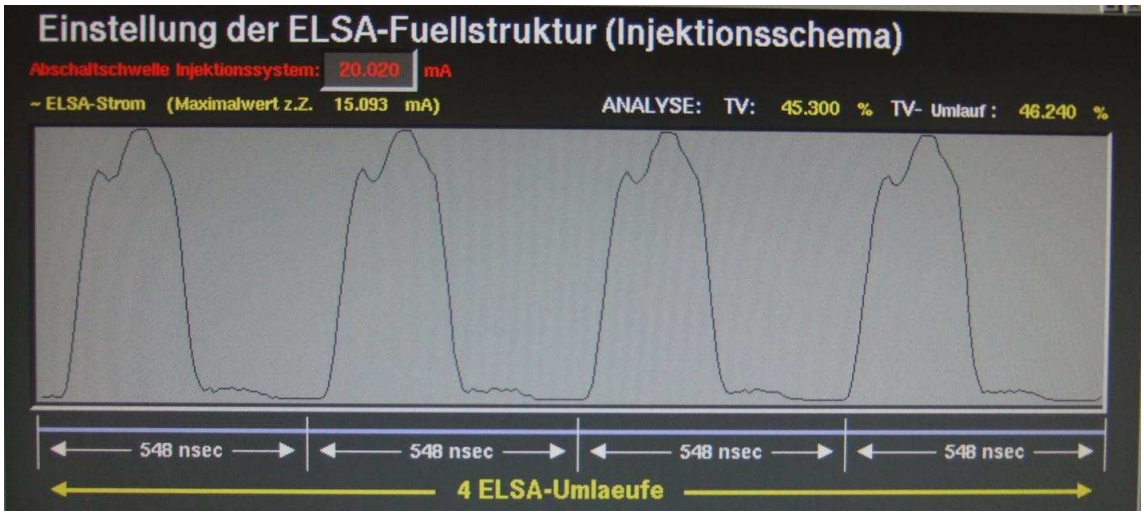

Figure 11.5: *Typical fill structure of the* Elsa *accelerator (graphic from 2009). Four revolutions of 548 ns each are depicted, roughly half of the available buckets are filled with electrons.*

10 to 250 pA, which translates to 35 to 700 electrons traversing the prototype channels per revolution period. The beam spot of the extracted electrons had a size of 1 to 2 mm.
The detector was filled with C_4F_{10} at a slight overpressure of about 130 mbar. The pressure was monitored with a pressure gauge, and found to be stable over the measurement series with each photodetector. The individual PMTs were operated over a few days each, and then exchanged for the next PMT to be tested. This frequent setup changes prevented pressure monitoring over periods longer than a week.
The program of each photodetector test consisted of

- **HV-scans** with a nominal extraction current of 100 pA to determine the optimal HV working point for the PMT,
- **x- and y-scans** with different box rotations about the y-axis. For the scans the beam was scanned over the detector front face along the x- and y-axis to determine the channel

position relative to the electron beam and to allow a subsequent deduction of detector misalignments.

- **Beam current scans (bc-scans)** for a fixed detector position and variable extraction currents. These were intended to measure the linearity of the Cherenkov detector.

For a first by-eye alignment, fluorescent KROMOX screens were attached to the detector entrance window, and in 2010 also to the exit window. One (two) CCD cameras were installed and connected to a switch panel to allow monitoring of the fluorescent screen(s) from the ELSA control room. Figure 11.6 shows typical signals recorded during the ELSA testbeam campaigns: (a) in 2009 and (b) in 2010. In (a) the gray filled histogram shows the dark current pedestal, when no electrons are extracted from ELSA. The pedestal position is given by the internal pedestal current of the QDC and depends on the gate length. With electrons extracted, a signal peak appears to the right at higher QDC counts. The 4 s to 1.1 s extraction/refill+acceleration cycle of ELSA is visible in the ratio of 4 to 1 of the signal and pedestal peaks. The signal height is given by the pedestal subtracted QDC response.

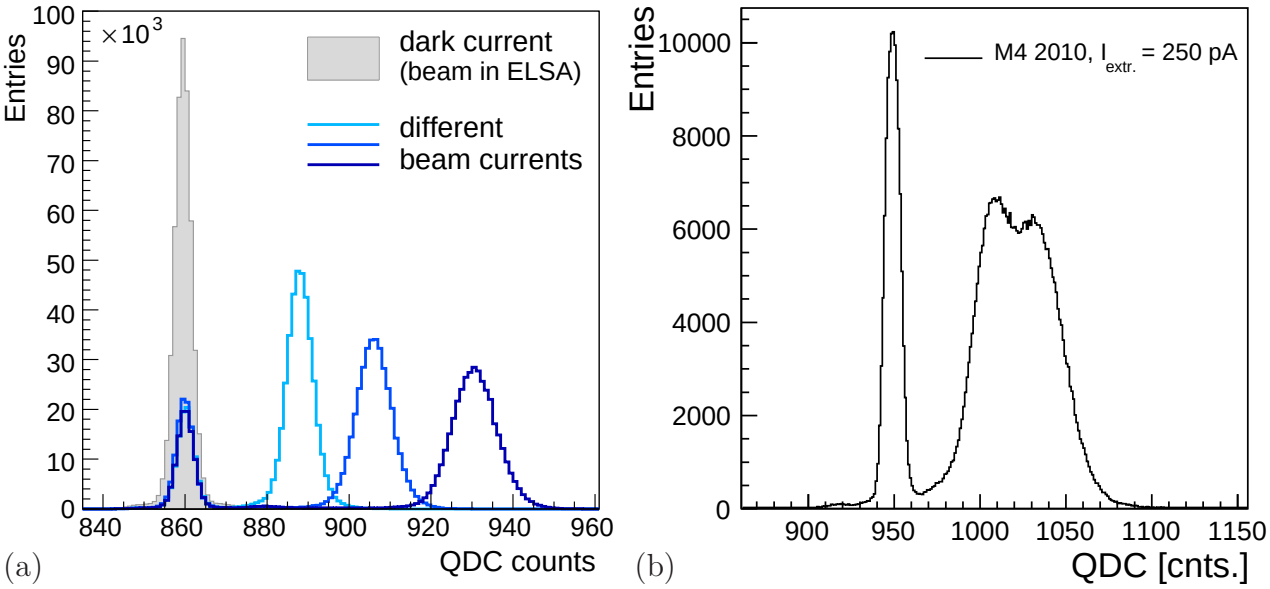

Figure 11.6: *(a) Typical QDC responses at* ELSA *for different extraction currents in 2009. The gray filled histogram shows the pedestal when no electrons are extracted. With increasing extraction currents, the signal peak to the right of the pedestal moves to higher QDC counts. The 4s to 1.1s extraction/refill cycle of* ELSA *is visible in the ratio of 4 to 1 of the signal and pedestal peaks for each of the three different beam currents. (b) Signal observed in 2010. No source of the unexpected double peak signal has been found in the measurement setup. One probable explanation are unstable beam conditions.*

In 2010, the beam conditions at ELSA were rather unstable. For high supply voltages and large extraction currents, a double peak signal structure has been observed, shown exemplary in Figure 11.6(b) for the M4 MAPM with a nominal extraction current of 250 pA. The reason for the observed double peak has not been found yet.
To exclude the PMTs as source of this signal structure, the measurements have been repeated

with all available PMTs. In addtition, each PMT has recorded data with the LED calibration system, showing the expected single peak signal shape. Furthermore both QDCs and all QDC channels have been tested. Different lengths and configurations of the readout cables have also been investigated. Since the double peak structure was only observed in beam data, it is supposed that the source of this peculiar structure lies within the ELSA accelerator itself. The double peak structure limited the supply voltages and extraction currents to a smaller range than in 2009, i.e. to values where the signal resembled more closely a single peak.
For measuring the response to the electrons passing the detector, the signal and pedestal peak of each run are fitted with a gaussian. The signal is then given by the difference of the gaussian means of signal and pedestal. In cases where the signal exhibits the afore mentioned double peak structure, the entire double peak is fitted with a single gaussian. This is necessary because neither the peak at lower QDC counts nor the one at higher counts continues the progression of signal heights for increasing extraction currents without a step in the expected linear behavior.

11.2 Detector alignment

Understanding and controlling the alignment of the detector w.r.t the electron beam is required to limit systematic errors on the analyzing power calibration for the final ILC polarimeter (cf. Sec. 9.3.3). In the scope of this analysis, different methods have been developed to validate the GEANT4 simulation with the data recorded at ELSA.
In the ELSA testbeam campaigns the experience gathered from the functional tests at DESY II was used to develop a fast method to determine the detector alignment from data. A more thorough alignment analysis has been performed after the testbeam periods, relying on extensive simulations of various translatory and rotational misalignments. Since different PMT types have been used, and because no decision on the final ILC Cherenkov detector has been made to date, the methods presented in the following sections can only provide a first outlook on alignment strategies at ILC.

11.2.1 Alignment during testbeam periods

In the two testbeam periods at ELSA, a first alignment of the detector with respect to the beam was performed using a spirit level to adjust the rotation about the z-axis. The precision of this adjustment is estimated to 2°. In simulations no influence on the analyzed observables from rotations of α_z only of this magnitude have been detected. For on-axis electrons in the channel center the system is fully symmetric about the z-axis. For off-axis electrons a rotation of α_z rotates the relative beam position on the channel entrance by distances of $\mathcal{O}(10^{-1})$ mm, negligible in comparison to the stepwidth of the movable stage and the profile of the extraced electron beam. However, effects from combined rotations about all three axes for point-like beams have to be considered and measured at future testbeam locations providing the corresponding beam and detector parameters.
The angle α_x was adjusted by eye to the electron beam slope of 7.5 degrees. In order to improve the alignment, the electron beam position has been monitored via the fluorescent plates attached to the detector entrance and exit windows. The box rotation about the x-axis was adjusted until the beam electrons entered and exited the detector box during the centers

of the KROMOX plates. The estimated precision on α_x is 1° in 2009 and 0.5° in the 2010 campaign, respectively. This difference in precision is due to the fact that in 2009 only the entrance window of the detector box was equipped with a KROMOX screen, while the beam exit position was roughly determined with photographic paper held into the beamline at the beginning of data-taking.
The remaining angle α_y about the y-axis was determined from data of a series of dedicated x-scans with different rotations α_y, adjusted with the rotational mechanism of the detector box base plate. Tilts of the detector box change the paths of the Cherenkov photons within the channel geometry and therefore the average number of reflections is tilt dependent. The maximal signal is expected for a perfectly aligned detector. Figure 11.7 shows the pedestal cor-

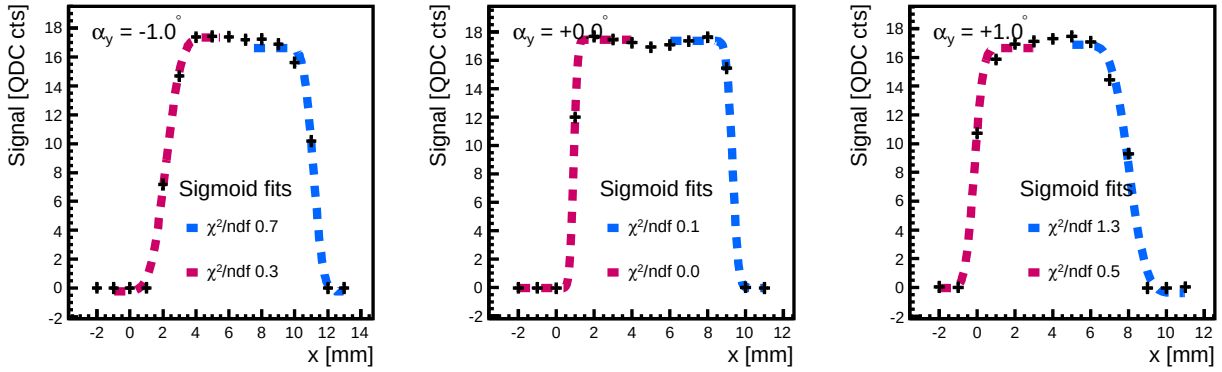

Figure 11.7: *Signal response of the R7400-06 in three x-scans with different rotations* $\alpha_y = -0.1,\ 0.0,\ +0.1$ *deg. Also shown are sigmoid fits to the signal flanks.*

rected detector response for three x-scans with different rotations $\alpha_y = -0.1°,\ +0.0°,\ +0.1°$ recorded with the R7400-06 SAPM in 2010. The signal edges are fitted with a sigmoid function (cf. Sec. 11.2.2), with values of χ^2/ndf from < 0.1 to 1.3. From each x-scan with a given angle the maximal recorded signal is histogrammed versus α_y, and the resulting curve fitted with a second order polynomial.
Figures 11.8 show the fit to the 2009 data for (a) the left and (b) the right detector channel. The alignment scans were recorded with the M4 MAPM. The fit results for the two channels differ by 0.18° taken as a systematic error. From simulation an additional uncertainty of 0.14° is estimated giving a total systematic uncertainty of 0.23°. The zero position has been set to 1.3° from these results.
In the 2010 campaign the alignment scans were recorded with the R7400-06 SAPM, see Figure 11.9. Since only one detector channel can be read out with this PMT, no comparison between the left and the right channel is possible and the systematic error of the α_y alignment for the 2010 data has been assumed to be the same as for the 2009 data. All PMTs had to be operated at lower voltages in 2010 than in 2009, because of unstable responses at higher voltages leading to lower signal levels. The lower signals are reflected in larger statistical errors in the angle determination, comparable to the systematic errors. Table 11.1 summarizes the systematic uncertainties on the rotational detector alignment for both the 2009 and the 2010 testbeam campaigns.

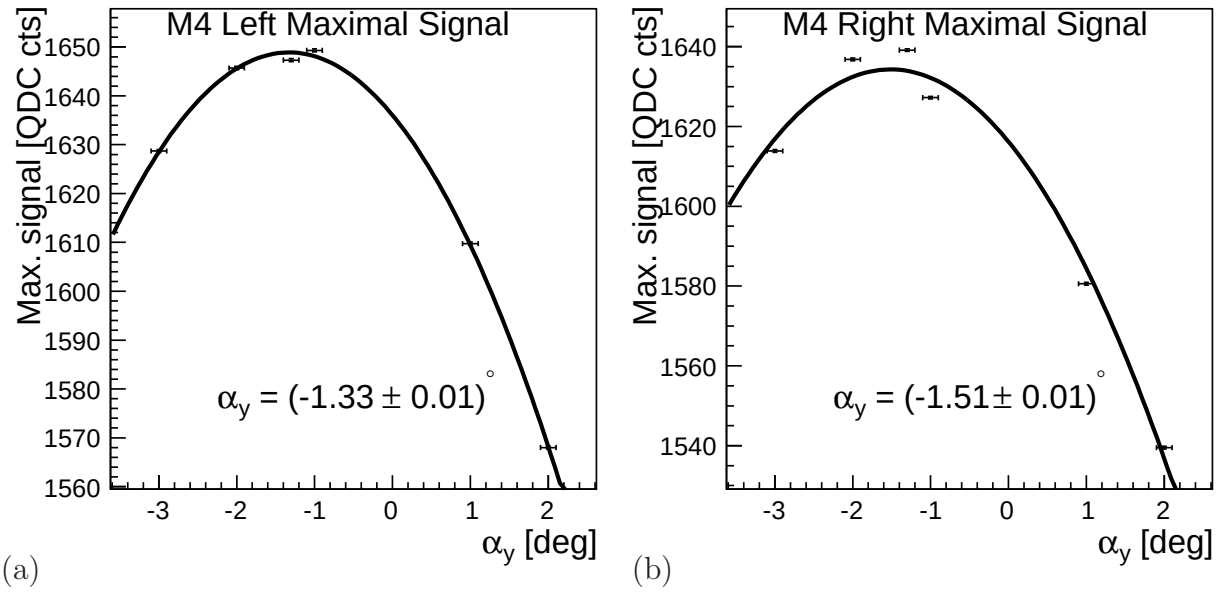

(a) (b)

Figure 11.8: *Maximal signal height in a series of x-scans as function of the angle α_y in the 2009 data. The data is plotted for (a) the left and (b) the right detector channel. The employed PMT is the M4 MAPM.*

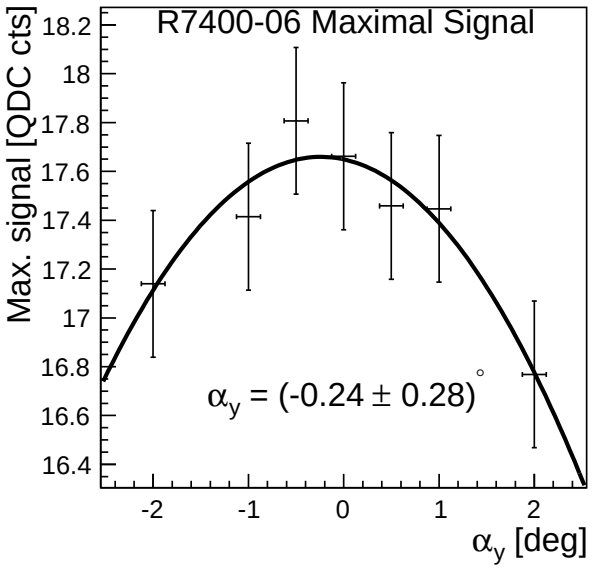

Figure 11.9: *Maximal signal height in a series of x-scans as function of the angle α_y in the 2010 data recorded with the R7400 SAPM. See also Figure 11.7.*

11.2.2 Alignment with simulated data

The detector box orientation has been analyzed after the testbeam campaigns by comparing data and simulation. Two methods have been explored: one is applicable to all photodetector types, the other method requires multi-anode PMTs that resolve the light distribution within a single detector channel.

	$\Delta\alpha_x$ sys.	$\Delta\alpha_y$ sys.	$\Delta\alpha_z$ sys.
2009	1.0°	0.23°	2.0°
2010	0.5°	0.36°	2.0°

Table 11.1: *Systematic errors on the detector alignment from the online analysis for the three angles α_x, α_y and α_z.*

The first method for a measurement of α_y relies on the determination of the observed channel width as a function of the signal threshold. This method works for all PMTs, since only the integrated light distribution for an entire channel is required. The channel width is determined by fitting the signal edges for a given x-scan with the gaussian error function which is given by the integral of a gaussian from 0 to x:

$$erf(x) = \frac{2}{\sqrt{\pi}} \int_0^x e^{-t^2} dt. \tag{11.1}$$

In the context of the PMT signal shape in an x-scan, the error function is the convolution of the gaussian beam profile in one dimension with the rectangular acceptance of the Cherenkov channel. The channel width at a given signal threshold T is measured as the distance of the intersections of a constant with value T% of the maximal signal, with the error functions on both edges of the signal shape (see Fig. 11.7). For an electron beam travelling parallel to the z-axis the observed channel width at 50% should be equal to the geometric channel width, when the influence of electromagnetic showers and scattered electrons in the channel walls are not considered.
The sigmoid slope at 50% is determined by the width of the beam profile, with steeper slopes for narrower beams. The width of the beam profile has been determined to $\sigma_{x,y} = 0.5$ mm from comparison of the data with simulations of different beam profiles.
With the influence of the channel walls taken into account, the observed channel width at 50% is larger than the geometric channel width. For a gaussian beam profile with a lateral width of $\sigma_{x,y} = 0.5$ mm, the geometric channel width is observed in simulations at ≈ 59% signal height.
The observed channel width as function of the threshold T for different rotations α_y about the y-axis is shown in Figure 11.10(a). The curves are simulated for the M64 MAPM, with the PMT response integrated over the full sensitive area of the PMT. The curves coincide for rotation angles with different signs, thus this method is only sensitive to the absolute value of α_y. With increasing rotation angles the geometric channel width is observed at successively lower thresholds, and the functional relationship between the threshold and the channel width becomes steeper. Also presented in Figure 11.10(a) are the channel widths determined from data recorded for the M64 MAPM in 2009 and 2010. A systematic shift to larger channel widths is observed in the data. In order to try and explain this behavior, different beam sizes and positional shifts of the PMT with respect to the channel center have been simulated, but consistency between data and simulation could not be established. A possible explanation is a systematically too small movement of the movable stage for a given input current to the stepping motors driving the stage. The stage has not been calibrated during the testbeam campaigns, and was not available afterwards. Other reasons are additional cross talk, not accounted for in the simulation, and effects from showering of electrons in the 0.15 mm box

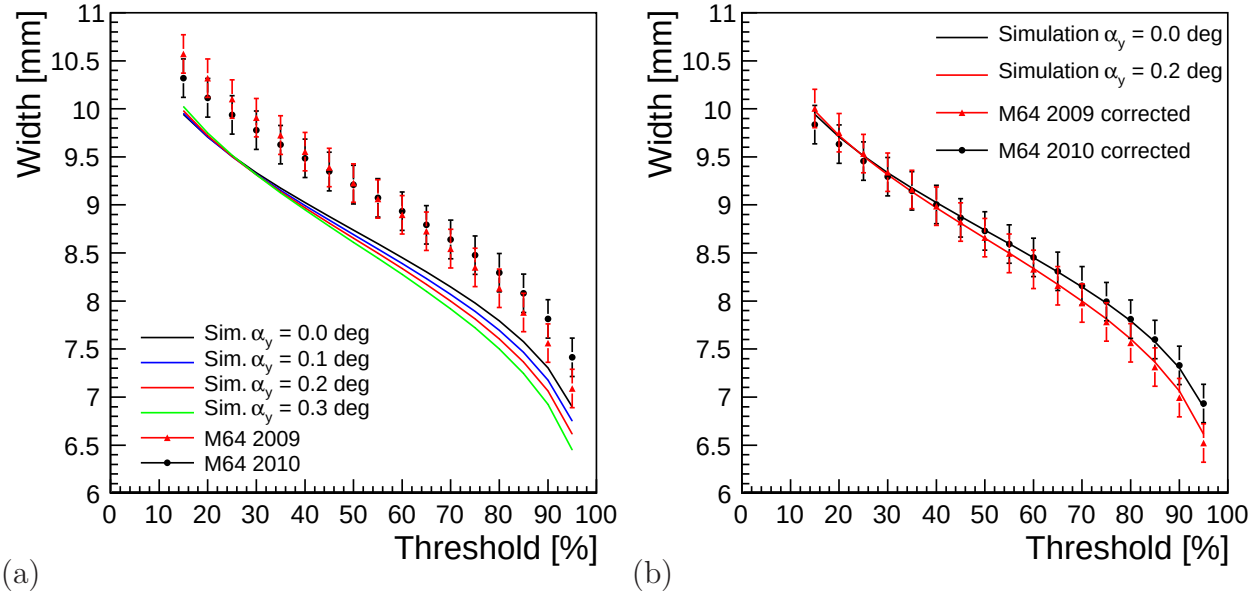

(a) (b)

Figure 11.10: *(a) Observed channel width as function of threshold for different box rotations $|\alpha_y|$ from 0.0 deg to 0.3 deg. The solid lines show the simulation results for the M64 MAPM. Also shown are the data points for two runs from 2009 and 2010, taken with the M64 MAPM. (b) The M64 channel width data corrected for the systematic bias observed in (a), and the best fit simulation curves shown as the solid lines.*

entrance window (cf. Sec. 10.1), not implemented in the simulation.
When the shifts in data are considered as a systematic constant bias, the data can be corrected and compared to the simulation. For each simulated angle α_y the data has been shifted, so that the geometric channel width of 8.5 mm is measured at the same threshold in the corrected data as in the simulation and the χ^2 is determined. The best concordance between the 2009 data and the simulation is found for an angle of $|\alpha_y| = 0.2° \pm 0.1°$. In the 2010 data, the width function is best described by the simulation with $|\alpha_y| = 0.1° \pm 0.1°$. The corrected data points alongside the corresponding simulated curves are shown in Figure 11.10(b). The data errors are purely systematic, and reflect the position resolution of the movable stage of 0.2 mm. Within the errors the results are compatible with the angles determined in the fast analysis during data taking. The sign of the rotation could be determined in future testbeam campaigns with a finer stepwidth in the adjusted rotation angles, giving the opportunity to determine the configuration with the smallest dependence of the observed channel width to the signal threshold.
Because of the fine segmentation of the anode plane, the M64 MAPM offers additional observables to determine the alignment of the detector box to the beam. With four anode pads of the configuration 2 (Fig. 10.5 on page 114) covering a single detector channel, four independent light yield asymmetries can be extracted from the data. The light yield asymmetries are defined as:

$$A_x = \frac{I_x^+ - I_x^-}{I_x^+ + I_x^-} \quad \text{and} \quad A_z = \frac{I_z^+ - I_z^-}{I_z^+ + I_z^-}, \tag{11.2}$$

where I_x^+ indicates the light yield (QDC signal in data) in the channel at higher values of x w.r.t the global coordinate system (i.e. the left half of the channel), while I_x^- stands for the collected light in the right half of the channel at lower values of x. In the same way the light asymmetries in z are to be interpreted. With the segmentation of the M64 MAPM each asymmetry can be determined twice, in case of the asymmetry A_x, it can be evaluated for the upper and lower half of the channel (from the anodes at higher and smaller values of z), while A_z can be constructed for the right and left half of each channel. In Figure 11.11(a) the asym-

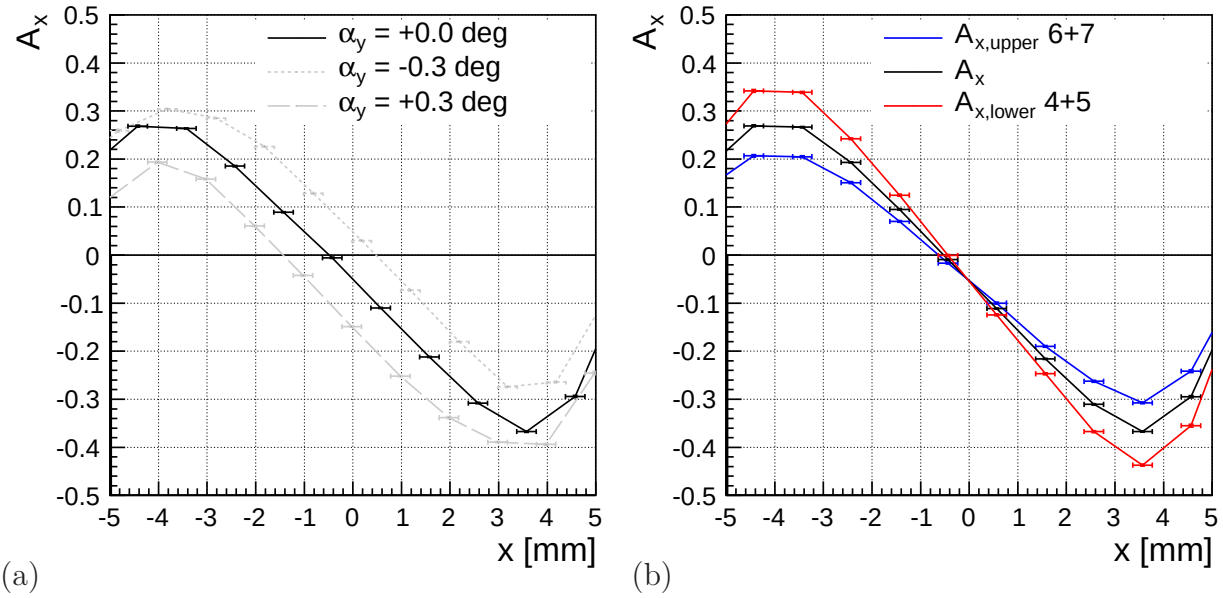

(a) (b)

Figure 11.11: *Simulated light asymmetry A_x for the M64 MAPM as function of the beam position on the channel entrance for rotations of (a) $\alpha_x = 0.0°$ and α_y ranging from $-0.3°$ to $0.3°$. (b) $\alpha_y = 0.0°$ and $\alpha_x = 0.3°$. Note that in (a) for $\alpha_y \neq 0.0°$ the zero crossing of A_x is observed at different beam positions and that in (b) the additional rotation about the x-axis lifts the degeneracy of A_x^{upper} and A_x^{lower}.*

metry A_x as function of the beam entrance position in x is shown for the left channel. The black solid line is the simulated asymmetry for an ideally aligned detector. The gray dashed and dotted lines are the light asymmetry for a rotation about the y-axis by $\alpha_y = +0.3°$ and $\alpha_y = -0.3°$, respectively. With a non-zero rotation about the y-axis, the zero-crossing as well as the values of the asymmetry maxima change. The asymmetry A_x for $\alpha_y = +0.0°$ shows an offset at $x = 0.0$ mm, which is a result of the anode channel coverage of the M64 MAPM. The sensitive area of one quadrant of the M64 is with 9×9 mm^2 larger than the cross sectional area of the detector channel of 8.5×8.5 mm^2. For a centrally placed PMT, the anode pads at the outer walls of the detector channels are only partially covered by the channel cross section, leading to a lower average $< I_x^+ >$ compared to $< I_x^- >$ for the left channel. Possible PMT misalignments introduce a new degree of freedom, which is in principle accessible by a thorough analysis of the measured light asymmetries.

The asymmetries for the upper and the lower half of the channel coincide with the full asymmetry calculated from the total light yield in the left and right channel halves. Introducing an additional rotation about the x-axis by $\alpha_x = 0.3°$ lifts this degeneracy, as shown in Fig-

ure 11.11(b), where A_x^{upper} for the upper half of the channel is shown in blue, and A_x^{lower} for the lower channel half in red. Also shown in black is the full (average) asymmetry, identical to the solid black line in Figure 11.11(a).

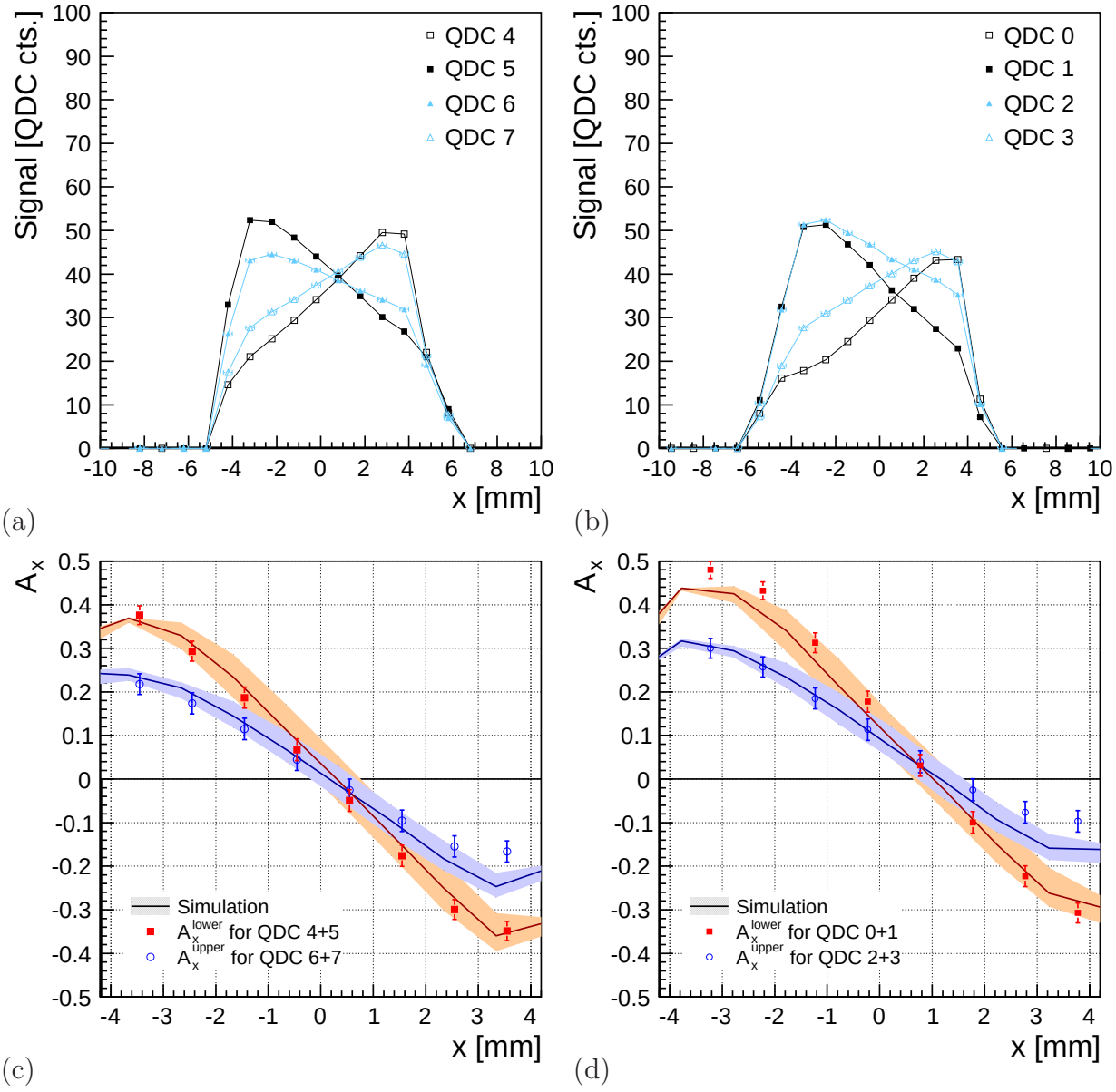

Figure 11.12: *Detector response of the M64 MAPM in a 2009 x-scan for (a) the left-hand and (b) the right-hand detector channel. (c) and (d) show the corresponding light asymmetries A_x^{upper} and A_x^{lower} for the upper and lower part of each channel, respectively. The data is described by the simulation for $\alpha_x = +0.2°$, $\alpha_y = -0.2°$ and $\alpha_z = +0.0°$. The error bands are determined from the envelope of A_x^{upper} and A_x^{lower} respectively, by variation of α_y by $\pm 0.1°$.*

The light asymmetry A_x for both detector channels has been measured with the M64 MAPM in both testbeam campaigns, 2009 and 2010.
Figures 11.12 (a) and (b) show the detector responses for an x-scan recorded with the M64 MAPM in 2009 for the left- and right-hand channel, respectively. The responses are adjusted

to the channel center, and each detector channel is read out with four anodes, i.e. the M64 in configuration 2 as illustrated in Figure 10.5 on page 114.
In Figures 11.12 (c) and (d) the corresponding light asymmetries A_x are presented. The filled red squares are the data asymmetry for the lower part of the corresponding channel, the open blue circles correspond to the data asymmetry for the upper part of each channel. For the left channel A_x^{lower} is calculated from the response of anodes 4 and 5, for the right channel from anodes 0 and 1. Analogously, A_x^{upper} for the left channel is derived from anodes 6+7, and for the right channel from anodes 2+3, respectively. The solid red and blue lines show the simulated asymmetries for the best fit angles of $\alpha_x = +0.2°$, $\alpha_y = -0.2°$ and $\alpha_z = +0.0°$. The error bands are given by the envelope of the simulated curves of A_x^{upper} and A_x^{lower} for $\Delta\alpha_y = \pm 0.1°$. Except for the channel edges at $x = \pm 4$ mm the data is described by the simulation.
The errors include only effects from systematic uncertainties on the anode gains g. Assuming a relative uncertainty $\delta g/g = \epsilon$ the maximal deviations in the intensity for $(1+\epsilon)$ and $(1-\epsilon)$ are used to estimate the influence on the light asymmetry. The light asymmetry A_x is rewritten as:

$$A_x(\epsilon) = \frac{I_x^+(1+\epsilon) - I_x^-(1-\epsilon)}{I_x^+(1+\epsilon) + I_x^-(1-\epsilon)}. \tag{11.3}$$

Using the relations

$$I_x^+ = \frac{1}{2}(1+A_x)(I_x^+ + I_x^-) \quad \text{and} \quad I_x^- = \frac{1}{2}(1-A_x)(I_x^+ + I_x^-), \tag{11.4}$$

the systematic error on the light asymmetry A_x is given by:

$$\delta A_x = \left(\frac{dA_x}{d\epsilon}\right)_{\epsilon=0} \epsilon = (1 - A_x^2)\epsilon. \tag{11.5}$$

For a relative gain uncertainty of $\epsilon = 2.5\%$, a maximal systematic uncertainty of $\delta A_x = 2.5\%$ is expected for $A_x = 0$. As can be seen from Figures 11.12(c) and (d), these estimated gain uncertainties are sufficiently large for the data to be compatible with the expectation within the errors. Even for smaller values of the gain uncertainty, compatibility of data and simulation can be sustained.
In the same way the asymmetry A_z as function of the y-position of the beam is calculated from the detector response and used to determine the accuracy of the angle α_x. Figures 11.13(a) and (b) depict the pedestal subtracted detector response to a y-scan for the left channel in the 2009 data and the corresponding light asymmetry A_z. The light asymmetry A_z^{right} is calculated from anodes 4 and 7, and A_z^{left} from anodes 5 and 6, respectively. Because of the channel geometry, the y-position of the beam translates directly to the z-coordinate on the PMT cathode. The simulated asymmetries A_z for different α_x show a similar behavior as the computed A_x (cf. Fig. 11.11(a)). For A_z the degeneracy of A_z^{right} and A_z^{left} is lifted by introducing an additional rotation about α_y. The data points of A_z^{right} and A_z^{left} are still degenerate, in contrast to the expectation for the fitted value of $\alpha_y = -0.2°$.
However, in all data runs taken with the M64 MAPM, anode 5 exhibited an excess of about 12% in comparison to the remaining three anodes on the same detector channel, compare Figures 11.12(a) and 11.13(a). This has been corrected for in the data. Unfortunately, this correction is partially responsible for the degeneracy of A_z^{right} and A_z^{left}. The solid black line

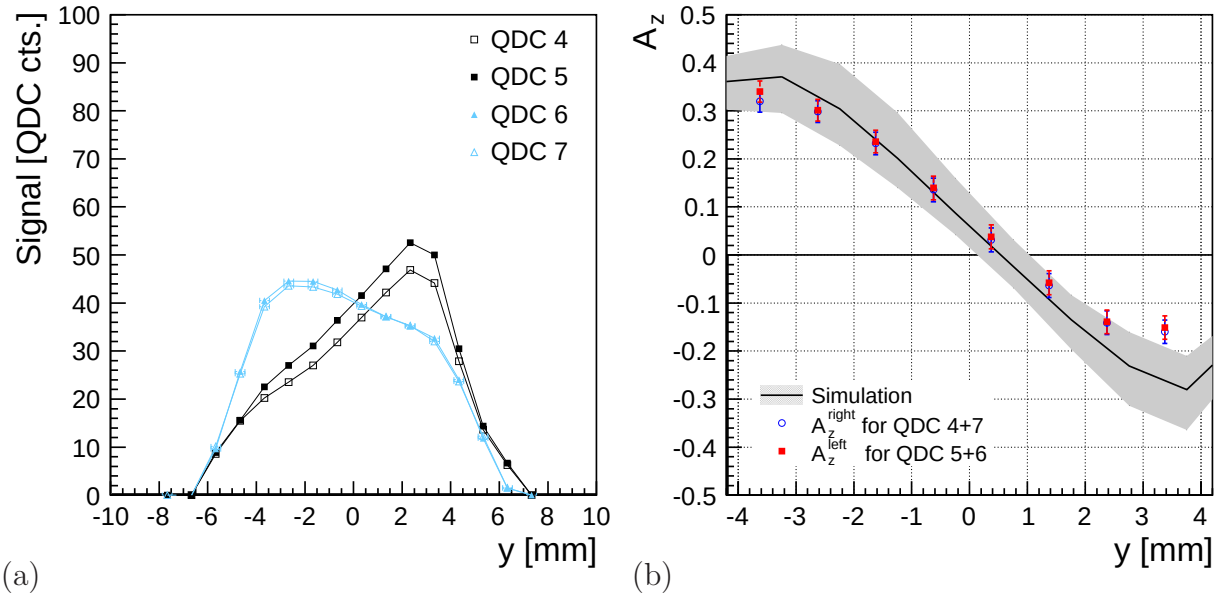

(a) (b)

Figure 11.13: *(a) Pedestal subtracted detector response of the left channel to a y-scan in 2009 recorded with the M64 MAPM. (b) Corresponding light asymmetries A_z. Because of the channel geometry, the y-position of the beam translates directly to the z-coordinate on the PMT cathode. The data can be described by the simulation for $\alpha_x = +0.2°$, $\alpha_y = -0.2°$ and $\alpha_z = +0.0°$. The error band is determined from the envelope of A_x^{right} and A_x^{left}, respectively, by variation of α_x by $\pm 0.1°$.*

is the simulated average asymmetry for $\alpha_x = +0.2°$, $\alpha_y = -0.2°$ and $\alpha_z = +0.0°$. The gray error band is the resulting envelope of the simulated A_x^{right} and A_x^{left} for an uncertainty of $\Delta\alpha_x = \pm 0.1°$.

In 2010 the observed data asymmetries A_x for the left and right detector channels, calculated from the detector response to an x-scan shown in Figures 11.14(a) and (b), are shown in Figures 11.14(c) and (d). The data is in concordance with the simulation for values of $\alpha_x = 0.1$, $\alpha_y = -0.1$ and $\alpha_z = 0.0$. The blue and orange error bands for A_x^{upper} and A_x^{lower} are determined from simulation by variation of α_y by $0.1°$.

Figure 11.15(a) shows the pedestal subtracted detector response to a y-scan in 2010 and the corresponding light asymmetries A_z^{right} and A_z^{left} in Figure 11.15(b). The data is compatible with the expectation for $\alpha_x = 0.1$, $\alpha_y = -0.1$ and $\alpha_z = 0.0$. The gray error band is calculated from the envelope of A_z^{right} and A_z^{left} by varying the angle α_x by $\pm 0.1°$. Again, as in 2009, A_z^{right} and A_z^{left} are still almost degenerate, despite the rotation of $\alpha_y = -0.1$ about the y-axis. Furthermore, the slightly different slopes of A_z^{right} and A_z^{left} with the values of A_z^{right} being slightly smaller than those of A_z^{left} at negative y (or z) values indicate a small positive value of α_y. The discrepancy between the results from A_x and A_z can currently not be explained.

In Table 11.2 the determined angles α_x, α_y and α_z are listed for the 2009 and 2010 data. Because of the channel symmetry, rotations about the z-axis (beam axis) have only very little influence on the asymmetries and channel width measurements and can not be determined to a precision comparable or better than estimated during data taking. The values for α_y determined from simulation are consistent for both the channel width method and the asym-

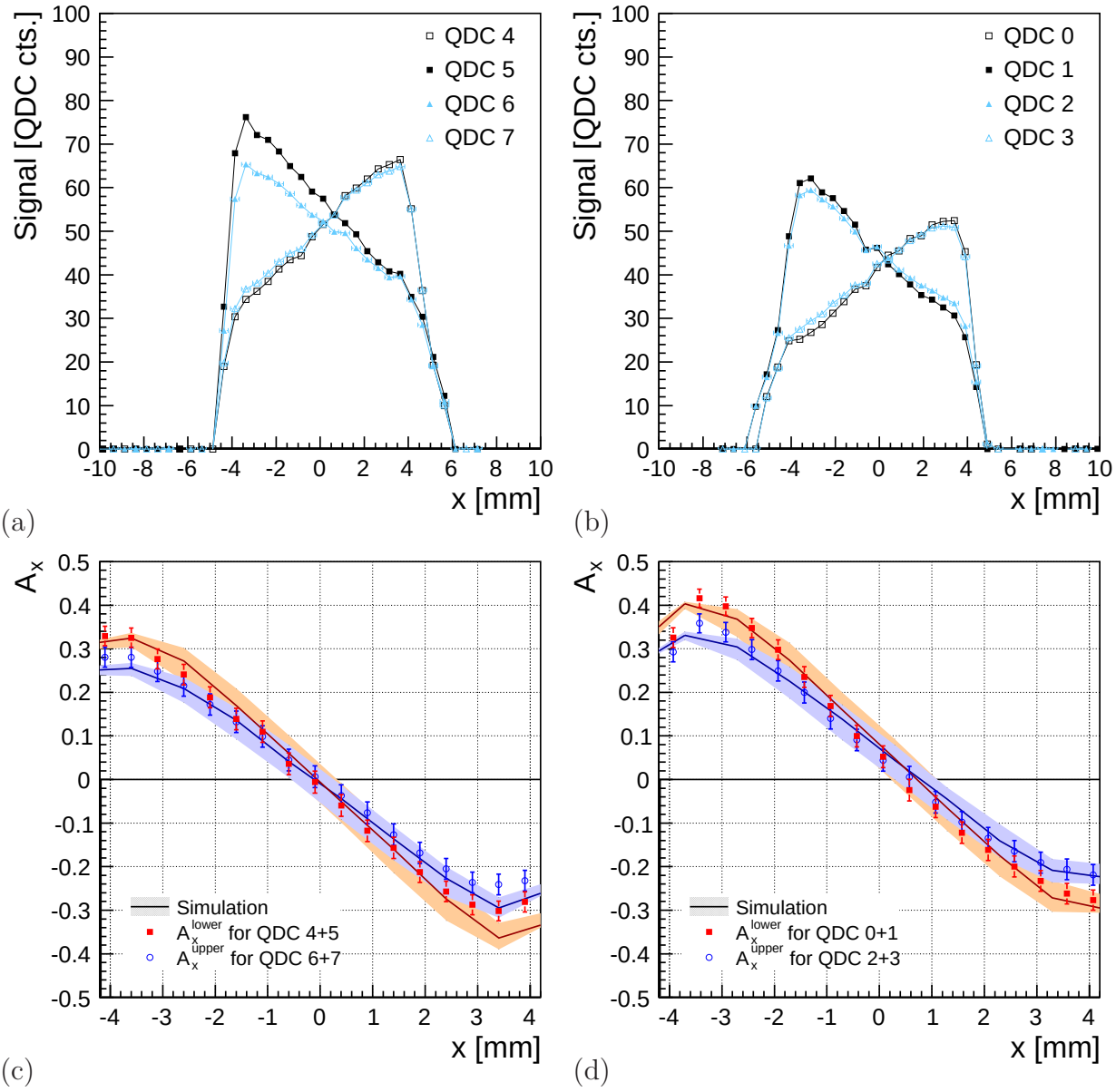

Figure 11.14: *Detector response of the M64 MAPM in a 2010 x-scan for (a) the left-hand and (b) the right-hand detector channel. (c) and (d) show the corresponding light asymmetries A_x^{upper} and A_x^{lower} for the upper and lower part of each channel, respectively. The data is described by the simulation for $\alpha_x = +0.1°$, $\alpha_y = -0.1°$ and $\alpha_z = +0.0°$. The envelopes of A_x^{upper} and A_x^{lower} for an $0.1°$ variation of α_y determine the respective orange and blue error bands.*

metry measurement, and all values are compatible with the errors estimated during the online analysis described in the previous section.

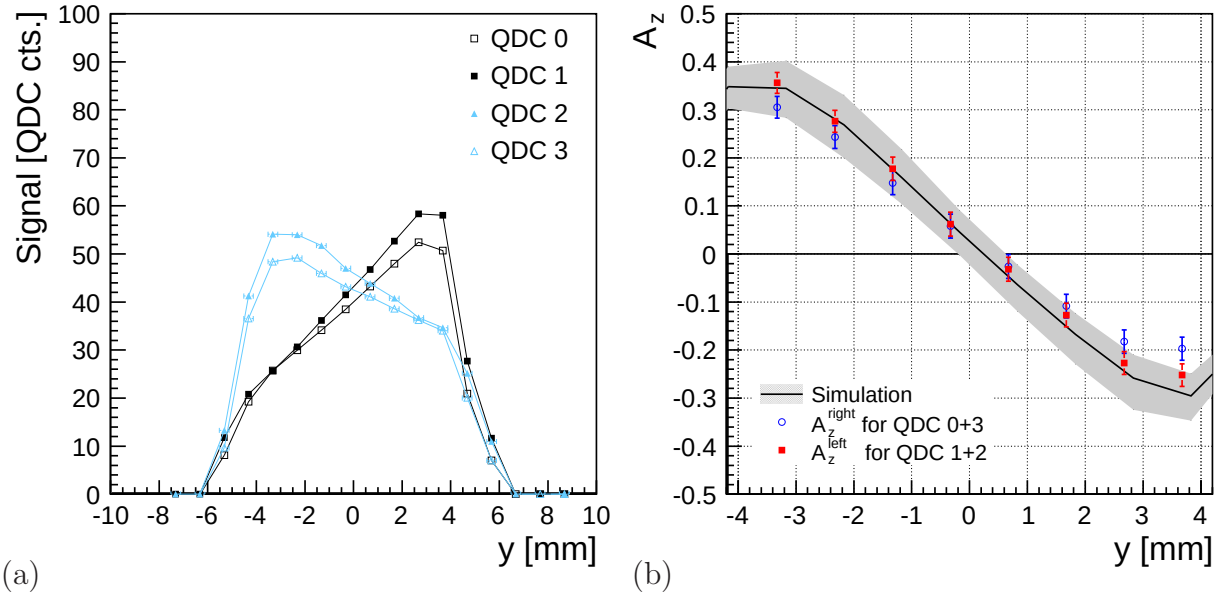

(a) (b)

Figure 11.15: *Light asymmetries A_z from the 2010 data, recorded with the M64 MAPM. The asymmetries are shown for the right detector channel. The data can be described by the simulation for $\alpha_x = +0.1°$, $\alpha_y = -0.1°$ and $\alpha_z = +0.0°$. The error band is determined from the envelope of A_z^{right} and A_z^{left} respectively, by variation of α_x by $\pm 0.1°$.*

	α_x	α_y	α_z
2009	$(0.2 \pm 0.1)°$	$(-0.2 \pm 0.1)°$	$(0.0 \pm 1.0)°$
2010	$(0.1 \pm 0.1)°$	$(-0.1 \pm 0.1)°$	$(0.0 \pm 1.0)°$

Table 11.2: *Systematic errors on the three rotation angles α_x, α_y and α_z, determined by comparing the measured asymmetries A_x and A_z to simulations of the M64 MAPM.*

11.3 Inter-channel wall reflectivity

While the reflectivity measurement of the inter-channel wall with the PerkinElmer spectrometer gave significantly lower limits for the wavelength dependent reflectivity in comparison with the diamond-cut aluminum for the remaining channel walls, the recorded data indicate a considerably higher reflectivity. In an x-scan the slope of the plateau for a perfectly aligned detector is a direct measure of the relative reflectivity r_{ref} of the inter-channel wall to the outer walls. As shown in Figure 11.16 in a simulation of the left channel with increasingly lower reflectivities the slope of the plateaus increases. The corresponding plateau slopes of the right channel decrease accordingly, the difference is only in the sign of the slope.

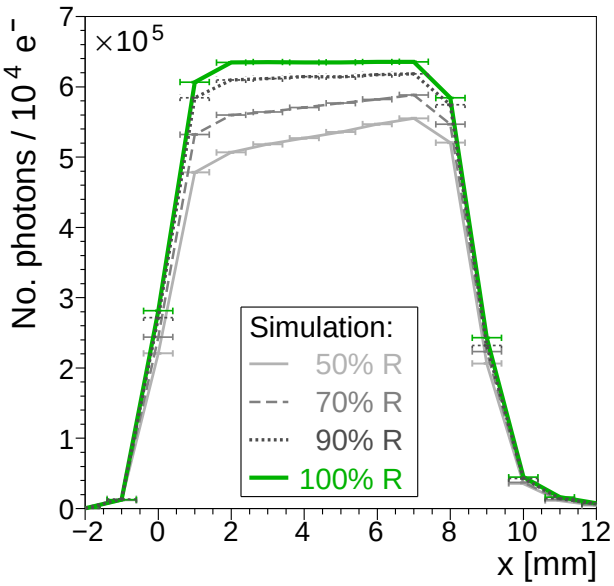

Figure 11.16: *Simulated x-scans for the M4 MAPM left channel anode. The signal shape varies for different reflectivity ratios r_{ref} of inter-channel wall and outer walls ranging from 50% to 100%. With a decreasing relative reflectivity, the plateau slope increase.*

Figure 11.17 depicts the fitted plateau slopes of all x-scans recorded at Elsa in (a) 2009 and (b) 2010. After aligning the detector the data points from the two MAPMs (the M4 and the M64) which enable simultaneous readout of both detector channels, scatter around zero (flat plateau) in both testbeam campaigns. Also drawn in the Figures are the average slope values in the data for the right-hand and left-hand channel. The 2009 data points are shifted towards positive slopes, while the 2010 data appears to be more central. However, the distance between the slope values of the left and right channels for the 2009 data are compatible with those of the 2010 data. The observed bias in both testbeam campaigns are accounted for by residual misalignments.
As the alignment analysis showed, larger rotations of the detector box about the x- and y-axis were observed in 2009 than in 2010 which is in agreement with the larger shift of the plateau slopes measurement in 2009.
For comparison, the expected plateau slopes for an inter-channel wall reflectivity of 85% simulated for the M64 MAPM are indicated by the black stars. The 2009 data is compared to a simulation with $\alpha_y = -0.3°$, which fits the data better than the previously determined

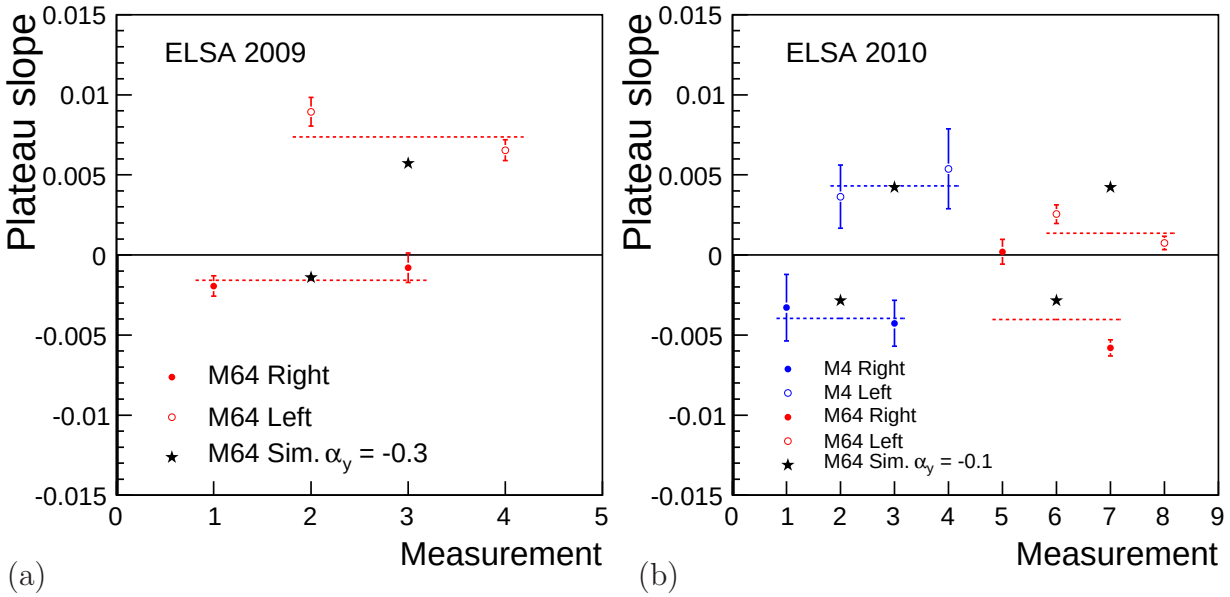

(a) (b)

Figure 11.17: *Observed plateau slopes of (a) the 2009 and (b) the 2010 testbeam campaigns after detector alignment. The data points for the left and right detector channel recorded with the M4 and M64 MAPMs scatter around zero, i.e. a flat plateau. The expected slopes for simulated x-scans with the M64 and the best detector alignment are overlaid in the black stars.*

angle of $\alpha_y = -0.2°$, but is still within the error of 0.1°. For the 2010 data, a simulation with $\alpha_y = -0.1°$ is overlaid.

11.4 Results

The analysis presented in the previous section can only be partially transferred to the future ILC polarimeter Cherenkov detector. While the alignment measurement with the channel width method would work as a supplementary method to the alignment determination at the ILC Cherenkov detector, the measurement of the light asymmetry requires segmented PMTs to gain intra-channel resolution, which is so far not foreseen for the final detector.
Other parameters, however, are important for the detector prototype, as well as for the ILC polarimeter detector. While for the measurement of rate asymmetries the absolute gain of the employed photo detectors cancel, any systematic bias in the PMT responses directly influences the measured beam polarization. Possible sources of a signal bias include physical background processes and unstable QDC pedestal substractions.

11.4.1 Systematic errors from backgrounds

The measured rate asymmetry A_i in the i^{th} detector channel is given by

$$A_i = \frac{N_i^+ - N_i^-}{N_i^+ + N_i^-} \quad \text{with} \quad N_i^+ = O_i^+ - B_i^+. \tag{11.6}$$

The number of observed electrons in channel i for positive (negative) laser helicity N_i^+ (N_i^-) is determined from the number of observed counts O_i^+ (O_i^-) minus the average number of background counts B_i^+ (B_i^-). Systematic uncertainties on the expected background rates propagate to the asymmetry A_i, and hence to the polarization measurement as

$$\frac{\Delta A_i}{A_i} = \frac{2}{N_i^+ + N_i^-}\Delta B_i = \overline{N_i}^{-1}\Delta B_i, \tag{11.7}$$

for backgrounds independent of the electron helicity. In Equation 11.7 $\overline{N}_i$ denotes the average of detected Compton electrons in channel i for both laser polarization states. From fast simulation studies the average number of electrons in the least populated channel 18 of the ILC polarimeter Cherenkov detector is about $\overline{N} \approx 600$. To limit the systematic errors to $\leq 0.1\%$ from helicity independent backgrounds, the background rate has to be known to $\Delta B_i \leq 0.6$ counts.

11.4.2 Pedestal stability

At ILC, the rate asymmetries in each detector channel will be determined from the QDC responses integrated over a series of laser pulses with positive and negative laser helicity, respectively. From the QDC response the expected background counts and the electronics pedestal have to be subtracted.
The electronics pedestal position can be regarded as a polarization independent background. Figure 11.18(a) shows the pedestal position over a time scale of two hours, recorded during

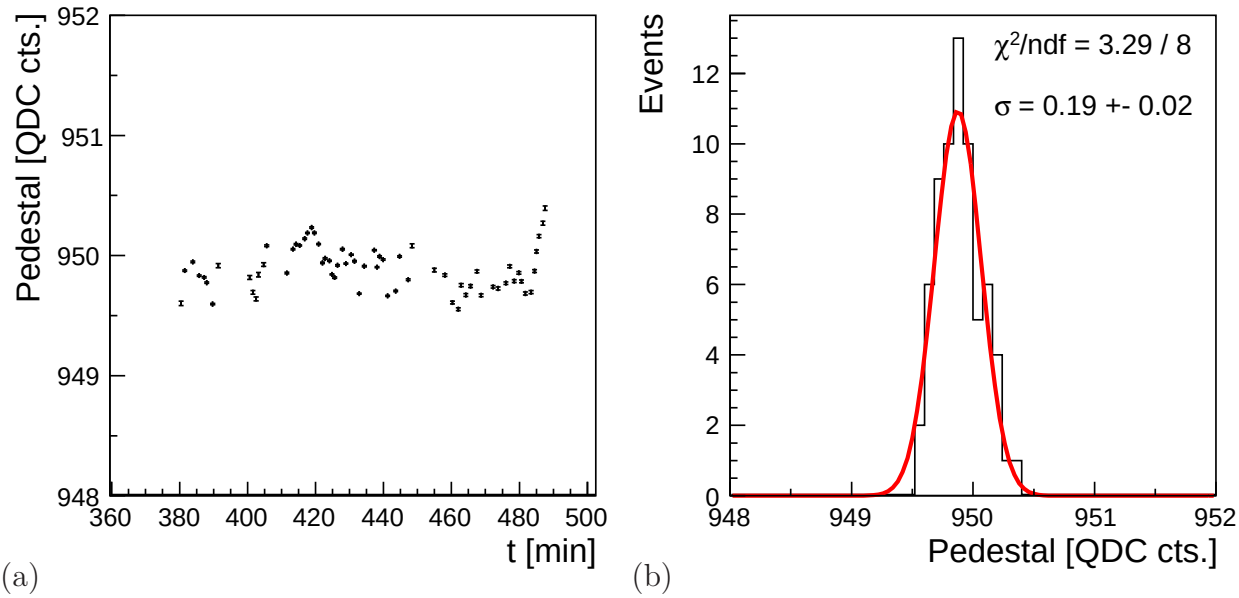

(a) (b)

Figure 11.18: *(a) Pedestal position in QDC counts as function of time for the M4 MAPM over 2 hours. The operating high voltage is 420 V. The run represents a beam current scan with extraction currents starting from 300 pA down to 50 pA. The beam spot is only slightly off the channel center. The pedestal positions are determined from a gaussian fit. (b) Distribution of the same pedestal positions. The spread in the pedestal position is* 0.19 ± 0.02 *QDC counts.*

a long sequence of runs of 500 minutes in 2010. The photodetector used is the M4 MAPM, operated at 420 V. The extracted nominal beam current ranges from 50 pA to 300 pA. Over the full two hours the pedestal position determined by a gaussian fit to the QDC spectrum remains stable with a spread of 0.19 ± 0.02 QDC counts, as shown in Figure 11.18(b). The spread is below the RMS of ± 1 QDC count for the electronics pedestal stability, as specified by the manufacturer for the low range sampling mode. Converting this spread to an equivalent of background counts B via

$$B = \text{QDC cts.} \times \kappa \times \frac{1}{\text{gain} \times \text{q}_{\text{e}^-}} \times \frac{\text{N}_{\text{c.e.}}}{\text{N}_{\text{p.e.}}} \tag{11.8}$$

with κ as the charge per LSB (25 fC/LSB), the PMT gain of $\approx 2 \times 10^4$ at 420 V [107], and the electron charge q_{e^-}. The average number $N_{p.e.}/N_{c.e.}$ of photoelectrons $N_{p.e.}$ per primary (Compton) electrons $N_{c.e.}$ is taken from simulations as $N_{p.e.}/N_{c.e.} \approx 6.5$ (c.f. Sec. 10.6.1). The observed spread is equivalent to $B \approx 0.23$. The factor with the most influence on the pedestal uncertainty is the PMT gain. Higher gain values are preferable, as long as increased PMT dark current rates are under control.

For a long term monitoring of the pedestal stability, its position over the full 500 minutes is shown in Figure 11.19(a). The time sequence is structured in several run periods with varying extraction currents and lateral detector positions. Except for a few data runs, the pedestal position is stable within 1 QDC count. The outliers in the figure are a relic of the fitting method with a simple gaussian that has difficulties to discern the pedestal from the signal peak for small signals.

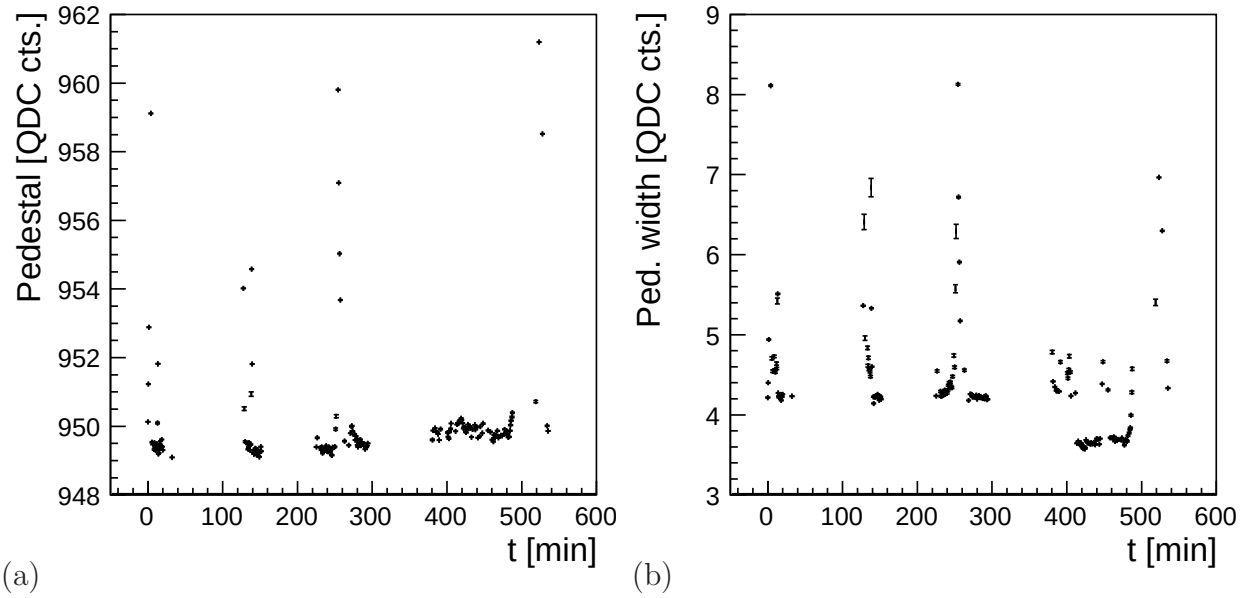

(a) (b)

Figure 11.19: *(a) Pedestal postion in QDC counts over a run sequence of 500 minutes with the M4 MAPM. The PMT supply voltage is 420 V. The run sequence is structured in x- and y-scans, as well as beam current scans. The outliers are a residual of the fitting method for small signals. (b) Width of the pedestal peak during the same run sequence. The width is stable to below 1 QDC count. The outliers correspond to the same runs as in Figure (a).*

Small signals occur for low extraction currents, and at the channel borders in x- and y-scans, where only a few electrons enter the active volumes, and hence only a few Cherenkov photons are detected. In these cases, the signal peak sits on the flank of the pedestal, thus changing the mean μ and width σ of the pedestal gaussian. In Figure 11.19(b) the pedestal width for the same runs is shown. Again, except for runs where the signal peak merges with the pedestal, the width is stable to below 1 count.

11.4.3 Signal stability

One objective of the ELSA testbeam campaigns was to determine the linearity of the full system of detector and data acquisition system (DAQ). Because of unstable beam conditions, this proved to impossible to a precision of the required 0.1% for ILC conditions. Furthermore, space for improvements of the prototype design has been identified.

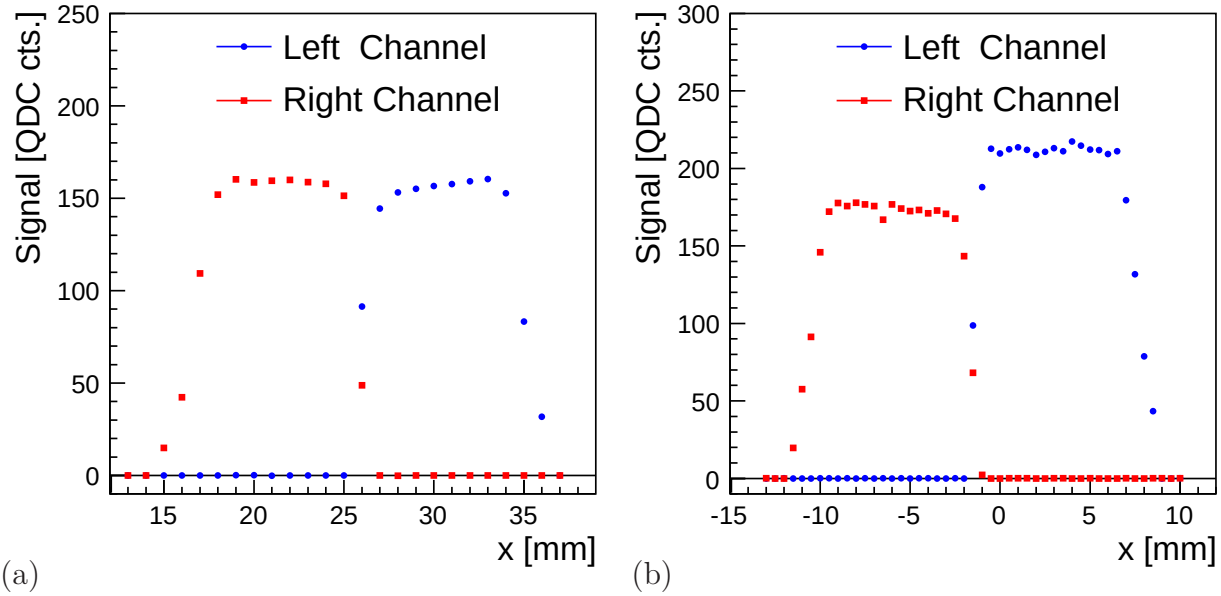

Figure 11.20: *Pedestal subtracted signal response for two x-scans in (a) 2009 and (b) 2010 recorded with the M64 MAPM and comparable supply voltages and gate lengths. The nominal extraction current is 100 pA in both scans. A large discrepancy between the left and right detector channel in 2010 is observed. It is most probably related to an imperfect connection of the PMT to its base.*

In Figure 11.20 the pedestal subtracted PMT responses for two x-scans over the full detector front in (a) 2009 and (b) 2010 are shown. In both cases the employed PMT is the M64 MAPM operated at 500 V and 600 V, respectively and with gate lengths of 300 ns and 350 ns. In both scans the nominal extraction current is 100 pA. In contrast to the 2009 data, the scan in 2010 shows a large discrepancy between the maximal responses for the left and right detector channel. Since the extraction current has been kept stable and no unexpected discontinuity is observed in the signal response of each channel over the sequence of the scan, a beam related source of the discrepancy is ruled out. The most probable source has been identified with the PMT base of the M64. The base is located inside the light-tight connector box, affixed

over the PMT mounting. The space inside the box is very limited, and the cabling inside, connecting the PMT base with the outer LEMO connectors experienced mechanical stress. This stress might have led to a loose connection between the PMT and its base, despite efforts to stabilize the connection. In future measurement campaigns a redesign of the light-tight connector box is therefore recommended.
From the data recorded during the testbeam campaigns an upper limit on the stability of the extraction current can be made, when other uncertainties in the experimental setup are ignored. In the alignment scans shown in Figure 11.8, the maximal signal for box rotations α_y close to the best alignment is expected to be of the same magnitude, since these scans were recorded for a constant extraction current of 100 pA and constant detector parameters. From the fluctuations of the three data points about the maximum an upper limit on the beam current stability of 1% is estimated. Another estimate is provided by the scatter of the pedestal subtracted signal in the plateau region during an x-scan with constant extraction current (cf. Figures 11.7 and 11.20). The residuals of the data points to a linear fit to the pedestal region is shown in Figure 11.21 for all x-scans recorded in 2009 and 2010. The RMS of the distribution is with 1% compatible to the estimate of the beam current stability from the alignment scans. However, it has to be noted, that these estimates neglect any uncertainties in the experimental setup of the detector box as, for example the stability of the HV supply.

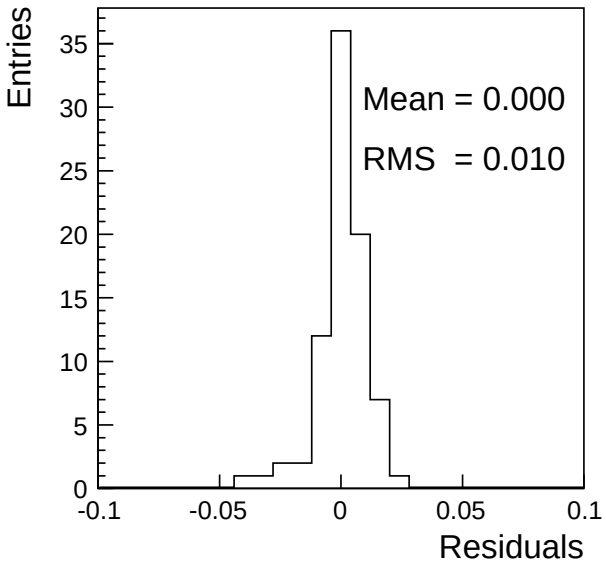

Figure 11.21: *Distribution of residuals of the data to a linear fit to the pedestal region for all x-scans recorded in 2009 and 2010. Taken as an estimate on the extraction current stability, the RMS of 1% is compatible with the estimate of 1% from the alignment scans.*

11.4.4 Accelerator backgrounds

The pedestal position depends not only on the pedestal current, but also on the thermal dark current rate of the PMTs, which warm up when HV is applied. Therefore the PMT dark current rate introduces a polarization independent background to the measured rate asymmetries in the polarization measurement at ILC. Furthermore, accelerator-induced backgrounds

from the beam contribute to the background rate and, hence, to the precision to which the polarization can be determined. At the ELSA testbeam the detector response to unpolarized electrons has been measured.
The setup and measurement objectives allowed to determine the PMT dark current rate, and the beam-induced background rate from electrons circling in the ELSA accelerator. Because of the very different experimental conditions, the latter can not be used for an extrapolation to the ILC polarimeter. They are, however, required for the analysis of the pedestal stability of Section 11.4.2.

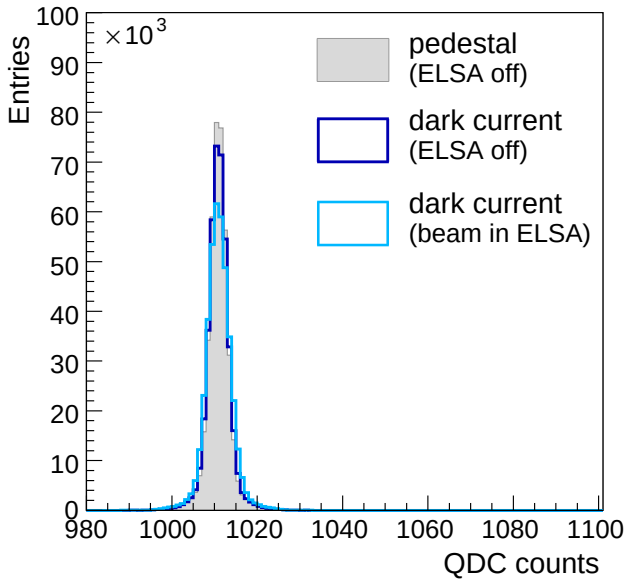

Figure 11.22: *Data recorded with the* 2×2 *MAPM (R7600U-03-M4):*
The pedestal with no HV supplied to the M4 MAPM and ELSA *shut off is shown as the gray filled histogram. The pedestal recorded with a supply voltage of 400 V is shown as the dark blue (dark gray) open histogram. The PMT thermal dark current slightly broadens the pedestal, but no shift in the mean position is observed. The influence of the* ELSA *accelerator backgrounds is shown by the light blue (light gray) histogram, with electrons circling in the accelerator but without extraction to the detector prototype. No systematic shift of the pedestal position is observed.*

For the investigation of the PMT thermal dark current rate, Figure 11.22(a) shows the QDC pedestal as the filled gray histogram. The pedestal has been recorded with ELSA turned off and no HV supplied to the M4 MAPM. Overlaid as the dark blue (dark gray) histogram, is the pedestal recorded with a supply voltage of 400 V to the M4 MAPM, after a warm-up time of several hours. The thermal noise from the PMT results in a slight broadening of the pedestal, but the central position of the pedestal remains unchanged.
The maximal expected dark current is given with 5 nA by the manufacturer. With a gate length of 400 ns and an LSB of 25 fC in the low range of the QDC (V965, see Section 10.4), the dark current rate is limited to 0.08 counts in the QDC low range, well below the resolution of the QDC. Hence, the influence of the thermal dark current is negligible for measurements with the current prototype setup.
Also shown in Figure 11.22(a) as the light blue (light gray) histogram is the pedestal recorded

with the same high voltage of 400 V applied to the M4 MAPM and with electrons circling in the Elsa accelerator, but with no extraction to the prototype. Again, only a minor broadening of the pedestal is observed with no shift of the pedestal mean position. Accelerator-related backgrounds were not present in a detectable order of magnitude during the Elsa testbeam campaigns.

11.4.5 Dynamic range of the prototype at Elsa

For operation at ILC the dynamic range of the detector has to cover the detection of simultaneously arriving electrons over one order of magnitude from $\mathcal{O}(10^2)$ to $\mathcal{O}(10^3)$. During the Elsa testbeam campaigns no precise absolute extraction current measurements were possible. Therefore no absolute determination of the dynamic range of the setup can be made. However, an approximate validation of the nominal extraction currents, and hence the range of detected electrons is possible by comparison with the single electron signals recorded at Desy II. In order to determine the optimal working point for each PMT in terms of the

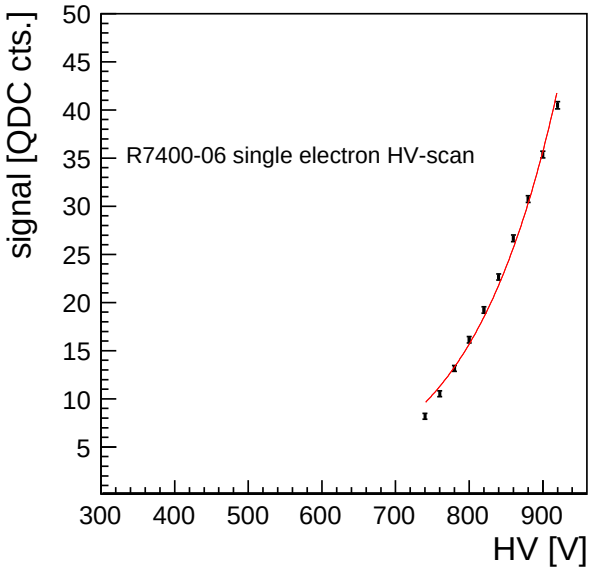

Figure 11.23: *HV-scan with the R7400-06 SAPM for single electron events at* Desy II. *The signal can not be directly extrapolated to the HV applied at the* Elsa *testbeam. A forced exponential fit gives 0.4 counts per electron at 350 V, the HV applied to this PMT at* Elsa.

applied high voltage, HV-scans have been performed during the Desy II and Elsa testbeam campaigns. Figure 11.23 shows the measured pedestal subtracted single electron signal during a HV-scan of the R7400-06 SAPM from 740 to 900 V. Extrapolation of the expected single electron signal to voltages of 350 V applied to the same PMT under Elsa conditions allows for an indirect beam current measurement. As seen from Figure 11.23, a direct extrapolation to a voltage of 350 V is not possible, as the signal becomes undetectable for voltages below 600 V, however, forcing an exponential fit to the data points suggests an equivalent single electron signal at Elsa of 0.4 counts.
Figure 11.24(a) shows the signal response of the R7400-06 SAPM to a beam current scan from 20 pA to 300 pA. An average nominal extraction current of 1 pA corresponds to 6.2×10^6

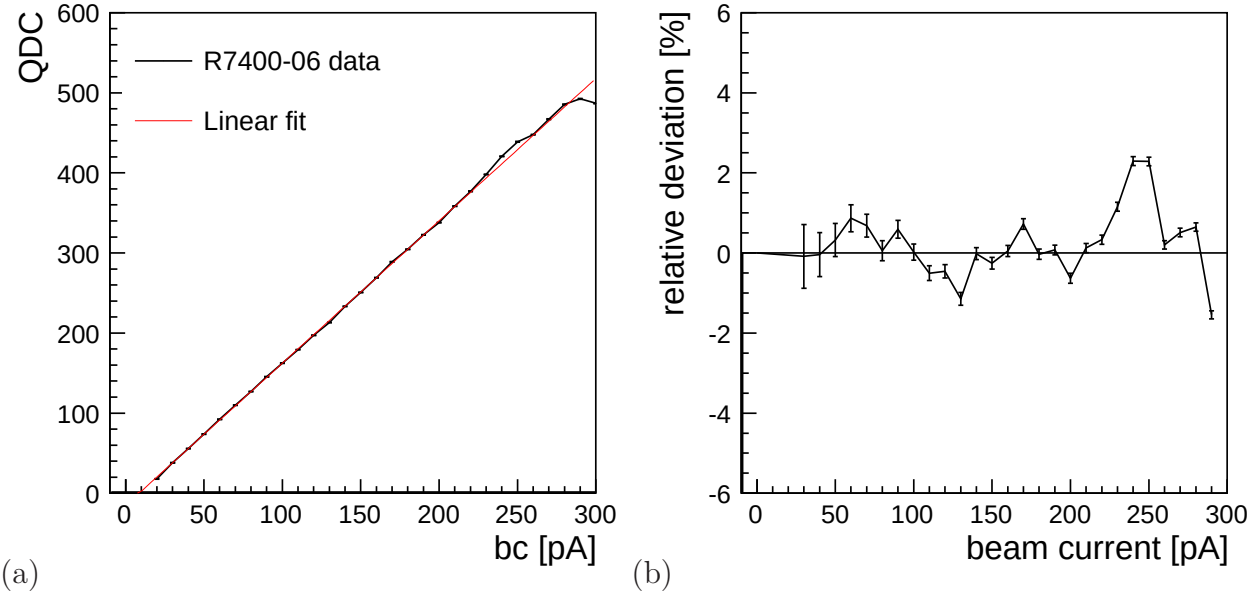

(a) (b)

Figure 11.24: *Exemplary beam current scan with the R7400-06 SAPM for extracted beam currents from 20 pA to 300 pA: (a) detector response with a linear fit, (b) the residuals between data and fit.*

electrons traversing the detector per second, or about 3.4 electrons per ELSA revolution of 548 ns. Given the single electron extrapolation from data recorded at DESY II, about 1.4 counts per pA are expected at ELSA. The slope of the fit to the data in Figure 11.24(a) gives about 1.78 counts per extracted pA. Because the voltage range used in the HV-scan for the single electron measurement at DESY II did not extend to below 740 V, the response behavior to single electrons at lower voltages of 350 V is not known. This unknown behavior at low voltages dominates the difference between the extrapolation of single electron events to the multi-electron events recorded at ELSA. With the single electron data, for an extraction current of 100 pA, 140 counts are expected, while 163 counts are observed. Corrected for the constant term of the linear fit the measurement yields ≈ 178 counts which is within 30% of the expectation from single electron data. Assuming that the order of magnitude of the nominal extraction current measurement is reliable, the numbers of detected electrons range from 170 to 1000 electrons.

Because of the observed signal instabilities (cf. Sec. 11.4.3) a precise determination of the detector linearity can not be made. Figure 11.24(b) shows the relative difference of the measured detector response to the expected response as function of the nominal extraction current obtained from the linear fit in Figure 11.24(a). The relative beam current measurements at ELSA were much more reliable than the absolute determination of the extraction current. Neglecting any uncertainty on the relative measurement, the deviation from observed to expected signal is below 2% over the full range of extracted currents. The observed fluctuations are comparable to the approximate signal stability of 1% in Section 11.4.3. More importantly, no further non-linearities not covered by the observed extraction current instability are visible over the full range of extracted currents.

For a precise measurement of the PMT and QDC integral and differential non-linearities, the

reader is referred to the thesis of C. Helebrant [101]. With the methods presented therein, the non-linearity of the M4 MAPM could be measured to $(0.5 \pm 0.05)\%$, with a sub-permille precision, as required for the ILC polarimeter detector. The PMT non-linearities are corrected for the QDC non-linearities, and the methods are also applicable to the other PMTs employed in the detector prototype.

11.4.6 Response function

For the analyzing power calibration it is essential to understand the response function ρ of the detector. In the determination of the $\mathcal{AP}$ for a specific detector channel this implies that the limits of the integral of Equation 9.3 on page 106 have to be known. The determination of the integration limits is subject of the next Section.
For an ideal detector channel, the response function is simply given by a stepfunction. In practice, however, the response function deviates from this expectation for several reasons. Backgrounds from additional showering in the adjacent beam pipe and channel walls smear the response function such that the channel width appears larger than it is in reality. Also, any material in front of the detector channels will lead to showering and backgrounds. Finally, the response function is convoluted with the geometrical acceptance of the PMT anodes. In principle also crosstalk between adjacent channels has to be considered. In case of the ILC Cherenkov detector, this is strongly reduced by the u-shaped channel geometry.

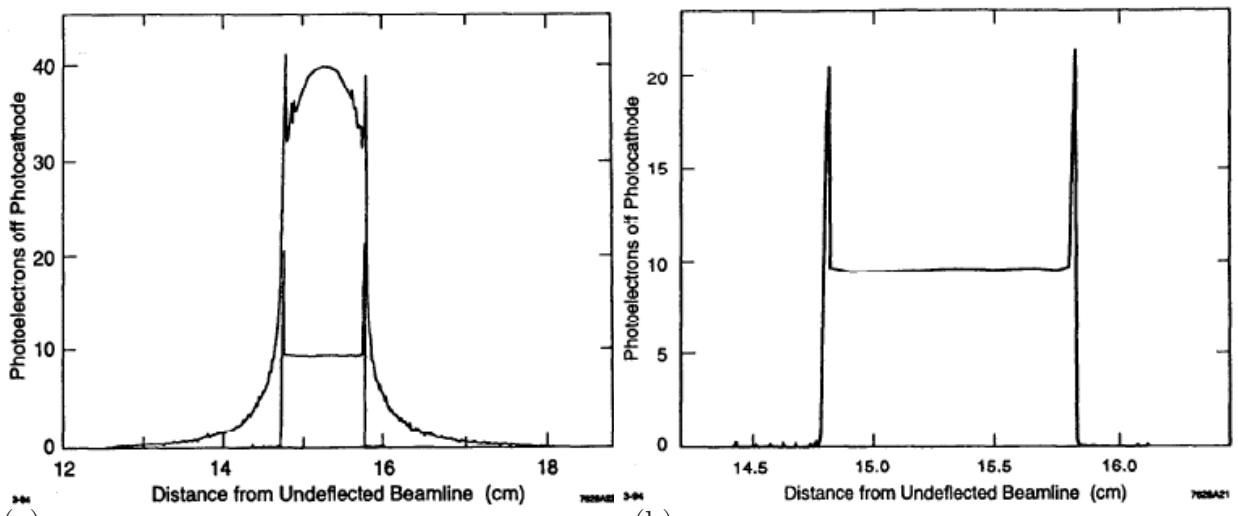

(a) (b)

Figure 11.25: *EGS4 Monte-Carlo simulation of the SLD Cherenkov detector response function ρ for detector channel 6 simulated (a) with a lead pre-radiator of 7.6 mm, (b) without the pre-radiator. This response function is also overlaid in (a) [100].*

For the SLD Cherenkov detector, the response function had been simulated by an EGS4 Monte-Carlo [100]. Figure 11.25(a) shows the response function for channel 6. The Compton edge was located in the adjacent channel 7. The response function shows long tails on both sides of the detector channel, which were attributed to the lead pre-radiator of 0.762 cm thickness. Without the pre-radiator (Fig. 11.25(b)) the response function is close to the

stepfunction, except for the spikes at the edges corresponding to the channel walls. Despite the pre-radiator the corrections from the Monte-Carlo to the $\mathcal{AP}$ calibration were only of the order of 1% [98] for channels 6 and 7 of the SLD polarimeter. The corrections were validated by data at a level of 0.5%.
The goals for the polarization measurement at ILC are more ambitious than at SLD. To achieve a total systematic uncertainty of $\delta P/P = 0.25\%$ on the polarization measurement, the $\mathcal{AP}$ has to be known to a level of 0.2%. This requires, that corrections from the response function have to be under control to at least the same level. In order to satisfy these requirements the detector simulation has to be excellent, with an accurate implementation of the detector geometry, the PMT acceptance and the physical background processes. Furthermore, the response function has to be validated by data.
As the geometry of the ILC polarimeter is conceptually simpler than the one of the SLD polarimeter, the response function is closer to the ideal step function. Most importantly, without a pre-radiator the tails of ρ beyond the channel dimensions are reduced to the comparably small influence from the detector channel entrance windows and the respective inter-channel walls.

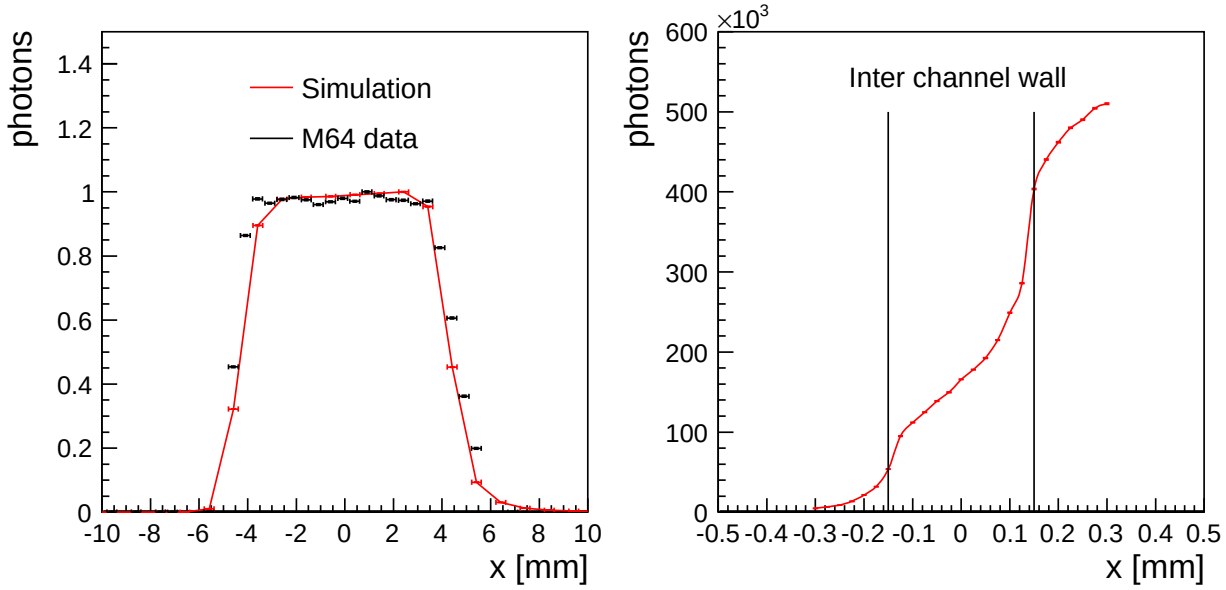

(a) (b)

Figure 11.26: *(a) Normalized detector response from a 2010 x-scan recorded with the M64 shown as the black data points. The data represents the channel response function convoluted with the beam profile at* Elsa*. Overlaid in red is the simulated curve for the best alignment parameters. (b) Fine simulation scan over the inter-channel wall with a point-like beam profile of $\sigma_x = \sigma_y = 1\ \mu m$. No spikes are observed from the channel wall at the simulated energy of 2 GeV.*

Translated to measurements with the detector prototype at Elsa the recorded x-scans represent a measurement of the channel response function convoluted with the beam profile. In Figure 11.26(a) the normalized response from an x-scan recorded with the M64 MAPM is shown in black. In the plateau region the data points scatter visibly, indicating unstable beam conditions (cf. Sec. 11.4.3). Overlaid in the red solid curve is the expectation from the simulation with the best alignment parameters, a relative inter-channel wall reflectivity of

85% and a lateral beam profile of $\sigma_x = \sigma_y = 0.5$ mm. The general features of the signal slopes at the channel borders and the mid-channel plateau are well modeled. However, the measured channel width deviates from the nominal simulated width of 8.5 mm by about 1 mm. This has been observed throughout the testbeam campaigns, see Section 11.2 and especially Figure 11.10 on page 137.

In contrast to the SLD response function, for the prototype detector no spikes from showering inside the channel walls are observed, neither in data, nor in the simulation. The influence of the inter-channel wall has been simulated with a fine x-scan and a gaussian beam profile with $\sigma_x = \sigma_y = 1$ μm and a beam energy of 2 GeV. Figure 11.26(b) shows the response function at the inter-channel wall. Some leakage below $x = -0.15$ mm can be seen from the finite beam size and the detector channel entrance window. The signal height reaches its maximum when the beam is fully contained inside the channel at $x = 0.3$ mm. No spikes are observed in the response function. The reason might lie in the electron energy, which is with 2 GeV considerably lower than the 28 GeV the SLD response function has been simulated for.

A quantitative comparison between simulation and data is difficult because of the afore mentioned signal instabilities and the deviations in the channel width. However, since the response function in the plateau region is expected to be flat the dominant corrections to the response function ρ will occur at the channel borders. Therefore the analysis of ρ in this thesis is concentrated on these regions. In Figure 11.27 the normalized signal response for a fine scan over the outer channel wall in the 2010 data is shown in black. The data has been recorded with the M4 MAPM. Also shown as the dashed blue line is the fit of the parameterized error

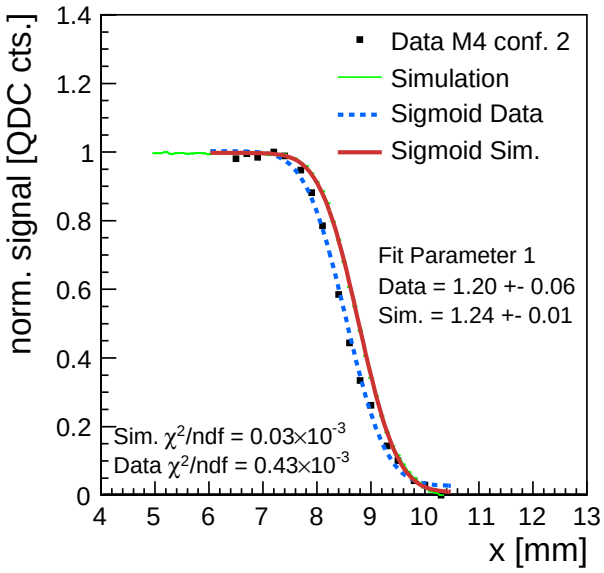

Figure 11.27: *Detector response (black data points) to a fine x-scan over the outer channel wall from the 2010 data, taken with the M4 MAPM. The dashed blue line is the result of a fit of the error function to the data. The thin green line shows the expected signal development from simulation, with the fitted error function in red. For better visibility, the simulation is shifted in x direction.*

function:

$$f(x) = p_0 \cdot erf(p_1 \cdot x - p_2) + p_3. \tag{11.9}$$

The parameter p_0 determines the height of the signal, p_2 the offset in x, and p_3 the lower bound of the error function. The most important information is given in the parameter p_1 which holds information on the slope of the error function which, in turn, is determined by the convolution of the beam profile with the rectangular channel acceptance. In the same Figure a simulated x-scan is shown as the thin green line with a sigmoid fit in red. The simulation points are shifted in x w.r.t the data to increase visibility. The sigmoid fits converge with χ^2/ndf values of $\mathcal{O}(10^{-4})$. The fit parameters p_1 are compatible within the errors. Given the uncertainty in the data this result validates the GEANT4 simulation for the implemented detector geometry and the beam parameters at ELSA.
Since in the final ILC polarimeter the channel walls will have considerably lower thicknesses compared to the prototype outer channel wall, an analogous measurement should be performed on the inter-channel wall. However, for the inter-channel wall no stable x-scan could be recorded during the ELSA testbeam campaigns which is partially due to the large beam profile in comparison to the limited stepwidth of the movable stage.

11.5 Analyzing power calibration

As discussed in Section 9.3, the precision of the analyzing power ($\mathcal{AP}$) calibration of the ILC Cherenkov detector depends on the channel response function ρ, the alignment of the detector with respect to the Compton fan, and the detector linearity over the full dynamic range. All these aspects have been studied with the detector prototype. The current understanding in view of the testbeam experience is summarized in this section. The main focus is on the implications of the testbeam results on the calibration and measurement techniques for the final ILC polarimeter detector.

11.5.1 Detector linearity

To keep the corrections to the $\mathcal{AP}$ calibration at a level of 0.1%, the detector has to be linear to 0.5%–0.75% over the full dynamic range. Per Compton interaction at the ILC, in the order of 10^2 to 10^3 Compton electrons are expected in the individual detector channels. With the data recorded at ELSA, this range has been covered. The results are preliminary, because of the limited knowledge of the beam conditions. Absolute beam currents could not be measured to the precision required, and the recorded signals indicated instabilities of the beam currents. An estimate of the ELSA extraction currents from a comparison of the ELSA data with the single electron data recorded at DESY II supports the observed range of the nominal extraction currents at ELSA.
The detector response to nominal beam currents from 50 pA to 300 pA (corresponding to about 170 to 1000 electrons) shows deviations from linearity at a level of 2%. The non-linearities are dominated by the uncertainty on the beam current measurement. Nevertheless, given the difficult beam conditions, the observed non-linearities are very close to the required 0.5% to 0.75%. In future testbeam campaigns with better current stability than at ELSA, these results will surely be improved. A further increase in precision is expected by a combination of testbeam data with data from LED calibration tests.

A dedicated experiment has shown, that PMT non-linearities can be measured to the sub-permille level [101]. Although the dynamic range studied has been lower than the one expected for ILC, it is feasible to extend the developed methods to higher signal ranges.

11.5.2 Channel response function

The channel response function ρ of the detector prototype has been measured and compared to MC simulations. The shape of the response function at the channel edge agrees well with the expectation. Signal spikes in the response function as observed for the SLD polarimeter, were neither seen in the simulations for the detector prototype, nor in the testbeam data. The spikes were a result from electrons showering in the channel walls. Since these spikes in the response function had a 1% effect on the analyzing power calibration at SLD, their absence is a positive result with respect to the $\mathcal{AP}$ calibration at ILC. However, further testbeam data and simulations are required to measure the behavior of the response function for electron energies of 25 GeV (at the Compton edge) and higher, since testbeam data was only recorded for 2 GeV electrons.
While the effects of the channel wall thickness on the response function were observed in the data as expected from simulation, the width of the response function determined from data differed by about 10% from the one extracted from simulations. More data with better beam conditions and a more accurate (and reproducible) detector setup are required for a better understanding of this difference.

11.5.3 Detector alignment

The alignment of the detector with respect to the Compton fan enters the analyzing power in two ways, see Section 9.3.3. First, the knowledge of the relative horizontal location is required to determine the integration limits for each detector channel. Secondly, any rotation of the detector distorts the Compton spectrum on the detector front, introducing systematic uncertainties.
For the ILC polarimeter, fast simulations indicate that the horizontal detector position in the plane orthogonal to the beam has to be calibrated to a precision below 0.4 mm to keep the systematic uncertainties on the measured polarization at a level of $\delta P/P = 0.1\%$ [125]. In the vertical (y) direction the Compton fan has a dimension of 200μm. A calibration of the Compton fan vertical position in each channel to the same order of magnitude as for the horizontal detector position, gives access to rotational detector misalignments about the beam axis. A precision on the rotation angle about the beam axis of $\alpha_z \approx 2$ mrad (0.1°) seems achievable for an array of 20 channels with a full array width of 200 mm.
In the direction of the beam (i.e. along the z-axis) the alignment requirements are not so stringent, since the dispersion of the Compton fan is about ~ 10 μrad and can be neglected for longitudinal detector displacements in the order of centimeters.
Rotational misalignments α_x, α_y and α_z about the coordinate axes have to be kept under control as well. At SLD, a rotation α_y about the vertical axis introduced corrections to the analyzing power of 0.03% to 0.08% per milliradian. For the ILC polarimeter, the rotational misalignment will be measured to a precision of the same order or better. Simulations have to be performed to determine the exact influence of detector rotations on the analyzing power.

With the detector prototype, two methods for the alignment measurement have been investigated at the ELSA accelerator with a gaussian beam profile. The first method of table scans involves periodic vertical and horizontal scans of the detector with respect to the beam. The second method relies on the intra-channel resolution of the Cherenkov light distribution and requires segmented multi-anode PMTs. Both methods are evaluated below regarding their applicability to the ILC polarimeter detectors.

Table scans

The rise and fall of the signal spectrum as a function of the relative beam position is recorded during a table scan, see Section 11.2. A fit of sigmoid error functions to the signal edges determines the channel width and center. For the detector prototype, the precision on the measurement of the channel centers has been limited to ~ 0.2 mm by the resolution of the movable stage. The observed channel widths were about 10% larger than predicted by simulations. Comparing the maximal recorded signal for a given detector rotation α_y about the y-axis to corresponding Monte Carlo simulations, the angle α_y could be determined to below 0.4°. When the observed channel widths were corrected for the 10% shift between data and simulation, the functional relationship between signal threshold and channel width (cf. Fig. 11.10 on page 137) could be used to measure α_y to a precision of 0.1° which is comparable to the requirements for ILC polarimetry.
At ILC, periodic table scans would be used for the determination of transverse (x, y) and rotational misalignments. In a vertical table scan, the information of where the fan enters the detector channels will be used in combination with the long lever arm of up to 20 adjacent channels to determine the detector rotation about the beam direction (α_z) to a high precision. In addition, the staggered design of the ILC Cherenkov detector gives access to rotations α_x about the horizontal x-axis.
In order to measure the horizontal alignment, the signal rise from the Compton edge is monitored in an endpoint scan. In contrast to the gaussian beam profile recorded with the detector prototype at ELSA, the expected signal from the Compton edge has to be simulated as the convolution of the channel response function and the Compton cross section. Using this method, the horizontal detector position was measured to a precision of 0.2 mm at the SLD polarimeter [98]. To account for possible beam motion in-between the endpoint scans, the zero asymmetry point was also monitored at SLD, allowing for a position calibration to a precision of 0.25 mm in-between endpoint scans [100, 98].
A combination of the endpoint calibration and the measurement of the zero asymmetry crossing point allows to estimate the systematic uncertainties from detector rotations, as well as uncertainties in the field maps of the bending dipoles of the polarimeter chicane. The position of the entire Compton spectrum is polarization independent. In particular, the positions of the zero asymmetry and the Compton edge are polarization independent, and their determination introduces no additional uncertainties on the polarization measurement via the analyzing power calibration.
Although table scans have been proven to deliver the required precision for the alignment measurement, this method has a serious drawback. Periodic table scans on a weekly or even daily basis result in a noticeable loss of luminosity, during which no polarization measurement is possible.

Light asymmetries

A second, at least equally precise method for alignment monitoring has been developed using the prototype detector. This method would reduce the beam time spent on table scans considerably and thus increase the amount of data for which polarization measurements are available. It requires segmented photomultipliers that are capable to resolve the light distribution within a single detector channel. Since the Compton fan can be considered point-like

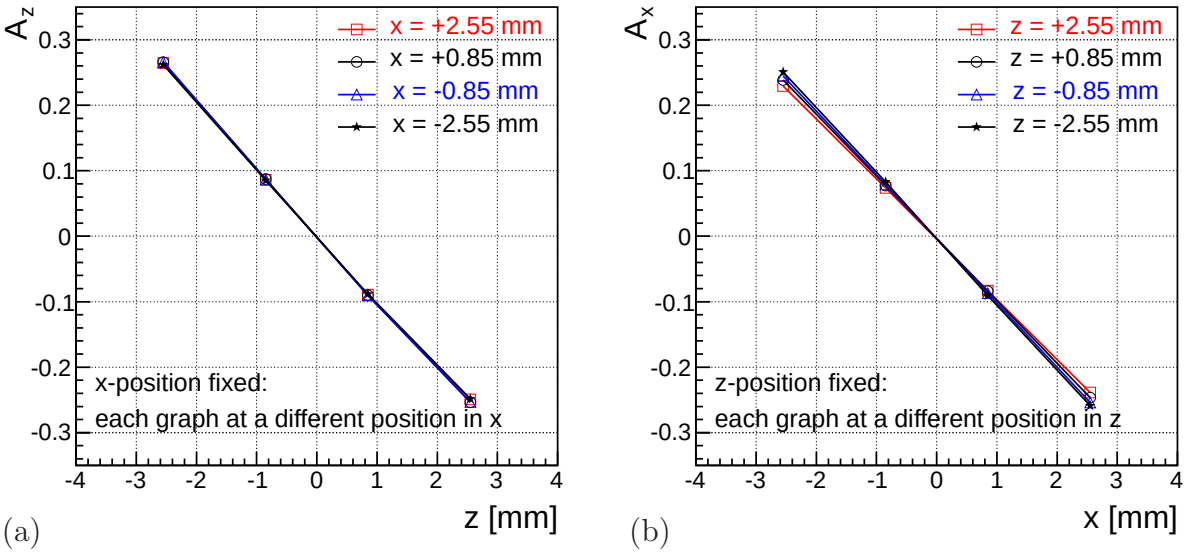

(a) (b)

Figure 11.28: *Light asymmetry (a) A_z for different x-positions and (b) A_x for different z-positions. The asymmetries are calculated directly from the light yield on the photocathode, without accounting for the specific anode positions of the employed photodetector. Therefore, no offset in A_x at $x = 0$ is observed, compared to Figure 11.11 on page 138. Due to the detector geometry, a beam y-position translates directly to a z-position in the readout plane.*

in the vertical direction and because the light asymmetry A_z is independent of the horizontal position (x) of the Compton electrons in the detector channel (Figure 11.28(a) and reference [106]), a measurement of the position dependent light asymmetry A_z in each detector channel could be used for the vertical detector alignment. Additional measurements of the light asymmetries A_z^{left} and A_z^{right} for the left- and right-hand side of the detector channel provide information of detector rotations about the y-axis. For the prototype, a precision of 0.1° on the measurement of both angles α_x and α_y has been achieved by evaluation of all available light asymmetries. Because of the high photon yield, the precision on measured asymmetries is limited by systematic effects. The dominant contribution to the uncertainties are gain variations of the individual anodes. For a precision of 0.2 mm on the detector position, the different anode gains have to be known to below 2.5%. To avoid polarization dependent uncertainties, the asymmetries should be evaluated for the combination of laser pulses with opposite helicities.
Segmented PMTs also allow for online monitoring of the Compton edge. The Compton edge

position is obtained by evaluating the measured light asymmetry A_x in the channel with the Compton edge and comparing the quantity

$$\mathcal{A}^{ch}(c.e.) = \frac{\int_0^{c.e.} \left(\frac{d\sigma}{dx'}\right)_{Compton} A_x(x')dx'}{\int_0^{c.e.} \left(\frac{d\sigma}{dx'}\right)_{Compton} dx'} \tag{11.10}$$

to simulations. The integral $\mathcal{A}^{ch}(c.e.)$ is the integrated light asymmetry $A_x(x')$ weighted with the Compton cross section $\left(\frac{d\sigma}{dx'}\right)_{Compton}$. The integration extends over the fraction of the channel width covered by the Compton spectrum from the channel edge ($x' = 0$) to the position of the Compton edge ($x' = c.e.$). In the construction of the integral, all position independent intensity fluctuations cancel, and therefore the integral itself is independent of e.g. luminosity fluctuations. The asymmetry A_x as a function of the x-position in Figure 11.28(b) shows a slight variation of the slope for different vertical beam positions y (corresponding directly to z in the readout plane), which is expected since the active Cherenkov length increases with y because of the mirrors at the front and end of the channel base. This variation has to be accounted for in the calculation of $\mathcal{A}^{ch}(c.e.)$. Implicitly, the integral depends on the channel response function ρ via the asymmetry $A_x(x')$. The integrated asymmetry $\mathcal{A}^{ch}(c.e.)$ is a monotonous function of the Compton edge position $c.e.$, allowing for an unambiguous determination of the Compton edge. The achievable precision depends on the knowledge of the response function, the beam polarization via the Compton cross section and the gain calibration of the PMT anodes. The size of these uncertainties has to be evaluated in further simulations.

Chapter 12

Conclusions

The ILC physics case comprises the study of the Higgs sector and the precise determination of the underlying structure of possible new physics. Of special interest are extensions to the SM including viable Dark Matter candidates.
Beam polarization is an essential ingredient for a precise measurement of the properties of Dark Matter candidates. Even if the longterm calibration of the luminosity weighted average polarization will come from e^+e^- collision data [99], corrections from polarimeters are required for high precision polarimetry. The required precision $\delta P/P$ on the polarization measurement has to be by a factor of at least two better than the best previous polarization measurement at SLD.

Model independent WIMP search

In the first part of this thesis, a model independent search for pair produced WIMPs in association with Initial State Radiation (ISR), $e^+e^- \to \chi\chi\gamma$, has been presented. The signal cross sections, the WIMP mass and the quantum number of the dominant partial wave of the production process are inferred from the energy spectrum of the detected photons.
A single photon signature was studied before in searches for supersymmetry at LEP [126, 127, 128, 129]. These analyses concentrated on the production of heavy particles in $e^+e^- \to XY$, with the subsequent decay $Y \to \gamma X$, where X is the lightest stable particle (LSP) and Y is the second lightest particle. For supersymmetric models including a viable Dark Matter candidate, X can either be the lightest neutralino $\tilde{\chi}_1^0$, or the gravitino $\tilde{G}$. Similar studies have also been performed for the ILC [130].
In contrast to the studies mentioned above, the analysis presented here investigates the direct pair production of neutral heavy particles. Direct production of the eligible particles, without having to produce heavier particles first and taking into account their subsequent decay, has the advantage that particle masses of up to half the available center-of-mass energy are accessible. In case SUSY is realized in nature and even though the next-to-lightest SUSY particle might be to heavy to be produced at ILC, the LSP can still be studied in detail.
The same production channel was studied before [131, 132, 133]. While in [132] only radiative neutrino pair production had been included in the signal backgrounds, this study incorporates further large SM backgrounds, i.e. multiple photon production $e^+e^- \to N\gamma$ ($N = 2, 3, 4$) and radiative Bhabha scattering. The emission of up to three "hard" photons is treated exactly in the event generation, by inclusion of the photon emission in the matrix elements on tree level.

Furthermore, multiple emission of additional ISR in the Weizsaecker-Williams-approximation, beamstrahlung and the $\gamma\gamma$ background are also accounted for. The analysis is performed with the full ILD detector simulation and for an ILC center-of-mass energy of $\sqrt{s} = 500$ GeV. The full simulation includes the beam energy spectrum, detector effects such as the energy resolution of the electromagnetic calorimeters, and the influence of the reconstruction algorithm.

The three investigated coupling structures of the WIMPs to electrons can be clearly distinguished for an integrated luminosity of $\mathcal{L} = 500$ fb^{-1} distributed to four polarization configurations with $|P_{e^-}| = 0.8$ and $|P_{e^+}| = 0.3$. The fully polarized cross sections $\sigma_{\{L,R\}}$ are determined to a precision of 25 fb to 40 fb when a total signal cross section of 100 fb is assumed in the signal region for unpolarized beams. Should the positron polarization be increased to $|P_{e^+}| = 0.6$, the precision on the polarized cross sections $\sigma_{\{L,R\}}$ increases by a factor of almost two depending on which polarized cross section is considered.

The measurement is systematically limited by the precision of the polarization measurement. Improving the precision of the polarization measurement from $\delta P/P = 0.25\%$ to $\delta P/P = 0.1\%$ yields a relative error of $\approx 5\%$ on the polarized cross section measurement. The combination of the polarized cross sections results in the measurement of the cross section for unpolarized beams, which can be determined to 3% for fully polarized beams. Again, this measurement is limited by the polarization uncertainty. The relative statistical errors on the unpolarized cross section σ_0 are of the same order as the relative systematic uncertainties for cross sections of $\sigma_0 \approx 50$ fb. For an integrated luminosity of $\mathcal{L} = 500$ fb^{-1} a WIMP signal with an unpolarized cross section of $\sigma_0 > 25$ fb is observable at the 5σ level.

For the mass measurement, the full integrated luminosity of $\mathcal{L} = 500$ fb^{-1} is used for one polarization configuration. Depending on the coupling scenario, the WIMP candidate mass is determined to a precision of 2% and below for fully polarized beams, systematically limited by the uncertainty on the beam energy spectrum. The comparison of the simulated data with theoretically predicted spectra provides information on the quantum number of the dominant partial wave in the production process, which can be an indication of CP-violation in SUSY scenarios. In addition to the model independent WIMP scenario, the lightest neutralino $\tilde{\chi}_1^0$ of the SPS1a' MSSM parameter point has been investigated. The results of the mass determination and cross section measurement are compatible with the model independent case.

The results are remarkably precise. Especially the accuracy of the mass measurement of the neutralino $\tilde{\chi}_1^0$ is only a factor of two worse than in the analysis of the leptonic decay $e^+e^- \to \tilde{\mu}_L\tilde{\mu}_L \to \tilde{\mu}_L\mu\tilde{\chi}_1^0$ [67]. This is unexpected in the presence of large SM and accelerator backgrounds. The most important reason is that the systematic uncertainty on the polarization measurement has been neglected in the determination of the WIMP (and neutralino) candidate mass, because for an increasing data statistics the mass measurement becomes more and more sensitive to the polarization independent signal threshold in the photon energy spectrum. For a future analysis, the full generation and simulation of signal and background data samples for a luminosity of $\mathcal{L} = 500$ fb^{-1} is strongly recommended. Such a large data sample would allow to demonstrate the negligible effects of the polarization uncertainty on the mass measurement for high data statistics.

However, the results presented here are compatible with similar studies presented in [132, 134]. In [134], a two-dimensional fit to the cross section and candidate mass yields WIMP masses with uncertainties of less than 15% for fully polarized beams and an integrated luminosity of

$\mathcal{L} = 500$ fb^{-1}. Apart from the single parameter fit of the mass, the analysis presented here differs in the choice of the full cross section being by a factor of about three larger, though still compatible with the cosmological DM constraints. Furthermore, this study includes the beam luminosity spectrum and effects from the detector simulation and, in addition, incorporates a detailed treatment of systematic uncertainties. Assuming that the uncertainty on the mass measurement scales with the signal cross section as $\delta M/M \sim 1/\sqrt{\sigma}$, then the relative mass resolution is $\delta M/M \approx 4\%$ for a cross section of $\sigma_0 \approx 30$ fb.

Cherenkov detector prototype

In the second part of this thesis, the design, construction, and simulation of a Cherenkov detector prototype for ILC polarimetry, as well as an analysis of first data recorded with this detector has been presented. The prototype has been designed and constructed keeping in mind the key requirements for the final ILC polarimeter detector. In three testbeam campaigns at DESY II (Hamburg) and at ELSA (Bonn), data for unpolarized electrons has been recorded with this prototype and compared to a detailed GEANT4 based detector simulation. The goals of the testbeam campaigns have been the overall validation of the functionality of the prototype, the determination of the detector alignment from data, and the study of important aspects of the detector setup impacting the final ILC polarimeter detector.
To reach a systematic precision of $\delta P/P = 0.25\%$ on the polarization measurement at ILC, the analyzing power $\mathcal{AP}$ has to be calibrated to below 0.2%. This requires a precise knowledge of the detector channel acceptance and the relative alignment of the detector w.r.t. the Compton fan. The primary methods for detector alignment at ILC will be similar to the methods used at SLD, which are periodic horizontal scans of the spectrum to locate the Compton edge and monitor the zero-crossing point of the measured rate asymmetry.
With the employed multi-anode photomultipliers (MAPM) during the testbeam campaigns, further observables can be exploited for detector alignment from the polarization data itself. This, in turn, could reduce the required time for alignment scans significantly. The light yield asymmetries available from the intra-channel resolution with segmented PMTs can be used in combination with the staggered design of the ILC Cherenkov detector to determine detector rotations about the axes perpendicular to the beam direction. For the prototype, rotations about both transverse axes could be determined with an accuracy of 0.1°, which is already very close to the required precision. The analysis results suggest that angular misalignments can be determined from the intra-channel light asymmetries to a precision below 0.05° given better experimental conditions. This advantage has to be assessed in the light of possible degrading effects. Due to the lower number of photons per readout channel, the influence of photodetector dark currents become more pronounced. Anode cross talk and different gains of the anode segments, as well as possible misalignments of the segmented photodetectors w.r.t. the detector channel it covers might introduce new uncertainties, and require a stronger calibration effort. In light of the achieved precision of the angular alignment, however, gain variations were under control for the detector prototype. A promising benefit from segmented PMTs is the possibility of online monitoring the position of the Compton edge via the light yield asymmetry. In combination with the monitoring of the zero-crossing point of the rate asymmetry, not only beam motions can be detected, but other systematics can be kept under control as well, for example uncertainties in the magnetic fields of the polarimeter chicane dipoles. From the results of this thesis, segmented PMTs with four anodes per detector chan-

nel present an interesting possibility for the Cherenkov detectors of the ILC polarimeters.
The channel acceptance has been measured and compared to MC simulations. The shape of the detector response near the channel edge agrees well with the simulations, although the observed width of the channel is typically 10% larger than predicted. In order to understand this, more data with better beam conditions and more accurate/reproducible detector movements (especially regarding rotations about the x- and z-axes) are needed. With respect to the future ILC polarimeter, uncertainties on the polarization independent backgrounds have been investigated. At Elsa no accelerator-induced backgrounds have been observed. Thermal noise from the PMTs and sampling errors in the digitization can be regarded as polarization independent backgrounds. For the employed PMTs, no systematic uncertainties from thermal noise were observed. Uncertainties in the signal pedestal were below the limit to keep their systematic contribution to a polarization measurement under ILC-like conditions at a level of 0.1%. The studied dynamic range in terms of detected electrons covered 100 to 1000 electrons, which is in the order of the expected rates at ILC. The detector linearity has been measured over this range and observed deviations at the percent level could be attributed to uncertainties on the measurement of the extraction current. To keep corrections to the analyzing power from detector non-linearities below 0.1%, the linearity has to be controlled at a level of 0.5%–0.75%. The required precision has nearly been achieved with the detector prototype, even though the data-taking conditions were not optimal.
The results obtained from the prototype operation suggest several improvements to the experimental setup. The reflectivities of the channel walls measured with a modified transmission spectrometer were strongly underestimated. The capability to obtain a relative measurement of the inter-channel wall reflectivity from the recorded data themselves, highlights the sensitivity of the Cherenkov detector prototype. However, for future measurements, an exact knowledge of the wall reflectivities is desirable. The high flexibility of the prototype design has to be better exploited, by employing different PMTs, LED calibration systems and wall materials. A re-design of the Cherenkov detector prototype with at least three detector channels would overcome the asymmetric setup of the current two detector channels with one thick and one thin channel wall, each with different reflectivities.
In case a staggered design of the channels is realized, the alignment studies could be extended to all three angles of rotation, and the impact of electrons showering in the walls of the first channel on the signal in the following channels could be studied. Furthermore, the channel structure could be changed from the u-shaped to a z-shaped design, with the front leg holding the calibration system pointing downwards. With such a geometry, the available Cherenkov length is independent of the vertical position. In the u-shape geometry, the two 45° mirrors at the beginning and end of the Cherenkov section shorten the effective length for electrons traversing in the lower part of the channel.
New testbeam campaigns should prefer sites providing ILC-like beam conditions in terms of the rates and bunch structure. Any test site should also provide excellent beam current measurements over a large range of extraction currents, to allow the recording of single- and multi-electron signals with consistent PMT gains.

Bibliography

[1] ATLAS Collaboration, *Physics TDR*. CERN-LHCC-99-14 and CERN-LHCC-99-15.

[2] CMS Collaboration, *Physics TDR*. CERN/LHCC/2006-021, June 2006.

[3] S. Weinberg, *A Model of Leptons*, Phys. Rev. Lett. **19** (1967) 1264–1266.

[4] S. L. Glashow, *Partial Symmetries of Weak Interactions*, Nucl. Phys. **22** (1961) 579–588.

[5] A. Salam and J. C. Ward, *Electromagnetic and weak interactions*, Phys. Lett. **13** (1964) 168–171.

[6] P. W. Higgs, *Broken symmetries, massless particles and gauge fields*, Phys. Lett. **12** (1964) 132–133.

[7] P. W. Higgs, *Broken symmetries and the masses of gauge bosons*, Phys. Rev. Lett. **13** (1964) 508–509.

[8] P. W. Higgs, *Spontaneous Symmetry Breakdown without Massless Bosons*, Phys. Rev. **145** (1966) 1156–1163.

[9] F. Englert and R. Brout, *Broken symmetry and the mass of gauge vector mesons*, Phys. Rev. Lett. **13** (1964) 321–322.

[10] Gargamelle Neutrino Collaboration, F. J. Hasert et al., *Observation of neutrino-like interactions without muon or electron in the Gargamelle neutrino experiment*, Phys. Lett. **B46** (1973) 138–140.

[11] ALEPH Collaboration, DELPHI Collaboration, L3 Collaboration, OPAL Collaboration, SLD Collaboration, LEP Electroweak Working Group, SLD Electroweak Group, SLD Heavy Flavour Group Collaboration, *Precision electroweak measurements on the Z resonance*, Phys.Rept. **427** (2006) 257–454, `arXiv:hep-ex/0509008 [hep-ex]`.

[12] Particle Data Group Collaboration, C. Amsler et al., *Review of particle physics*, Phys. Lett. **B667** (2008) 1.

[13] LEP Working Group for Higgs boson searches Collaboration, R. Barate et al., *Search for the standard model Higgs boson at LEP*, Phys. Lett. **B565** (2003) 61–75, `arXiv:hep-ex/0306033`.

[14] C. Hoffmann, *Bestimmung einer unteren Masse des leichtesten Neutralinos mit dem ALEPH Detektor in e^+e^-- Kollisionen bei Schwerpunktsenergien bis 172 GeV*, PhD thesis, Johannes Gutenberg-Universitaet Mainz (1998) .

[15] F. Zwicky, *On the Masses of Nebulae and of Clusters of Nebulae*, Astrophys. J. **86** (1937) 217–246.

[16] L. Volders, *Neutral hydrogen in M 33 and M 101*, Bulletin of the Astronomical Institutes of the Netherlands **14 (492)** (1959) 323–334.

[17] V. C. Rubin and W. K. Ford, Jr., *Rotation of the Andromeda Nebula from a Spectroscopic Survey of Emission Regions*, Astrophys. J. **159** (feb, 1970) 379–+.

[18] A. A. Penzias and R. W. Wilson, *A Measurement of excess antenna temperature at 4080- Mc/s*, Astrophys. J. **142** (1965) 419–421.

[19] Gamow, G. , *The Origin of Elements and the Separation of Galaxies*, Phys. Rev. **74** (Aug, 1948) 505–506.

[20] G. Gamow, *The evolution of the universe*, Nature **162** (1948) 680–682.

[21] Alpher, Ralph A. and Herman, Robert C., *On the Relative Abundance of the Elements*, Phys. Rev. **74** (Dec, 1948) 1737–1742.

[22] G. F. Smoot et al., *Structure in the COBE differential microwave radiometer first year maps*, Astrophys. J. **396** (1992) L1–L5.

[23] WMAP Collaboration, J. Dunkley et al., *Five-Year Wilkinson Microwave Anisotropy Probe (WMAP) Observations: Likelihoods and Parameters from the WMAP data*, Astrophys. J. Suppl. **180** (2009) 306–329, `arXiv:0803.0586 [astro-ph]`.

[24] P. Peebles, *Principles of Physical Cosmology*. Princton University Press, 1993.

[25] E. W. Kolb and M. S. Turner, *The Early universe*, Front. Phys. **69** (1990) 1–547.

[26] CDF Collaboration, F. Abe et al., *Evidence for top quark production in $\bar{p}p$ collisions at $\sqrt{s} = 1.8$ TeV*, Phys. Rev. **D50** (1994) 2966–3026.

[27] D0 Collaboration, S. Abachi et al., *Observation of the top quark*, Phys. Rev. Lett. **74** (1995) 2632–2637, `arXiv:hep-ex/9503003`.

[28] CDF Collaboration, F. Abe et al., *Observation of top quark production in $\bar{p}p$ collisions*, Phys. Rev. Lett. **74** (1995) 2626–2631, `arXiv:hep-ex/9503002`.

[29] CDF and D0 Collaboration, *Combined CDF and D0 Upper Limits on Standard Model Higgs- Boson Production with up to 6.7 fb^{-1} of Data*, `arXiv:1007.4587 [hep-ex]`.

[30] ILC Collaboration, J. Brau, (Ed.) et al., *ILC Reference Design Report Volume 1 - Executive Summary*, `arXiv:0712.1950 [physics.acc-ph]`.

[31] ILC Collaboration, G. Aarons et al., *ILC Reference Design Report Volume 2 - Physics at the ILC*, `arXiv:0709.1893 [hep-ph]`.

[32] ILC Collaboration, N. Phinney, N. Toge, and N. Walker, *ILC Reference Design Report Volume 3 - Accelerator*, arXiv:0712.2361 [physics.acc-ph].

[33] ILC Collaboration, T. Behnke, (Ed.) et al., *ILC Reference Design Report Volume 4 - Detectors*, arXiv:0712.2356 [physics.ins-det].

[34] H. Li, *Higgs Recoil Mass and Higgs-Strahlung Cross-Section Study for the ILD LOI*, arXiv:1007.2999 [hep-ex].

[35] H. Li, *Higgs Recoil Mass and Cross-Section Analysis at ILC and Calibration of the CALICE SiW ECAL Prototype*. PhD thesis, 2009. LAL-09-118.

[36] ILD Concept Group - Linear Collider Collaboration, T. Abe et al., *The International Large Detector: Letter of Intent*, arXiv:1006.3396 [hep-ex]. FERMILAB-LOI-2010-01.

[37] J. Goldstein et al., *Analysis of the higgs hadronic branchin ratios in the $ZH \to llqq$ channel*. http://www.ilcild.org/documents/ild-letter-of-intent/ild-loi-material/ .

[38] H.-U. Martyn, *Supersymmetry physics at linear colliders*, arXiv:hep-ph/0302024.

[39] J. A. Aguilar-Saavedra et al., *Supersymmetry parameter analysis: SPA convention and project*, Eur. Phys. J. **C46** (2006) 43–60, arXiv:hep-ph/0511344.

[40] ILC GDE Collaboration, N. W. M. Ross and A. Yamamoto, *SB2009 Proposal Document*. 2009. http://lcdev.kek.jp/SB2009/SB20091217B.pdf .

[41] M. Berggren, *ILC Beam-Parameters and New Physics*, arXiv:1007.3019 [hep-ex].

[42] V. Balakin, *Travelling Focus Regime for Linear Collider VLEPP*, Proc. 77th ICFA Workshop on Beam Dynamics, Los Angeles (1991) .

[43] T. Maruyama, D. Luh, A. Brachmann, J. Clendenin, E. L. Garwin, et al., *A Systematic study of polarized electron emission from strained GaAs/GaAsP superlattice photocathodes*, Appl. Phys. Lett (2004) .

[44] T. Nishitani et al., *Highly polarized electrons from GaAsGaAsP and InGaAsAlGaAs strained-layer superlattice photocathodes*, J. Appl. Phys. **97** (2005) 094907.

[45] T. Nakanishi et al., *Polarized electron source for a linear collider in Japan*, NIM **A 455** (2000) 109.

[46] G. A. Moortgat-Pick et al., *The role of polarized positrons and electrons in revealing fundamental interactions at the linear collider*, Phys. Rept. **460** (2008) 131–243, arXiv:hep-ph/0507011.

[47] S. Boogert et al., *Polarimeters and Energy Spectrometers for the ILC Beam Delivery System*, JINST **4** (2009) P10015, arXiv:0904.0122 [physics.ins-det].

[48] B. Aurand et al., *Beam Polarization at the ILC: the Physics Impact and the Accelerator Solutions*, arXiv:0903.2959 [physics.acc-ph].

[49] K. Monig, *Polarisation measurements with annihilation data*. Prepared for International Conference on Linear Colliders (LCWS 04), Paris, France, 19-24 Apr 2004.

[50] A. Blondel, *A scheme to measure the polarization asymmetry at the Z pole in LEP*, Phys. Lett. **B202** (1988) 145.

[51] GLD Concept Study Group Collaboration, K. Abe et al., *GLD detector outline document*, arXiv:physics/0607154.

[52] LDC Working Group Collaboration, Kisielewska et al., *Detector Outline Document for the Large Detector Concept*. 2006. www.ilcild.org/documents/ldc/outlinedoc/view .

[53] M. A. Thomson, *Particle Flow Calorimetry and the PandoraPFA Algorithm*, Nucl. Instrum. Meth. **A611** (2009) 25–40, arXiv:0907.3577 [physics.ins-det].

[54] M. A. Thomson, *Status of Particle Flow Calorimetry*, Presentation at Calor 2010, Beijing, May 2010 . http://www.hep.phy.cam.ac.uk/~thomson/talks/PFA_Plenary_Thomson.pdf .

[55] B. Parker and A. Seryi, *Compensation of the effects of detector solenoid on the vertical beam orbit in NLC*, Phys.Rev.ST Accel.Beams **8** (2005) 041001.

[56] A. Seryi, T. Maruyama, and B. Parker, *IR Optimization, DID and anti-DID*. 2006. http://www-project.slac.stanford.edu/lc/bdir/Meetings/beamdelivery/2005-09-27/index.htm .

[57] CALICE Collaboration, J. Repond et al., *Design and Electronics Commissioning of the Physics Prototype of a Si-W Electromagnetic Calorimeter for the International Linear Collider*, JINST **3** (2008) P08001, arXiv:0805.4833 [physics.ins-det].

[58] C. Adloff et al., *Response of the CALICE Si-W electromagnetic calorimeter physics prototype to electrons*, Nucl. Instrum. Meth. **A608** (2009) 372–383.

[59] CALICE Collaboration, C. Adloff et al., *Response of the CALICE Si-W Electromagnetic Calorimeter Physics Prototype to Electrons*, vol. 160, p. 012065. 2009. arXiv:0811.2354 [physics.ins-det].

[60] CALICE Collaboration Collaboration, F. Simon, *Hadronic showers in the CALICE calorimeter prototypes*, Nucl.Instrum.Meth. **A623** (2010) 228–230, arXiv:0904.2991 [physics.ins-det].

[61] H. Abramowicz, A. Abusleme, K. Afanaciev, J. Aguilar, P. Ambalathankandy, et al., *Forward Instrumentation for ILC Detectors*, JINST **5** (2010) P12002, arXiv:1009.2433 [physics.ins-det].

[62] A. Birkedal, K. Matchev, and M. Perelstein, *Dark matter at colliders: A model-independent approach*, Phys. Rev. **D70** (2004) 077701, arXiv:hep-ph/0403004.

[63] Atlas Collaboration Collaboration, G. Aad et al., *Search for squarks and gluinos using final states with jets and missing transverse momentum with the ATLAS detector in sqrt(s) = 7 TeV proton-proton collisions*, Phys.Lett. **B701** (2011) 186–203, arXiv:1102.5290 [hep-ex].

[64] Atlas Collaboration Collaboration, G. Aad et al., *Search for supersymmetry using final states with one lepton, jets, and missing transverse momentum with the ATLAS detector in sqrts = 7 TeV pp*, Phys.Rev.Lett. **106** (2011) 131802, arXiv:1102.2357 [hep-ex].

[65] H. Baer, C. Balazs, A. Belyaev, and J. O'Farrill, *Direct detection of dark matter in supersymmetric models*, JCAP **0309** (2003) 007, arXiv:hep-ph/0305191.

[66] G. Degrassi, S. Heinemeyer, W. Hollik, P. Slavich, and G. Weiglein, *Towards high-precision predictions for the MSSM Higgs sector*, Eur. Phys. J. **C28** (2003) 133–143, arXiv:hep-ph/0212020.

[67] N. D'Ascenzo, *Study of the neutralino sector and analysis of the muon response of a highly granular hadron calorimeter at the International Linear Collider*. PhD thesis. DESY-THESIS-2009-004.

[68] H. K. Dreiner, O. Kittel, and U. Langenfeld, *Discovery potential of radiative neutralino production at the ILC*, Phys. Rev. **D74** (2006) 115010, arXiv:hep-ph/0610020.

[69] S. Y. Choi, K. Hagiwara, H. U. Martyn, K. Mawatari, and P. M. Zerwas, *Spin analysis of supersymmetric particles*, Eur. Phys. J. **C51** (2007) 753–774, arXiv:hep-ph/0612301.

[70] S. Y. Choi, *Neutralino pair production and 3-body decays at e+ e- linear colliders as probes of CP violation in the neutralino system*, Phys. Rev. **D69** (2004) 096003, arXiv:hep-ph/0308060.

[71] H. K. Dreiner, O. Kittel, and U. Langenfeld, *The role of beam polarization for radiative neutralino production at the ILC*, Eur. Phys. J. **C54** (2008) 277–284, arXiv:hep-ph/0703009.

[72] F. A. Berends, G. J. H. Burgers, C. Mana, M. Martinez, and W. L. van Neerven, *Radiative corrections to the process e+ e- → neutrino anti-neutrino gamma*, Nucl. Phys. **B301** (1988) 583.

[73] G. Montagna, M. Moretti, O. Nicrosini, and F. Piccinini, *Single- and multi-photon final states with missing energy at e+ e- colliders*, Nucl. Phys. **B541** (1999) 31–49, arXiv:hep-ph/9807465.

[74] A. Freitas, W. Porod, and P. M. Zerwas, *Determining sneutrino masses and physical implications*, Phys. Rev. **D72** (2005) 115002, arXiv:hep-ph/0509056.

[75] J. Kalinowski, W. Kilian, J. Reuter, T. Robens, and K. Rolbiecki, *Pinning down the Invisible Sneutrino*, JHEP **10** (2008) 090, arXiv:0809.3997 [hep-ph].

[76] A. Vogel, *Beam-induced backgrounds in detectors at the ILC*. PhD thesis. DESY-THESIS-2008-036.

[77] K. Wichmann, *Influence of beam related background on ILD reconstruction*, arXiv:1007.2440 [physics.ins-det].

[78] W. Kilian, T. Ohl, and J. Reuter, *WHIZARD: Simulating Multi-Particle Processes at LHC and ILC*, arXiv:0708.4233 [hep-ph].

[79] M. Moretti, T. Ohl, and J. Reuter, *O'Mega: An optimizing matrix element generator*, arXiv:hep-ph/0102195.

[80] D. Schulte, *Study of Electromagnetic and Hadronic Background in the Interaction Region of the TESLA Collider*. 1996. TESLA 97-08.

[81] W. Kilian, T. Ohl, and J. Reuter, *WHIZARD 1.96: A generic Monte-Carlo integration and event generation package for multi particle processes MANUAL*. 2001. LC-DET-2001-039.

[82] J. Allison et al., *G4–a simulation toolkit*, Nuclear Instruments and Methods in Physics Research Section A: Accelerators, Spectrometers, Detectors and Associated Equipment **506** (2003) no. 3, 250 – 303.

[83] Mokka *webpage*. http://polzope.in2p3.fr:8081/MOKKA/ .

[84] MarlinReco *webpage*. http://ilcsoft.desy.de/portal/software_packages/marlinreco/ .

[85] Marlin *webpage*. http://ilcsoft.desy.de/portal/software_packages/marlin/ .

[86] *LCIO webpage*. http://lcio.desy.de/ .

[87] A. Rosca, *BeamCal electron reconstruction*. http://ilcagenda.linearcollider.org/getFile.py/access?contribId=0&resId=0&materialId=slides&confId=4878 .

[88] R. Brun and F. Rademakers, *ROOT: An object oriented data analysis framework*, Nucl. Instrum. Meth. **A389** (1997) 81–86.

[89] Root *webpage*. http://root.cern.ch/drupal/ .

[90] *International Linear Collider Database webpage*. http://www-flc.desy.de/simulation/databaseinput/ .

[91] K. Wichmann, *Beam backgrounds at ILD: Review*, Presentation at ILD Workshop 2011 at LAL, Paris . http://ilcagenda.linearcollider.org/conferenceOtherViews.py?view=standard&confId=4901 .

[92] SLD Collaboration, M. Woods, *The scanning Compton polarimeter for the SLD experiment*, arXiv:hep-ex/9611005.

[93] V. N. Baier and V. A. Khoze, *Determination of the transverse polarization of high-energy electrons*, Sov. J. Nucl. Phys. **9** (1969) 238–240.

[94] M. Beckmann et al., *The longitudinal polarimeter at HERA*, Nucl. Instrum. Meth. **A479** (2002) 334–348, arXiv:physics/0009047.

[95] V. Gharibyan, N. Meyners, and P. Schuler, *The TESLA Compton polarimeter*. LC-DET-2001-047.

[96] Klein, O. and Nishina, T., *Über die Streuung von Strahlung durch freie Elektronen nach der neuen relativistischen Quantendynamik von Dirac*, Zeitschrift für Physik A Hadrons and Nuclei **52** (1929) 853–868. 10.1007/BF01366453.

[97] A. Seryi, *BDS at reduced beam parameters*, Presentation at GDE Baseline Assessment Workshop 2011 at SLAC, Stanford . http://ilcagenda.linearcollider.org/contributionDisplay.py?contribId=12&sessionId=1&confId=4612 .

[98] R. C. King, *A precise measurement of the left-right asymmetry of Z boson production at the SLAC linear collider*. PhD thesis. SLAC-0452.

[99] I. Marchesini, *Triple gauge couplings and polarization at the ILC and Leakage in a highly granular calorimeter*. PhD thesis. DESY THESIS, to be published.

[100] R. D. Elia, *Measurement of the left-right asymmetry in Z boson production by electron - positron collisions*. PhD thesis. SLAC-0429.

[101] C. Helebrant, *In search of new phenomena using polarization: HERA and ILC*. PhD thesis. DESY-THESIS-2009-049.

[102] J. D. Jackson, *Classical Electrodynamics*. New York, USA: Wiley (1998).

[103] G. A. Moortgat-Pick et al., *Depolarization and Beam-beam Effects at the Linear Collider*. EPAC'08, 11th European Particle Accelerator Conference, 23- 27 June 2008, Genoa, Italy.

[104] I. F. Ginzburg, G. L. Kotkin, V. G. Serbo, and V. I. Telnov, *Colliding gamma e and gamma gamma Beams Based on the Single Pass Accelerators (of Vlepp Type)*, Nucl. Instr. Meth. **205** (1983) 47–68.

[105] V. I. Telnov, *Problems of obtaining gamma gamma and gamma epsilon colliding beams at linear colliders*, Nucl. Instrum. Meth. **A294** (1990) 72–92.

[106] C. Bartels et al., *Design and Construction of a Cherenkov Detector for Compton Polarimetry at the ILC*, arXiv:1011.6314 [physics.ins-det].

[107] *Hamamatsu R7600U-03-M4 (2007)*. http://sales.hamamatsu.com/assets/pdf/parts_R/R5900U_R7600U_TPMH1291E03.pdf .

[108] *Hamamatsu R7600-00-M64 (2006)*. http://sales.hamamatsu.com/index.php?id=13195917 .

[109] *Hamamatsu R7400U-06(03) (2004)*. http://sales.hamamatsu.com/assets/pdf/parts_R/R7400U_TPMH1204E07.pdf .

[110] *Photonis XP1911/UV (1999).* http://www.photonis.com/upload/industryscience/pdf/pmt/XP1911UV.pdf .

[111] U. Velte, *Aufbau eines Teststandes fuer Photodetektoren und Teststrahlmessungen fuer die Strahlpolarisationsmessung am ILC*, Diploma thesis. DESY-THESIS-2009-005.

[112] E. Fokitis et al., *The Fabry-Perot interferometer for the DELPHI ring imaging Cherenkov detector*, Nucl. Phys. Proc. Suppl. **44** (1995) 246–251.

[113] E. Albrecht et al., *VUV absorbing vapours in n-perfluorocarbons*, Nucl. Instrum. Meth. **A510** (2003) 262–272.

[114] *Agilent Technologies, LED,*T-1 3/4 (5 mm) Precision Optical Performance InGaN Blue and Green Lamps. 2002. http://www.agilent.com .

[115] C. S.p.A., *Technical Information Manual: V965/V965A 16/8 channel Dual Range QDC, revision 6.* 2007. http://www.caen.it .

[116] Tektronix, *Arbitrary/Function Generators AFG 3011 / 3021B / 3022B / 3101 / 3102 / 3251 / 3252.* 2008. http://www.tek.com .

[117] PerkinElmer, *Lambda 800 Spectrometer.* http://las.perkinelmer.com/Catalog/CategoryPage.htm?CategoryID=Lambda+800+Spectrometer .

[118] A. D. Rakic, *Algorithm for the determination of intrinsic optical constants of metal films: application to aluminum*, Appl. Opt. **34** 4755–4767.

[119] *Refractive Index webpage.* http://refractiveindex.info/?group=METALS&material=Aluminium .

[120] *GEANT4 – Physics Reference Manual.* http://geant4.web.cern.ch/geant4/UserDocumentation/UsersGuides/PhysicsReferenceManual/fo/PhysicsReferenceManual.pdf .

[121] A. Bideau-Mehu et al., *Measurement of refractive indices of neon, argon, krypton and xenon in the 253.7-140.4 nm wavelength range. Dispersion relations and estimated oscillator strengths of the resonance lines*, J. Quant. Spectrosc. Radiat. Transf. **25** .

[122] *Testbeams at DESY, webpage.* http://adweb.desy.de/home/testbeam/WWW/ .

[123] ELSA *webpage.* http://www-elsa.physik.uni-bonn.de/ .

[124] W. Hillert, *The Bonn electron stretcher accelerator ELSA: Past and future*, Eur. Phys. J. **A28S1** (2006) 139–148.

[125] J. List, *Analyzing power calibration*, Presentation at Workshop on Polarization and Beam Energy Measurement at the ILC, Zeuthen (2008) . https://indico.desy.de/getFile.py/access?contribId=23&sessionId=8&resId=0&materialId=slides&confId=585 .

[126] ALEPH Collaboration, R. Barate et al., *Search for supersymmetry in the photon(s) plus missing energy channels at s**(1/2) = 161-GeV and 172-GeV*, Phys. Lett. **B420** (1998) 127–139, arXiv:hep-ex/9710009.

[127] LEP Collaboration, M. Gataullin, *Single- and multi-photon events with missing energy in e+ e- collisions at LEP*, Int. J. Mod. Phys. **A20** (2005) 3273–3276.

[128] DELPHI Collaboration, J. Abdallah et al., *Photon events with missing energy in e+ e- collisions at s**(1/2) = 130-GeV to 209-GeV*, Eur. Phys. J. **C38** (2005) 395–411, arXiv:hep-ex/0406019.

[129] DELPHI Collaboration, P. Abreu et al., *Search for pair produced neutralinos in events with photons and missing energy from e+ e- collisions at S**(1/2) = 130-GeV to 183-GeV*, Eur. Phys. J. **C6** (1999) 371–384.

[130] N. Wattimena, *Calorimetry at the International Linear Collider: From simulation to reality*. PhD thesis. DESY-THESIS-2010-006.

[131] P. Konar, K. Kong, K. T. Matchev, and M. Perelstein, *Shedding Light on the Dark Sector with Direct WIMP Production*, New J. Phys. **11** (2009) 105004, arXiv:0902.2000 [hep-ph].

[132] C. Bartels, *Model-independent WIMP searches at the International Linear Collider*, Diploma thesis, 2007. Hardcopy at DESY.

[133] C. Bartels and J. List, *WIMP Searches at the ILC using a model-independent Approach*, arXiv:0901.4890 [hep-ex].

[134] N. Bernal, A. Goudelis, Y. Mambrini, and C. Munoz, *Determining the WIMP mass using the complementarity between direct and indirect searches and the ILC*, JCAP **0901** (2009) 046, arXiv:0804.1976 [hep-ph].

List of Figures

List of Tables

Appendix A

Data samples

		Generator:	WHIZARD		
Process	P_{e^-}	P_{e^+}	N_{events}	σ [fb]	$\mathcal{L}$ [fb^{-1}]
$\nu_e\nu_e\gamma$	-1.0	$+1.0$	$3,832,650$	14990.0	255.7
$\nu_e\nu_e\gamma$	$+1.0$	-1.0	$198,643$	397.3	500.0
$\nu_e\nu_e\gamma\gamma$	-1.0	$+1.0$	$988,847$	1977.7	500.0
$\nu_e\nu_e\gamma\gamma$	$+1.0$	-1.0	$38,897$	77.8	500.0
$\nu_e\nu_e\gamma\gamma\gamma$	-1.0	$+1.0$	$67,453$	134.9	500.0
$\nu_e\nu_e\gamma\gamma\gamma$	$+1.0$	-1.0	$4,414$	7.6	580.8
$\nu_\mu\nu_\mu\gamma$	-1.0	$+1.0$	$310,232$	620.5	500.0
$\nu_\mu\nu_\mu\gamma$	$+1.0$	-1.0	$197,947$	395.9	500.0
$\nu_\mu\nu_\mu\gamma\gamma$	-1.0	$+1.0$	$60,632$	121.3	499.9
$\nu_\mu\nu_\mu\gamma\gamma$	$+1.0$	-1.0	$38,752$	77.5	500.0
$\nu_\mu\nu_\mu\gamma\gamma\gamma$	-1.0	$+1.0$	$5,878$	11.8	498.1
$\nu_\mu\nu_\mu\gamma\gamma\gamma$	$+1.0$	-1.0	$4,407$	7.6	579.9
$\nu_\tau\nu_\tau\gamma$	-1.0	$+1.0$	$309,482$	619.0	500.0
$\nu_\tau\nu_\tau\gamma$	$+1.0$	-1.0	$197,361$	394.7	500.0
$\nu_\tau\nu_\tau\gamma\gamma$	-1.0	$+1.0$	$60,535$	121.1	499.9
$\nu_\tau\nu_\tau\gamma\gamma$	$+1.0$	-1.0	$38,827$	77.7	499.7
$\nu_\tau\nu_\tau\gamma\gamma\gamma$	-1.0	$+1.0$	$5,937$	11.9	498.9
$\nu_\tau\nu_\tau\gamma\gamma\gamma$	$+1.0$	-1.0	$4,364$	7.5	581.9

Table A.1: *The $\nu\nu\gamma$ SM background generated with* WHIZARD *after preselection cuts. All final states are listed separately for each neutrino generation and beam polarization configuration. The generated statistics for the $\nu_e\nu_e\gamma$ final state with $(P_{e^-}; P_{e^+}) = (-1.0; 1.0)$ correspond to a luminosity of only $\mathcal{L} = 255\,\text{fb}^{-1}$.*

Generator: WHIZARD					
Process	P_{e^-}	P_{e^+}	N_{events}	σ [fb]	$\mathcal{L}$ [fb^{-1}]
$\gamma\gamma$	-1.0	$+1.0$	51994	12998.3	4.0
$\gamma\gamma$	$+1.0$	-1.0	129912	12991.2	10.0
$\gamma\gamma\gamma$	-1.0	$+1.0$	21580	2158.0	10.0
$\gamma\gamma\gamma$	$+1.0$	-1.0	21594	2159.4	10.0
$\gamma\gamma\gamma\gamma$	-1.0	$+1.0$	1941	194.1	10.0
$\gamma\gamma\gamma\gamma$	$+1.0$	-1.0	1942	194.2	10.0
$e^+e^-\gamma$	$+1.0$	-1.0	1738455	17469600.0	0.1
$e^+e^-\gamma$	$+1.0$	$+1.0$	1718495	17275000.0	0.1
$e^+e^-\gamma$	-1.0	$+1.0$	1750065	17525700.0	0.1
$e^+e^-\gamma$	-1.0	-1.0	1723995	17265000.0	0.1

Table A.2: *Additional SM background generated with* WHIZARD *without preselection cuts.*

Danksagung

Mit Abgabe dieser Arbeit enden für mich vier ereignisreiche und spannende, beizeiten aber auch anstrengende Jahre in der FLC-Gruppe am DESY. Für die Unterstützung, die ich in dieser Zeit erhalten habe, und ohne die es für mich nicht möglich gewesen wäre, diese Arbeit zu schreiben, möchte ich mich bei vielen Personen bedanken.
Meinen Dank möchte ich zuerst Dr. Jenny List aussprechen, die es mir ermöglicht hat, diese Doktorarbeit zu diesem spannenden Thema anzufertigen. Insbesondere für ihre hervorragende Betreuung, und ihre Bereitschaft, auch die einfachsten Fragen, wenn nötig mehrmals, zu beantworten, bin ich dankbar. Nicht zu vergessen natürlich ihre Unterstützung in den letzten hektischen Monaten, durch die ich nie den Blick für das große Ganze verloren habe.
Desweiteren möchte ich mich bei meinen Bürokollegen Daniela, Christian, Moritz, Benedikt und Ulli für die angenehme Atmosphäre und die vielen hilfreichen Gespräche bedanken. Und für die von Euch, die diesen Trubel nicht schon hinter sich haben: Viel Erfolg!
Außerdem gibt es natürlich noch weitere DESYaner mit denen ich kein Büro geteilt habe, und zu denen ich immer mit Fragen kommen konnte: Mikael Berggren, Anthony Hartin, Gudrid Moortgart-Pick und noch vielen anderen, ein herzliches Dankeschön.
Ganz besonders möchte ich Dir danken, Johanna! Ohne Dich hätte ich die harte Zeit des letzten halben Jahres sicher nicht durchgestanden. Es ist schön, sich so auf Dich verlassen zu können und jemanden zu haben, der einem den Rücken freihält. Und natürlich Danke für die vielen Mittagessen, die ich nicht in der Kantine einnehmen musste...
Abschließend danke ich meinen Eltern für die liebevolle Unterstützung durch die langen Jahre des Studiums.